

Computational fluid simulations in clinical datasets for understanding thrombus formation before and after left atrial appendage occlusion

Jordi Mill Tena

DOCTORAL THESIS UPF / Year 2022

THESIS SUPERVISORS

Prof. Oscar Camara

Dr. Jérôme Noailly

Dr. Andy L. Olivares

Department of Information and Communication Technologies



*A les meves dos avies, Elisa i Rosa.
Allà des de on estiguen mirant, espero que estiguen orgullosos.
Cor i disciplina en tot el que es faci a la vida.*

Acknowledgements

*No bird soars too high,
If he soars with his own wings
-William Blake*

Avui em sento molt afortunat de poder escriure aquestes línies i compartir-ho amb vosaltres. La gent sol pensar que això es un viatge de quatre anys; també que en els agraïments no es pot donar gràcies a tothom.

Bé, respecte al primer punt, per mi no és un viatge de quatre anys, sinó un moment important d'un viatge que va començar molt abans. A la UPF, ja en són nou anys (que es diuen ràpid). D'aquests nou, sis simulant en el camp de l'enginyeria biomèdica i específicament en el cor (per tant, començant abans del PhD). Tot això m'ha fet arribar fins aquí. D'aquesta manera, aquesta tesi no és només el fruit de la feina feta durant quatre anys. I no hi hauria arribat sense l'ajuda, la formació i la bondat -i també la paciència- de la gent que m'ha envoltat en cada un d'aquests anys. La frase del William Blake amb la que comença aquesta secció es pot interpretar de moltes maneres si no hi ha un context¹. Malauradament, hi ha gent que agafa la visió més egoïsta d'aquesta frase, però en el context en què jo em vaig trobar i de qui me la va donar, l'entenc en el sentit que si estàs ben guiat i rodejat podràs aconseguir coses que ni havies pensat que podies fer, i la veritat és que això és el que ha passat amb aquesta tesi. D'aquesta manera espero que, tot i sabent que hi ha/hi haurà coses molt més importants a la vida, tots els mencionats avui us senti aquesta tesi una mica vostra en un dia tant important per mi.

Respecte al segon punt, no hi estic d'acord. Estic agraïdíssim a tothom qui ha col·laborat en major o menor mesura en aquest procés, per tant, prepareu-vos perquè venen uns agraïments llargs.

Per ordre cronològic vull començar donant per donar les gràcies als meus pares per la seva estima cap a mi i pel suport incondicional, però sobretot per ajudar-me a ser com soc avui. Gràcies a la meva germana Ester, per ensenyar-me que la base és el treball i la constància.

Gràcies a les meves àvies, a l'àvia Rosa per estar amb mi cada vespre i cada matí abans d'anar a l'escola perquè els meus pares treballaven. Encara recordo quan em vas ensenyar a cordar-me les sabates. A la meva àvia Elisa, per totes

¹L'autor va morir abans que es descobrís aquesta nota i per tant no se sap amb quin context la va escriure.

les tardes de diumenge que incloïen berenars i cartes, però sobretot per quan li deies a la mare: “Mira Jordi que buen chico es, puedes estar orgullosa”. No ho vaig reconèixer mai, però sincerament, era el meu moment preferit de la tarda. És impossible tenir millors àvies i sentir-se més estimat.

Gràcies a tota la resta de la família, però en especial al meu cosí Nil. Encara recordo quan a l'estiu del 2013, a la platja de Sant Salvador, mentre ens recuperàvem de les PAU em vas dir que havies canviat d'opció d'estudis i que havies triat enginyeria biomèdica a la UPF perquè t'havies llegit un llibre del Ricard Solé i que per tant, faríem la carrera junts. La resta crec que ja és història. Sempre he pensat que som uns privilegiats de poder haver viscut el que hem viscut durant quatre anys (i sumant) com amics, però també com a família.

Gràcies al Guillem Paz, a la Clara Vidal, a la Júlia Verdaguer, al Joan Garcia, al Bernat Torres, l'Adrià Garcia i a la Marta Espinosa. Gràcies per deixar-me respirar sempre, per refrescar-me i per confiar sempre en mi en els meus moments més baixos i transformar-los en bons. És un súper-poder molt infravalorat que vosaltres teniu. En especial vull donar les gràcies al Guillem, per estar des del dia u, literal, vint-i-quatre anys des de que ens vam conèixer. Podria escriure pàgines senceres de les coses que he après i admiro de tu, però em quedo en què sempre que ho necessitem, ens quedarà la plaça del barri on fer una cervesa fins altes hores de la nit. Sempre que em paro a pensar quines eren les possibilitats que teníem de trobar-nos acabo amb la mateixa conclusió: A mi ja m'ha tocat la loteria.

De la meva experiència a la UPF estic segur que sense saber el que m'espera en un futur sempre estarà com una de les millors experiències de la meva vida. Tot va començar preguntant-li al Pablo si jugava a bàsquet (amb un 1.95 m d'altura és la millor estratègia per trencar el gel), a l'Oscar que si em podria saltar una pràctica obligatòria per anar a fer l'examen del carnet de conduir i preguntant-li al Josep si em convidava a Eivissa amb tot el morro. A partir d'aquí comença un viatge (als campus de Poble Nou i del Mar, però també en altres ciutats europees) que tot i que semblaria que acabaria al cap de quatre anys, gràcies a déu encara continua i sé que si els necessito, tot i està súper-ocupats perquè són uns autèntics genis, sempre estaran allà. Gràcies a la Marta Molina, al Joan Puig, a la Núria Armengol, a l'Alejandro Antunes, al Pablo Miki Martí, al Sergio Moya, al Mikel Domingo, a la Irene Tena, a la Joana Gelabert, al Josep Soriano, a la Marina Bujosa i al Guillem Torrente. Però sobretot, moltes gràcies a tu, Roser. Com amb el Guillem podria estar hores argumentant perquè tothom hauria de posar una Roser Sanchez Todo a la seva vida, tanmateix avui només vull que sàpigues que cada vegada que faig una videotrucada la gent veu com al fons de la meva pantalla hi ha el pòster del Michael Jordan amb la frase que encapçala aquesta secció.

El pòster que em vas regalar abans que marxessis d'Erasmus a Islàndia. Aquest pòster em seguirà tota la vida. Un autèntic tresor, com ho és la nostra amistat.

Gracias a Eduardo Soudah, a Mariano Vázquez, a Abel Gargalló, y a Juan Carlos Cajas. Con ellos empezó todo. A los dos primeros por inspirarme con sus charlas que me motivaron a introducirme al mundo de la simulación y su ayuda durante estos años. A l'Abel per ensenyar-me tot sobre malles; han passat sis anys i encara perduren les teves lliçons. Com sempre et deia: “quina llàstima que no facis coses biomèdiques!”. A Juan Carlos Cajas por su supervisión durante mis meses al BSC, donde hice mi primera simulación seria, ni más ni menos que una FSI en aorta.

Capítulo aparte para ti, Alfonso, creo que ya te lo he dicho alguna vez, pero has sido mi hermano mayor en esta aventura de la ingeniería biomédica. Gracias por tratarme siempre tan bien desde que era un renacuajo recién llegado al BSC hasta el día de hoy. Siempre preocupándote, siempre enseñándome, siempre teniendo tiempo para mí, eres un ejemplo a seguir. Cuando me preguntan quién es el mejor ingeniero biomédico del mundo, digo sin pestañear: Alfonso Santiago. Junto con Messi de lo mejor que me ha dado Argentina.

After BSC, I had the opportunity to be at KCL simulating coronary arteries. I want to thank Mari Nieves Velasco, Nick Byrne, Simone Rivolo, Esther Puyol and Jack Lee for treating me so well while I was enjoying London. But special thanks to Ludovica Beraldi and Caleb Gakpetor who until today we have maintained a beautiful friendship and although they are far (also being super successful), I want to keep them close. Grazie Ludovica. Con te ho scoperto che i difensori di Mourinho possono essere anche bellissime persone. Thank you Caleb. I still remember the workshop where we met. I don't know when we will have time for this, but we have pending: 1) a trip to Ghana; 2) you to spend a whole summer (not a few days) in Barcelona; and 3) watch together a Man. Utd. – F.C. Barcelona game (hoping both teams will be recovered from their current setbacks and they will be dominating the continent again).

Entre la carrera i el doctorat vaig fer una petita i insignificant traïció a la UPF i vaig anar a fer el màster a la UB (el TFM, però, amb l'Oscar i l'Andy a la UPF; com he dit, petita traïció sense importància). La veritat és que va ser una etapa molt divertida. Bascos, valencians, irlandesos, suecs, mexicans i catalans, què podia sortir malament? Gràcies, Eskerrik asko, Gracias, Tak, Thanks to Adrián Perez, Ane Motoso, Alex Brugueroles, Alvaro Oyarbide, Ander Sainz, Ben Hesketh, Carlos Prieto, Jezyel Martinez, Jon Zabalo, Jorge Ferragud, Jorge Verdú i Lisa Månsson. Pero en especial al Álvaro Fernandez y a Ibai Genua por los momentos que compartimos durante el TFM.

Quan vaig decidir de fer-ho en ordre cronològic, realment m'ho vaig pensar dues vegades perquè els meus supervisors de tesi quedarien molt avall. No em preocupava el fet de no coincidir amb el format de les tesis actuals, sinó que no expressés de forma acurada la meva gratitud i el mèrit que realment es mereixen. Tanmateix, crec que el més important és que ells, personalment, ja saben la importància que han tingut en aquest viatge i lo agrait que estic. Gràcies al Oscar Camara, al Jérôme Noailly i al Andy L. Olivares.

Gràcies, Oscar. Crec que molt poques persones han dipositat en mi la fe que em tens tu. De vegades, i com t'he dit, encara no l'entenc. Hi ha moltes coses que les veiem diferent, i havent sigut així sempre me les has deixat compartir i les has tingut en compte, és realment bonic. El gran mestre Yoda va suar de valent per entrenar al jove Luke al episodi cinc de la guerra de les galàxies. No aspiro arribar a ser el salvador de la galàxia com el jove Luke (de fet, espero tenir una vida més tranquil·la que ell) però com ell fa, sempre recorreré a tu quan em noti perdut, ja sigui en el món laboral o el personal.

Gràcies, Jérôme, per tenir sempre un moment per mi quan tenia dubtes, per adaptar-te al que sentia que em venia de gust per fer recerca i donar-m'hi suport. Gràcies també per donar una visió diferent de la que podíem tenir l'Oscar i jo a causa del nostre background. Ha sigut un plaer tenir-te de supervisor.

Y a ti, Andy. Mientras estoy escribiendo esto aún no sé si se podrá añadirte de manera oficial como tercer supervisor o no. Pero como te dije, yo siempre diré que tú fuiste mi supervisor. Siempre estamos haciendo broma sobre el “mood chill” cubano. La gente que nos escuche podrá pensar, equivocadamente, que es porque los cubanos no se estresan o no les importa nada. Nada más lejos de la realidad. Es la capacidad de mantener la calma en momentos de alto estrés, lo admiro. Realmente una de las cosas que he mejorado más durante mi PhD es a manejar esas situaciones y separarlo de mi vida fuera de la oficina. Y eso es básicamente gracias a ti y a las interminables horas que hemos pasado trabajando juntos.

Grazas Marta Núñez por estar tan pendiente de min o primeiro ano para que todo saíse ben. Al igual que Amelia Jiménez, insuperable compañera de desktop y “hermana mayor” de toda la oficina. Que todo el mundo hable tan bien de ti y te quieran tanto lo dice todo. No podría añadir mucho más. Gracias, Amelia. Grazie Andrea per gli infiniti discorsi sul calcio. Sono sicuro che se non li avessimo fatti, avrei ottenuto il mio dottorato di ricerca prima, ma sarebbe stato molto più noioso.

També donar les gràcies a Milica Vujovic, Jordina Avilés, Adrià Arbués, Adrián

Martín, Rúben Doste, Oualid Benkarim, Guillermo Jiménez, Eric Lluch, Enric Perera, Mario Ceresa, Gabriel Bernardino, Cristina Gonzalez, Irem Cetin, Ainhoa Aguado, Carlos Yagüe i al team UB (Cristian Izquierdo, Victor Campello i Carlos Martin) pel tracte que han tingut amb mi en els moments que hem coincidit durant el doctorat. Moltes gràcies al Gerard Martí. Per tots els moments passats junts en els que inclouen tardes/nits al Camp Nou, però en especial tots els moments viscuts junts a la UPF.

A part de l'Oscar, el Jérôme i l'Andy, aquest PhD va començar amb un altre trio sense els quals no es podria explicar aquesta tesi: el Dr. Victor Agudelo, el Dr. Xavi Freixa i el Dr. Dabit Arzamendi. Gràcies a tots tres, però especialment els dos últims. Les hores de formació (en el seu temps "lliure") que m'han donat són impagables. La seva visió ha sigut crucial per aquesta tesi, però es que, a més, hi van creure des del minut zero. A part d'això, m'han deixat experiències molt boniques que per mi seran difícils d'oblidar com el meu primer CSI LAA a Frankfurt amb ells el 2018 o com el meu primer (i únic!) desmai a quiròfan al Clínic amb el Xavi.

Un dels matins que estava a l'Hospital de la Santa Creu i Sant Pau i que m'havia de reunir amb el Victor vaig rebre un missatge seu cinc minuts abans dient-me "se va unir un compañero mío, el Dr. Abdel H. Moustafa, que es doctor, pero que es muy friki, ya verás, te caerá bien". *God bless frikis then!* Sabeu la sensació aquesta des del minut u que parleu el mateix idioma? És extraordinari, no saps si era un metge o un enginyer biomèdic, l'heu de conèixer. Tot va ser molt fàcil amb ell. Al seu gran cor si afegeix una humilitat i unes ganes d'aprendre i connectar els dos mons (enginyeria i medicina) que fa goig. *Shukran*, Abdel, espero que la nostra amistat ja duri per sempre.

Però aquesta actitud no és només de l'Abdel. El Dr. David Viladés, el Dr. Lluís Asmarats, el Dr. Xavi Millán, el Dr. Pedro Li, la Dra. Laura Sanchis, el Dr. Pedro Cepas sempre han tingut una disposició magnífica a l'hora de respondre'm preguntes, via correu o inclús per telèfon. Aquesta autopista de coneixement i transferència que s'ha generat crec que és única (no confondre amb una simple col·laboració amb un hospital). És quelcom molt bonic, que s'ha de cuidar i que ha de marcar com ha de ser un futur on la medicina i l'enginyeria biomèdica treballin juntes per millorar cada dia la salut dels ciutadans. Gràcies a ells i a l'Hospital de la Santa Creu i Sant Pau i a l'Hospital Clínic de Barcelona.

Outside Barcelona I also found this attitude. Merci beaucoup Dr. Hubert Cochet not only for helping me all these four years and trusting on what we were doing in Barcelona but also to teach me how to assess thrombi on cardiac CT. It

seems insignificant but it has been crucial for this thesis.

Al 2019 vaig tenir l'oportunitat d'anar a Sendai (Japó) per una conferència internacional. Si ja de per se es una experiència única que et permet el doctorat, el fet de trobar-hi i conèixer el Pau Romero la va fer inoblidable . Poder visitar amb ell ciutats com Kyoto o el bosc de bambú, i establir amistat amb ell és un dels motius pels quals haver fet el doctorat ja val la pena. Gràcies Pau. Un matemàtic i valencià excel·lent.

El meu primer any de tesi va ser molt intens, entre d'altres coses perquè va ser la meva primera vegada donant classes. Tot i així, ara miro enrere i va ser un plaer ajudar en el que vaig poder als i a les alumnes d'aquella generació de màster i grau que van participar en les assignatura de MOS i CC (tal i com ells em van ajudar a mi perquè com a primer any donant classes, tenia moltes coses a millorar). D'aquesta generació han sortit grans enginyers i enginyeres biomèdiques, però n'hi ha dos que es mereixen menció especial ja que han acabat sent companys indispensables en aquest viatge. Parlo d'en Carlos Albors i en Xabier Morales que han acabat sent estudiants de doctorat a Physense. Són dos persones que si em diguessin de triar dos companys d'equip, sempre els triaria a ells. Ara em podria posar una medalla i dir que amb el meu ull d'observador de talents ja els havia detectat quan vaig ser professor seu (a les proves em remeto a on li enviava correus a l'Oscar dient que els necessitàvem per la causa), però es que, honestament, no era molt difícil d'adonar-se'n. Són dues persones que estàs uns minuts amb ells i ja veus que són especials. Eskerrik asko Xabier, t'ho he dit moltes vegades, però crec que ets una de les persones amb més talent que conec. Crec que ets capaç d'aprendre tot el que et proposis i això, juntament amb la bona persona que ets, fa que un es preguntis fins on pots arribar. Em moro de ganes de veure't progressar encara més com a enginyer biomèdic, però sobretot com a persona. A tu Carlitos, primer de tot dir-te que deixis de ser del Madrid. Quan hakis fet això, crec que ja no et quedaran gaires punts febles més. Gràcies, Carlos, crec que una de les coses que més em costarà acostumar-me ara que això que s'acaba és mirar al costat i no tenir un company com tu. Que sàpiga tant, que tingui una ètica de treball tan bona i que sobretot sigui tan bona persona. Et trobaré molt a faltar.

També és una (gran) sort per la universitat que acabessin aquí la Mireia Alenyà i la Mireia Masias. Gràcies per la vostra generositat. En un dels meus llibres preferits² vaig llegir que en el món hi havia dos tipus de persones: persones que només pensen en elles mateixes, i que menyspreen a la resta pel fet de sentir-se importants; i gent que fa el contrari, que és capaç d'imaginar el que senten els

²Obama, B.(2020). Una tierra prometida. Penguin Random House Grupo Editorial.

altres i s'esforça per ajudar-los a ser més feliços. Vosaltres clarament, esteu al segon grup, a part de ser unes investigadores brillants.

Com he dit, de la generació dels anys 2016-2020 han sortit grans enginyers i enginyeres biomèdiques. A part del Carlos i el Xabi també vaig tenir com alumnes dues enginyeres que un any després es convertiren en les meves primeres alumnes que supervisaria les seves tesis de grau. Parlo de l'Helena Montoliu i la Mariabel Pons. Gràcies per la paciència i la confiança. És un orgull veure ara com avanceu imparables en les vostres carreres professionals, però sobretot que encara us recordeu de mi de tant en tant per xerrar i posar-nos al dia. També donar gràcies als que han vingut després, on més que supervisar crec que es podria dir que hem fet ciència junts. He après un munt. Gràcies Eric Planas, Marian Iglesias i Mònica Font.

Una de les coses que més ràbia em fa del COVID19 (entre moltes d'altres), és que va fer que no pogués conèixer els estudiants de doctorat que entraven aquell any al departament. Això va fer que conegués a la Maria Segarra i l'Anaïs Espinosa relativament tard, tot i que a l'Anaïs ja l'havia vist defensar el TFM i ja vaig pensar que aquesta noia apuntava maneres (va fer una defensa de TFM brutal). Quins dos diamants tenen el Jerome i el Ralph! Moltes gràcies, Maria i Anaïs, per aportar sempre tan bon humor a tothom i transmetre-me'l a mi especialment. És parlar amb vosaltres i acabar rient sempre.

Gracias (merci beaucoup) a Benjamin Lalande, Valentin Comte (I hope one day I will be able to pronounce properly Bordeaux), Estefano Muñoz, Marta Saiz, Álvaro Bocanegra, Jorge Mateos, Pablo Acedo y Àngel Herrero. Ha sido corto, pero el futuro del departamento está en muy buenas manos y, además, ha sido un placer estar con vosotros.

Gràcies a la Lydia Garcia per acompanyar-me durant el doctorat i tenir una paciència infinita amb mi. Gràcies a la Carme Buisan per entendre i ajudar-me a compaginar inquietuds que m'anaven sortint durant el doctorat.

I felt in love with Norway when in 2018 I travelled for first time to this country with my family. Having the opportunity to live there for some months whereas I was doing a PhD stay at Simula three years later just made this feeling stronger. What an amazing country, and Oslo, what an amazing city. This great experience cannot be explained without Ehsan Khalili, Henrik Kjeldsberg, Kristian Valen-Sendstad, Hermenegild Arevalo, Maria Hernandez and the rest of Comphy group and staff. *Tussen tak!*. Also *tussen tak*, to Sirkurd Vittersø. It was not coincidence we met at Ullevaal Stadion (we have to give credit to Henrik for the assistance).

Thanks for the great discussions we had about FCB and to be such a faithful Barcelona fan although being so far.

Merci beaucoup Josquin Harrison. For all the science we did during pandemic. It was tough, but thank you for your work. I think at the end, we both can say it has been worth it.

Unfortunately, it had to be short, but I had a great and intense experience in Boston, a nice manner to end my PhD. All those years studying the computational side. . . and to watch Keegan Mendez and Manisha Singh how they manage and understand the cardiac mechanics from the flow loop it was like I was discovering a new research field. I really appreciate how well they and the rest of the Roche Lab at MIT treated me when I was there. An exemplary team as Keegan would say.

But it was not all said in Boston. The world is so big and so small at the same time. One afternoon I was on my way of leaving from the MIT Medical building when I saw one student leaving from the classrooms located at the ground floor. I knew that guy, he was Akshay! I met Akshay Jaggi during my 2nd year of PhD while he was doing a stay at UPF and from all the hundreds of students who cross the MIT campus we crossed ways. Thank you Akshay for the moments when you were in Barcelona, but also for the wonderful evening at Lamplighter Brewery plenty of interesting discussions. I am sure you will be an amazing physician from Harvard.

Per acabar donar gràcies a la Dra. Judit Novo. Encara recordo com en una consulta et vaig dir: “Si passo això i a més aconseguixo escriure la tesis et posaré a agrairments.” De cop vas riure i vas dir “No cal home!”. Però jo ho deia seriosament. Moltíssimes gràcies per estar allà. No es pot tenir millor metge de família, i un recordatori que la sanitat pública s’ha de defensar sempre.

Abstract

Atrial fibrillation is considered the most common arrhythmia in humans. Because the left atrium of the heart stops beating properly and begins to do so in an arrhythmic manner, the blood may become stagnant in a small cavity attached to the left atrium called the left atrium. If this happens, a thrombus forms in this cavity which can lead to a stroke. One of the possible treatments, especially if the patient has contraindications to anticoagulants is the closure of the left atrial appendage with a device introduced non-invasively. However, the reason why some shapes of left atrial appendages form a thrombus or not, or why after the intervention some patients form them on the device surface is not entirely clear. Blood velocity is known to be one of the most important factors in the process of thrombogenesis, but current imaging techniques do not have enough resolution to assess flow so locally. For this reason flow simulations based on computational fluid dynamics and numerical methods, already used in other sectors of the industry (e.g. aeronautics or automotive), could be used to predict which patients will form thrombus or not in a personalized manner. The thesis below aims to help clarify the role of flow in the thrombus formation process in patients with atrial fibrillation using computational fluid dynamics simulations personalized to each patient. To do this, the thesis is divided into three main contributions. First, a sensitivity analysis to test all the approaches published so far and new methods developed during the course of this thesis. Second, it will be shown how pulmonary veins, an understudied factor, have a key role in the hemodynamics of flow within the left atrium and therefore in thrombus formation along with other cavity morphological factors using the largest simulated cohort of patients to this date. Finally, it will be shown how the position of the device is key when creating local flow re-circulations at low velocities which can then activate the coagulation process forming a thrombus.

Keywords: left atrial appendage, occluder devices, sensitivity analysis, modelling parameters, patient-specific.

Resum

La fibril·lació auricular esta considerada la arítmia més comuna en humans. Degut a que la aurícula esquerra del cor deixa de bategar correctament i ho comença fer de una forma arítmica, la sang es pot quedar estancada en una petita cavitat adjunta a la aurícula esquerra anomenada orelleta esquerra. Si això passa, es forma un trombe en aquesta cavitat que pot derivar en una embòlia. Un dels possibles tractaments, sobretot si el pacient té contraindicació als anticoagulants es el tancament de la orelleta esquerra amb un dispositiu introduït de manera no-invasiva. Tot i així, el motiu per el qual algunes orelletes formen trombe o no, o perquè després de la intervenció alguns pacients en formen sobre la superfície dispositiu no esta del tot clar. Se sap que la velocitat de la sang es un dels factors més importants en el procés de trombogènesis, però les actuals tècniques d'imatge no tenen prou resolució per avaluar el flux de forma tant local. Per aquest motiu les simulacions de flux basades en la dinàmica de fluids computacional i en mètodes numèrics, ja utilitzades en altres sectors de la industria (p. e. aeronàutica o automobilística), podrien arribar a predir quins pacients formaran trombe o no de forma personalitzada. La tesis que trobareu a continuació intenta ajudar a esclarir el paper del flux en el procés de formació de trombe en pacients amb fibril·lació auricular utilitzant simulacions de dinàmica de fluid computacional personalitzades a cada pacient. Per fer-ho, la tesis es divideix en tres aportacions principals. En primer lloc, anàlisis sensitius, per testejar tots els mètodes provats fins ara i a on també es provaran mètodes nous desenvolupats durant el transcurs d'aquesta tesis. Segon, es mostrarà com les venes pulmonars, un factor molt poc estudiat, tenen un paper clau en la hemodinàmica del flux dintre de l'aurícula esquerra i per tant, en la formació de trombe juntament amb altres factors morfològics de la cavitat utilitzant el cohort de pacients simulat més gran fins el dia d'avui. Per últim, es mostrarà com la posició del dispositiu es clau a la hora de crear recirculacions de flux local a velocitats baixes que després poden activar el procés de coagulació formant un trombe.

Paraules clau: Orelleta esquerra, dispositius de tancament d'orelleta esquerra, anàlisis sensitiu, paràmetres de modelització, medicina personalitzada.

Contents

| | |
|--|-------------|
| List of figures | xx |
| List of tables | xxii |
| List of acronyms | xxii |
| 1 INTRODUCTION | 1 |
| 1.1 Motivation | 1 |
| 1.2 Research goals and context | 3 |
| 1.3 Outline of the thesis | 4 |
| 2 CLINICAL AND METHODOLOGICAL BACKGROUND | 7 |
| 2.1 Left atrial appendage characteristics | 7 |
| 2.2 Atrial fibrillation and left atrial appendage: a deadly relationship | 9 |
| 2.2.1 Atrial fibrillation and its management | 11 |
| 2.2.2 Virchow's triad | 15 |
| 2.2.3 Pulmonary veins and left atrial haemodynamics in medical imaging | 18 |
| 2.3 Modelling pipeline for patient-specific 3D fluid simulations in the left atrium | 19 |
| 2.3.1 Medical image segmentation and generation of the 3D surface and volumetric meshes | 21 |
| 2.3.2 Simulation setup | 23 |
| 2.3.3 Analysis of blood flow simulation results | 27 |
| 3 SENSITIVITY ANALYSIS OF FLUID SIMULATIONS IN THE LEFT ATRIA TO PREDICT THROMBUS FORMATION | 31 |
| 3.1 Introduction | 31 |
| 3.2 Methods | 32 |
| 3.2.1 Databases | 32 |
| 3.2.2 Mesh convergence and cardiac beat analyses | 33 |

| | | |
|----------|---|-----------|
| 3.2.3 | Inlet/outlet boundary conditions and rigid/dynamic mesh left atrial movement | 34 |
| 3.2.4 | Left atrial movement from dynamic computed tomography images | 36 |
| 3.2.5 | Analysis of fluid simulations | 39 |
| 3.3 | Results | 39 |
| 3.3.1 | Mesh and cardiac beat convergence studies | 39 |
| 3.3.2 | Inlet/outlet boundary conditions and rigid/dynamic mesh left atrial movement | 40 |
| 3.3.3 | Dynamic mesh approach for left atrial wall motion from dynamic computed tomography images | 44 |
| 3.4 | Discussion | 54 |
| 3.4.1 | Mesh and cardiac cycle convergence analysis | 54 |
| 3.4.2 | Boundary condition scenarios | 55 |
| 3.4.3 | In-silico indices of device-related thrombus | 56 |
| 3.4.4 | Left atrial wall motion from dynamic computed tomography images | 57 |
| 3.5 | Conclusions | 59 |
| 4 | ROLE OF LEFT ATRIAL MORPHOLOGY AND IN-SILICO HAEMODYNAMICS IN THROMBUS FORMATION | 61 |
| 4.1 | Introduction | 61 |
| 4.2 | Methods | 62 |
| 4.2.1 | Databases | 62 |
| 4.2.2 | Joint analysis of left atrial morphological parameters and in-silico haemodynamic indices | 64 |
| 4.2.3 | he role of the pulmonary veins on left atrial haemodynamics and thrombus formation | 67 |
| 4.3 | Results | 70 |
| 4.3.1 | Joint analysis of left atrial morphological parameters and in-silico haemodynamics | 70 |
| 4.3.2 | The role of the pulmonary veins on left atrial haemodynamics and thrombus formation | 73 |
| 4.4 | Discussion | 93 |
| 4.4.1 | Joint analysis of left atrial morphological parameters and in-silico haemodynamic indices | 93 |
| 4.4.2 | The role of the pulmonary veins on left atrial haemodynamics and thrombus formation | 94 |
| 4.5 | Conclusions | 97 |

| | | |
|----------|--|------------|
| 5 | IN-SILICO HAEMODYNAMICS TO IDENTIFY THE LEFT ATRIAL APPENDAGE OCCLUSION SETTINGS INDUCING DEVICE-RELATED THROMBUS | 99 |
| 5.1 | Introduction | 99 |
| 5.2 | Methods | 101 |
| 5.2.1 | Databases | 101 |
| 5.2.2 | The role of the pulmonary ridge on device-related thrombus | 104 |
| 5.2.3 | Prediction of device-related thrombus with fluid simulations | 106 |
| 5.2.4 | Influence of left atrial appendage occluder positioning and design on device-related thrombus | 107 |
| 5.3 | Results | 111 |
| 5.3.1 | The role of the pulmonary ridge on device-related thrombus | 111 |
| 5.3.2 | Prediction of device-related thrombus with fluid simulations | 112 |
| 5.3.3 | Influence of left atrial appendage occluder positioning and design on device-related thrombus | 116 |
| 5.4 | Discussion | 119 |
| 5.4.1 | The role of the pulmonary ridge on device-related thrombus | 119 |
| 5.4.2 | Prediction of device-related thrombus with fluid simulations | 120 |
| 5.4.3 | Influence of left atrial appendage occluder positioning and design on device-related thrombus | 122 |
| 5.5 | Conclusions | 124 |
| 6 | GENERAL DISCUSSION AND CONCLUSIONS | 127 |
| A | HEARTS IN THE ANIMAL KINGDOM | 135 |
| B | SENSITIVITY ANALYSES | 137 |
| B.1 | In-silico thrombogenic indices from the first sensitivity analysis | 137 |
| B.2 | Reynolds number in left atrial simulations | 139 |
| B.3 | Second sensitivity analysis: Flow in the LAA | 140 |
| C | ANALYSIS WITH FLUID-BASED PARTICLES | 145 |
| D | IN-SILICO HAEMODYNAMICS TO IDENTIFY THE LEFT ATRIAL APPENDAGE OCCLUSION SETTINGS INDUCED DEVICE-RELATED THROMBUS | 147 |
| D.1 | Device positioning | 147 |
| D.2 | Discrete phase modelling | 149 |
| D.3 | Analysis of the blood flow re-circulations | 151 |
| D.4 | Vorticity analysis | 152 |
| | Publications | i |

List of Figures

| | | |
|------|--|----|
| 2.1 | LAA Anatomy | 8 |
| 2.2 | Heterogeneity of the LAA | 9 |
| 2.3 | LAA types | 11 |
| 2.4 | Decision tree for LAA occlusion | 13 |
| 2.5 | LAAO devices | 14 |
| 2.6 | Virchow's triad | 17 |
| 2.7 | PV schemes from Kato's and Altinkayanak's | 18 |
| 2.8 | General fluid modelling pipeline | 20 |
| | | |
| 3.1 | Fluid modelling pipeline of the sensitivity analysis | 35 |
| 3.2 | Curves extracted from dCT | 38 |
| 3.3 | Beat convergence results | 40 |
| 3.4 | Results of the sensitivity analysis scenarios | 42 |
| 3.5 | Velocity results near the device | 44 |
| 3.6 | ECAP results for the different scenarios | 45 |
| 3.7 | Volume curves | 46 |
| 3.8 | Displacement of the LA | 47 |
| 3.9 | dCT validation using US | 48 |
| 3.10 | Validation of the different scenarios | 49 |
| 3.11 | LA and LAA patterns | 50 |
| 3.12 | S1 Pressure | 51 |
| 3.13 | haemodynamic indices results | 53 |
| | | |
| 4.1 | Cohort organisation and study workflow | 63 |
| 4.2 | LAA morphological parameters | 65 |
| 4.3 | LAA and LA angles | 68 |
| 4.4 | Velocity measurement plane | 70 |
| 4.5 | LA and LAA volume distribution | 73 |
| 4.6 | Description of the PVs types found in the cohort | 75 |
| 4.7 | The role of the PVs in LA haemodynamics | 77 |
| 4.8 | Results gamma angle | 79 |
| 4.9 | Groups for particles evaluation | 80 |

| | | |
|------|---|-----|
| 5.1 | Explanatory figure of DRT | 101 |
| 5.2 | DRT evolution - Case from H.Clínic | 105 |
| 5.3 | Different scenarios to study the influence of the PR | 105 |
| 5.4 | Examples of PR definition | 106 |
| 5.5 | Scheme of the patient-specific computational workflow to predict the risk of DRT formation after LAAO implantation | 107 |
| 5.6 | LAAO positions | 109 |
| 5.7 | PR flow-dynamics simulations results | 112 |
| 5.8 | Results of the computational modelling analysis to predict DRT | 115 |
| 5.9 | Particle distribution at the LAA | 118 |
| 5.10 | DPM results | 119 |
| A.1 | Porcine heart | 136 |
| A.2 | Computational workflow for feline heart simulations | 136 |
| B.1 | ECAP and RRT results. All scenarios. Patients 1 and 2 | 138 |
| B.2 | ECAP and RRT results. All scenarios. Patients 3 and 4 | 138 |
| B.3 | ECAP and RRT results. All scenarios. Patients 5 and 6 | 139 |
| B.4 | Velocities at the ostium for all the scenarios | 140 |
| B.5 | Flow in the LAA - early systole | 141 |
| B.6 | Flow in the LAA - late systole | 142 |
| B.7 | Flow in the LAA - late diastole | 143 |
| C.1 | 5 PV outliers boxplot | 145 |
| D.1 | CAD devices | 148 |
| D.2 | Wall-film separation | 149 |
| D.3 | Particles attached to the LAA - Plot | 150 |
| D.4 | Average velocity near the device - Plot | 151 |
| D.5 | Streamlines near the device - mid-end systole | 153 |
| D.6 | Streamlines near the device - end diastole | 154 |
| D.7 | λ_2 results - mid-end systole | 155 |
| D.8 | λ_2 results - end diastole | 156 |

List of Tables

| | | |
|------|--|-----|
| 2.1 | Variability of left atrial appendage features | 10 |
| 2.2 | Review of DRT in literature | 15 |
| 2.3 | Review of LA simulations literature | 22 |
| 2.4 | Review of haemodynamic indices in the literature | 30 |
| 3.1 | Information about the cohort | 32 |
| 3.2 | Mesh convergence study-1M | 40 |
| 4.1 | Significant morphology features | 71 |
| 4.2 | haemodynamic indices results | 72 |
| 4.3 | Clinical data of the cohort | 74 |
| 4.4 | Significant statistics | 78 |
| 4.5 | Result of the particle study, grouped by number of PVs and type of alignment. | 81 |
| 4.6 | Pulmonary vein contribution - 3 PV | 82 |
| 4.7 | Pulmonary vein contribution - 4 PV | 84 |
| 4.8 | Pulmonary vein contribution - Type A (4 PV) | 84 |
| 4.9 | Pulmonary vein contribution - Type NA (4 PV) | 85 |
| 4.10 | Pulmonary vein contribution - Type CW (4 PV) | 85 |
| 4.11 | Pulmonary vein contribution - 5 PV | 87 |
| 4.12 | Pulmonary vein contribution - Type A (5 PV) | 87 |
| 4.13 | Pulmonary vein contribution - Type NA (5 PV) | 88 |
| 4.14 | Pulmonary vein contribution - Type CW (5 PV) | 88 |
| 4.15 | Pulmonary vein contribution - 6 PV | 89 |
| 4.16 | Pulmonary vein contribution - Type A (6 PV) | 90 |
| 4.17 | Pulmonary vein contribution - Type NA (6 PV) | 90 |
| 4.18 | Pulmonary vein contribution - Type CW (6 PV) | 91 |
| 4.19 | Pulmonary vein contribution - 7 PV | 92 |
| 5.2 | Patients of the control group | 103 |
| 5.1 | Patients of the DRT group | 104 |
| 5.3 | Velocity and ECAP results | 113 |

| | | |
|-----|--|-----|
| 5.4 | Mean velocities in systole and diastole | 116 |
| B.1 | Reynolds numbers of the models | 140 |
| D.1 | Device sizes | 148 |
| D.2 | Device volumetric compression | 149 |
| D.3 | Presence of flow re-circulation and stagnation | 152 |

List of Acronyms

| | |
|-------|--|
| ABP | agent-based particles. |
| AF | atrial fibrillation. |
| AIC | Akaike Information Criterion. |
| ALE | arbitrary lagrangian-eulerian method. |
| BC | boundary conditions. |
| BMI | body mass index. |
| BSA | body shape area. |
| BSRLL | basilar segment right lower lobe pulmonary vein. |
| CAD | coronary artery disease. |
| CFD | computational fluid dynamics. |
| CT | computed tomography. |
| CVA | cerebrovascular accident. |
| CW | chicken wing. |
| dCT | dynamic CT. |
| DM | dynamic mesh. |
| DRT | device-related thrombus. |
| ECAP | endothelial cell activation potential. |
| FDM | finite difference method. |
| FEM | finite element method. |
| FSI | fluid-structure interaction. |
| FVM | finite volume method. |
| GCV | great cardiac vein. |
| GT | ground truth. |
| IB | immersed boundary. |
| KE | kinetic energy. |

| | |
|------|-------------------------------------|
| LA | left atrium. |
| LAA | left atrial appendage. |
| LAAO | left atrial appendage occlusion. |
| LCX | left circumflex artery. |
| LIPV | left inferior pulmonary vein. |
| LLL | left lateral ridge. |
| LOM | ligament of Marshall. |
| LPN | left phrenic nerve. |
| LS | left side. |
| LSPV | left superior pulmonary vein. |
| LV | left ventricle. |
| LVEF | left ventricular ejection fraction. |
| MPR | multiplanar reconstruction. |
| MR | mitral regurgitation. |
| MRI | magnetic resonance imaging. |
| MV | mitral valve. |
| NOAC | novel oral anti-coagulation. |
| NS | navier-stokes. |
| OAC | oral anticoagulants. |
| OSI | oscillatory shear index. |
| PA | pulmonary artery. |
| PDL | peri-device leaks. |
| PR | pulmonary ridge. |
| PV | pulmonary vein. |
| PVs | pulmonary veins. |
| Qc | Q-criterion. |
| RF | residual fraction. |
| RIPV | right inferior pulmonary vein. |
| RLL | right lower lobe pulmonary vein. |
| RML | right middle lobe pulmonary vein. |
| RRT | relative residence time. |
| RS | right side. |

| | |
|-------|---|
| RSME | root mean square error. |
| RSPV | right superior pulmonary vein. |
| RT | residence time. |
| RUL | right upper lobe pulmonary vein. |
| SR | shear rate. |
| SSR | shear strain rate. |
| SSRLL | superior segment right lower lobe pulmonary vein. |
| TA | thermal analysis. |
| TAWSS | time-averaged wall shear stress. |
| TC | tracer concentration. |
| TIA | ischaemic attack. |
| TOE | trans-oesophageal echocardiogram. |
| TTE | trans-thoracic echocardiography. |
| US | ultrasound. |
| VENC | velocity sensitivity. |
| WSS | wall shear stress. |

Chapter 1

INTRODUCTION

1.1 Motivation

Atrial fibrillation (AF) is considered the most common of human arrhythmias. According to the Global Burden of Disease, the estimated prevalence of AF is up to 33.5 million individuals, as it affects 2.5–3.5% of populations in several countries [95, 61].

AF is currently seen as a marker of an increased risk of stroke since it favours thrombus formation inside the left atrium (LA). Around 99% of thrombi in non-valvular AF are formed in the left atrial appendage (LAA), a muscular ear-shaped cavity in the LA [22]. LAA shapes are complex and variable among the general population; researchers have sought to classify LAA morphologies and relate them to the risk of thrombus formation. However, none of these classifications have achieved a scientific consensus due to their qualitative interpretation and lack of consistent results [140].

First-line treatments for non-valvular AF patients are anticoagulants. Unfortunately, a non-negligible number of patients have a high risk of bleeding or other contraindications to anticoagulants, due to other comorbidities. Alternative treatments for those patients include: percutaneous epicardial approaches for LAA ligation [120]; external closure of the LAA (e.g., AtriClip procedure; Atricure, Inc., Westchester, OH, USA) [10]; and the implantation of a device for left atrial appendage occlusion (LAAO), where the endothelium is replaced by a nitinol surface after LAAO. However, sub-optimal implantation of the device can lead to device-related thrombus (DRT). DRT increases the rate of stroke and has become an important concern, since the different anti-thrombotic therapies used after LAAO have not lowered its incidence, i.e., around 2-5% [6, 38, 82].

Hence, identifying potential factors that promote thrombus formation is essential to ensure an optimal and personalized device implantation, as well as a

tailored post-procedural follow-up. Surprisingly, very few studies have considered the pulmonary veins (PVs) as a factor for thrombus formation although PVs directly affect LA haemodynamics [24, 45, 36, 92]. On the other hand, PV configuration and orientation have been proved to be a key player in radiofrequency ablation therapy (e.g., PVs isolation) since they are a preferential origin of ectopic foci in atrial fibrillation [23]. Some large-scale studies have classified PV configurations into different anatomical categories [5], but they have never been considered as a factor in thrombus formation. The studies that have studied PV orientation in thrombus formation were using a very small cohort [70]. Moreover, there is high anatomical variability among the population, where most humans have 4 PVs but there are reported cases of 3, 5, 6 or even 7 PVs present. Even more, the orientation of how the PVs are inserted into the LA can differ substantially from patient to patient.

In both cases, thrombi inside the LAA and at device's surface, blood flow haemodynamics is a factor to consider for the assessment of the risk of thrombus formation, following Virchow's triad principles [138]. Low velocities and stagnated flow have been associated with the triggering of the inflammatory process and, therefore, the risk of thrombus generation [7, 85].

However, on daily clinical practice, LA haemodynamics can only be studied using echocardiography images, usually simplified to a single blood flow velocity value at one point in space and in time (e.g., centre of LAA ostium at end-diastole) [11]. Advanced imaging techniques such as 4D flow magnetic resonance imaging (MRI), allowing a more complete blood flow analysis, are emerging, but they still provide limited information in the left atria [85]. At this juncture, patient-specific models (e.g., digital twin concept [19]) based on computational fluid dynamics can provide a better haemodynamic characterisation of the LA and LAA, deriving in-silico indices describing blood flow at each point of the geometry over time. In the last decade, there have been several attempts to develop fluid simulation frameworks for the blood flow analysis of the human LA and LAA in relation to thrombogenic risk, including explicit models of thrombus formation [136, 110]. In addition, the effect of LAA closure has been modelled [143, 63, 25], the most advanced investigations having incorporated LAAO devices [1, 25] and the relation thereof to DRT [93]. However, they have only been applied to a very limited number of patient-specific cases, except in a two recent studies with a cohort of simulated patients above fifty [92, 115].

Beyond differences on number of patients, the cited works use a wide range of boundary conditions and of modelling choices in terms of inlet/outlet setup (e.g., velocities and pressures in the pulmonary veins and mitral valve; from literature or patient-specific), LA wall behaviour (e.g., rigid, modelled dynamic mesh, deformation from medical images or fluid-structure interaction), number of simulated cardiac cycles (e.g., from 1 to 20), and mesh resolution (e.g., from 0.4 to

30×10^5 mesh elements), among other factors. Unfortunately, the absence of joint benchmark studies with reliable ground truth makes it difficult to identify which are the optimal configurations to achieve realistic simulations. Moreover, there is no consensus on the most appropriate metrics for the quantification of blood flow simulations. Due to the extensive range of modelling options reported in LA computational fluid dynamics, there is a need for best practice guidelines to build robust models and achieve reliable simulations as regards relevant clinical outcomes in LAAO. Systematic verification and validation studies, following the ASME VV40 guidelines [134] with in-vitro and/or ex-vivo data, are also missing due to the difficulties to obtain ground-truth data.

Computational fluid dynamics (CFD) allows testing of different possible therapeutic scenarios before the intervention, thus reducing operation costs with enhanced efficiency [98], and accelerating research and development for understanding fluid mechanics within device testing [135]. However, comprehensive preoperative simulations may take between hours and days depending on the complexity of the anatomy and potential interactions between cardiac tissue and the blood flow to be modelled [135], thus limiting its application in a clinical environment.

Motivated by the clinician's questions on the interaction between haemodynamics and thrombus formation, and how to translate the findings to daily clinics, we designed computational modelling pipelines to demonstrate how in-silico simulations can help on AF and LAAO treatment management, specially to avoid thrombus formation.

1.2 Research goals and context

The overall objective of this thesis is to analyse different in-silico simulation setups and workflows so the thrombus formation process in AF can be better understood and, therefore, improve medical treatments and follow-up strategies to avoid LA thrombus-related stroke. Despite the known relationship between blood stagnation and thrombus formation, it is not still clear why some AF patients will develop thrombus and others will not. Simulations may shed some light on it, since they can capture flow phenomena with high spatio-temporal resolution. However, getting large enough clinical datasets to design robust computational modelling pipelines and to validate the realism of simulations (e.g., prediction accuracy on thrombus formation) is difficult. As a result, there is a large heterogeneity of modelling workflows leading to very different results, without reaching a consensus in the community, and hampering their translation onto clinical environments.

The overall objective can be broken down into the following contributions:

1. To analyse the current state of the art of fluid modelling in the LA. We

studied the different boundary conditions used in the literature, identifying their strengths and weaknesses, and potential improvements.

2. To understand the effect of LA haemodynamics and PV on thrombus formation in patients with non-valvular AF. This could allow to find better thrombotic risk indices, better stratify the patient's risk and improve the subsequent treatment.
3. To understand the influence of LA haemodynamics and device positioning on DRT after LAAO implantation. A better understanding of DRT could lead to improve the success procedure rates, the current devices design and have better follow-up management of patients after LAAO implantation.

1.3 Outline of the thesis

To fulfil the objectives mentioned above, the present document is divided in the following five chapters.

Chapter 2: Clinical and methodological background. In this chapter, the key clinical and methodological concepts of the manuscript are presented. It can be divided in two main sub-parts: 1) Clinical problem: we review atrial fibrillation and its relation with LAA-related thrombus, paying special attention to the Virchow's triad, and medical treatments for avoiding thrombus formation; 2) Computational tools: we review the main computational modelling steps and parameters commonly used to assess thrombus formation.

Chapter 3: Sensitivity analysis of fluid simulations in the left atria to predict thrombus formation. In this chapter, we study the boundary conditions (BC) and setups present in the literature to model LA haemodynamics, also proposing improvements to make simulations more realistic. More specifically, the use of CFD and dynamic meshes schemes with different inlet/outlet configurations are analysed. Clinical data was used for the validation of simulation results since thrombus characteristics at follow-up was available for a dataset of LAAO patients.

Chapter 4: Role of left atrial morphology and in-silico haemodynamics in thrombus formation. In this chapter, we investigate the relationship between LA/LAA morphological characteristics, blood flow patterns and thrombus formation in non-valvular AF patients. We demonstrate the importance of PV configuration and LAA orientation on LA/LAA haemodynamics (e.g., LAA washing

in/out) in the largest cohort of patient-specific LA fluid simulations created so far.

Chapter 5: In-silico haemodynamics to identify left atrial appendage occlusion settings inducing device-related thrombus. In this chapter, the relevance of the pulmonary ridge (PR) in LAAO device positioning for device-related thrombus (DRT) is proven with computational fluid simulations in a small dataset of patients. Other factors related to DRT such as the influence of the device's design are also investigated. Finally, a score based on in-silico haemodynamics indices is proposed to predict the risk of thrombus formation.

Chapter 6: General discussion and conclusions In this chapter, we conclude the dissertation by summarising and discussing the main findings of the present work, suggesting new directions for future research.

Chapter 2

CLINICAL AND METHODOLOGICAL BACKGROUND

When people talk about human heterogeneity they basically think about physical characteristics (e.g., eye colour, hair, height, etc.). At the same time, there is a feeling that when you talk about internal organs they are much more homogeneous. For example, the heart will always be a heart, when healthy having four cavities with the same arteries and veins going in and out, independently on the person. Some differences appear when comparing among species (in fact, the pig and dog hearts are considered close enough to the human heart to use them for medical experiments, Figure A.1). Nothing could be further from the truth. In the studies presented on this manuscript, approximately one hundred fifty LA have been processed. The author of this manuscript was not able to find two equal LAs. Beyond size differences, there were two structures that make the LA extremely heterogeneous: PVs, with varying number and orientation; and LAA. The variability in PVs and LAA could be the key to understand why some patients who suffer from AF develop thrombi and others do not. In this chapter we try to describe those structures, how they are related to thrombus formation, and how the modelling community is facing such a complex problem.

2.1 Left atrial appendage characteristics

In the primitive atrium, developed in the fetus during the third week, a small cavity is formed just over the mitral valve (MV), in the antero-lateral LA wall, below the left PVs, only separated by the PR. Just below the LAA the left circumflex artery can be found (See Figure 2.1)[66].

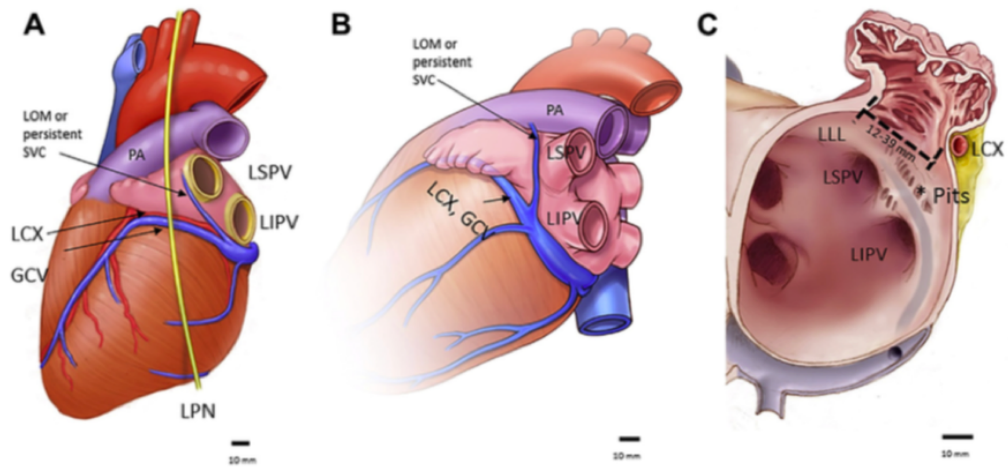


Figure 2.1: Left atrial appendage (LAA) structure. The posterior side of the LAA lies close to the left superior pulmonary vein (LSPV), the left inferior pulmonary vein (LIPV), and the ligament of Marshall (LOM). The superior side of the LAA (A, B) is related to the pulmonary artery (PA) and left PA. The left circumflex artery (LCX), the great cardiac vein (GCV), and the left ventricle (LV) lie in close proximity to the inferior LAA side. The left phrenic nerve (LPN) crosses postero-laterally. On the endocardial side (C), the left lateral ridge (LLL) at the corresponding area of the LOM separates the LAA ostium from the LSPV. There are several pits or diverticula around the indistinct border of the ostium. Figure from [100].

Some researchers have hypothesised the LAA cavity could act as a decompression chamber [3]. In sinus rhythm, when the left atrium is filling the LAA could act as a conduit, and as additional volume reservoir to the LA thanks to his trabecular tissue and major distension than the LA. Moreover, the LAA contracts in the end of ventricular diastole to help the filling of the left ventricle. The LAA is also related to the endocrine function, being one of the main sites of production of atrial natriuretic peptide [3].

The LAA presents an extreme 3D heterogeneity, adopting many shapes and orientations, as can be seen in Figure 2.2, where different LAA cases analysed in our work are shown. Table 2.1 from Cresti and Camara [21] summarises the the variability of LAA in different morphological parameters. Because of the LAA heterogeneity, researchers and physicians have proposed classifications according to LAA shape. The most adopted one includes four LAA shape categories (see Figure 2.3): 1) Chicken wing (CW); 2) Cactus; 3) Windsock; and 4) Cauliflower [137]. However, a consensus among the community has not been reached on the usefulness of such classification since it is based on qualitative descriptions of the LAA shape (see caption of Figure 2.3). Furthermore, Bai et al. [9] found

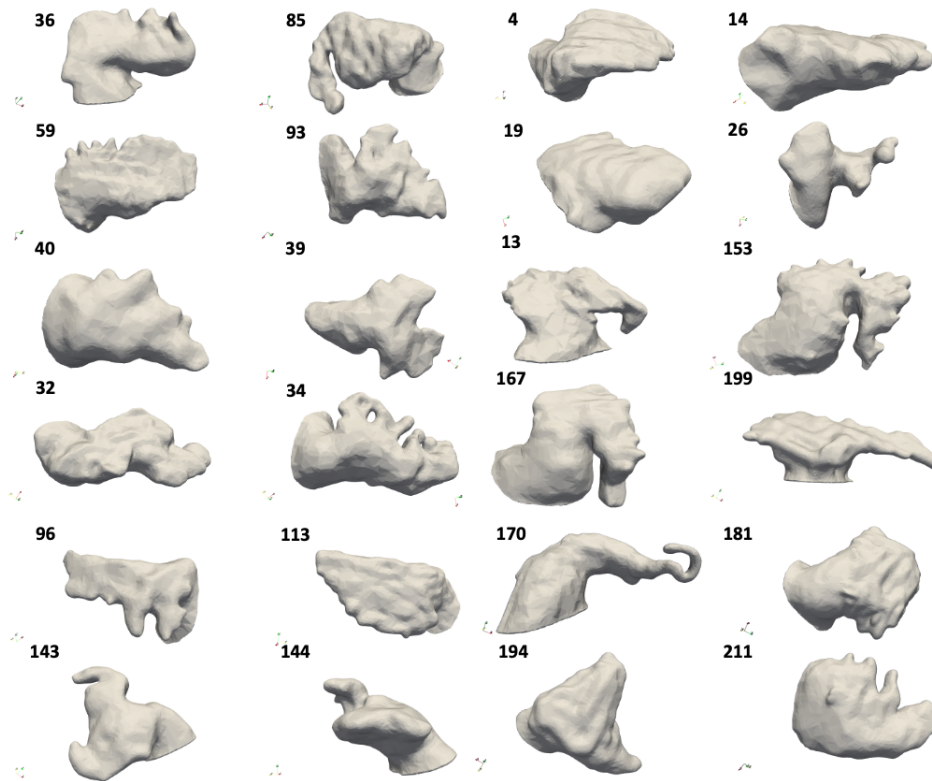


Figure 2.2: Different left atrial appendage (LAA) morphologies analysed with the developed computational techniques. Among them, LAA shapes corresponding to the different categories in the classical classification of Di Biase et al.[27] can be found, including chicken wing (i.e., n°199), windsock (i.e., 85), cactus (i.e., 40) and cauliflower (i.e., 93) cases. Also a seahorse shape can be found (199). Depending on the 2D point of view, the perception of the 3D shape can significantly change.

statistically significant bias in LAA morphology classification by operators when using different imaging modalities. In consequence, new morphologies such as the seahorse shape [12] have been proposed, and new ways to classify LAAs, as the one proposed by Yaghi et al. [141] that is based on the angulation of the LAA's base with respect to the tip.

2.2 Atrial fibrillation and left atrial appendage: a deadly relationship

The LAA variability discussed in the previous section arouse interest because, as Johnson et al. [64] defined in 2000s, the "LAA is the most lethal attachment

Table 2.1: Variability of the left atrial appendage. Table extracted from Cresti and Camara, 2022 [21]. LAA: left atrial appendage; CW: chicken wing; CT: computed tomography; TOE: trans-oesophageal echocardiogram; HV: Horizontal View; VV: Vertical View; MPR: multiplanar reconstruction.

| Feature | Description | Normal Values | References |
|-------------------|---|---|---------------|
| Morphology | 3D conformation of the LAA | CW (48%) Cactus (30%) Windsock (19%) Cauliflower (3%) | [137] |
| Area | Planimetric area as measured at mid-esophageal 2-chamber TOE view | 4.4 ± 1.1 (HV) 3.6 ± 1.2 (VV) | [96] |
| Volume (mL) | CT/TOE | 9.21 ± 3.18 (CT) 4.54 ± 1.70 (3D TOE) | [9] |
| Axial orientation | The conformation and the direction along the long axis | Tip usually antero-superior, sometimes inferior or posterior | [66] |
| Curvature | The grade of body curving | In 75% of cases in turns $90^\circ \pm 20^\circ$ after 14 ± 4 mm | [129] |
| Thickness | Wall thickness as measured at mid-esophageal 2-chamber TOE | 0.4 – 1.5 mm | [59] |
| Lobe | The number of lobes that forms the LAA | Single lobe (20% – 70%) 2 lobes (16% – 54%) 3 – 4 lobes (remaining) | [132] [27] |
| Ostium width | Larger diameter | 16 – 7 – 21.7 mm | [102] |
| Ostium depth | The longest distance from LAA Orifice to the tip | 20 – 31.2 mm | [102] |
| Orifice area | MPR 3D TOE | 1.57 – 3.19 cm | [102] |
| Emptying velocity | The speed of emptying as assessed with pulsed Doppler | 58 ± 18 cm/s | [96] |

to the heart”. According to Cresti et al.[22] 99% of the thrombus in patients who suffer non-valvular AF are generated in the LAA. Those thrombi are very likely to produce an stroke after a while. AF can be defined as a heart condition that produces an irregular and fast heart rate. It is the most common of human arrhythmias and its incidence is specially high in elderly people [111].

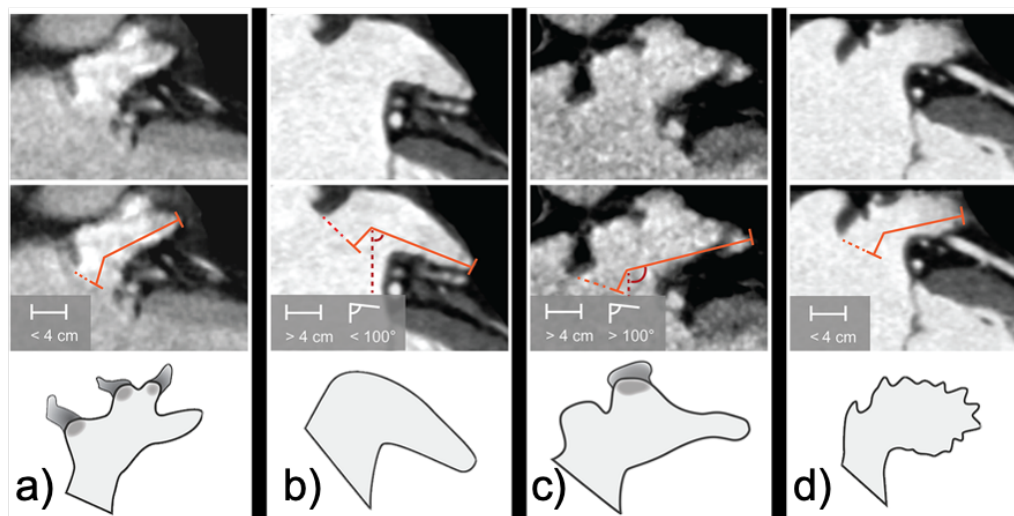


Figure 2.3: a) Cactus: dominant lobe and hosts secondary lobes on superior and inferior surfaces; b) Chicken wing: Has a dominant lobe but with bends and may have secondary lobes; c) Windssock: Has a dominant lobe, the location and number of secondary lobes varies, can have even tertiary lobes; d) Cauliflower: No dominant lobe, the number is variable, it has a complex internal structure and irregular orifice. Image from Korkhonen et al., 2015 [71].

2.2.1 Atrial fibrillation and its management

AF can be identified in the ECG due the absence of the P wave, producing a disorganised auricular activity that is replaced by flutter waves going from 350 to 600 bpm, and generating a variable and irregular conduction to the ventricles. In addition, AF can be observed for the lack of both, the X wave in the jugular pulse, and the A wave (atrial kick) at the the mitral flow Doppler signal.

Depending on how much it lasts, the AF can be classified into: paroxysmal, when the patient recovers spontaneously within the first week, normally the first 24-48 h; persistent, when AF does not disappear during the first week; and permanent when AF is chronic.

As it will be detailed in the following section, AF and thrombus formation are strongly related. When a patient suffers from AF one of the first things to be decided is whether the patient needs to follow anti-thrombotic treatment. According to the guidelines there are two scenarios when anti-thrombotic treatment is needed: 1) the patient has a mechanical valve prosthesis or suffers from other structural heart diseases; or 2) the patient has an score of two (3 in women) or higher in the CHA₂DS₂-VASc score. The latter is the most widely score for stroke risk stratification in AF patients. It is based the following conditions (following name order): congestive heart failure, hypertension, age \pm 75 years, diabetes,

prior stroke or transient ischaemic attack or thromboembolism, vascular disease, age between 65 and 74 years and sex. However, for assessing the risk of left atrial appendage thrombus, other factors are needed to make it more accurate, leading to another scales such as the CHA₂DS₂-VASc-RAF [90]. For instance, the type of AF has the same weight in CHA₂DS₂-VASc, not differentiating among paroxysmal, persistent or permanent categories. Other parameters that are strongly related with thrombotic risk such as chronic kidney disease, obesity, sedentary lifestyle, obstructive sleep apnea syndrome, and the type and severity of underlying heart disease, are missing.

Therefore, to better evaluate LAA function and thrombogenic risk, additional imaging parameters have been evaluated in the literature, such as the LAA ejection fraction [9]. Reduced LAA contractility, measured by speckle-tracking echocardiography, E/e' and e' velocity, as well as LA strain, have been found to independently correlate with LAA thrombus in non-valvular AF [21]. Currently, these parameters are not routinely used to assess LA performance, and inferring LAA thrombotic risk, due to difficulties in defining appendage boundaries and ostium dimensions, in addition to absence of technical standards and normal reference values.

When it comes to AF treatment in relation with thrombogenic risk, the first option is oral anticoagulants (OAC). However, a non-negligible proportion (30% to 50%) of eligible patients of non-valvular AF cannot not receive OAC due to contraindications or perceived risks of bleeding [101]. Another option is long-term therapy with warfarin or novel oral anti-coagulation (NOAC), but last studies have shown that it is associated with lifetime major bleeding risks of 2.1% to 3.6% per year [106, 18, 51]. In addition, patients with renal and liver dysfunctions, high risk of falls, noncompliance, and those requiring dual anti-platelet therapy after stenting, can be counter-indicated to NOAC treatment, too. As for warfarin, there are additional issues with drug and diet interaction, the need for monitoring, and a narrow therapeutic window with time in therapeutic range of only 50% to 60% [47, 57]. Even with the relatively well-tolerated NOAC, the proportion of patients discontinuing NOAC during study follow-up was estimated between 15% to 25% [106, 18, 51]. At this juncture, over the recent years the left atrial appendage occlusion has emerged as an alternative strategy to lifelong oral anti-coagulation and NOACs to treat patients with non-valvular AF, and specially with risk of bleeding [112, 58] (see Figure 2.4).

Left atrial appendage occlusion

The left atrial appendage occlusion procedure starts with the insertion of a catheter into the body through the femoral vein. From there, the catheter advances through the bloodstream until it reaches the right atrium. Once there, the physician looks

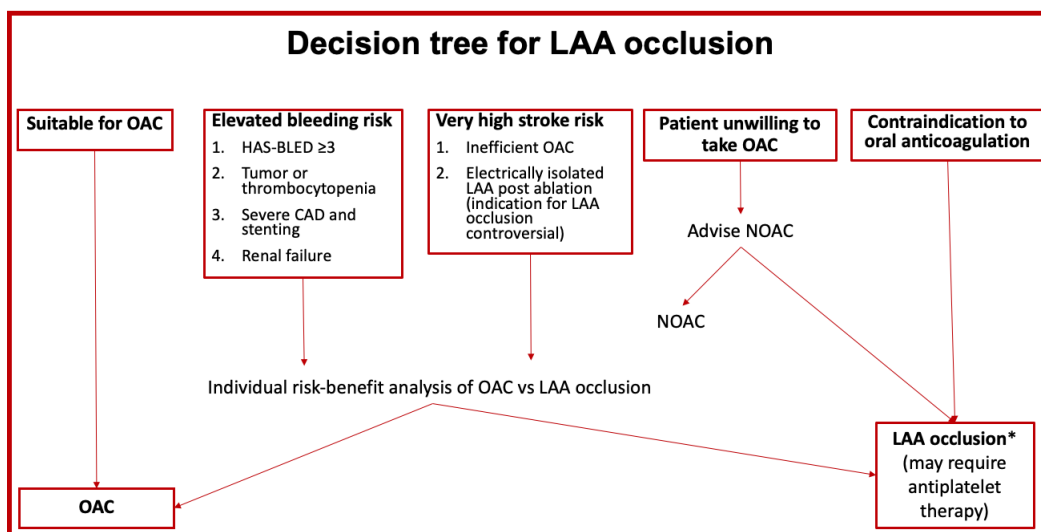


Figure 2.4: Decision tree for left atrial appendage closure. LAA: left atrial appendage; OAC: oral anticoagulant; NOAC: novel oral anti-coagulation; CAD: coronary artery disease. From Glikson et al., [48]

for the fossa ovalis, where a puncture will be made to move from the right atrium to the left one, through the inter-atrial septum. The physician then pushes the device through the delivery catheter into the left atrial appendage, where the LAAO device opens up like an umbrella and is permanently implanted. Once the device is in place, a thin layer of tissue grows over it in about 45 days (i.e., endothelialisation). Depending on the cardiologist's experience and the available imaging resources, the procedure can be performed with general or local anaesthesia.

Glikson et al. [48] divided the current catheter-based devices for LAAO in three groups (see Figure 2.5):

1. Plug device: Endovascular delivery of a device lobe or umbrella obstructing the neck of the LAA, thereby preventing blood flow into the body of the LAA. LAA exclusion relies on sealing/endothelialisation of the device lobe/umbrella. In this sub-group we can find the WATCHMAN and WATCHMAN FLX (Boston Scientific, Marlborough, MA, USA), the WaveCrest (Biosense Webster, Diamond Bar, CA, USA) and the CLAAS (Conformal Medical, NH, USA).
2. Pacifier device: Endovascular delivery of a device with a lobe or umbrella and an additional disc to seal the ostium of the LAA from the left atrial side. LAA exclusion relies on sealing/endothelialisation of the device lobe/umbrella. This sub-group is composed by: AMPLATZER Cardiac Plug (ACP), Amulet

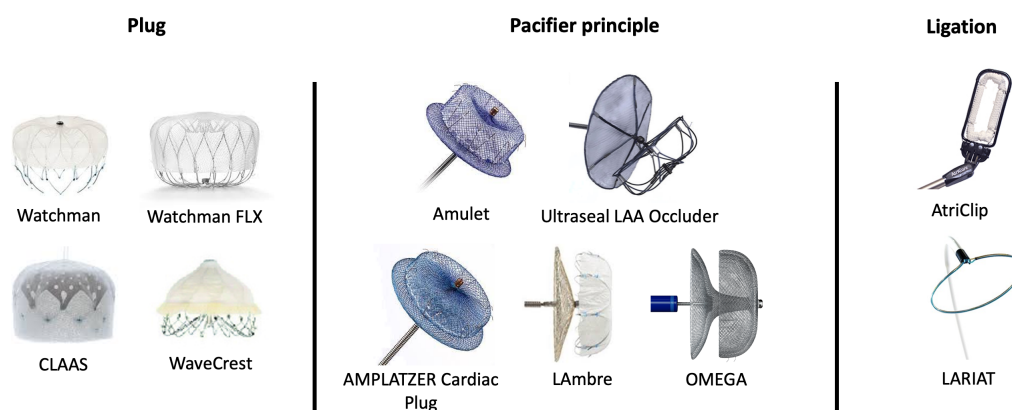


Figure 2.5: Types of left atrial appendage devices and classification of most used devices.

(both Abbott Vascular, Santa Clara, CA, USA), Ultraseal (Cardia, Inc., Eagan, MN, USA), LAMBRE (Lifetech, Shenzhen, China), Omega (Vascular Innovations, Thailand).

3. Ligation device: To snare and ligate the body of the LAA using an endocardial and epicardial approach. LAA exclusion relies on complete ligation of the neck of the LAA. The systems included in this sub-group are the LARIAT (SentreHEART, Inc., Redwood City, CA, USA) and AtriClip procedure (Atricure, Inc., Westchester, OH, USA).

The endovascular devices mentioned above are usually based on nitinol, and are deployed through a dedicated sheath, either by retracting the sheath or by pushing the device out, or a staged combination of the two. This procedure requires pre-procedural planning, either with echocardiography (usually trans-esophageal echocardiography, TOE) or computed tomography (CT) imaging. After the procedure, specialists recommend follow-up and surveillance every six or twelve months to control the presence of peri-device leaks (PDL) or device-related thrombus (DRT). In fact, DRT has become a major concern due to its incidence rate (2% to 5%, see Table 2.2) and the increased rate of associated strokes (Table 2.2). Despite the use of different anti-thrombotic therapies, the rate of DRT has not changed [14]. Regarding the PDL, the cutoff of 5 mm to separate benign leaks from those that require continued anticoagulation is an arbitrary cutoff and has generated a lot of controversy [97] about when consider a PDL benign or not. In fact, a recent study from Alkhouli et al., [4] showed how small (>0-5 mm) leaks after LAAO were associated with a modestly higher incidence of thromboembolic and bleeding events whereas large leaks (>5 mm) were not associated with adverse events, although higher proportions of these patients were maintained on anticoagulation.

Table 2.2: Review of the different clinical trials and studies about device-related thrombus (DRT) and associated stroke rates. TIA: transient ischaemic attack.

| Study | N | Device | DRT | Associated Stroke |
|----------------------------------|------------|-----------------------|--------------|-------------------------|
| PROTECT [113] | 478 | Watchman | 4.2% | 3/20(15%) |
| ASAP [114] | 150 | Watchman | 4% | 1/6(16.7%) |
| ACP Multicentre [124] | 339 | ACP | 3.2% | 0% |
| Lempereur et al., [78] | 2, 118 | Watchman, ACP, Amulet | 3.9% | TIA 2.4% Stroke 4.9% |
| Lakkireddy et al., [72] | 712 | Lariat | 2.5% | - |
| Pillarisetti et al.,[107] | 259 219 | Lariat Watchman | 1.6% 3.7% | - |
| EWOLUTION [13] | 1, 025 | Watchman | 3.7% | 0/28(0%) |
| Amulet PMR [73] | 1, 088 | Amulet | 1.5% | 1/10(10%) |
| PROTECT, PREVAIL, CAP, CAP2 [31] | 1, 739 | Watchman | 3.7% | 17/65(26.2%) |

Arguably, adding or intensifying anti-coagulant therapy has proven to effectively reducing the thrombotic burden in patients diagnosed with DRT [8]. However, intensive anti-thrombotic therapies in these high-risk patients may translate into a higher risk of bleeding. Therefore, identifying predictors of DRT is essential to individualise suitable anti-thrombotic treatments post-LAAO, and identify those patients who would need a closer follow-up. According to the literature [42, 48], potential factors that can increase the risk of DRT are patient-related (e.g., poor left ventricular ejection fraction (LVEF), poor compliance with anti-thrombotic therapy, smoking, spontaneous echo contrast, history of thromboembolism) and implant-related (e.g., uncovering of the pulmonary ridge, deep implantation, incomplete LAA occlusion). Yet there is no consensus on which of these factors are the most critical ones.

2.2.2 Virchow's triad

The name relates to Rudolf Virchow (1821-1902), a physician that elucidated the mechanisms of pulmonary thromboembolism, defining the terms embolism and thrombosis. The Virchow's triad tries to explain the process of thrombosis and consists of three factors [138]:

1. **Endothelial damage of the wall.** The endothelial damage in the LA is produced by the remodelling of the cavity resulting from the underlying arrhythmia. The LA size will favour blood stasis and other valvulopathies such as mitral stenosis [118]. However, patients with MV regurgitation are protected against thrombus formation, due to the high velocities produced

in that area [22]. Also, changes on the extracellular matrix induces fibrosis, myocyte hypertrophy and/or sclerosis. However, evidence suggests that abnormal changes in the extracellular matrix are not related to the presence of atrial fibrillation itself, but are probably a consequence of various co-existing co-morbidities (e.g., hypertension). All these injuries create a favourable prothrombotic state [84].

2. **Hypercoagulability.** In healthy individuals, when there is an injury, the inflammation process is triggered, von Willebrand factor and interleukin 6 are delivered, which activate the coagulation cascade that leads to the formation of thrombin (factor II). Thrombin converts fibrinogen into fibrin (factor I), which forms a tightly connected mesh that stabilizes the platelet plug. In patients with AF, a part from the damage of the wall, abnormal changes in the promoters of the coagulation cascade and other blood constituents are produced which lead to an state of hypercoagulability. Specially, the increased fibrin turnover has been reported in patients with acute and onset or chronic atrial fibrillation as well as abnormal prothrombotic indices (e.g. fibrin D-dimer) [83, 116, 84].
3. **Blood stasis.** Finally, increase of haematocrit is required for thrombus formation since it will be the core of the thrombus. The clustering of the red blood cells will be produced by blood stasis due to wall motion abnormalities [138] caused by the arrhythmia and the platelet activation. In addition, the presence of the AF seems to promote the progressive LA dilatation, thus, amplifying the potential of stasis [122]. In presence of mitral stenosis, LA dilatation is even more increased and leads to further propensity of stasis and thrombosis. On the other hand, mitral regurgitation seems to reduce the risk of a cardiovascular event with AF [99].

Therefore, the LA and LAA morphologies are not enough to explain the complex process of thrombosis; haemodynamics have a key role too. Lately, several studies [27] have claimed that LAA with chicken-wing shapes are somewhat protected against thrombus formation. It does not mean that CW LAA shapes do not form thrombi; actually, the 13% of the thrombus cases in our studies had a CW LAA morphology. Other morphological parameters such as the ostium, LAA length, main lobe could also have a role on promoting thrombus generation [44]. None of the mentioned morphological parameters has been able to discern patients who are going to develop thrombus. In fact, in some of them different studies published contradictory results, for instance, Lee et al., [77, 76] found that the large ostiums were a good predictor for stroke. On the contrary, Khurram et al., [69] found the opposite, that small orifices were associated with a higher risk of stroke, and this may explain the association between cauliflower LAA morphology and

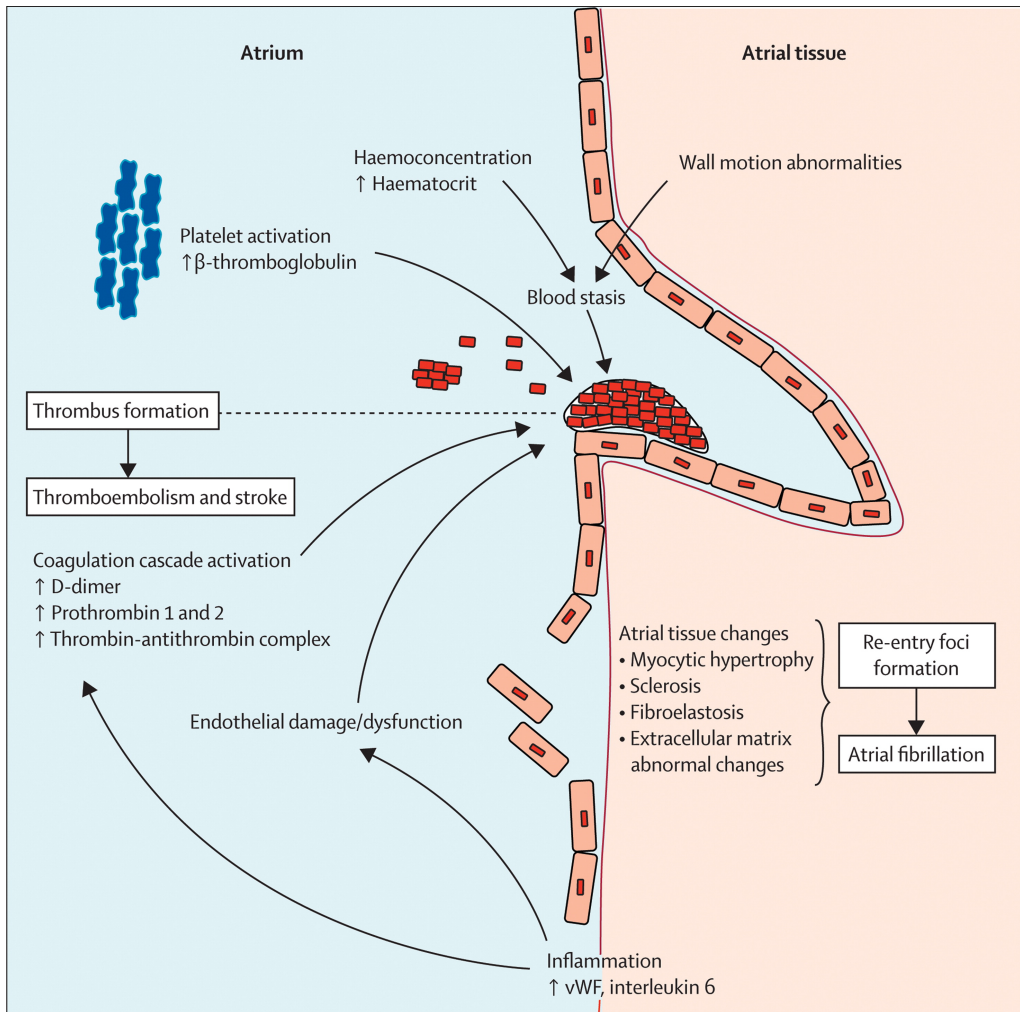


Figure 2.6: Components of Virchow's triad for thrombogenesis in atrial fibrillation. Image from Watson et al. [138].

stroke. Those differences could be produced also by the lack of standardisation of measuring points. Therefore, there is a need to further incorporate haemodynamic indices to generate better predictors and improve our understanding of thrombus formation.

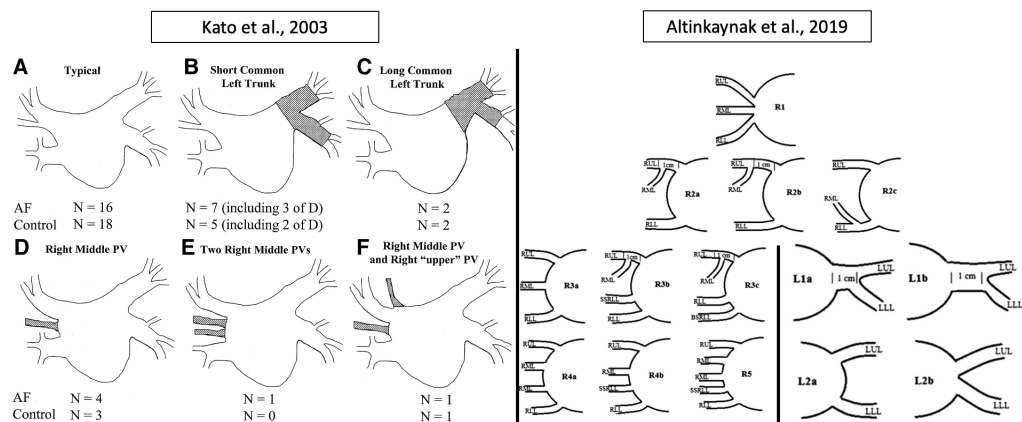


Figure 2.7: Left: Branching pattern of pulmonary vein (PV) anatomy in atrial fibrillation (AF) patients and controls. Shaded portions indicate different parts from typical anatomy. A: Typical branching pattern. B: Short common left trunk. C: Long common left trunk. D: Right middle PV. E: Two right middle PVs. F: Right middle PV and right “upper” PV. Image from [68]. Right: Modified diagrams showing right pulmonary venous drainage patterns by Marom et al., [87]. BSRL: basilar segment right lower lobe pulmonary vein; RLL: right lower lobe pulmonary vein; RML: right middle lobe pulmonary vein; RUL: right upper lobe pulmonary vein; SSRL: superior segment right lower lobe pulmonary vein. 1 cm: distance from the ostium. Image from [5].

2.2.3 Pulmonary veins and left atrial haemodynamics in medical imaging

Pulmonary vein configurations

Beyond LAA variability, another part of the LA that is equally or more variable than the LAA, are the pulmonary veins (PVs). Kato et al. [68] were pioneers on describing PV heterogeneity, sparked by the discovery of the importance of PVs in catheter ablation procedures for AF patients (i.e., pulmonary vein isolation). Kato et al. [68] divided the studied (27) patients in five groups according to their PV configuration (see Figure 2.7). The number of PV ranged from three to six: Group A was the most common group, having 4 PVs; Group B and Group C patients had 3 PVs, differing on where the left inferior PV (LIPV) merges with the left superior one (LSPV); Group D cases had 5 PVs; and Group E and Group F individuals had 6 PV, but with variations on the right PV orientations. Years later, several studies in small cohorts [109, 65] found PV configurations similar to Kato et al. [68].

Marom et al. [87] re-organised the types of PV configurations proposed by Kato et al. [68] after studying CT images from a cohort of 201 patients. Their first differential contribution was to group the right side and left side separately. Secondly, they found a higher variability of the PVs on the right side that, combined

with the left side PVs, could reach 7 PVs in total. More recently, Altinkaynak et al. [5] analysed a dataset of 550 cases, in agreement with PV configurations proposed by Marom et al. [87], with a slight modification at the left PVs (see Figure 2.7).

Left atrial haemodynamics: vortices and the influence of the PVs

Fyrenius et al. [43] studied haemodynamics and blood flow vortices inside the LA using MRI in 11 healthy patients. In all analysed subjects, a main vortex was observed in the atrium during systolic and diastolic diastasis (mean duration of systolic and vortices of 280 ms and 256 ms, respectively). The blood volume within the vortices predominantly originated from the left pulmonary veins; inflow from the right PVs passed along the vortex periphery, constrained between the vortex and the atrial wall. Later, Suwa et al. [128], examined 32 patients with 4D flow MRI to understand vortex formation at the LA, observing the same vortex as Fyrenius et al. [43]. Subsequently, Markl et al. [86], was one of the first to study blood flow dynamics in the LA and LAA in AF patients using 4D flow MRI in 75 patients (60 AF, 15 control). However, the study was more focused on the velocity magnitude for blood stasis rather than the velocity patterns, probably due to the lack of resolution of the images.

One of the first papers to study LA haemodynamics with computational simulations was performed by Dahl et al. [24], analysing how the PV configuration determines the flow inside the LA, and showing complex blood flows inside the cavity. However, they assumed the LA wall to be rigid, and the study only included one real case, the other examples being modifications of the PV from the original ones, lacking proper and rigorous validation of the obtained results. Years later, Koizumi et al., [70] run patient-specific simulations based on 4D flow MRI data to study thrombus formation in the LA and validating computational model results. They found in the 4D flow MRI same vortices as in Suwa et al. [128], but they could not be replicated by the simulations, likely due to simplified information about LA wall motion. Years later, Duenas-Pamplona et al., [30] replicated successfully those vortices through an in vitro model but using an idealised LA geometry. Nevertheless, in that study the authors highlight the importance of the PVs orientation to generate vorticity inside the LA.

2.3 Modelling pipeline for patient-specific 3D fluid simulations in the left atrium

From an engineering point of view, the heart is extremely complex to model. As Santiago et al. [123] claimed, three physics mechanisms converge in the heart: 1)

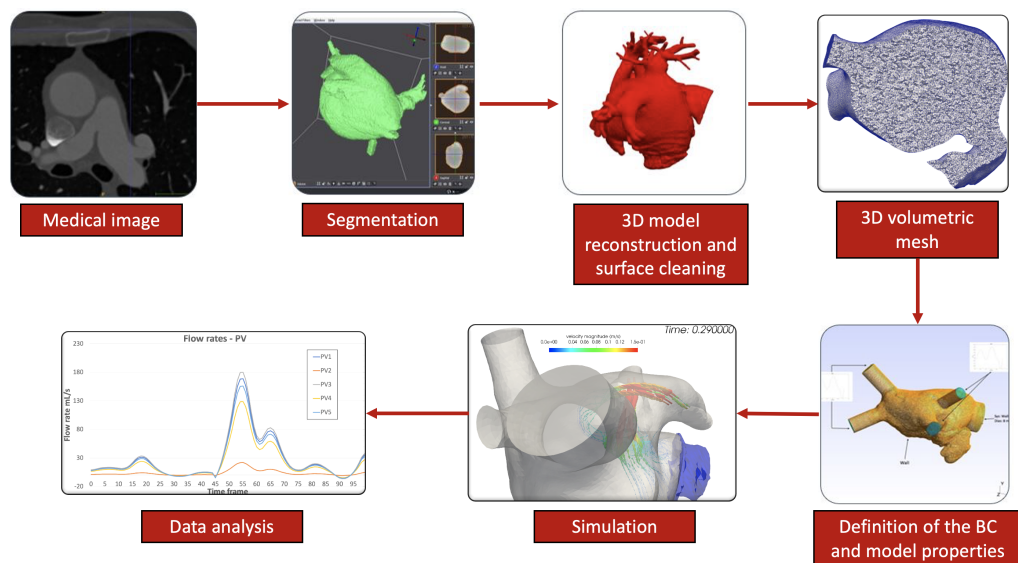


Figure 2.8: Generic modelling pipeline for patient-specific 3D fluid simulations of the left atria: 1) Segmentation of the medical images; 2) Cleaning and preparation of the surface 3D model; 3) Generation of the volumetric mesh; 4) Definition of boundary conditions (BC) and model properties; 5) Running the solver; and 6) Analysis of the simulation results.

electrical depolarisation; 2) tissue mechanics; and 3) blood dynamics. Modelling each one independently is already difficult; trying to couple the three of them can truly be a titanic task. For this reason, it is important to simplify the problem to be able to study the phenomenon of interest without losing precision.

Figure 2.8) illustrate a typical modelling pipeline for patient-specific 3D fluid simulations of the left atria, including: segmentation of the medical images; creation of 3D surface and volumetric meshes; definition of boundary conditions and simulation setup; running the solver; and analysis of the simulation results. In LA blood flow modelling, the most used scheme to study the relationship between LA morphology, haemodynamics and thrombus formation is Computational Fluid Dynamics. The geometrical domain is usually discretised into a mesh of varying number of elements, ideally built based on patient-specific anatomies obtained from medical images. Moreover, the number of mesh elements is another important modelling aspect to consider, with a trade-off between computational cost and model accuracy. Specifically for LA-based fluid simulations, the number of cardiac cycles to simulate is an additional relevant factor, usually with the first cardiac beats disregarded to reach convergence. To obtain realistic simulations, it is also key to find the right combination of inlet/outlet boundary conditions (i.e., pressures, velocities), based on as much patient-specific data as possible. More-

over, blood flow patterns can largely be influenced by atrial wall motion, specially in healthy subjects; in AF patients, it is a matter of debate. In any case, most advanced and rigorous LA fluid simulation studies include LA wall motion in different ways, through imposing generic- or image-based LA wall deformation (e.g., dynamic mesh approaches) or with fluid-structure interaction (FSI) methods.

All these modelling choices and the lack of benchmarking data has led to a large variety of modelling pipelines (see Table 2.3), without a consensus on the optimal choices to obtain more realistic simulations. Additionally, there is also a great variability in how fluid simulations are analysed, and which parameters are used to study thrombus formation (see Table 2.4).

2.3.1 Medical image segmentation and generation of the 3D surface and volumetric meshes

Independently of the physics to be simulated, every simulation process starts with the definition of the domain where the simulation is going to be run. For 3D patient-specific modelling of the LA, a computational pipeline is needed starting by the extraction of the anatomical part of interest from the medical images to the 3D volumetric mesh where the simulation will be run.

The anatomy of the LA can be extracted from medical images such as CT, MRI or 3D rotational angiography (3DRA), among others. Open-Source software tools such as Slicer 4.10.1¹, with semi-automatic region-growing techniques could be employed to create binary masks of the LA. Subsequently, surface meshes can be created with the classical Marching Cubes algorithm, followed by smoothing processes to correct irregularities generated by the segmentation process, often involving manual removal of self-intersecting faces and non-manifold edges. Subsequently, some modifications of the meshes are made to define the inlet/outlet BC areas and to ensure simulation convergence and flow development such as adding tubes at the MV or the PVs. For instance, it is important to define standard criteria for PV length such as cutting before the first branch coming out from the LA. Software tools such as Meshlab 2016.12², and Meshmixer 3.5³ can be used to build these surface meshes and apply the required mesh edition manipulations. In order to simulate blood flow patterns inside the LA, a volumetric mesh needs to be generated. The Delaunay algorithm is usually applied, which is available in Open-source tools such as Gmsh 4.0.4⁴, creating a tetrahedral mesh. Additionally, the Netgen⁵ software can also be used for further optimisation of the

¹<http://www.slicer.org/>

²<http://www.meshlab.net>

³<http://www.meshmixer.com>

⁴<http://gmsh.info>

⁵<https://ngsolve.org>

Table 2.3: Review of boundary conditions and different modelling choices for left atrial fluid simulations reported in the literature. PV: pulmonary veins; MV: mitral valve; geoms: number of geometries; lit: literature; vels: velocities; press: pressures; dCT/MRI: dynamic computed tomography/magnetic resonance imaging; diff: DM: dynamic mesh; Diff: diffusion; SB: spring-based;FSI: fluid–structure interaction; IB: immersed boundary method; * synthetic LA and realistic LAA geometries; ** estimated value from element size reported in the paper; *** 256 synthetic and 114 real LAA; *4 one real case but it is modified to create a cohort N=10.

| Study | PV Inlet | MV Outlet LV Systole/Diastole | Wall Behaviour | Cardiac Cycles | Mesh Elements ($\times 10^5$) | Geoms |
|----------------------|--------------------|-------------------------------|----------------|----------------|---------------------------------|---------|
| Zhang [143] | Lit. vels. | Wall/0 mmHg | FSI | 3 | 2 | 1 |
| Dahl [24] | Patient flow | Added mass flux | Rigid | 1 | 21 | 1 |
| Koizumi [70] | 10 mmHg | Wall/8 mmHg | dMRI | 5 | 1.5 | 1 |
| Orani [105] | dCT vels. | Wall/dCT flow | dCT DM | 5 | 3.6–5.5 | 2 |
| Bosi [16] | 0 mmHg | Lit. vels. | Rigid | 4 | 22–30 | 4 |
| García-Isla [45] | Lit. vels. | Wall/8 mmHg | Rigid | 1 | 3.5–5.0 | 36 * |
| Dillon-Murphy [28] | 0 mmHg | dMRI flow | dMRI DM | 10 | 12 ** | 2 |
| Masci-a [89] | Flow balance | Lit. flow | Sinusoidal | 5 | 17–19 | 5 |
| Aguado [1] | Lit. vels. | Wall/8 mmHg | Rigid | 1 | 2–9.6 | 2 |
| Jia [63] | Synthetic vels. | Wall/0 mmHg | Rigid | 10 | 0.4 | 1 |
| Feng [39] | Lit. press. | Lit. press. | FSI | 2 | 1 | 1 |
| Masci-b [88] | Flow balance | Lit. flow | Sinusoidal | 7 | 8–10 | 2 |
| Wang [136] | 10 mmHg | Lit. flow | Rigid | 20 | 24 | 1 |
| Mill-a [93] | Lit vels. | Wall/8 mmHg | Diff. DM | 2 | 5 | 2 |
| D’Alessandro [25] | Flow balance | Lit. vels. | Sinusoidal | 5 | 17–19 | 2 |
| Qureshi [110] | Synthetic vels. | Unknown | dMRI DM | 15 | 4 | 2 |
| García-Villalba [46] | Flow balance | Wall/Open | Rigid/dCT | 20 | 5–9 ** | 6 |
| Fang [36] | AF vels. | Wall/0 mmHg | FSI | 4 | Unknown | 1 * |
| Sanathkani [119] | Lit. vels. | Open/0 mmHg | Rigid | 25 | 3.5–5 | 16 |
| Fanni [37] | Pressure | Lit. vels. | Rigid | 25 | 23–42 | 4 |
| Mill-b [92] | AF press. | AF vels. | SB. DM | 3 | 8–9 | 52 |
| Morales [94] | Lit. vels. | Wall/8 mmHg | Diff. DM | 3 | 3.5–9 | 370 *** |
| Mill-c [91] | AF press. | personalized vels. | Rigid/Diff. DM | 1–2 | 1–5 | 6 |
| Corti [20] | Pressure and vel. | Pressure | harmonic DM | 6 | 1–2 | 4 |
| Dueñas-Pamplona [29] | Velocity | 0 mmHg | Rigid | 4 | 8 | 10*4 |
| Gonzalo [50] | personalized vels. | 0 mmHg | dCT | 15 | dCT DM | 6 |
| Rigatelli [115] | personalized vels. | IB | Wall/Open | 16 | Unknown | 60 |
| Pons [108] | AF press. | Lit. vels. | SB. DM | 3 | 8–9 | 30 |

resulting volumetric meshes. Hexahedral meshes can also be built, even if they have more difficulties to cope with patient-specific complex geometries.

2.3.2 Simulation setup

Computational fluid dynamics

Computational Fluid Dynamics (CFD) can be defined as the simulation of fluid engineering systems using mathematical models and numerical methods (i.e., discretisation methods, solvers, numerical parameters, and grid generations). The properties and the behaviour of the fluid, required to solve the physical problem, are described by Navier-Stokes (NS) equations. However, they need to be discretised with numerical techniques, from its analytical form, to be solved in a computer. The most popular numerical methods used in CFD are Finite Difference (FDM)⁶, Finite Element (FEM)⁷ and Finite Volume (FVM) methods⁸. In this manuscript CFD simulations were run based on the FVM scheme available at the commercial solver Ansys Fluent 19 R3 (ANSYS Inc, United States).

NS equations are based on the conservation law of physical properties of fluid. Blood is regularly modelled as Newtonian and incompressible in the literature, as density is considered constant. However, there are interesting recent studies exploring non-Newtonian behaviour in LA-based fluid simulations[50]. In a fluid with Newtonian behaviour the viscous stresses produced by the flow are linearly correlated at every point with the local strain rate, which is the rate of change of its deformation over time. Therefore, stresses are proportional to the rate of change of the fluid's velocity vector. An incompressible fluid refers to a flow in which the density is constant in a infinitesimal volume that moves with the velocity⁹.

Inlet/outlet boundary conditions and model properties

Boundary conditions (BC) are constraints necessary for the solution of a boundary value problem. A boundary value problem is a differential equation (or system of differential equations) to be solved in a domain on whose boundary a set of conditions is known. Boundary value problems are extremely important as they model a vast amount of phenomena and applications, from solid mechanics to heat transfer, from fluid mechanics to acoustic diffusion. Thus, when in this manuscript we talk about BC, we talk about the data imposed in the limits of our domain. The boundaries of our domain, the LA, can be divided in three parts, the inlets (the

⁶https://en.wikipedia.org/wiki/Finite_difference_method

⁷https://en.wikipedia.org/wiki/Finite_element_method

⁸https://en.wikipedia.org/wiki/Finite_volume_method

⁹<https://www.grc.nasa.gov/www/k-12/airplane/nseqs.html>

PVs), the outlet (the MV), and the wall of the LA. The best and reliable data is defined and used, the best will be the solution given by the equations. To the LA wall, to indicate that it is wall, pardon the redundancy, velocity is defined equal to 0. Then movement can be applied if DM is used. But inlets and outlets are where there is more variety of configurations (see Table 2.3). In these regions, either pressures or velocities can be defined. We try to ensure that there is always one of each, and that not all the domain is defined by the same type of BC (e.g., velocity at both inlet and outlet), otherwise the problem is considered to be over-defined. Also sometimes the outlet (MV in our case) is treated as rigid wall, but as we have mentioned, what you are really doing is defining zero velocity there. One of the reasons for the lack of consensus among the community, it relates with the difficulty to have access to data that will completely condition your entire setup and modelling strategy. First, you will try to get patient-specific data, if it is available, the type of data will determine your settings. For example, if from a patient dataset, the velocity curves to their MV are available, then you will try to take advantage of it and use velocity to the mitral valve even if that forces you to use pressure to the pulmonary veins (and vice versa). If no patient data is available, you will have to search in clinical papers or generate artificial curves that mimics the behaviour you want to simulate (see Table 2.4).

Left atrial wall motion behaviour

Fluid-structure interaction: In CFD, we are not solving how the flow interacts with the solid structure that surrounds it. If this wants to be studied, then a FSI scheme can be used instead. FSI is the process where a fluid and a solid interact through a wet surface, with forces and displacements influencing each other. In our clinical problem, it could be seen as the contact layer between blood (CFD) and tissue (solid mechanics simulation). In that system there are two domains, the fluid and the solid. In the fluid domain, NS equations are solved while meshes are simultaneously deformed. There are two main solvers for deforming meshes: (1) the arbitrary Lagrangian-Eulerian (ALE) method, which deforms the fluid mesh using the imposed boundary displacements; or (2) the immersed boundary (IB) technique, which uses a fixed mesh in the fluid and interpolates the wet surface position from the Lagrangian solid mesh.

Consequently in the solid domain, the model for tissue mechanics is solved. On that layer the continuity of the displacements and normal stresses of both domains needs to be fulfilled. As in this scheme, two physics problems needs to be solved and coupled, the process is more computational demanding than CFD. Moreover, FSI requires a good knowledge of atrial wall characteristics, including its morphology (e.g., atrial wall thickness) and material properties (e.g., elasticity). Unfortunately, LA tissue properties are still under study and have not been

completely unveiled. Moreover, the thickness of the LA wall is very irregular and variable between different patients [121, 41]. For all these reasons, few LA simulation studies using FSI are available in the literature (see Table 2.3, and with small number of patient-specific geometries or even synthetic cases).

Dynamic meshes methods: For simplicity purposes, some of the initial studies on LA fluid modelling used CFD with rigid walls (see Table 2.3). From a clinical point of view, the argument was that patients who suffer from AF had almost no LA wall movement, therefore, the assumption of rigid walls was justified. However, even in the most severe AF types, LA wall motion can happen due to the passive forces induced by the left ventricle, specifically in the longitudinal excursion of the mitral valve annulus ring. However, between CFD and FSI there is a middle point, the dynamic mesh (DM) approach, which allows to use CFD by moving the walls of the geometry.

DM schemes are based on the premise that you know beforehand the movement of the object you want to simulate. Thus, the movement over time can be imposed onto the solid domain, omitting the mechanical model. Therefore, the process is computationally less demanding than FSI schemes. From the available medical imaging modalities, dynamic computed tomography (dCT) scans are the ones providing better spatio-temporal resolution to capture LA wall motion dynamics in 4D (obviously, echocardiography have better temporal resolution but limited to certain 2D views, or noisy 3D anatomy). However, dCT scans are rarely available for AF patients due to the associated costs and patient radiation, being difficult to create large cohorts. Some researchers have tried MRI as an alternative [70, 28, 25], but they are even more costly and provide lower spatio-temporal resolution than dCT. Due to the unavailability of patient-specific 4D information of LA wall motion for most cases, researchers have proposed different schemes to include LA wall dynamics into the fluid simulations based on DM approaches, from diffusion [91] to sinusoidal methods [89].

As an example, diffusion-based and spring-based methods are available in Ansys Fluent 19 R3. Physiologically speaking, both approaches aims to mimic the passive movement of the LA produced by the contraction of the left ventricle (LV), omitting the LA radial movement since AF patients rarely have strong active contraction. A MV annulus ring displacement function such as the one measured by Veronesi et al. [133], can be used, assuming similar longitudinal behaviour in non-valvular AF and healthy subjects (i.e., from 8 to 10mm), as shown in [33].

In the diffusion-based method, the mesh motion is governed by the following diffusion equation:

$$\nabla \cdot (\gamma \nabla \vec{u}) = 0, \quad (2.1)$$

where \vec{u} is the mesh displacement velocity and γ is the diffusion coefficient that

can be defined as :

$$\gamma = \frac{1}{d^\alpha}, \quad (2.2)$$

where d is a normalised boundary distance and α is a diffusion parameter introduced by the user. α can be set to 0, which yields a uniform diffusion of the boundary motion throughout the mesh (range between 0 and 2); the smallest the value, the more movement is absorbed by the element close to the boundary where the function has been defined, which could lead to poor quality elements and convergence issues. Usually α is empirically set (e.g. 1.5). The function in Equation 2.1 requires a remeshing step at every time step before computing the equations. After the remeshing step, a mesh check is performed to ensure that all the elements have the minimum quality required for the simulation. This step adds computational time, but it is still cheaper than FSI methods.

The spring-based method only applies single-axis motion, being computationally cheap. For modelling MV longitudinal motion, it will provide similar results as for the diffusion-based method, but orders of magnitude faster. This method is based on modelling the edges between two nodes as a network of springs. A displacement at a boundary node will generate a "spring force" and using Hooke's law, which can be written as:

$$\vec{F}_i = \sum_j^{n_i} k_{ij} (\Delta \vec{x}_j - \Delta \vec{x}_i), \quad (2.3)$$

where $\Delta \vec{x}_i, \Delta \vec{x}_j$ are the displacements of a node i and its neighbour j , n_i is the number of nodes connected to i , being k_{ij} the spring constant:

$$k_{ij} = \frac{k_{fac}}{\sqrt{|\vec{x}_i - \vec{x}_j|}}, \quad (2.4)$$

with k_{fac} being the spring constant factor (between 0 and 1). At equilibrium, the net force from all the springs connected to the node must be zero. This condition results in an iterative equation such that:

$$\Delta \vec{x}_i^{m+1} = \frac{\sum_j^{n_i} k_{ij} \Delta \vec{x}_j^m}{\sum_j^{n_i} k_{ij}}. \quad (2.5)$$

At convergence, the positions are updated such that:

$$\vec{x}_i^{m+1} = \vec{x}_i^m + \Delta \vec{x}_i^{\text{converged}}. \quad (2.6)$$

One can control the solution of the this iterative equation by convergence tolerance and number of iterations. The iterative solutions stops when any of these conditions are met. The user can control the "stiff" of the mesh using the spring

constant factor (the value can be set between 0 and 1). A lower value will give a less "stiff" mesh, whereas a higher value will mainly deform the nodes adjacent to the moving wall.

2.3.3 Analysis of blood flow simulation results

There is also heterogeneity in the literature on the analysis and quantification of blood flow simulation results, as can be seen in Table 2.4. Most studies report velocity profiles in relevant points of interest (e.g., filling/emptying velocities in the LAA), typically complemented with estimations of time-averaged wall shear stress, oscillatory index, endothelial cell activation potential, residence times (RT), shear rate (SR), kinetic energy (KE), particle tracking/residence analysis, and vortex visualisation with the Q-criterion or the Lambda2 metrics. Qualitative analyses of the blood flow patterns with streamline-based visualisation are commonly included. Arguably, the published investigations are usually based on only a few (<10) sets of patient-specific LA geometries, although lately some studies has surpassed 50 cases (see Table 2.3). Yet the most recent LA flow simulation studies [92, 94] propose automatic modelling pipelines that allow substantial improvements in the capacity to process increased numbers of cases. Moreover, most of studies do not include patient-specific functional data (i.e., velocities, pressure) for model validation 2.4. Below, some haemodynamic indices are further explained for the sake of understanding.

Endothelial cell activation potential and relative residence time

Endothelial cell activation potential (ECAP) was developed by Di Achille et al. [26] to detect the areas prone to produce thrombi in aneurysms. ECAP is based on the wall shear stress (WSS) index, which it can be defined as the tangential force done by the flow towards the wall. From the WSS, oscillatory shear index (OSI) and time average wall shear stress (TAWSS) can be computed and, subsequently, ECAP can be derived. First, TAWSS can be written as a simple WSS average over time:

$$TAWSS = \frac{1}{T} \int_0^T WSS dt. \quad (2.7)$$

On the other hand, OSI is an index to assess flow complexity over time. It can reach values from 0 to 0.5. A value of 0 means an unidirectional flow, whereas a 0.5 means a bidirectional flow. It reads as follows:

$$OSI = \frac{1}{2} \frac{\int_0^T WSS dt}{\int_0^T WSS dt}. \quad (2.8)$$

The computation of ECAP is performed as the ratio between the TAWSS (related to flow velocities) and the OSI (related to flow complexity) indices, as follows:

$$ECAP = \frac{OSI}{TAWSS}. \quad (2.9)$$

In addition, the relative residence time (RRT) [56], is an in-silico haemodynamic index that combines WSS and OSI estimates to reflect the residence time of blood particles near the wall, as follows:

$$RRT = [1 - (2 \cdot OSI) \cdot TAWSS]^{-1} \quad (2.10)$$

Vorticity indices: Q-criterion and Lambda 2

While the concept of vortices and vorticity is generally understood among the community, its detection and quantification in a flow field is not as straightforward. Visualisation of the coherent vortical structures in the flow can provide valuable understanding of the flow-field.

Often, the vorticity magnitude might be used to visualise these structures either through a maximum vorticity threshold or isosurfaces of vorticity. The Q-criterion has become one of the most used techniques for vortex visualisation (see 2.4).

In tensor notation, the Q value comes from the definition of the velocity gradient tensor $\delta u_i / \delta x_j$ which can be broken out into two parts such that:

$$\delta u_i / \delta x_j = 1/2 [(\delta u_i / \delta x_j) + (\delta u_j / \delta x_i)] + 1/2 [(\delta u_i / \delta x_j) - (\delta u_j / \delta x_i)], \quad (2.11)$$

where the symmetric part will be denoted as S , being known as the strain rate tensor as defined by:

$$S = 1/2 [(\delta u_i / \delta x_j) + (\delta u_j / \delta x_i)], \quad (2.12)$$

and the anti-symmetric part denoted as Ω , being the rotation rate or vorticity tensor defined by:

$$\Omega = 1/2 [(\delta u_i / \delta x_j) - (\delta u_j / \delta x_i)]. \quad (2.13)$$

Let us recall the definition of the viscous stress tensor:

$$T = \mu [(\delta u_i / \delta x_j) + (\delta u_j / \delta x_i)]. \quad (2.14)$$

Positive values of Qc are indicative of areas in the flow field where the vorticity dominates, with negative values signalling strain rate or viscous stress dominated

areas. It is very important to take into account that the definition and resolution of resulting isosurfaces are entirely dependent on the mesh resolution in the areas of interest.

The Lambda 2 (λ_2) criterion, which defines the vortex of the fluid flow as the minimum local pressure of a fluid domain. First, a gradient velocity tensor (J) is defined as:

$$J \equiv \Delta \vec{u} = \begin{bmatrix} \partial_x u_x & \partial_y u_x & \partial_z u_x \\ \partial_x u_y & \partial_y u_y & \partial_z u_y \\ \partial_x u_z & \partial_y u_z & \partial_z u_z \end{bmatrix}, \quad (2.15)$$

where \vec{u} is the velocity field. Matrix J is decomposed in the symmetric and anti-symmetric part:

$$S = \frac{J + J^T}{2}; \Omega = \frac{J - J^T}{2}, \quad (2.16)$$

where J^T is the transpose of J. Then, the three eigenvalues of $S^2 + \omega^2$ are computed. The eigenvalues are ordered: $\lambda_1 \geq \lambda_2 \geq \lambda_3$. A vortex can be defined as a connected region where $\lambda_2 < 0$.

Streamlines

Streamlines are a family of curves whose tangent vectors constitute the velocity vector field of the flow. They show the direction in which a mass-less fluid element will travel at any point in time. Streamlines can be defined as follows:

$$\frac{d\vec{x}_S}{ds} \times \vec{u}(\vec{x}_S) = 0, \quad (2.17)$$

where "×" denotes the vector cross product and $\vec{x}_S(s)$ is the parametric representation of just one streamline at one moment in time. If the components of the velocity are written $\vec{u} = (u, v, w)$, and those of the streamline as $\vec{x}_S = (x_S, y_S, z_S)$, we deduce [52]:

$$\frac{dx_S}{u} = \frac{dy_S}{v} = \frac{dz_S}{w}. \quad (2.18)$$

It is common to study flows with streamlines, even though they only represent a specific instant in time. If you have a highly variable flow system, and the observed pattern is not maintained over time, it will be difficult to describe the system with single time step pathways. Thus, different time steps would need to be analysed during the simulation. You cannot consider it as the pathway that the particle would follow, since the velocity field that you see in one time step may change in the next.

Table 2.4: Review of the haemodynamic indices used for the assessment of the left atrial fluid simulations. Strm: streamlines; Vel: velocity; Part: particles; Qc: Q-criterion; SR: shear rate; RF: residual fraction; ED: energy dissipation; TA: thermal analysis; TC: tracer concentration; ABP: agent-based particles; KE: kinetic energy; ECAP: endothelial cell activation potential; WSS: wall shear stress; TAWSS: time average wall shear stress; OSI: oscillatory shear index; RRT: relative residence time; RT: residence time. * Dahl et al., [24] has one patient with patient specific simulations, but they modified the geometry to increase the cohort. **LAAO studies.

| Study | Pat specific BC | Haemodynamic indices studied |
|----------------------|------------------------|---|
| Zhang [143] | No | Strm |
| Dahl [24] | Yes* | Strm, Vel and λ_2 |
| Koizumi [70] | Yes | OSI, TAWSS, RRT and Strm |
| Otani [105] | Yes | Qc, Strm, RF |
| Bosi [16] | No | Strm, RF and SR |
| García-Isla [45] | No | Qc, Vel, ECAP, OSI, TAWSS |
| Dillon-Murphy [28] | Yes | KE, ED, Part, TA |
| Masci-a [89] | Yes | Vel, Part, Qc |
| Aguado [1]** | No | TAWSS, OSI, ECAP, Strm, Vel |
| Jia [63] | No | Vel, Strm, Qc |
| Feng [39] | Yes | Vel, Strm, Strain |
| Masci-b [88] | Yes | Vel, Qc, Part |
| Wang [136] | No | P-AB , WSS, Strm |
| Mill-a [93]** | No | Vel, Strm, ECAP |
| D'Alessandro [25]** | No | Flow rate, Vel, Qc |
| Qureshi [110] | No | Thrombin concentration, Vel, Strm |
| García-Villalba [46] | Yes | Vel, KE, RT |
| Fang [36] | No | Strm, Vel, Part |
| Sanatkhani [119] | No | RT, TC |
| Fanni [37] | No | Strm, Vel |
| Mill-b [92] | No | Vel, ECAP, Strm |
| Morales [94] | No | ECAP |
| Mill-c [91]** | Yes | Strm, ECAP, Vel |
| Corti [20] | No | ECAP, TAWSS, Flow stasis |
| Dueñas-Pamplona [29] | Yes | Flow, PAB, TAWSS |
| Gonzalo [50] | Yes | Qc, Vel, KE, SR, RT |
| Rigatelli [115] | Yes | RT |
| Pons [108] | No | Qc, λ_2 , ECAP, OSI, TAWSS, Vel |

Chapter 3

SENSITIVITY ANALYSIS OF FLUID SIMULATIONS IN THE LEFT ATRIA TO PREDICT THROMBUS FORMATION

3.1 Introduction

Due to the extensive range of modelling options reported in LA computational fluid dynamics, there is a need for best practice guidelines to build robust models and achieve reliable simulations, thus obtaining relevant clinical outcomes in LAA simulations. Works in the literature use a wide range of boundary conditions and of modelling choices in terms of inlet/outlet setup (e.g., velocities and pressures in the pulmonary veins and mitral valve; from literature or patient-specific), LA wall behaviour (e.g., rigid, modelled dynamic mesh or deformation from medical images, and fluid–structure interaction), number of simulated cardiac cycles (e.g., from 1 to 20), and mesh resolution (e.g., from 0.4 to 30×10^5 mesh elements), among other factors. Table 2.3 shows a complete review of the corresponding modelling strategies reported in the literature. Unfortunately, the absence of joint benchmark studies with reliable ground truth makes it difficult to identify which are the optimal configurations to achieve realistic simulations.

Accordingly, we performed a sensitivity analysis with variations in the main LA fluid modelling options, using patient-specific imaging data from six patients who underwent LAAO, including three DRT cases at follow-up. For each simulated case, the respective effects of four different boundary conditions scenarios (Scenarios 1–4 in Figure 1) were explored, with varying inlet/outlet configurations (e.g., pressure and velocity profiles at PV and MV, and rigid vs. dynamic mesh

Table 3.1: Left atrial (LA) and clinical characteristics of the studied cases. PV: pulmonary veins; AF: atrial fibrillation; DRT: device-related thrombus.

| Case ID | Number of PV | LA Volume (mL) | AF Type | DRT |
|-----------|--------------|----------------|------------|-----|
| Patient 1 | 5 | 201 | Permanent | No |
| Patient 2 | 5 | 261 | Paroxysmal | No |
| Patient 3 | 6 | 215 | Paroxysmal | No |
| Patient 4 | 5 | 143 | Permanent | Yes |
| Patient 5 | 6 | 281 | Permanent | Yes |
| Patient 6 | 4 | 176 | Permanent | Yes |

LA wall behaviour), to determine the ones that allow optimal predictions of the risk of DRT after LAAO. Mesh and cardiac cycle convergence analyses were also performed.

Furthermore, to study the incorporation of patient-specific left atrial motion from dynamic computed tomography (dCT) images, we performed an additional set of experiments with dCT data available from one patient. Six scenarios were tested, with each LA wall motion strategy (i.e., rigid walls, DM and dCT) being applied in two different inlets/outlets scenarios. The influence of mesh resolution and the number of simulated cardiac beats was also analysed.

3.2 Methods

3.2.1 Databases

The initial study was based on a dataset of six patients from Hospital de la Santa Creu i Sant Pau (Barcelona) who underwent a LAAO. All patients had an implanted Amulet device (Abbott Vascular, Santa Clara, CA, USA). The selection of patients was based on the availability of a complete CT study at follow-up including the whole atrium anatomy and an echocardiography (transesophageal, TOE) study with mitral flow analysis. All patients had non-valvular atrial fibrillation, with four of them being permanent and the remaining two paroxysmal (see Table 3.1). One of them (Patient 2) also presented severe mitral regurgitation. Three patients (4–6) had a history of DRT after LAAO. The study protocol was approved by the local ethical committee of the hospital, and patient written consents were obtained.

CT images were acquired at least twice, between months 1–3 and months 3–6 after LAAO implantation, respectively. Prospective cardiac-gated computed tomography angiography was performed with a Phillips Brilliance iCT scanner.

A volumetric scan from heart to diaphragm (14–16 cm) was acquired. Cardiac phase reconstruction was performed at 30–40% of the RR interval. Initial digital image post-processing and reconstruction were achieved with the Brilliance Workstation™ to assess LAAO device positioning and presence/location of DRT. DRT was defined as a CT hypodensity at the left atrial extremity of the device: (1) not explained by imaging artefacts; (2) inconsistent with normal healing; (3) visible in multiple CT planes; and (4) in contact with the device. Patient data were anonymised prior to any computational processing. Two-dimensional and Doppler echocardiography were performed within 7 days from CT follow-up acquisition. Trans-mitral flow pulsed-wave Doppler velocities were recorded from the apical four-chamber view, the Doppler samples being placed between the tips of the mitral leaflets. Finally, pressure curves in the PV and the MV from an AF patient, different from the six cases analysed in our study, acquired with invasive catheterisation, were available to setup inlet boundary conditions and to estimate pressure gradients to be compared with the simulated ones.

The 3D models were generated (see Chapter 2 and Figure 2.8) and the LA morphology of the six studied patients was different, as can be seen in Table 3.1. For instance, LA volumes ranged between 143 mL and 281 mL. Additionally, the number of PV also differed (from 4 to 6 PV), while their inclination, particularly for the right PV, was more pronounced in some cases (e.g., Patient 2) than in others.

To study the use of dynamic computed tomography images (dCT) for imposing patient-specific left atrial wall motion in fluid simulations, a retrospective cardiac-gated computed tomography angiography was performed with a Somatom Force (Siemens Healthineers, Erlangen, Germany). A biphasic contrast injection protocol was used: 70 cc of iodinated material (Iomeprol 350 mg/ mL Bracco, Italy) were infused through an 18-gauge cubital catheter at a rate of 5mL/s followed by a saline flush of 40 mL. The bolus-tracking method was used for the arterial phase images, being the region of interest on the ascending aorta with a 100 HU threshold. A volumetric scan from heart to diaphragm (14 cm to 16 cm), with slice thickness of 2 mm without overlap, was acquired. A full cardiac beat was acquired with a cardiac phase reconstruction at every 5% of the cardiac cycle (0 to 99% of R-R interval). Transthoracic echocardiography (TTE), including MV velocity curves, was available for the same patient, which was used for validation purposes.

3.2.2 Mesh convergence and cardiac beat analyses

The initial fluid simulations performed during the thesis had the limitation imposed by the use of the academic licence of Ansys Fluent 19.2, limiting the mesh resolution to 5×10^5 elements. A convergence study was performed creating

meshes of 1×10^5 , 2×10^5 , 3×10^5 , 4×10^5 , and 5×10^5 elements.

At a later stage, without mesh resolution restrictions, extended convergence analyses could be performed to study the dependence of the solver solution with the number of mesh elements, also testing meshes of up to 10×10^5 elements. Maximum and mean velocities from fluid simulations were extracted from the same slice of one pulmonary vein (left superior PV) in each mesh to estimate their differences. When including LA wall motion from dCT images, a mesh of 13×10^5 elements was used to cope with the required remeshing ensuring good mesh element quality after wall motion.

In addition, one geometrical model was chosen to study the convergence of simulations over 15 cardiac beats. In this work we also computed the Reynolds numbers (Re) at the MV and PVs to identify the regime of our fluid. The velocity used to compute the Re number for each patient was gathered at the left superior pulmonary vein where a pressure BC was defined.

3.2.3 Inlet/outlet boundary conditions and rigid/dynamic mesh left atrial movement

Studied simulation scenarios

Different configurations of inlets and outlets, respectively, at the pulmonary veins and mitral valve, were tested. Fluid pressure or velocity profiles at the PV (inlet) and MV (outlet) were selected, either from the literature or from patient-specific data. Furthermore, the impact of considering the dynamic behaviour of the LA wall was compared to the classical assumption of rigid walls using diffusion-based method for dynamic mesh (Figure 3.1).

Scenario 1: constant (null) inlet pressure, imaging-based personalized outlet velocities, and rigid wall.

The first scenario consisted of setting up a constant inlet pressure equal to 0 mmHg (as in [16, 28]), while a patient-specific Doppler-based velocity profile was defined in the MV outlet. Mitral velocities from Doppler data were quite variable for different patients, from 0.4 to 3 m/s. The LA wall was considered rigid, i.e., without movement, resulting in a pure CFD modelling study. Such an assumption is a common approach in the literature (Table 2.3), which is based on the reduced wall movement in patients with atrial fibrillation.

Scenario 2: generic patient pressure wave as inlet, imaging-based personalized outlet velocities, and rigid wall.

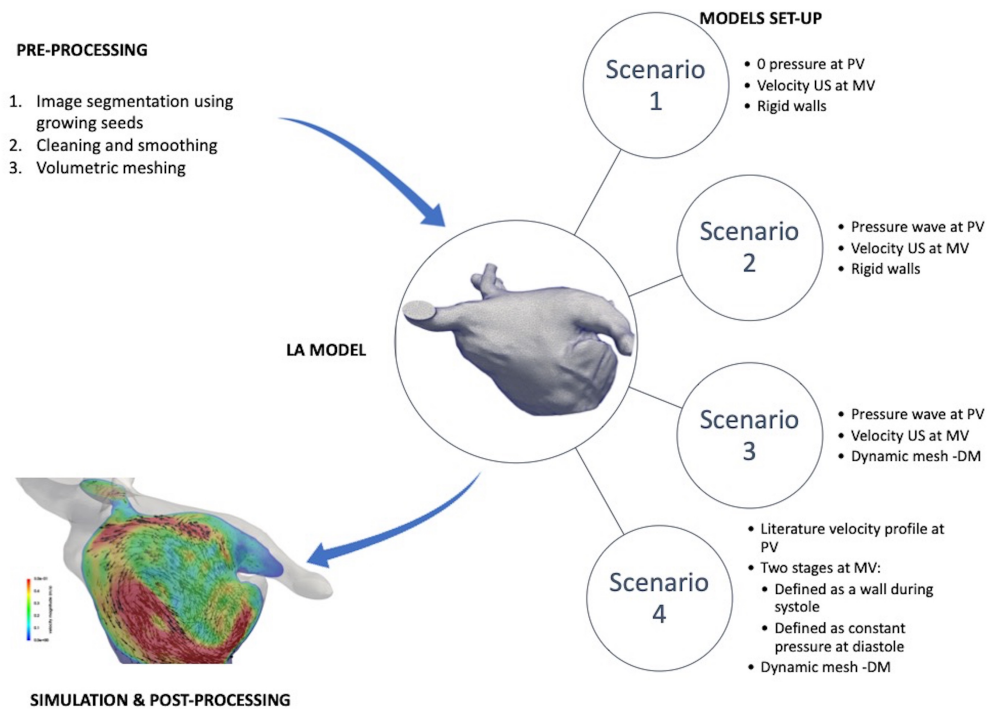


Figure 3.1: Fluid modelling pipeline, including pre-processing steps to build patient-specific left atria (LA) meshes and four different boundary conditions scenarios. PV: pulmonary veins; MV: mitral valve; US: ultrasound imaging; DM: dynamic mesh.

The second scenario replaced the constant inlet pressure in Scenario 1 with the available pressure waves in the pulmonary veins of an AF patient. Nevertheless, that patient was in sinus rhythm at the moment of the acquisition. For each simulated case, this AF pressure wave was personalized, as it was adapted to the cardiac rhythm of each patient, derived from the ECG. A smoothing filter was also applied to the pressure wave, using MATLAB R2018a (Mathworks, Natick, MS, USA), to remove the noise in the signal. Similarly to Scenario 1, patient-specific velocities were set up as outlet boundary conditions and the LA wall was assumed as rigid.

Scenario 3: generic patient pressure wave as inlet, imaging-based personalized outlet velocities, and dynamic mesh wall deformation.

Scenario 3 incorporated deformation of the LA wall to study the differences with respect to the rigid wall assumption in the previous scenarios. In the literature, some studies imposed LA deformation extracted from the processing of CT

or MR images into the fluid simulations [70, 105, 28, 89, 88, 110, 46], while others developed advanced fluid–structure interaction models [143, 39, 36]. When dynamic medical images are not available, an interesting alternative is to use a dynamic mesh approach [25, 93, 92, 94] with displacements generated either synthetically or from literature data.

In this work, the diffusion dynamic mesh approach explained in the previous section based on diffusion approach was also applied to the LA meshes. The resulting dynamic mesh displacements were also synchronised to each patient, based on the cardiac rhythm extracted from each individual ECG and using linear interpolation functions available in MATLAB R2018a (Mathworks, Natick, MS, USA), as described above for the pressure waves.

Scenario 4: literature velocity profile as inlet, mitral valve as wall (systole) or constant pressure (diastole), and dynamic mesh wall deformation.

The fourth studied scenario represented a different set of boundary conditions, often found in the literature (see Table 2.3). A velocity profile was imposed in the PV inlets, while the mitral valve was modelled as a wall during ventricular systole and with a constant pressure at diastole (equal to 8 mmHg in our study). A generic PV velocity profile from literature [40] was used in all analysed cases since it was not possible to obtain reliable PV velocity curves from all the available echocardiographic studies (i.e., due to an insufficient visual window in some locations such as the right superior pulmonary vein). The LA wall behaviour was modelled with the dynamic mesh approach, as in Scenario 3.

3.2.4 Left atrial movement from dynamic computed tomography images

Cardiac movement characterisation from dynamic computed tomography images

To extract LA wall motion from the dCT data the first step was to perform the registration of the images acquired every 5 % of the cardiac cycle. The image registration step was performed using a concatenation of different models using the ANTs software ¹: (1) rigid registration (i.e., only rotation and translation); (2) affine registration (i.e., adding scaling and shearing); and (3) a symmetric normalization registration (i.e., adding a free-form deformation-based deformable transformation with mutual information as optimization metric). The reference mesh always was the cardiac frame starting from ventricular systole (frame 0, i.e., 0 %

¹<http://stnava.github.io/ANTs/>

of cardiac cycle). Therefore, 19 image registrations were performed, from frame 0 to frame 5, from frame 0 to frame 10 and so on, until reaching the last time-frame of the dCT. For each registration, the output was a matrix of displacements for each image voxel. In addition, the image corresponding to the first time-frame was manually segmented, generating a corresponding 3D surface mesh. Subsequently, displacement matrices extracted from the image registration step were applied to the 3D surface mesh using a piece-wise cubic Hermite interpolating polynomial (PCHIP), displacing the nodes to the following time-frame. MATLAB R2018a (Mathworks, Natick, MS, USA) was used for the image processing and mesh warping steps described above.

The resulting 3D surface mesh and set of displacements at each time-step was then mapped to simulation time in an Ansys file format to be applied as a boundary condition for the LA wall movement. As mentioned above, after every time step of the simulation, a remeshing process was performed, checking the mesh quality and improving it if it was necessary. The final volumetric meshes had $\times 12^5$ mesh elements to ensure a good mesh quality.

Patient-specific flow boundary conditions

If ultrasound imaging data is not available but there is an available dCT dataset, patient-specific velocity curves can be estimated and used as flow boundary conditions. In this work, we followed a methodology for the estimation of the flow BC inspired by Gonzalo et al. [50]. Initially, volume curves for the left atria and ventricle were computed from the segmentation of these structures in every frame of the dCT. Flow can be estimated from volume curves as the derivative of volume change over time, allowing to determine blood flow volume going through the MV. The mass conservation law in the LA can read as follows:

$$Q_{MV} + Q_{PVs} + dV_{LA}/dt = 0. \quad (3.1)$$

Flow of the pulmonary veins, Q_{PVs} , can be computed from Equation 3.1. Gonzalo et al. [50] used the same flow rates at each PV, obtaining different PV velocities since PV cross-sectional areas were different (e.g., if Q_{PV} is the same, then $v_{PV} = Q_{PV}/A_{PV}$ will vary because A_{PV} is different). In our case, we set blood velocities to be the same for each PV, thus with varying flow (due to PV cross-sectional area changes) due to the complexity of the studied LA geometry, having 5 PV, and including a very small one, as can be seen in Figure 3.2). Imposing 1/5 of the total flow rate in the tiny PV, blood velocities would have been abnormally high (i.e., > 2.5 m/s, which corresponds to physiological flow), also potentially inducing numerical instabilities or excessive computational costs (e.g., satisfying the Courant condition would require a very small time-step).

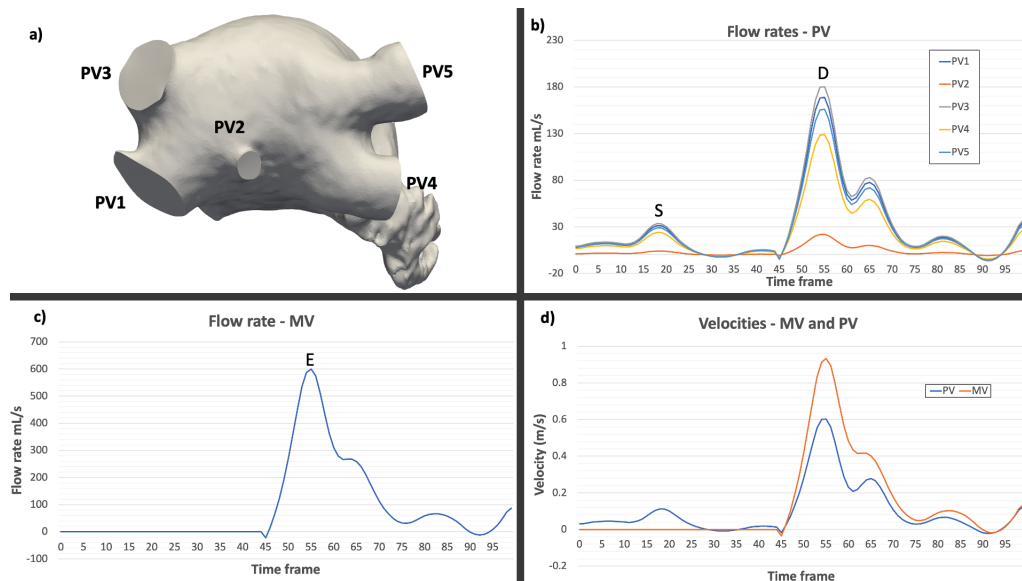


Figure 3.2: Mitral valve (MV) and pulmonary vein (PV) flow and velocity curves extracted from the dynamic computed tomography images. a) Studied left atrial geometry, including 5 PV. b) Flow rates through the different PVs. S and D stands for systolic and diastolic curves, respectively. c) Flow rate at the MV. d) Velocities at the left superior PV and the MV.

Studied simulation scenarios

The different approaches to incorporate LA wall motion in fluid simulations that were studied were the following: 1) DM based on information derived from the dCT data; 2) DM based on the spring-based method; 3) rigid walls. Each movement was tested with two configurations of inlets and outlets.

The first inlet/outlet scenario (Setup 1) used a velocity curve at the PV and a mixed BC at the MV, as shown in Figure 3.2d). During ventricular systole, a constant value of 8 mmHg was imposed at the MV, based on the similarity of the simulated MV velocity curve with the one from the available ultrasound images. As pressure was defined at the MV outlet, the simulated velocity curve was compared with the one estimated from dCT. The second scenario used a generic pressure wave from an AF patient at the PV (while in fibrillation) and a velocity curve at the MV. Each simulation was run for 3 beats, but only the results of the third one were analysed, the first two beats, being run as warming up.

3.2.5 Analysis of fluid simulations

Several in-silico haemodynamic indices were estimated from the fluid simulations to compare the different studied scenarios. First, blood flow velocities were estimated in several parts of the atrial anatomy, including the ostium, LAA, MV and PV in different cardiac instants. A slice was cut on each anatomical part, averaging the blood flow velocity. Additionally, the area between the end of the left superior PV (LSPV) and the device surface (see Figure 5.4), including the pulmonary ridge, was studied. This area is very relevant for DRT modelling since it is where thrombi tend to form due to low blood flow velocities and complex fluid patterns. Flow patterns were also qualitatively analysed with velocity streamlines around the different areas of interest. From fluid simulations, quantitative thrombogenesis risk indices such as TAWSS, OSI, ECAP and RRT were equally estimated.

Finally, unlike most of the LA fluid modelling literature, we also analysed the simulated pressure distributions and gradients in the whole atrium and the LAA, which could be compared with invasive measurements from AF patients. Post-processing and visualisation of the simulation results were performed using ParaView 5.4.1². In some cases, a quasi-conformal (i.e., angle-preserving) flattening [103] was also applied to obtain 2D disk-like representations of the LA (mapping the MV contour to the external boundary of the 2D disk) for visualisation and inter-study comparison purposes.

3.3 Results

3.3.1 Mesh and cardiac beat convergence studies

Mesh convergence

In the initial mesh convergence study (up to 5×10^5 elements, with Scenario 3 of the sensitivity analysis), the reference mesh was the one with 5×10^5 elements. The mesh with 4×10^5 elements had a mean difference of 0.8% (maximum error of 3%) in blood velocities compared to the reference; it was substantially lower than coarser meshes (10.2% with 1×10^5 elements, 5.5% with 2×10^5 elements, and 2.7% with 3×10^5 elements).

The results of the extended convergence analysis, without mesh element limitations and a reference mesh of 10×10^5 elements, are presented in Table 3.2. The error associated with mesh resolutions above 7×10^5 elements were similar; variations might be due to noise. Therefore, meshes in this study were of 7×10^5 elements as a trade-off between simulation accuracy and computational costs.

²<https://www.paraview.org/>

Table 3.2: Mesh convergence analysis. Differences in simulated blood flow velocity at the left superior pulmonary vein of different mesh resolutions with the reference one (10×10^5 elements). Max: Maximum.

| | 500.000 | 600.000 | 700.000 | 800.000 | 900.000 |
|---------------------|----------------|----------------|----------------|----------------|----------------|
| Error max (%) | 11.82 | 9.04 | 4.27 | 7.20 | 4.93 |
| Average error (%) | 2.65 | 1.97 | 1.45 | 1.54 | 1.39 |
| Error max (m/s) | 0.09 | 0.08 | 0.04 | 0.06 | 0.04 |
| Average error (m/s) | 0.02 | 0.02 | 0.01 | 0.01 | 0.01 |

Cardiac beat convergence

Figure 3.3 illustrates the ECAP maps for 15 simulated cardiac cycles for one case in our study (Scenario 3 boundary conditions). The initial couple of beats were required for warming up and numerical stabilisation. From beat 3 on, initial areas with higher values of ECAP emerged, especially around the LAA and PV, which were maintained over all cycles. After beat 6–7, the main regions with high ECAP were established, with values tending to increase over the cardiac cycles.

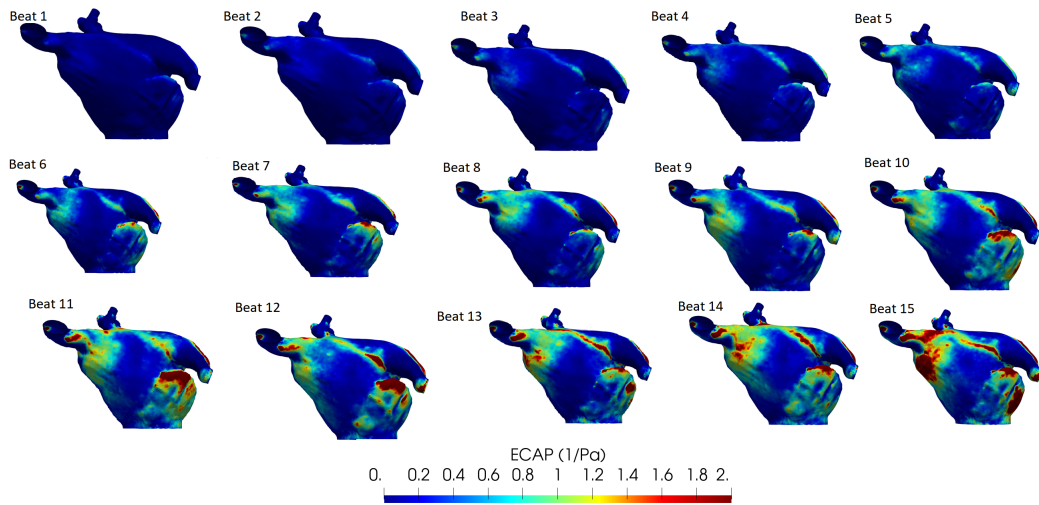


Figure 3.3: Endothelial cell activation potential (ECAP) maps for 15 simulated cardiac cycles/beats. Higher values (red colour) indicate a higher risk of thrombosis.

3.3.2 Inlet/outlet boundary conditions and rigid/dynamic mesh left atrial movement

Figure 3.4 shows a qualitative comparison of haemodynamic in-silico indices obtained with different inlet/outlet and wall behaviour BC in one DRT patient, out of

the six studied clinical cases. It includes velocity and pressure profiles as well as ECAP maps (i.e., high values of ECAP indicating more thrombogenic risk since they reflect low velocities and more complex flows). For a simplified visualisation of in-silico haemodynamic indices and easier comparison among the different cases, a flattening algorithm [103] was applied to the LA 3D meshes so that a 2D common representation of the LA was obtained. The white holes in the 2D maps correspond to the pulmonary veins.

Scenario 1: constant (null) inlet pressure, imaging-Based outlet velocities, and rigid-wall.

Scenario 1 provided simulated pressure values from -100 Pa (-0.75 mmHg) to 300 Pa (2.25 mmHg), which were substantially lower than the ones measured with invasive catheters, ranging from 6 mmHg to 12 mmHg. In addition, the simulated mean pressure gradient between the PV and MV was of 190 Pa (1.43 mmHg), much higher than those acquired in the clinical setup (between 0.07 mmHg and 0.5 mmHg). Velocity magnitudes were within the physiological range, with blood flow patterns (see Figure 3.4) qualitatively simpler than in other scenarios, without obvious re-circulations despite the clinical evidence of DRT. Pressure values were homogeneous in the whole LA. The highest values of ECAP (i.e., linked to higher thrombogenic risk) were obtained at the LAAO device's surface, at the upper part, near the pulmonary ridge.

Scenario 2: patient pressure wave as inlet, imaging-based outlet velocities, and rigid-wall.

The inclusion of an AF patient pressure wave at the inlet BCs in Scenario 2 (i.e., pressure wave from an AF patient at the inlet pulmonary veins, velocity curve from a generic ultrasound images as mitral valve outlet, with rigid wall behaviour) provided a more realistic simulated pressure map than in Scenario 1, as illustrated in Figure 3.4. Pressure values ranged from 125 Pa (0.94 mmHg) to 1110 Pa (8.33 mmHg), while the mean PV–MV gradient was of 15 Pa (0.11 mmHg), which were closer to clinical measurements than in Scenario 1. Velocity streamlines showed more re-circulations with low velocities (blue-green in Figure 3.4) near the device than in Scenario 1. Regions of high ECAP were similarly located as in Scenario 1, but with slightly higher values.

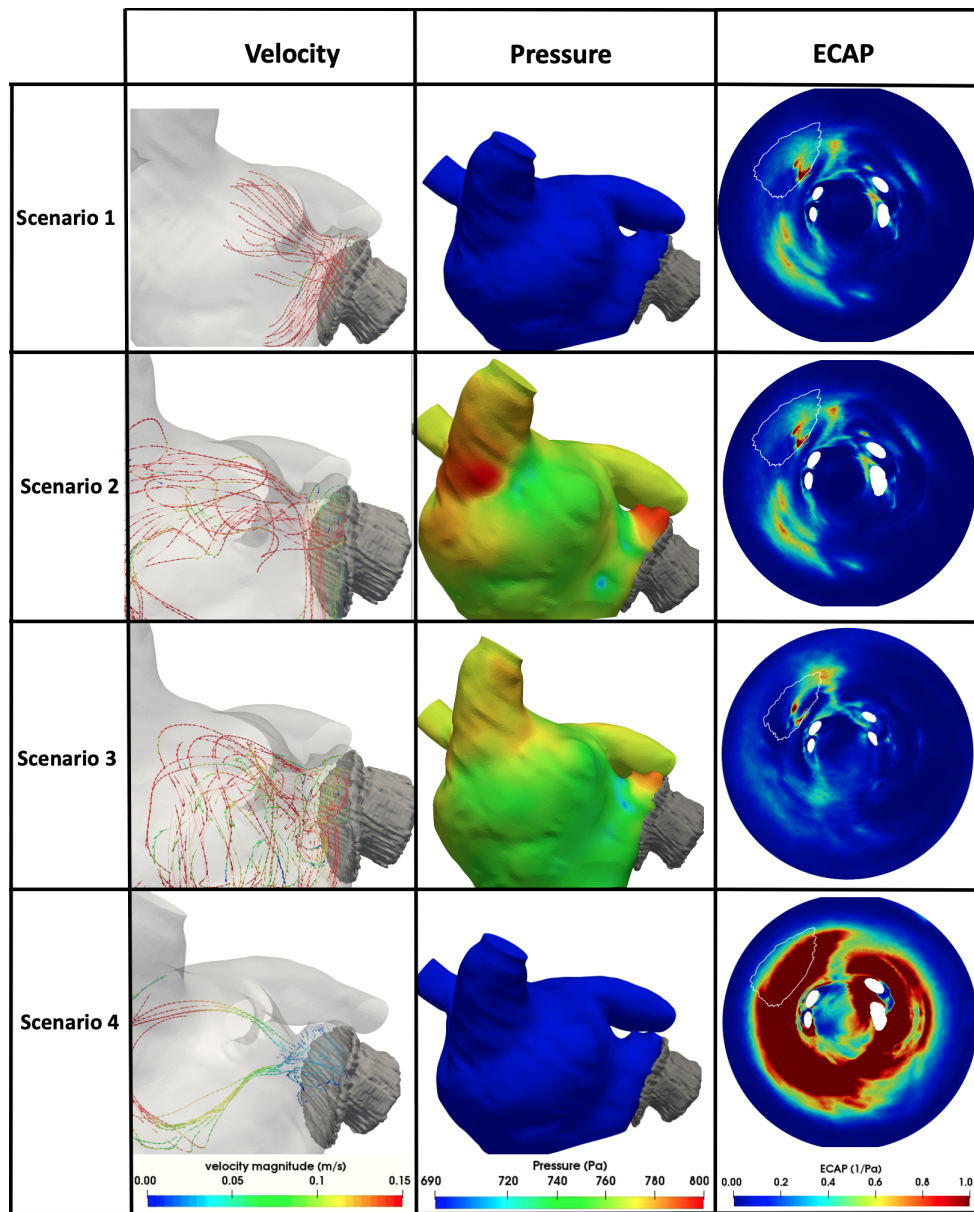


Figure 3.4: Three-dimensional and flattening visualisations of haemodynamic in-silico indices obtained with different boundary condition scenarios (1–4). The white line in the endothelial cell activation potential (ECAP) maps indicates the position of the implanted device. Scenario 1: null inlet pressure, imaging-based outlet velocities, and rigid wall; Scenario 2: as Scenario 1 but with patient pressure wave as inlet; Scenario 3: as Scenario 2 but with dynamic mesh wall deformation; Scenario 4: literature velocity profile as inlet, mitral valve as wall (systole) or constant pressure (diastole), and dynamic mesh wall deformation.

Scenario 3: patient pressure wave as inlet, imaging-based outlet velocities, and dynamic mesh wall-deformation.

The inclusion of a dynamic mesh-based movement in Scenario 3 led to lower pressure values near the device's surface compared to Scenario 2. Pressure values ranged from 174 Pa (1.31 mmHg) to 1240 Pa (9.30 mmHg), with the average PV–MV pressure gradient of 11 Pa (0.08 mmHg). The blood flow patterns in Scenario 3 (see Figure 3.4) showed more re-circulations than the other scenarios, with complex haemodynamic areas near the LAAO device, including low velocities. Interestingly, the ECAP map of Scenario 3 presented a new area with high risk of thrombus formation, at the right side of the device, in addition to the area identified in previous scenarios.

Scenario 4: literature velocity profile as inlet, mitral valve as wall (systole) or constant pressure (diastole), and dynamic mesh wall deformation.

Fluid simulations with Scenario 4 boundary conditions diverged in four out of the six analysed cases, whereas convergence was reached for all cases in the rest of the scenarios. With its opposite BC strategy (i.e., velocities at inlets and pressures at outlets), Scenario 4 provided substantially different haemodynamic in silico indices compared to the other three scenarios. Pressure maps provided during ventricular systole (i.e., MV closed without outlet pressure BC) were similar to Scenario 1 (around 0 Pa). With the opening of the mitral valve in ventricular diastole and the application of constant outlet pressure BC, the pressure raised up to 1200 Pa (9 mmHg), resulting in the largest pressure range in all scenarios. In contrast, the pressure gradient between the PV and MV was 4 Pa (0.03 mmHg), i.e., the lowest in any of the tested boundary conditions. High blood velocities were found in the superior part of the LA, in contrast to other scenarios. However, blood flow stagnation was also largely pronounced in the inferior part of the LA, presenting very low velocities (blue streamlines in Figure 3.4). The consequence of this flow over-stagnation was an ECAP mapping with high values almost all over the LA, making it difficult to distinguish thrombogenic from healthy areas.

Figure 3.5 shows the mean blood flow velocities near the surface of the implanted LAAO device in all analysed cases, including simulations with different boundary conditions scenarios. It can easily be observed that DRT cases (Pat 4–6) had lower velocities (< 0.20 m/s) than patients without thrombogenic history (Pat 1–3), independently of the BC scenarios. Interestingly, the second case (Pat 2), which suffered from a severe mitral regurgitation (MR), presented substantially higher velocities than the remaining cases.

Two-dimensional flattened maps of the LA showing the distribution of the ECAP and RRT in silico haemodynamic indices in the six studied cases using

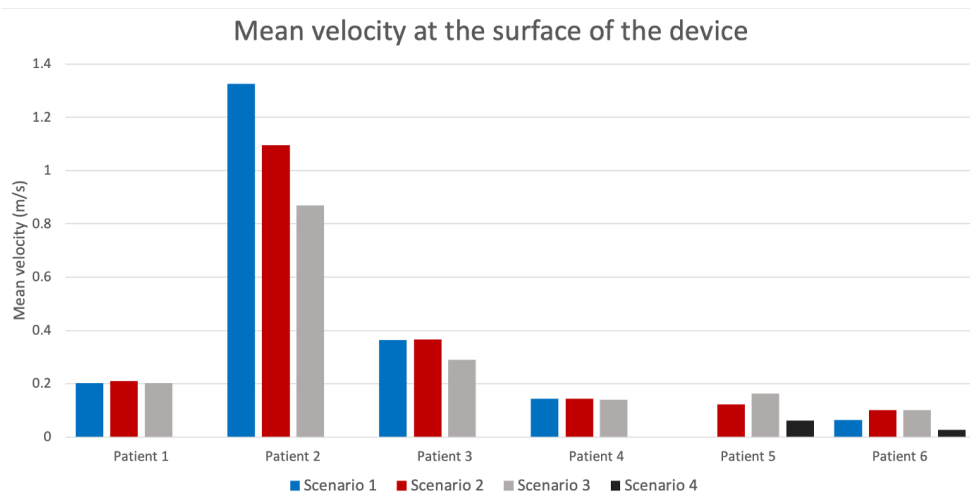


Figure 3.5: Average blood flow velocities near the device surface for the different simulated scenarios in all analysed patients. Pat 1–3 and Pat 4–6 were without and with device-related thrombus, respectively. Missing bars in some patients indicate simulation divergence.

Scenario 3 are presented in Figure 3.6. It is the one which presented better sensitivity when it came to DRT prediction. Similarly to the analysis of the blood flow velocities near the device surface, DRT and non-DRT cases present substantial differences in ECAP and RRT, with the former showing larger values, especially in the device surroundings. Both ECAP and RRT maps depicted comparable distribution maps, with RRT showing more areas with maximum values. When the results were validated with the follow-up CT scans, it could be observed a good agreement between thrombus localisation and areas with low blood flow velocities and complex patterns in the fluid simulations. To see the results obtained with all the scenarios please see Figures B.1, B.2 and B.3 in Appendix.

3.3.3 Dynamic mesh approach for left atrial wall motion from dynamic computed tomography images

Image registration to estimate left atrial wall motion

A video/images of the resulting movement from the registration can be found in Appendix as well as the volume curve. The LA wall motion extracted from the dCT images of the AF patient was heterogeneous, with some areas contracting earlier than others, which is typical for these patients. The radial movement of the LA was minimal while the longitudinal one was small (approximately 3 mm), below the one (around 8 mm) found in the literature [133].

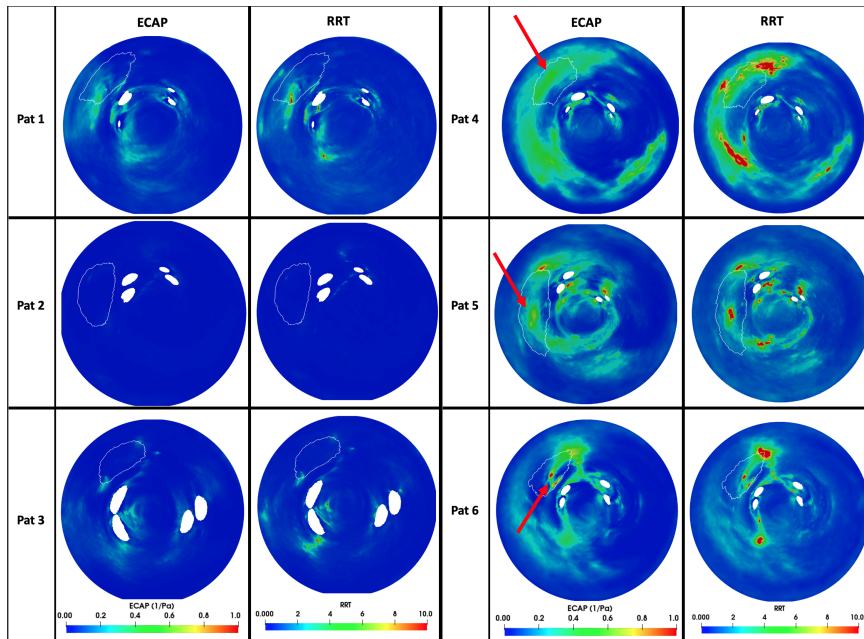


Figure 3.6: In-silico haemodynamic indices for the prediction of device-related thrombosis (DRT) after left atrial appendage occlusion in the six analysed cases: Pat 1–3 were controls and Pat 4–6 had DRT. Higher values (red colour) indicate a higher risk of thrombosis. The white line in the 2D maps signals the position of the implanted device. ECAP: endothelial cell activation potential; RRT: relative residence times. The red arrows indicate the positions where the thrombus were found in the post-procedural computed tomography images.

Blood velocity patterns

Figure 3.9 shows that the MV velocity curve extracted from the dCT was not far from the one obtained in the US data. Velocity magnitudes were in the same range (maximum of 0.94 m/s and 0.93 m/s for US and dCT, respectively). A very little "A wave" was detected in the US image, even smaller in dCT, with some flow regurgitation (red line in Figure 3.9), being a consistent AF behaviour, with the A curve disappearing or being reduced [34] due to the absence of the atrial kick. The shift between the US and dCT velocity curves plotted in Figure 3.9 is due to different cardiac beat characteristics (e.g., systole/diastole duration, beats per minute) during the two image acquisitions.

Figure 3.10 shows the velocity curves at the MV and PV (for Setup 1 and Setup 2, respectively) for the different approaches to incorporating left atrial wall motion into fluid simulations. In addition, the root mean square error (RMSE) of the simulated velocity curves compared with the ones directly derived from the dCT data is included. Results in Figure 3.10 d) depicts minimal differences



Figure 3.7: Volume curves of the left atria (LA) and left ventricle) for a healthy case and an atrial fibrillation (AF) patient, extracted from dynamic computed tomography images (dCT). The volumes are in mL. The x axes are different due to the different number of frames in the dCT images of the two cases.

between the different approaches in diastole, with an increasing error in systole for Setup 1, due to the assumption of no flow through the MV when estimating velocity curves from dCT data. Blood flow velocities in ventricular systole (up to 0.4 in temporal x axis) for DM strategies were around 0.10 m/s, whereas it was close to zero with the rigid wall assumption, the latter potentially inducing over-stagnation in regions near the implanted LAAO device and the MV.

None of the studied strategies produced the A wave in the velocity curves of the MV, thus accurately simulating the AF condition without an atrial kick. Nevertheless, a physiological blood flow pattern in the PV was not fully reproduced, not even from the dCT estimation itself (GT-dCT). The S wave in the PV velocity curves, which is produced during ventricular systole, was very small, when theoretically it should have a more similar height to the D wave (diastole), which otherwise was well represented in the GT-dCT curve. The DM-dCT also replicated the S wave, which was not the case for the DM-Spring and rigid approaches.

Figure 3.10 displays the simulated blood velocities at the ostium. The Setup 1 of boundary conditions (i.e., velocities at the PV) provided ostium velocities that were generally higher than for Setup 2. Velocity values simulated with the different LA wall motion strategies were quite similar, without a clear distinctive pattern, being less relevant that the inlet/outlet configuration, as can also be appreciated when analysing ostium velocities over time (see Figure B.4 in the Appendix).

Nevertheless, blood flow patterns in the LAA are different with the chosen

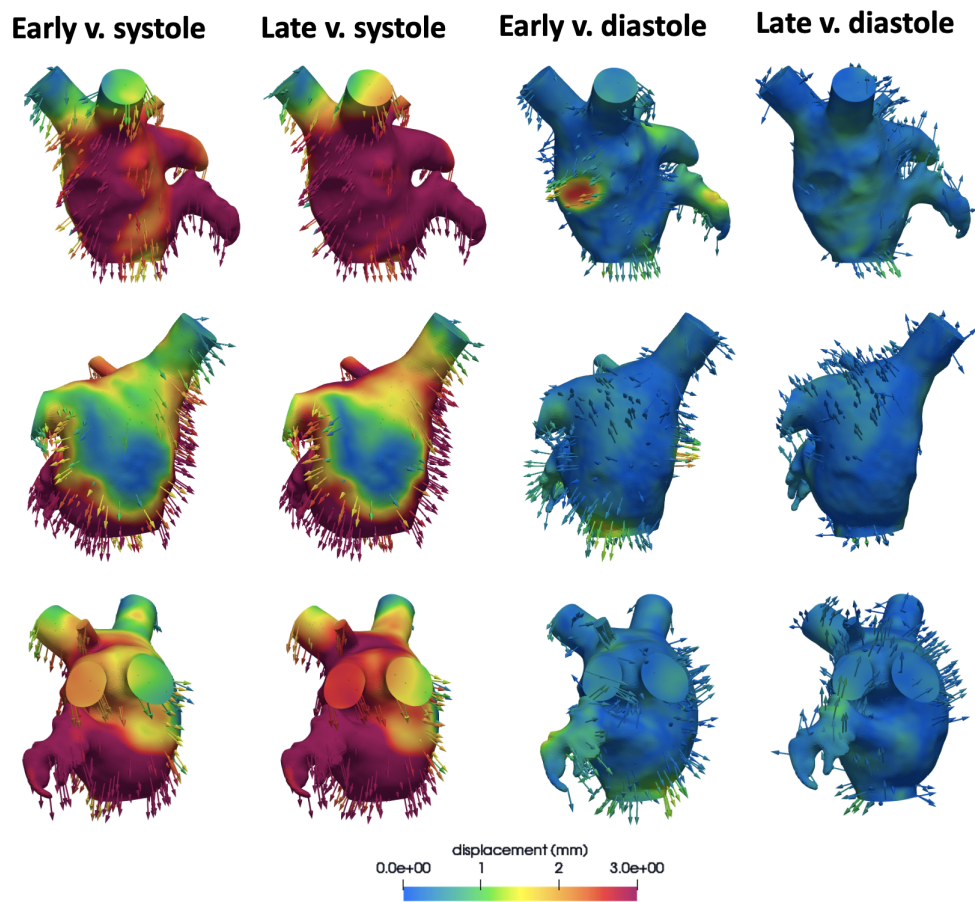


Figure 3.8: Displacement extracted from the dCT. Every column is a different moment of the beat. v: ventricular. Every row is a different point of view. The displacement is represented through the colour map. Units are in mm.

BC strategy, as shown in Figure 3.11 at early diastole (additional time-frames are available in Figure B.5, Figure B.6 and Figure B.7 of the Appendix). At the neck of the LAA, where the ostium is located, the DM-dCT, DM-Spring and rigid strategies provided similar blood flow velocity distributions. However, at the deeper part of the LAA, towards its apex/tip, the DM-dCT shows a better blood flow washing than the alternative approaches, with most LAA parts having velocities higher than 0.1 m/s. The longitudinal movement imposed in the DM-Spring scheme seems insufficient to have a strong effect in the apical part of the LAA, achieving similar results as with rigid wall assumptions. Differences between inlet/outlet configurations (Setup 1 and Setup 2) can also be observed in Figure 3.11, having better blood washout with flow velocities defined as inlets (Setup 1).

When qualitatively analysing streamlines of blood flow patterns in the differ-

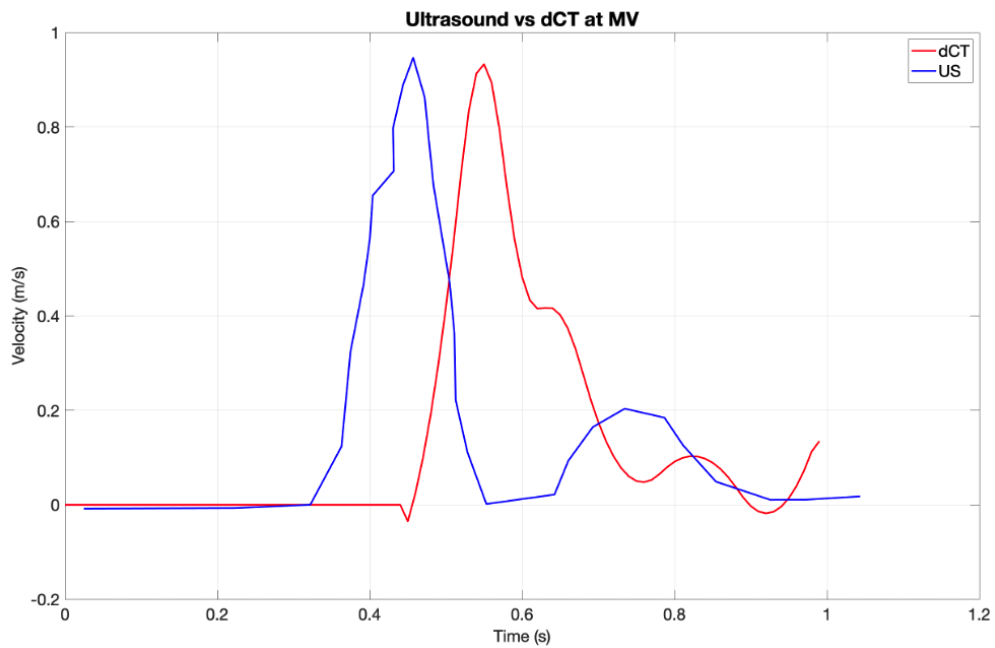


Figure 3.9: Velocity curves at the mitral valve (MV) from ultrasound (US) images (blue), and estimated from the left atrial movement derived from dynamic computed tomography (dCT) data (red). There is a lack of the atrial kick from US data, with a small regurgitation from dCT.

ent BC configurations (also in Figure 3.11), they were overall quite similar, with small vortices created by blood coming from the left inferior PV, and its collision with the right superior PV [43]. Black arrows in Figure 3.11) signal these vortices. On the other hand, no configuration managed to replicate a larger vortex that is reported in the literature [43] at ventricular systole.

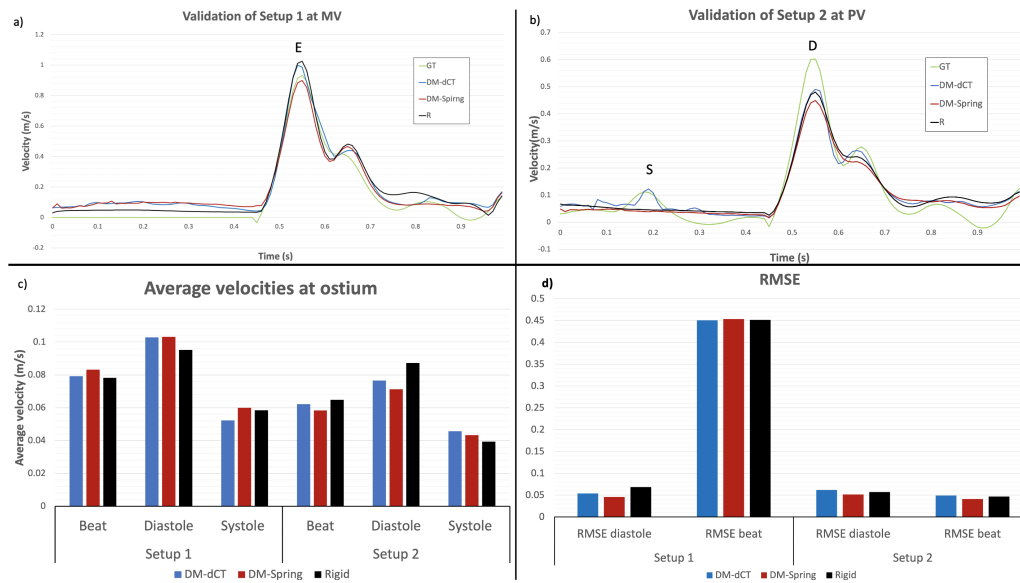


Figure 3.10: a) Velocity curves at the mitral valve (MV) in scenario 1 (Setup 1; velocity curve at the pulmonary vein as inlet and pressure values at the MV as outlet) provided by the different approaches for incorporating left atrial wall motion into fluid simulations. The E wave is displayed. b) Velocity curves at left superior pulmonary valve (LSPV) in scenario 2 (Setup 2; measurement point at the LSPV. Pressure curve as inlet and velocity curve at the mitral valve as outlet) provided by the different approaches of left atrial wall motion. The S and D waves are plotted. c) Average velocities in the left atrial ostium for the studied boundary condition scenarios and the different atrial wall motion into fluid simulations. Beat, diastole and systole refers to the velocity average of the whole cardiac beat or only diastolic and systolic ventricular phases, respectively. d) Root mean square error (RMSE) obtained from comparing the velocity curves obtained from the simulations with the ones obtained from the theoretical method of volume change. RMSE beat refers to the RMSE average of the whole beat, whereas RMSE diastole it is only computed during ventricular diastole phase. GT-dCT: Ground truth (GT), estimated from the volume curves derived from the dynamic computed tomography (dCT) images (green), with Equation 3.1. DM-dCT (blue): dynamic CT curve. DM-Spring (red): dynamic mesh using spring-based method. R (black): Rigid wall.

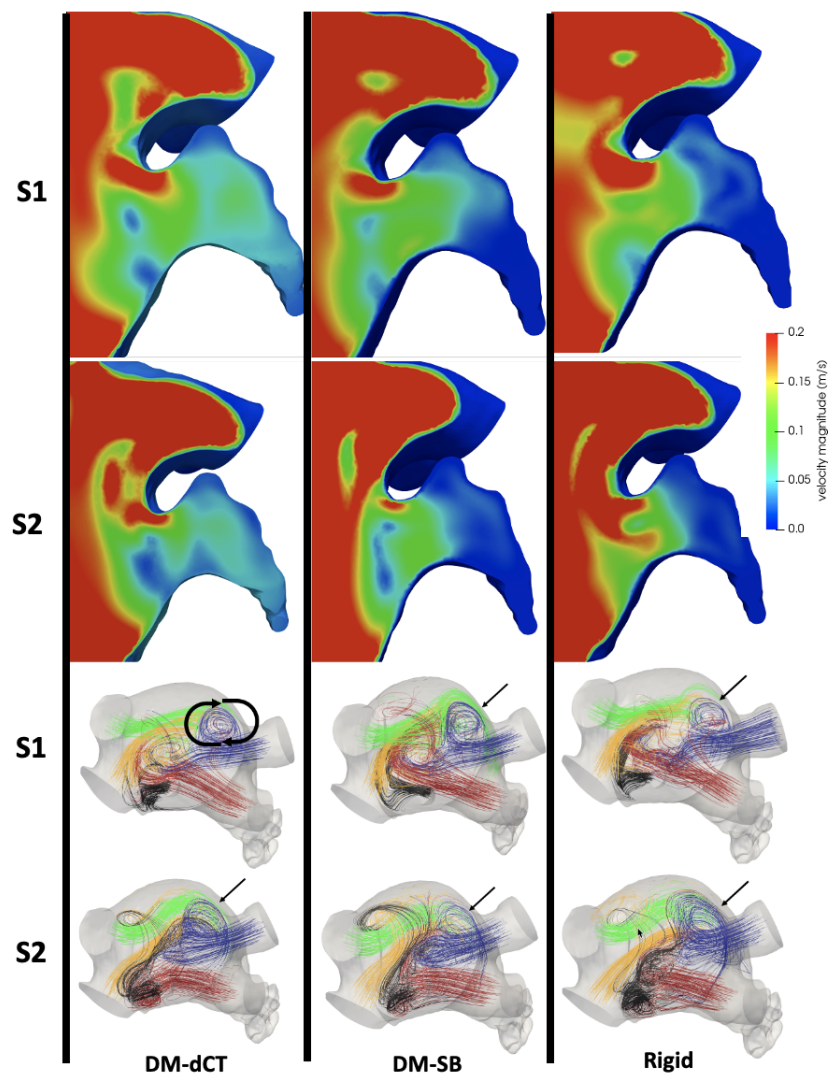


Figure 3.11: First two rows: Clipping of the left atrial (LA) geometry with colourmaps showing the simulated blood flow velocities during early diastole for the different boundary condition scenarios (Setup 1 and 2) and approaches for adding LA wall motion into the fluid simulations (different columns). S1: Setup 1, with velocity curve at the pulmonary vein as inlet and pressure values at the MV as outlet. S2: Setup 2, with velocity curve at the LSPV as inlet and pressure values at the mitral valve as outlet. DM-dCT and DM-SB: dynamic mesh strategies based on dynamic computed tomography data and on spring generic approaches, respectively. Last two rows: Streamlines from simulated blood flow patterns during early diastole for the different boundary condition scenarios (Setup 1 and 2) and approaches for adding LA wall motion into the fluid simulations (different columns). Colours indicate the pulmonary vein (PV) origin of the blood flow: left/right inferior PV being blue/green; left/right superior PV being red/orange; and black corresponding to the right central PV. Black arrows show blood flow re-circulations.

Blood pressure patterns

In terms of blood pressure distributions, the BC defined by Setup 2 created more coherent and smooth pressure gradients than with Setup 1, as can be seen in Figure 3.12 (less drastic change in colourmaps throughout the cardiac cycle). The reason for instabilities and unrealistic patterns with Setup 1 BCs is the large jump in absolute value pressures when the MV opens (8 mmHg) compared to ventricular systole, when there is not a pressure reference. However, all analysed BC scenarios achieved PV-MV pressure gradients around 70 Pa (i.e., 0.5 mmHg), except during MV opening, which agrees with clinical data.

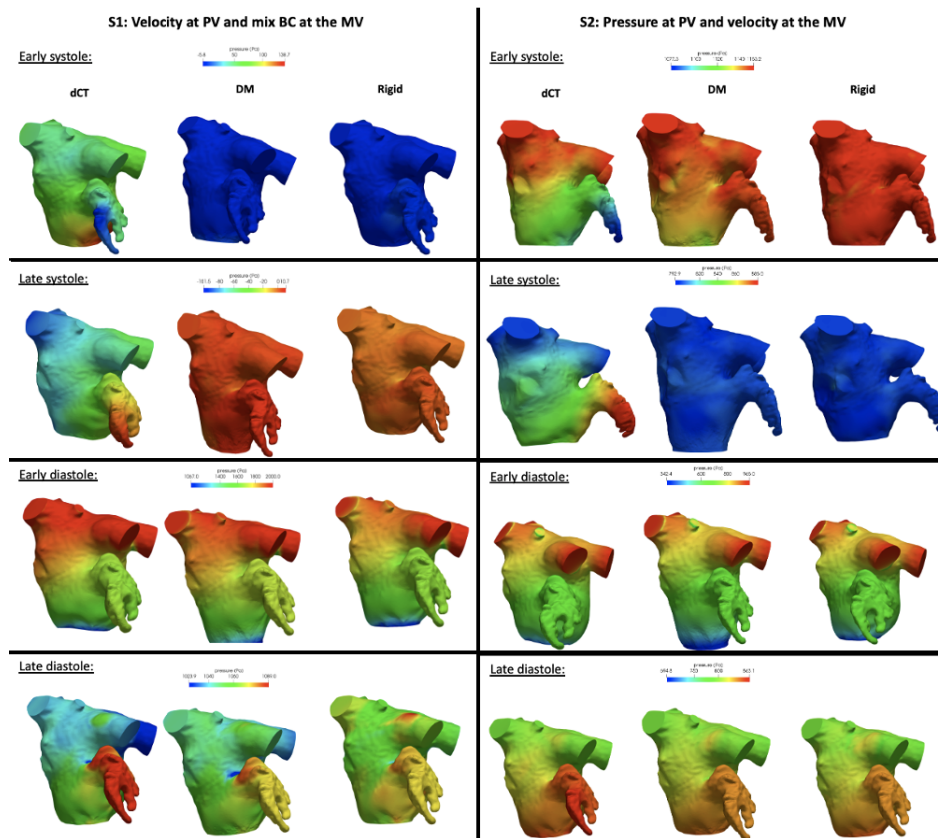


Figure 3.12: Left:pressure maps obtained from each movement scheme using Setup 1 (S1). This setup is composed by the following BC: Velocity at the PV; MV treated as a wall during the ventricular systole; and a constant pressure of 8mmHg during the ventricular diastole. Right:pressure maps obtained from each movement scheme using Setup 2 (S2). This setup is composed by the following BC: Velocity at the MV; and a pressure wave during at the PV.

The DM-dCT strategy provided the largest PV-MV gradients due to its associated larger LA volume increase compared to the other two approaches, which is better observed during ventricular systole in Figure 3.12. This is in agreement with complementary findings reported above, with the DM-dCT being the only strategy reproducing a small "S" wave, and having higher systolic velocities in Setup 2 (i.e., velocity not imposed in the PV) due to the pressure difference created by the larger volume increase. A similar trend is observed in DM-Spring results, but they are very small to have an impact on velocity distributions.

Regionally, higher pressures were found in the LAA at late systole for all analysed BCs, which is consistent with hypothesis on the role of the LAA as a decompression chamber of the LA. A similar pattern was found at end diastole; however, as patient is in AF and no atrial kick will occur at ventricular diastole, flow in the LAA could not be ejected.

In-silico thrombogenic indices

The in-silico thrombogenic indices estimated with the different analysed BC scenarios, shown in Figure 3.13 were consistent with the velocity distributions discussed above. First, the TAWSS index confirmed that using LA wall motion coming from the dCT data, blood flow could reach deeper parts of the LAA, thus making a better washing, and avoiding over-estimation of flow stagnation. TAWSS maps obtained for DM-Spring and rigid schemes were very similar, with the latter providing slightly higher values. As observed above, inlet/outlet scenarios did not result in large difference, with a bit larger TAWSS values when velocities are defined at PV as inlets.

The OSI index values created by the DM-dCT strategy were higher than other alternatives, characterising more complex flow patterns with re-circulations in the ostium and in the distal lobes of the LAA. OSI values were higher in the DM-Spring strategy than in the rigid one, due to the longitudinal movement imposed at the MV.

Finally, the ECAP index summarising the TAWSS and OSI, the DM-dCT achieved the lowest values of ECAP (i.e., lowest risk of thrombus formation) due to the higher TAWSS values. As for the DM-Spring and rigid schemes, the ECAP distribution maps are similar, as depicted in Figure 3.13. Regarding the inlet/outlet BCs, differences could not be appreciated in the estimated in-silico thrombogenic indices, being more relevant how to incorporate the LA wall motion strategy into the fluid simulations.

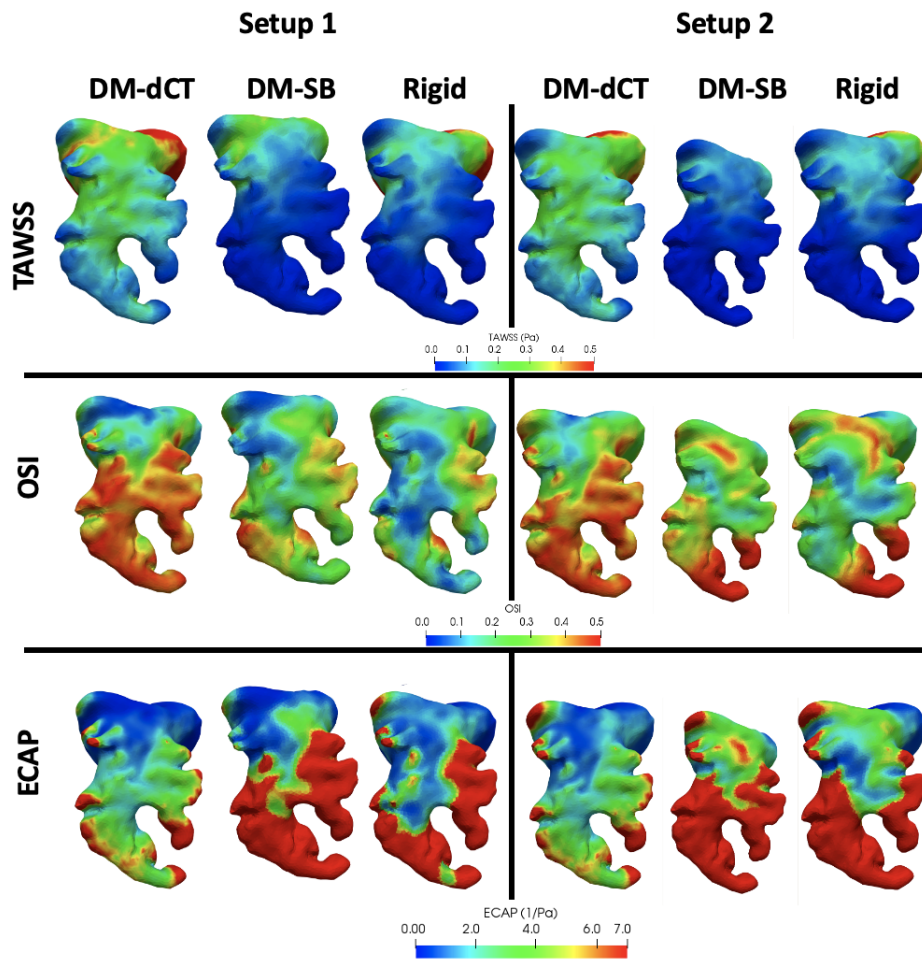


Figure 3.13: In-silico haemodynamic indices time average wall shear stress (TAWSS), oscillatory shear index (OSI), and endothelial cell activation potential (ECAP) maps obtained from each movement scheme using both setups. Left: Setup 1. This setup is composed by the following BC: Velocity at the PV; MV treated as a wall during the ventricular systole. Right: Setup 2. This setup is composed by the following BC: Velocity at the MV; and a pressure wave during at the PV. Every column is a movement scheme: DM-dCT: dynamic mesh movement extracted from the dynamic CT; SB-DM: dynamic mesh movement based on spring-based methods; Rigid: rigid walls.

3.4 Discussion

3.4.1 Mesh and cardiac cycle convergence analysis

Although mesh convergence analysis is a common requirement for a sound modelling study, mesh resolutions found in LA fluid modelling (see Table 2.3) are far from being consistent, ranging from 0.4 to 30×10^5 number of elements. In the initial mesh convergence study we performed, limited by the constraints of the used commercial solver, we observed small differences between the two largest meshes (i.e., 4 and 5×10^5 elements). When later extended up to 10×10^5 elements, we fixed the mesh resolution to 7×10^5 elements, as a good compromise between the accuracy of the simulations and the associated computational cost. A minimum of $4\text{--}5 \times 10^5$ (approximately equivalent to element size of 1.5 mm, as in [105]) should be required and it was useful to identify the most appropriate boundary conditions. In any case, mesh resolution will always depend on the particular LA geometry to model, the selected boundary conditions, and which in-silico indices are estimated.

In a similar fashion, there is not a consensus on the required number of cardiac cycles to reach numerical stabilisation, even if most published studies are between 2 and 7, with some outliers [136, 110, 46, 119] going beyond 15 heartbeats, at the expense of higher computational costs. In our study, we could already identify meaningful differences in boundary conditions scenarios with 3 heartbeats, requiring 1–2 for warming up. However, the cardiac cycle convergence analysis performed in one of the studied LA geometries showed consistency in the most relevant ECAP areas around the LAA after around 5 beats, but still with unstable maximum ECAP values up to 15 beats. Interestingly, there were areas next to the PV (e.g., under the right superior PV) with high ECAP values after 10 beats. These areas are too far from the LAA to be associated with thrombogenesis processes related to DRT. The high ECAP values at the PV could be the result of numerical artefacts due to accumulating dyssynchrony between inlet boundary conditions and LA wall deformation over several beats after using non-specific boundary conditions. Further investigations are required to confirm this hypothesis.

As for future work, advanced mesh and cardiac cycle convergence analysis should be performed with more elements and cardiac beats for better identifying the necessary spatio-temporal resolution to get accurate and stable simulation results. However, using meshes with 5×10^5 elements and 3 heart beats represented an acceptable simplification with reasonable computational times that was useful enough to identify the most appropriate boundary conditions. It could also be interesting to explore the use of mixed meshes including prisms close to the LA wall for a more accurate model of local haemodynamics.

3.4.2 Boundary condition scenarios

Our sensitivity analysis demonstrated the relevance of the most important modelling choices in LA fluid modelling for the prediction of DRT after LAAO implantation, using patient-specific geometries from CT scans of six patients. The obtained results with four different scenarios of boundary conditions confirmed that they are critical for achieving accurate predictions, despite using the same (commercial) solver. The most important consideration is having a good synchronisation between the LA wall movement, anatomy, and volume changes, with the inlet/outlet parameters (i.e., velocities and pressures) selected at the pulmonary veins and mitral valve, respectively.

In the absence of a good synchronisation of these factors, which could be due to using generic or literature-based pressure/velocity constant values or waves in conjunction with assuming rigid LA wall in complex LA geometries, fluid simulations could easily have continuity issues leading to divergence and providing unrealistic blood flow patterns. The recommended approach is to leverage as many patient-specific data as possible to personalise the fluid models, especially velocity/pressure waves at the PV/MV and LA wall deformation from medical images such as echocardiography and dynamic CT/MR scans, ensuring a good match between blood flow (velocities), LA volume changes, and wall deformation. Despite being difficult to obtain all the required data for every case, it should be sufficient to acquire either velocity profiles (easier at the MV for outlet BC) or LA wall movement, and set up the remaining boundary conditions accordingly.

The evaluated boundary condition configurations of Scenarios 2 and 3 provided the most realistic pressure and in-silico haemodynamic indices (see Figure 3.4) due to the generic pressure wave from an AF patient imposed at the PV and patient-specific velocity profiles at the MV outlet, despite having different LA wall dynamics (rigid and dynamic mesh LA wall for Scenarios 2 and 3, respectively). Scenario 1 provided the largest differences in pressure ranges comparing to cathlab measurements since the inlet pressure was constant, unlike the generic pressure wave used in the other scenarios. As LA walls were also considered rigid in Scenario 1 (i.e., lack of LA volume change), PV–MV differential pressure could not be easily created, leading to unrealistic pressure gradients inside the LA.

Unlike the other scenarios (with pressure BC at the inlets), Scenario 4 had a velocity profile obtained from literature in the PV, which led to continuity problems in the fluid simulations in 4/6 analysed cases due to the difficulties for properly synchronising the velocity profile from literature with the different LA anatomies and wall movements, although a dynamic mesh approach was used. Moreover, simulated pressure curves were not realistic, with a square shape. Even in the two cases that converged, blood flow velocities were abnormally low, creating over-stagnation and ECAP maps that could not differentiate different DRT risk areas

(too many red areas in the ECAP map of Scenario 4 in Figure 3.4). The main issue with Scenario 4 was that the amount of flow entering the LA through the PV was not fully absorbed by the LA volume increase created with the dynamic mesh approach.

In the remaining scenarios (all of them converged), with pressure values defined during ventricular systole, the system had more freedom to adapt, estimating the inlet velocities at the PV to match the velocity profile at the MV outlet and the LA wall deformations, fulfilling the mass conservation law. Another advantage of using echocardiographic-based boundary conditions at the outlet is that they captured potential little leaks that occurred even in healthy mitral valves, which was not possible in Scenario 4 with the MV treated as a wall. In LAAO patients, mitral regurgitation may play a protective role, contributing to a proper washing of the LAA and avoiding DRT [22]. Finally, divergence issues in Scenario 4 could be related to the proximity of the inlet (just before the first main PV bifurcation) with the LA main cavity, preventing flow development; García-Isla et al. [45], using similar boundary conditions as in Scenario 4, solved this problem artificially by adding tubes in each PV, which adds operator-dependence into the 3D model creation.

The inclusion of LA wall deformation guided by the MV annulus ring displacement in the DM approach of Scenario 3 produced small changes (e.g., new possible high DRT risk area next to the device) in pressure and ECAP maps comparing to Scenario 2, which assumed rigid LA walls. On the other hand, using a DM approach contributed to make blood flow re-circulations in the LA more realistic, also generating a small peak in PV velocity profiles due to blood flow going into the LA during ventricular systole (S curve reported in the literature), which was absent in the scenarios with rigid LA walls (Scenarios 1 and 2).

Dueñas-Pamplona et al. [29] recently published a complete boundary condition analysis in fluid simulations on an idealised left atrium in-vitro (rigid) model, combined with particle image velocimetry to obtain ground truth data. The authors compared five different combinations of velocity and pressure boundary conditions in the inlets and outlets, including some equivalent to the scenarios in our work. They found practically negligible differences in the simulations with different boundary conditions, in disagreement with our results, which could be explained by the idealised LA geometry and lack of LA wall movement in their in-vitro setup.

3.4.3 In-silico indices of device-related thrombus

Among the evaluated boundary conditions, scenarios that converged (all except Scenario 4) found lower blood flow velocities next to the LAAO device's surface in DRT cases (see Figure 3.5), below the threshold (0.20 m/s) reported for

thrombosis risk [44]. Out of the evaluated scenarios, ECAP and RRT maps from Scenario 3 (generic AF pressure wave as PV inlet, echocardiography-based velocity profile as MV outlet, and dynamic mesh LA wall behaviour) were the most accurate to assess DRT risk and predict the possible localisation of the formed thrombus. Figure 3.6 clearly shows elevated ECAP and RRT values around the implanted LAAO device in DRT cases compared to non-DRT cases. Equivalently, the same areas presented blood flow re-circulations and lower velocities in DRT cases, as can be observed in Figure 5.8, and will be further discussed in Chapter 5. For instance, in-silico haemodynamic indices for Pat 6 perfectly predicted DRT in the superior-anterior part of the LAAO device (as shown by the red arrows in the figures). Nevertheless, ECAP maps might not be specific enough to identify the exact location of DRT in cases where the pulmonary ridge (the space between the LAA and the LSPV) is not covered. Furthermore, it is not obvious to define a consistent threshold in the ECAP and RRT maps to determine the risk of DRT for all cases. In the studied cases, ECAP values larger than 0.5 Pa^{-1} were associated to DRT areas but we could not find a conclusive threshold for RRT, which should be computed in more than two cardiac cycles. Despite the mentioned limitations of ECAP and RRT indices, the former one was a good descriptor of the overall LA haemodynamics that, combined with velocity magnitudes and blood flow re-circulation analysis, can be used to assess the risk of DRT.

3.4.4 Left atrial wall motion from dynamic computed tomography images

The initial sensitivity analysis showed the usefulness of including LA wall motion, even if simplified as a mere longitudinal movement of the MV. Imposing full LA displacements derived by the processing of dynamic medical images such as in [70, 105, 28, 110, 46], or applying sinusoidal-controlled small displacements over the entire LA [89, 88, 25], could help to better model PV velocity profiles and synchronise LA volume changes with inlet/outlet boundary conditions. Unfortunately, obtaining dynamic CT or MR scans of candidates undergoing LAAO implantation is rarely available in clinical routine, unlike echocardiographic studies. Fluid–structure interaction can also be a valid modelling alternative to include LA wall movement, as in [143, 39, 36], at the expense of higher computational costs and the uncertainty on material properties to be assigned to the LA wall (i.e., wall thickness, elasticity, and fibre orientation).

The contribution of the second study presented in this chapter has been the incorporation of LA wall motion extracted from dCT data, available from one patient, into fluid simulations, and comparing it with the other BC strategies already discussed. The dCT image processing steps were performed with state-of-the-art

Open-Source software tools. Interestingly, the MV ring excursion found in the analysed case was smaller to the one found in literature (8 mm uniformly in the MV [133]). One possible reason can be the existence of a non-uniform displacement field at the MV, as suggested by Faletra et al. [35]. Additionally, cine-MRI sequences could be an interesting alternative to ultrasound data, the limited spatial resolution of which may also explain some of the found discrepancies.

One of the main advantages of dCT data is that velocity curves can also be extracted (through mass conservation law) and used them as patient-specific BCs. In our experiments, the resulting dCT velocity curve at the MV was similar to the one measured with ultrasound data, with equivalent maximum values and with a reduced A wave due to AF. The observed differences could be explained by varying patient heartbeat, time between acquisitions, or different positions of velocity measurement in the two modalities. As for the simulated PV velocity curve, it was similar to the one directly derived from dCT data. However, none of them succeeded on properly replicating the complex ventricular systole dynamics at the PV, as already noticed in previous works [50].

Although there were not many global differences in simulated blood flow patterns with the DM-dCT approach (e.g., similar blood flow velocity magnitudes at the ostium), we have demonstrated how it induces to a better LAA washing and more blood re-circulations. However, none of the tested BC configurations was able to replicate the systolic vortex reported in the literature [43], which could be related to velocity curve inaccuracies. In addition, the analysed LA geometry had 5 PV, while literature results are usually reported on 4 PV geometries; having a right central PV could have an influence on the creation of the ventricular vortex. Recent imaging techniques such as 4D flow MRI could contribute to shed some light into these questions.

Combined with the dynamic mesh approach for LA wall motion modelling, Setup 2 (i.e., imposing velocity at the MV), provided lower ostium velocities and a more coherent and smooth pressure map distribution over the cardiac cycle. The DM-Spring and rigid approaches generated some unrealistic pressure peaks, the latter not creating any pressure differential during ventricular systole. In the initial sensitivity analysis, the rigid wall assumption (Scenario 1, similar to [16]) created pressure differential by imposing a zero pressure at the MV. Moreover, the combination of rigid walls assumption with Setup 1 BC (i.e., imposing velocities at PV) should have issues fulfilling the mass conservation law, but simulations converged in all cases with correct residuals in our experiments, using Ansys Fluent. Caution needs to be taken in case there exist internal processes in the commercial solver to ensure convergence, even in complex scenarios.

In summary, the DM-dCT seems to be a better strategy for including LA wall motion into fluid simulations than DM-Spring and rigid strategies. In agreement with our findings, García-Villalba et al. [46] recently demonstrated the benefit of

in-silico haemodynamic indices for assessing the risk of LAA thrombogenesis in a database of six patients, having better patient stratification, based on residence times and kinetic energy, when using moving-wall simulations compared to rigid LA walls. In an elegant way, the authors set up flow boundary conditions at the PV/MV based on volume changes of the LA and the left ventricle extracted from available dynamic CT scans and applying mass conservation. Unfortunately, it is not obvious to acquire dCT data on a regular basis, being complicated to create large cohorts, and it does not fully capture ventricular systole dynamics. Alternatives need to be investigated in the future to transport knowledge on LA wall motion from dCT images available on a small dataset of cases onto each LA to be modelled or to recover as much LA wall motion as possible from 2D-3D echocardiographic data.

3.5 Conclusions

In-silico fluid simulations have the potential to play a major role in the optimisation of medical procedures. The use case of left atrial appendage occluder devices is a good test since in-silico models can contribute to a better understanding of haemodynamics of the LA and after LAAO implantation to avoid adverse outcomes such as the formation of thrombus or DRT. As discussed above, despite several LA-based fluid models being available in the literature, there is a lack of consensus on the most appropriate set of boundary conditions (see Table 2.3) to generate realistic simulations. Systematic verification and validation studies, following the ASME V&V40 guidelines [134] with in vitro and/or ex vivo data, are also missing due to the difficulties to obtain ground truth data. Therefore, there is a need for building credibility of LAAO-based in-silico models to integrate them as part of the medical device certification procedures by organisations such as the Food and Drug Administration (FDA).

From results obtained in our experiments, we can conclude that the assumption of LA rigid walls should be avoided. Additionally, imposing blood flow velocity curves at the PV is limiting. Although commercial solvers such as Ansys Fluent may make the models converge, a set up with such boundary conditions is difficult to justify. Imposing pressure boundary conditions at the PV could partially overcome the problem but, then, there is almost no blood flow dynamics in the system, leading to blood velocities lower than they should be and over-estimating blood stasis.

The use of a dynamic mesh strategy based on a generic longitudinal movement of the MV is a better overall approach than assuming LA rigid walls. It can be justified due to the absence of the atrial kick in AF patients, being the main LA volume change due to the passive movement produced by the LV; however,

this assumption is not valid for healthy hearts. We showed in our study that the DM-Spring approach was useful for detecting DRT, but it had some problems to properly estimate the risk of LAA thrombus generation. A possible reason is the proximity of the area of interest in the DRT use case with LA wall movement (i.e., device being close to the MV), whereas DM-Spring approach fails to translate the movement to the deepest LAA areas. In conclusion, without a LAAO device, it is recommended to include overall LA wall dynamics, if possible provided by patient-specific images such as dCT; our experiments demonstrated best general simulation results with the DM-dCT approach, although ventricular systole dynamics were not fully replicated. Unfortunately, it is not possible to obtain dCT data for all AF patients to be modelled, thus alternatives such as estimating LA wall movement from echocardiographic data should be considered. If patient-specific LA wall motion is not available, other approaches proposed in the literature [89, 136, 20] should be studied, despite their strong physiological assumptions (e.g., LA wall motion being sinusoidal).

Patient-specific data is also key for setting the inlet/outlet boundary conditions better simulating thrombus formation due to its dependence on blood flow velocities. Using velocity curves from ultrasound images of the patient to model ensures mimicking complex haemodynamics behaviour such as the presence of the S wave at the PV, still difficult to recover with dCT images. It is also important to acquire the multi-modal images (e.g., CT and US) required for a complete model in a short temporal window to minimise differences in heart status between the acquisitions, both prior to the LAAO implantation and at follow-up. Therefore, good coordination between the modellers and the medical team is key.

Further investigations are still needed to determine the optimal in-silico haemodynamic indices to estimate the risk of thrombus formation and set up robust thresholds to stratify patients (e.g., for ECAP or the Q-criterion). In our experiments, an ECAP value equal to 0.5 properly separated control vs DRT cases, using personalized BC, but it needs to be tested in more cases to evaluate its generalisation. In addition, we found useful to study pressure distributions, which is not usually considered in LA fluid modelling, despite being a crucial indicator of left atrial function. Future work should also focus on a more extensive sensitivity analyses to determine the optimal mesh resolution and type of elements, as well as the number of cardiac cycles to properly simulate LA haemodynamics with reasonable computational times able to fit with clinical routine timings (e.g. often getting pre-operative images a couple of days before the LAAO implantation).

Chapter 4

ROLE OF LEFT ATRIAL MORPHOLOGY AND IN-SILICO HAEMODYNAMICS IN THROMBUS FORMATION

4.1 Introduction

Despite a substantial amount of clinical and physiological research, a plausible explanation of the relationship between the LAA morphologies and thrombus formation is still missing. To overcome this problem and improve thrombogenic risk and stroke sub-type stratification, the morphology of the LA/LAA has been characterised with multiple indices [17, 62, 108] such as volumes and areas, width and height of the LAA, ostium parameters (minimum/maxim diameters), LAA bending angles and tortuosity, among others. Classification systems based on morphology had been proposed such as the one based on the LAA angulation (LAA-H/L)[141], defining as low-risk morphology (LAA-L) the ones with an acute angle bend or fold from the middle and proximal part of the LAA, and high-risk (LAA-H) otherwise. However, none of these classifications have achieved a scientific consensus due to their qualitative interpretation [140]. Additionally, few works have considered the configuration of the pulmonary veins as a morphological factor that could play a key role in thrombus formation, despite being key for LA haemodynamics.

One of the possible reasons for failing to link LA shape characteristics with thrombus formation is to study LA morphology independently of other factors, despite thrombus formation being a multi-factorial phenomenon. Following Virchow's triad, low velocities and stagnated flow have been associated with the trig-

gering of the inflammatory process and, therefore, the risk of thrombus generation [138]. Some pioneering works describing LA haemodynamics in healthy volunteers date from 2001 [43], although they were not related to thrombus formation in atrial fibrillation patients. Detail analysis of in-vivo LA haemodynamics in 4D (i.e., 3D plus time) in AF patients is difficult due to the spatio-temporal resolution of current imaging modalities used in clinical practice. Advanced imaging techniques such as 4D flow MRI, allowing a more complete blood flow analysis, are emerging, but they still provide limited information in the left atria [85, 70]. In consequence, several modelling studies have focused on simulating LA blood flow patterns, as listed in Chapter 2, but rarely investigating their relation with LA morphology. Some exceptions include analysis of PV configuration and fluid simulations [24, 70], but only in one LA geometry.

Therefore, the aim of the work presented in this chapter was to jointly analyse LA morphology and haemodynamics in relation with the risk of thrombus formation, paying special attention to the role of PV configuration. To this end, two studies were carried out. The first study was focused on extracting a complete list of LA morphological parameters and combined them with in-silico haemodynamic indices to better stratify the risk of thrombus formation in AF patients. Following conclusions from sensitivity analyses of Chapter 3, a dynamic mesh approach based on spring method (DM-Spring) was adopted (not dCT was available) to simulate LA haemodynamics in 30 AF patients, 15 with transient ischaemic attack (TIA) or cerebrovascular accident (CVA) and 15 without. The second study was specifically focused on the influence of the PV configuration in LA haemodynamics and its relation with thrombus formation, since it will determine how the flow enters the LAA, allowing a better or worst washout. A large cohort of 131 AF cases, including follow-up information on which subjects developed LAA-based thrombus or suffered CVA/TIA events. At the time, both in-silico studies were the largest cohort of patient-specific LA fluid simulations performed so far.

4.2 Methods

4.2.1 Databases

For the first study, the initial patient cohort consisted of a total of 83 patients with AF from OLV Hospital in Aalst, Belgium. Non-valvular patients ($n = 71$) were split into two groups based on whether or not they had suffered TIA/CVA; patients with valvular AF ($n = 12$) were discarded. All patients from our study had undergone radio-frequency ablation of the pulmonary veins and were on permanent anti-coagulation. All patients gave written informed consent. The 3D LA models were acquired by reconstructing 3D rotational angiography (3DRA) im-

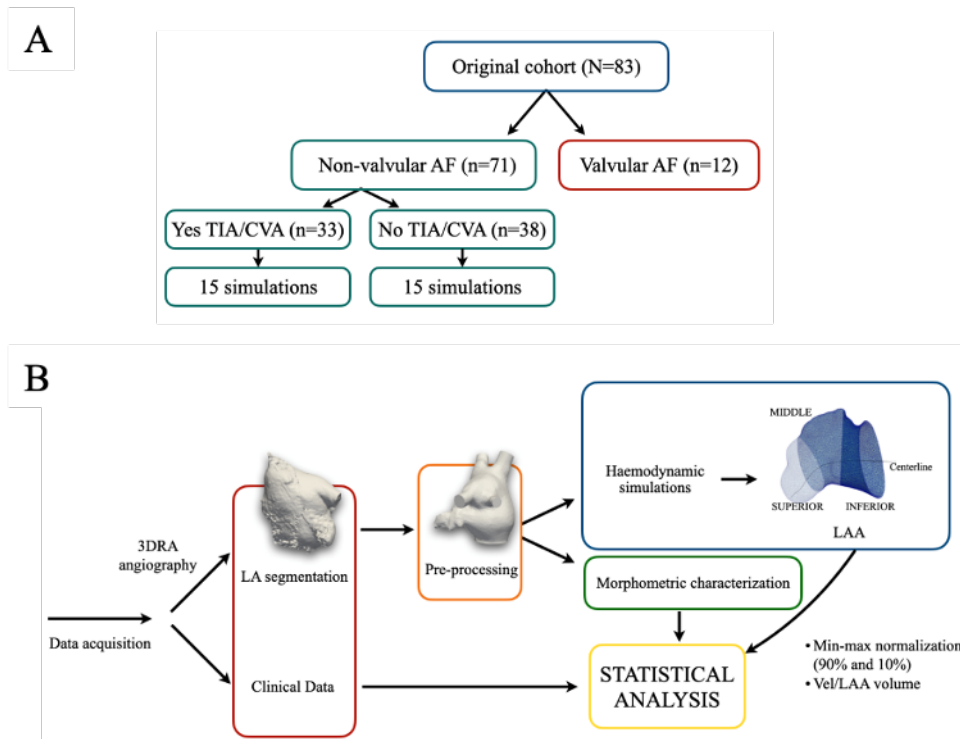


Figure 4.1: (A) Organisation of the cohort of patients with atrial fibrillation (AF), transient ischemic attack (TIA) and cerebrovascular accident (CVA). (B) Computational pipeline followed in the study: data acquisition, left atrium (LA) segmentation from medical images, pre-processing, morphological characterisation of the LA and left atrial appendage (LAA), haemodynamic simulations, post-processing and statistical analysis of the data.

ages obtained using an Innova 3D system (GE Healthcare, Chalfont St Giles, UK) and reconstructed into isotropic 3D volumes through the scanner workstation, providing isotropic 3D images with 0.23 mm or 0.45 mm volumetric pixel size, for 512 or 256 pixels per dimension, respectively. Segmentation of the left atria was achieved with semi-automatic thresholding and region-growing algorithms available at the scanner console.

Morphological parameters were extracted from all non-valvular patients. However, based on the quality of acquisitions, in-silico simulations were only run on 30 patients (15 with history of TIA/CVA and 15 without), as shown in Figure 4.1. The available clinical data included weight, age, body mass index (BMI), body shape area (BSA) and the LAA morphology type (e.g., chicken-wing, cactus, windsock, or cauliflower, labelled by experts). The type of AF was also included, employing a distinction between paroxysmal or persistent (if lasting a maximum of 7 days or longer, respectively). The CHA2DS2-VASc score was as-

signed assuming that TIA/CVA cases had no history of thrombus before grading, which means that a high value of the score depends on other factors considered by the method. Mitral valve insufficiency was defined according to the angiographic grading and CHA2DS2-VASc score. Figure 4.1 B), break down the steps followed in our study, including the advanced statistical classification.

The clinical data of the study focused on PV configuration were provided by Hospital Haut-Lévêque (Bordeaux, France), including AF patients that underwent a left atrial occlusion (LAAO) intervention and with available pre-procedural high-quality CT scans. 131 patients were available for this study. 62 CT images were acquired in systole and 69 in diastole. Out of the 131, 53 had either a thrombus spotted in the LAA or had a stroke or CVA history, the rest were allocated to the control group. Cardiac CT studies were performed on a 64-slice dual source CT system (Siemens Definition, Siemens Medical Systems, Forchheim, Germany). Images were acquired using a bi-phasic injection protocol: 1mL/kg of Iomeprol 350mg/mL (Bracco, Milan, Italy) at the rate of 5mL/s, followed by a 1mL/kg flush of saline at the same rate. The study was approved by the Institutional Ethics Committee, and all patients provided informed consent.

4.2.2 Joint analysis of left atrial morphological parameters and in-silico haemodynamic indices

Morphological parameters

The analysed LAA morphological parameters in this study were the following: the LAA volume and area; the neck height (h_{LAA}), the distal point length (h_{θ}), the LAA anterior and posterior distances (d_A and d_P , respectively in Figure 4.2) between the LAA centre of mass (p_{mass}) and the most distal points in the x direction, as well as its sum (anterior-posterior distance, d_{AP}); the LAA centreline, using the VIDAA software [1]; and LAA tortuosity (η_{LAA}). Additionally, the LAA ostium was characterised by its maximum and minimum diameters (D_{max} , D_{min} , respectively), its area and perimeter.

Simulation setup

CFD simulations with a dynamic mesh approach based on the spring-based method and MV annulus ring longitudinal movement were carried out by using ANSYS Fluent Solver 19.2, as described in Chapter 3, including 3 cardiac cycles. In this work we applied the BC setup with a pressure inlet at the PV and a velocity outlet at the MV. A pressure waveform was extracted from one patient with AF in sinus rhythm through catheterisation, while the velocity profile was extracted from a Doppler echocardiography acquisition from our database, being both non-patient-

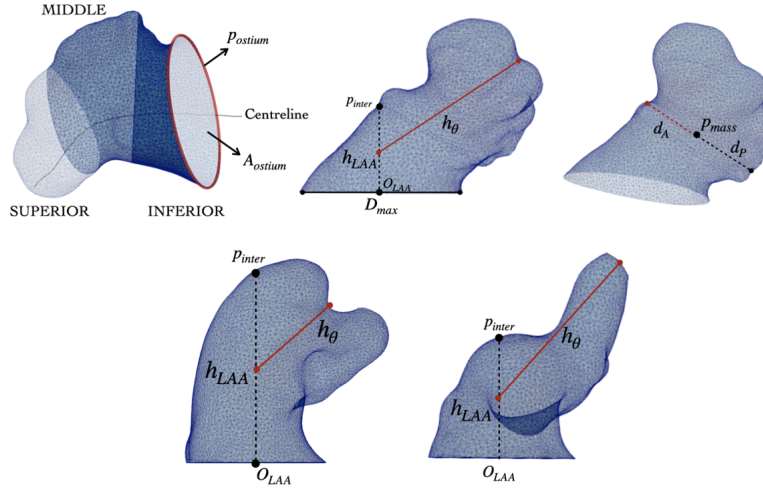


Figure 4.2: First row: left atrial appendage division in three regions for the haemodynamic analysis (left) and morphological indices: ostium perimeter (p_{ostium}) and area (A_{ostium}), neck height (h_{LAA}), distal point length (h_{θ}), maximum ostium diameter (D_{max}), origin of the LAA (O_{LAA}), intersected point (p_{inter}), anterior (d_A) and posterior (d_P) distance of the LAA and LAA, and centre of mass (p_{mass}). Second row: examples of LAA with high and low tortuosity (left and right, respectively).

specific BC. The reasons for using velocity at the MV instead of the PV are mainly two: (1) the easier access to US data and better quality in the MV than in the PV in our database; (2) the better convergence and a reduced computational time comparing to applying velocities at the pulmonary veins. Since it is not patient-specific, if a flow or velocity inlet is defined at the pulmonary veins, the DM volume increment has to be perfectly synchronised, having the solver less degrees of freedom than if velocity is defined at the MV and pressure in the PV. Haemodynamic indices from fluid simulations such as blood flow velocities were estimated averaging values of the second and third simulated beats (including systolic and diastolic phases), since the first one was used to stabilise the simulations. Blood flow stagnation inside the LAA was assessed by integrating the flow rate at the ostium. The TAWSS, OSI, RRT, and ECAP indices were also computed from the fluid simulations. Finally, the Q-criterion and Lambda 2 indices were also calculated to study the vorticity of the simulations.

Statistical analysis

The statistical analysis was performed using R Studio 1.2.1335. It can be divided into two main blocks: exploratory analysis and inferential analysis. Results are presented in terms of median (minimum - maximum) for continuous and non-normally distributed variables, mean \pm standard deviation (SD) for continuous and normally distributed variables whilst categorical data is characterised as count (percentage). Student t-test, Mann-Whitney – Wilcoxon and X² tests were used depending on the nature of the variable studied. The level of significance (α) was set to 0.05. Relevant parameters in terms of significant differences (p-value $<$ 0.05) were considered potential risk factors. For more information about the statistical analysis models, the interested reader is referred to [108].

Afterwards, a step-wise regression model with only those morphological parameters that were statistically significant in the aforementioned statistical analysis was performed. For these step-wise regression models the Akaike Information Criterion (AIC)[2] was used to study their prediction accuracy. A lower AIC represents a smaller information loss by the model, so the smaller the AIC, the higher the quality of the model. The output of the best morphology-based model was combined with the haemodynamic parameters to perform a joint analysis. Moreover, machine learning algorithms such as random forest were implemented to corroborate which parameters might play a critical role to classify cases in controls and TIA/CVA, as a complement to the classical statistical tests and regression models. The input for the random forest was the morphological parameters (LAA and LA volume, ratio LAAv/LAv, length of the centreline, LAA height, ostium anterior distance, maximum ostium diameter, ostium area, and LAA shape) found in the literature that contribute in the process of thrombus formation [27, 75, 77, 130], together with haemodynamic ones (ECAP, OSI, RRT, TAWSS, and velocity). Relevance parameters were obtained finding the best hyperparameters with a grid search procedure (number of trees = 500, variables sampled at each split = 4, maximum number of terminal nodes = 90). The Gini index was used to assess the importance of each predictor.

For the in-silico haemodynamic indices (ECAP, TAWSS, OSI, and RRT), the data was normalised applying a minimum – maximum sampling approach in all the studies. Percentiles 90% and 10% were discarded to be robust against outliers while analysing the whole LAA, and its regions. For the blood flow velocity within the LAA, data were normalised by the total volume of the LAA in each case.

4.2.3 The role of the pulmonary veins on left atrial haemodynamics and thrombus formation

The LA geometries were segmented from the available CT images by a researcher which was not involved in the modelling process, in order to maintain the study blind to the modellers. The final volumetric meshes were between 7 and 9×10^5 elements, depending on the volume of the LA. The same BC and simulation setup applied in the first study presented in this chapter were applied to this one, i.e., using the DM-Spring strategy. Post-processing and visualisation of simulation results were performed using ParaView 5.4.13.

Morphological descriptors

Initially, the morphological descriptors of the LA and LAA computed in the first study (see Section 4.2.2) were also used in here. To study the influence of the PV configuration, the population was manually classified by the number of pulmonary veins. Additionally, a set of angles describing the topological relationships between the PV, the LAA, the MV and the main cavity of the LA, were computed in close collaboration with researchers at Inria Sophia-Antipolis (France), following the approach presented in [53, 92].

To estimate the LA and LAA angles each pulmonary vein was labelled in the analysed LA meshes. To label every mesh, a diffeomorphic surface registration (using the Deformetrica software[15]) was firstly applied between a previously labelled template LA shape and the rest of the LA meshes. After the surface registration, labels from the LA template were transferred to all cases. Please notice that the LA anatomy will always be reduced to 4 PV, as in the LA template.

Subsequently, the barycentre of each PV was computed, together with the centre of the ostium (e.g., interface with the LA cavity) of each label, producing a two-point representation of each vein (which it is called a branch). Furthermore, for the LAA angle, an additional landmark was included: the LAA was cut at the barycentre with the normal plane to the LAA centreline; followed by the computation of the barycentre of the outermost half. Finally, the barycentre of the LA main body was added. When linking the extracted landmarks with straight lines, a skeleton-like simplified representation of the LA is obtained, as illustrated in Figure 4.3.

From the detected landmarks we choose to compute the following morphological angles and lengths:

- α angle: between the right inferior and superior PVs (RIPV and RSPV, respectively);

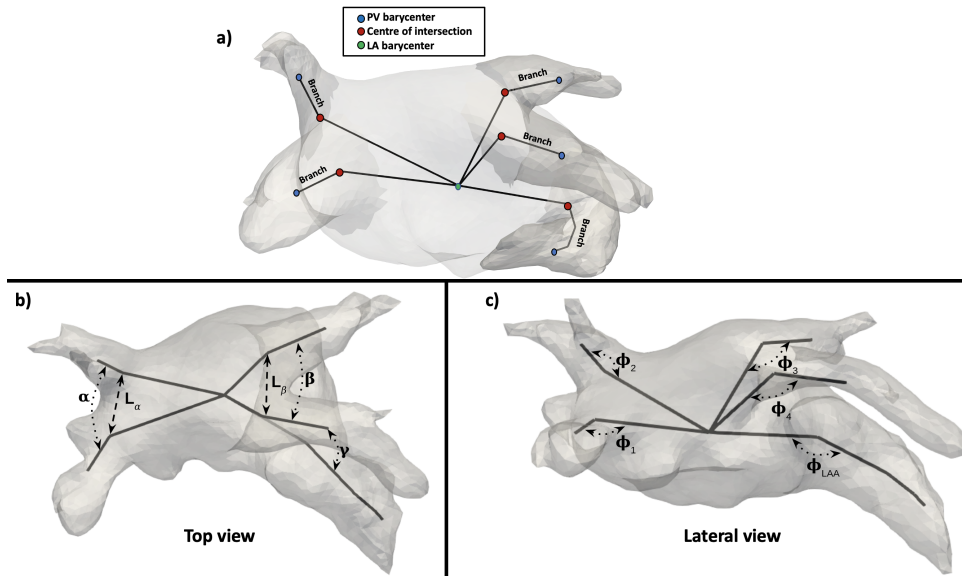


Figure 4.3: Example of a left atrial (LA) geometry with the angles estimated to characterise the topological relationships between the LA main body, the left atrial appendage ostium and the pulmonary veins. a) The LA skeleton, depicted in black, is computed linking the barycentres of the different LA sub-structures; b) top view of the left atrium α , β , γ angles, together with the distances L_α and L_β ; c) lateral view of the left atrium with the computed ϕ angles.

- β angle: between the left inferior and superior PVs (LIPV and LSPV, respectively);
- L_α length: between the RIPV and RSPV ostia;
- L_β length: between LIPV and LSPV ostia;
- α/β and L_α/L_β , being their respective ratios;
- ϕ angles: between the lines linking PV ostium centre with the PV and LA main body barycentres, characterising the inclination of each PV. From these angles, additional features can be computed such as the mean inclination of all the PVs ($1/4(\phi_1 + \phi_2 + \phi_3 + \phi_4)$), the right PVs ($1/2(\phi_1 + \phi_2)$), and the left PVs ($1/2(\phi_3 + \phi_4)$);
- ϕ_{LAA} angle: representing the LAA bending angle, being computed between the lines linking the LAA barycentre with its tip and ostium centre;
- γ angle: between the LAA ostium and the LSPV, requiring a rigid transformation of the LSPV branch and the LAA to have a common point (e.g., bringing the LAA ostium and the LSPV ostium centres to the same point).

Regarding the statistical analysis of the analysed variables, first a Shapiro-wilk test was performed to assess their distribution. For the variables failing the test, a Wilcoxon Mann Whitney test was then performed; otherwise, a simple t-test was used. The significant p-value threshold was set to 0.05.

Haemodynamic and thrombogenic descriptors

To assess LA haemodynamics and to localise the position where the main collision between the PV flows was produced (e.g., from the right and left PV), which can be defined as the instant when the flow coming from each PV crosses with each other, streamlines were created, placing 50 seeds in each PV. The streamlines were visually analysed in the following time-frames of the whole cardiac cycle: 1) at the beginning of the ventricular systole; 2) just before MV opening; 3) when the maximum blood flow velocity is reached within the E wave (early diastole, after MV opening); 4) middle time-frame between the E and A waves; and 5) when the maximum velocity of the A wave is reached (end diastole, just before MV closing and start of the next cardiac cycle). The analysis was repeated for two heart beats per case.

Furthermore, 100 particles were distributed in the different pulmonary veins (50 seeds in each side) to estimate the PV origin of the flow entering the LAA. Initially, particles were evenly distributed (e.g., in the case of 4 PV, 25 for each one). However, the varying number of PV in the population needed to be considered. Therefore, we used the PV diameters to ensure that the largest ones had more particles than the others in the same side of the LA. Notice that the number of particles for each LA side (equal to 50) is independent of the number of PVs, in order to assess which side has a more predominant blood flow.

The radius from the seed points to the sphere of particles was 2 mm. Nevertheless, in some cases where the diameter of the PV was very small, this had to be modified to ensure that all particles could fit inside the LA geometry. Afterwards, the particles were traced through the cardiac cycle computing their pathlines through the velocity vector field from the seed points. After running the fluid simulation, the number of particles in the LAA was measured, as well as their PV origin. Moreover, the particle age and velocity at the end of the beat were estimated.

The flow rate was measured from the fluid simulations at the entrance of the LAA, selecting a 2D plane below the first lobe before the LAA bending (see Figure 4.4). Blood flow entering the LAA was considered as positive, thus ongoing flow being negative. Subsequently, the obtained flow rate curve was integrated over time to compute the final volume crossing the selected 2D plane. A zero value in the integration would mean that all flow entering the LAA leaves it at the end of the two analysed cardiac cycles. Therefore, a large positive value would

indicate that a lot of blood goes inside the LAA without leaving, i.e., potentially signalling flow stagnation. In order to consider the large LAA volume variation in the population, the obtained values were estimated as a percentage of the LAA volume for each case, i.e., obtaining the amount of flow volume staying in the LAA with respect to its volume. Velocity magnitude was also measured at the same point. The ECAP and RRT in-silico haemodynamic indices were also calculated from the resulting fluid simulations.

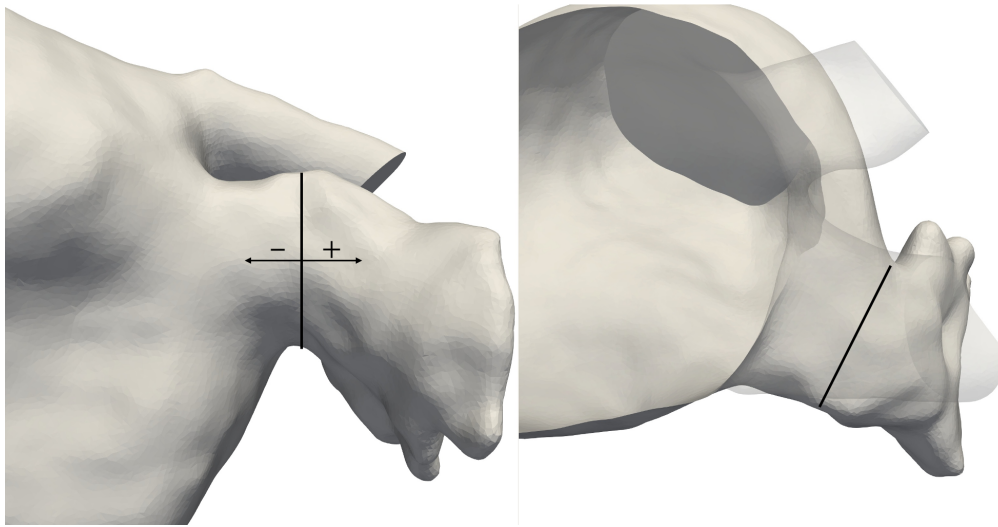


Figure 4.4: Two points of view of the 2D plane (black line) used for the blood flow rate computation, being placed below the first lobe of the left atrial appendage bending. Blood flow was considered positive if entering the LAA, and negative otherwise.

4.3 Results

4.3.1 Joint analysis of left atrial morphological parameters and in-silico haemodynamics

Clinical and morphological analysis

Significant differences between TIA/CVA and control groups were found in morphological parameters such as the maximum ($p < 0.001$), minimum ($p = 0.01$), and mean ($p = 0.001$) diameters of the ostium, as well as its minimum radius ($p = 0.02$). The length of the LAA centreline was also significant ($p = 0.05$), as well as all ostium diameters, being larger in the TIA/CVA group. The LAA shape was not significantly different between controls and TIA/CVA neither when classifying the LAA in chicken-wing versus non-chicken-wing (which were the majority

Table 4.1: Morphological descriptors of the left atria (LA) in atrial fibrillation patients. AP: anterior-posterior; CVA: cerebrovascular accident; Max: maximum; Min: minimum; TIA: transient ischaemic attack. Data were unclear for 3 TIA/CVA cases. Results are presented as mean \pm SD or median (min–max) or n (%). In bold, the significant values (p-value $<$ 0.05).

| Feature | Control (n=38) | TIA/CVA (n=33) | p-value |
|--------------------------------------|---------------------|---------------------|------------------|
| Max. ostium diameter (mm) | 25.77 \pm 4.40 | 30.20 \pm 4.90 | <0.001 |
| Min. ostium diameter (mm) | 17.46 \pm 3.66 | 19.63 \pm 2.95 | 0.01 |
| Mean ostium diameter (mm) | 21.62 \pm 3.70 | 24.91 \pm 3.66 | 0.001 |
| Min. ostium radius (mm) | 6.99 \pm 2.37 | 8.20 \pm 1.81 | 0.02 |
| Ostium area (mm ²) | 367.18 \pm 125.16 | 486.35 \pm 148.42 | <0.001 |
| Ostium perimeter (mm) | 71.16 \pm 12.27 | 80.99 \pm 12.14 | 0.001 |
| LAA height (mm) | 14.80(9.18 – 22.93) | 15.34(8.83 – 30.63) | 0.25 |
| Length of the centerline (mm) | 34.48 \pm 7.06 | 38.82 \pm 8.74 | 0.05 |
| Tortuosity | 0.79(0.50 – 0.96) | 0.77(0.45 – 0.88) | 0.36 |
| LAA anterior distance (mm) | 13.87 \pm 3.75 | 16.03 \pm 3.18 | 0.01 |
| LAA posterior distance (mm) | 11.38 \pm 3.17 | 12.83 \pm 3.54 | 0.08 |
| LAA anterior-posterior distance (mm) | 25.26 \pm 6.70 | 28.86 \pm 6.38 | 0.02 |
| Bending (degrees) | 114 \pm 17.55 | 103 \pm 23.84 | 0.07 |
| LA volume (mL) | 163(82 – 256) | 164(100 – 269) | 0.94 |
| LAA area (mm ²) | 2225(1183 – 3918) | 2677(1747 – 6006) | 0.03 |
| LAA volume (mL) | 6.63(2.59 – 15.50) | 8.09(4.12 – 15.88) | 0.02 |
| Chicken-wing | 6(15.79%) | 4(13.33%) | 0.53 |
| Cauliflowers | 10(26.32%) | 8(26.67%) | 0.82 |
| Cactus | 13(34.21%) | 7(23.33%) | 0.26 |
| Windsock | 9(23.68%) | 11(36.67%) | 0.82 |

of cases, 86%) nor in the classical four LAA types. Ostium diameter, perimeter and area, anterior distance, LAA area, and centreline length were the ones better differentiating TIA/CVA from control cases. However, the AIC obtained in morphology-based models was high among all the other ones (AIC= 85.96), thus on the lower range of accuracy.

Haemodynamic analysis

Lower blood flow velocities in the whole LAA were found in the TIA/CVA group compared with controls, as summarised in Table 4.2. In addition, higher ECAP, OSI, and RRT, all indicators of a higher risk of thrombus formation, were found in the TIA/CVA group. The TIA/CVA group also presented a worse flow washout from the LAA, indicating a higher percentage of stagnated blood in comparison with the control group (19.77% vs. 12.39%, respectively). Despite these trends, differences were not statistically significant between controls and TIA/CVA groups for any of the estimated haemodynamic indices. In all patients, vortex structures

Table 4.2: Haemodynamic indices from in-silico fluid simulations of atrial fibrillation patients. CVA: cerebrovascular accident; ECAP: endothelial cell activation potential; LAAv: left atrial appendage volume; OSI: oscillatory shear index; RRT: relative resident time; TAWSS: time average wall shear stress; TIA: transient ischaemic attack; Vel: velocity. Higher values of ECAP, OSI, and RRT as well as lower values of TAWSS and Vel/LAAv indicate a higher risk of thrombus formation.

| | Control | TIA/CVA | p-value |
|----------------------|----------------|----------------|----------------|
| TAWSS (PA) | 0.31 ± 0.12 | 0.35 ± 0.14 | 0.40 |
| ECAP (1/Pa) | 0.87 ± 0.61 | 1.08 ± 0.69 | 0.35 |
| OSI | 0.15 ± 0.05 | 0.17 ± 0.04 | 0.17 |
| RRT (s) | 10.03 ± 5.97 | 11.38 ± 7.04 | 0.62 |
| Vel/LAAv (m·ml/s/ml) | 0.99 ± 0.80 | 0.84 ± 0.35 | 0.93 |

were visually present, but no substantial qualitative differences were found in terms of vorticity between TIA/CVA and control groups.

Higher blood flow velocities, statistically significant ($p = 0.04$), were obtained for the chicken-wing group vs. the non-chicken-wing cases, consistently decreasing from the ostium to the superior LAA region. On the other hand, most of the remaining haemodynamic indicators of thrombogenic risk (ECAP, OSI, RRT) were higher in the chicken-wing group, led by large differences in the superior part of the LAA.

Joint analysis of morphological and haemodynamic parameters

The joint analysis of morphological and haemodynamic indices identified that the most significant morphological indices (e.g., ostium characteristics, LAA area, and centreline length) were always good predictors of TIA/CVA. However, when in-silico haemodynamic indices were added to the analysis, the results substantially improved the AIC metric obtained with morphological indices alone. A model with an AIC value of 14 was obtained when adding haemodynamic indices (versus 85.96 with only morphological ones) such as RRT and TAWSS, along with some morphological indices (LAA volume, ostium area, anterior distance, and length of the centreline) that were reported as potential indicators of TIA/CVA history.

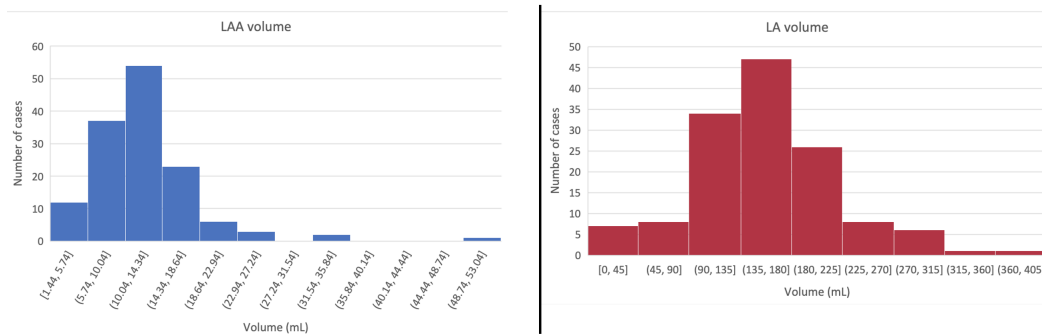


Figure 4.5: Histograms of the left atrial (LA) and left atrial appendage (LAA) volume distribution (in mL).

4.3.2 The role of the pulmonary veins on left atrial haemodynamics and thrombus formation

Volumetric analysis and topological distribution of pulmonary veins

Figure 4.5 shows the distribution of our cohort with respect to LA and LAA volumes, with the majority of cases having LAA volumes between 10 and 14 mL, and LA volumes between approximately 135 and 180 mL. The number of cases depending on the number of PV is presented in Table 4.3, with a majority of them having 4 PV (51.1%), followed by 5 PV (32.8%); cases with 3 and 7 PV were rare (3.1% each).

Differences were also found when looking at the mean LA volume separated by the number of pulmonary veins. The mean LA volume was slightly higher in subjects with 6 and 7 PV (185 and 190 mL, respectively) than the ones with 3, 4 and 5 PV (152, 161 and 166 mL, respectively). No significant relationship was found between the incidence of cardiovascular accident or thrombus history with the number of pulmonary veins, as can be seen in Table 4.3).

The topological characterisation of the PV was further analysed with the number of PV in each side (left vs right) of the LA, resulting in the identification of eleven different PV configurations, as depicted in Figure 4.6. For instance, LA with 5 PV include cases with 3 vs 2 PV in the right and left side, respectively (left LA in 5 PV row of the figure), or 4 vs 1 PV, which could in itself had two central PV together or quite separated (middle and right LA in 5 PV row of the figure, respectively). Most of the PV configurations found in this study have already been described in the literature, except the one with 3 PV on the left side in the 5 and 7 total PV group, which was present in two cases.

Table 4.3: Distribution of the analysed cases based on the number of pulmonary veins (PV) and cardiovascular even incidence. T/S: thrombus/stroke. C: control. ND: non-determined. The last column indicates the percentage of cases with cardiovascular events in each PV group.

| | Cases per group | T/S | C | ND | % of T/S |
|-------|-----------------|-----|----|----|----------|
| 3 PV | 4 | 1 | 3 | 0 | 25 |
| 4 PV | 67 | 25 | 39 | 3 | 37.31 |
| 5 PV | 43 | 19 | 23 | 1 | 46.51 |
| 6 PV | 13 | 6 | 7 | 0 | 46.15 |
| 7 PV | 4 | 1 | 3 | 0 | 25 |
| Total | 131 | 52 | 75 | 4 | - |

Orientation of pulmonary veins

The orientation of the pulmonary veins was also studied since it has an obvious impact on LA haemodynamics, especially on the location of flow collisions in the LA and how flow is reaching the LAA, thus potentially influencing blood stasis in that area. Figure 4.7 depicts blood flow patterns with different PV orientations. First, it can easily seen in the figure how with the same number of PV but different positions and orientations, blood flow patterns substantially change (e.g., Scenario 3 and 4 in Figure 4.7).

Another important finding is that when blood flow from the left PV collides at the superior part of the LA, due to their orientation, it is subsequently directed to the LAA ostium, which is usually located just under the LSPV. In consequence, the α and β angles, which characterise the angular difference between the PV in the same LA side (left and right, respectively), had a considerable effect on the resulting blood flow patterns. In our cohort, the angle between the left PV (β) varied less than the right PV one (α).

The most common PV configuration in the analysed cases was composed of LA with 4 PV, with the collision between PV flows taking place at the centre of the LA, as shown in Scenario 1 of Figure 4.7. With a higher α angle between the right PV, the right side flow could go laterally through the sides of the LA to reach the LAA (Scenarios 2 and 3 in Figure 4.7). Additionally, the inclination of the right PVs with respect to the main LA cavity (ϕ angles in Figure 4.7) determined whether the blood went vertically down towards the MV or to the centre of the LA (dashed lines in Figure 4.7). The obtained results suggest that the right side PV configuration is the main factor guiding the whole LA haemodynamics.

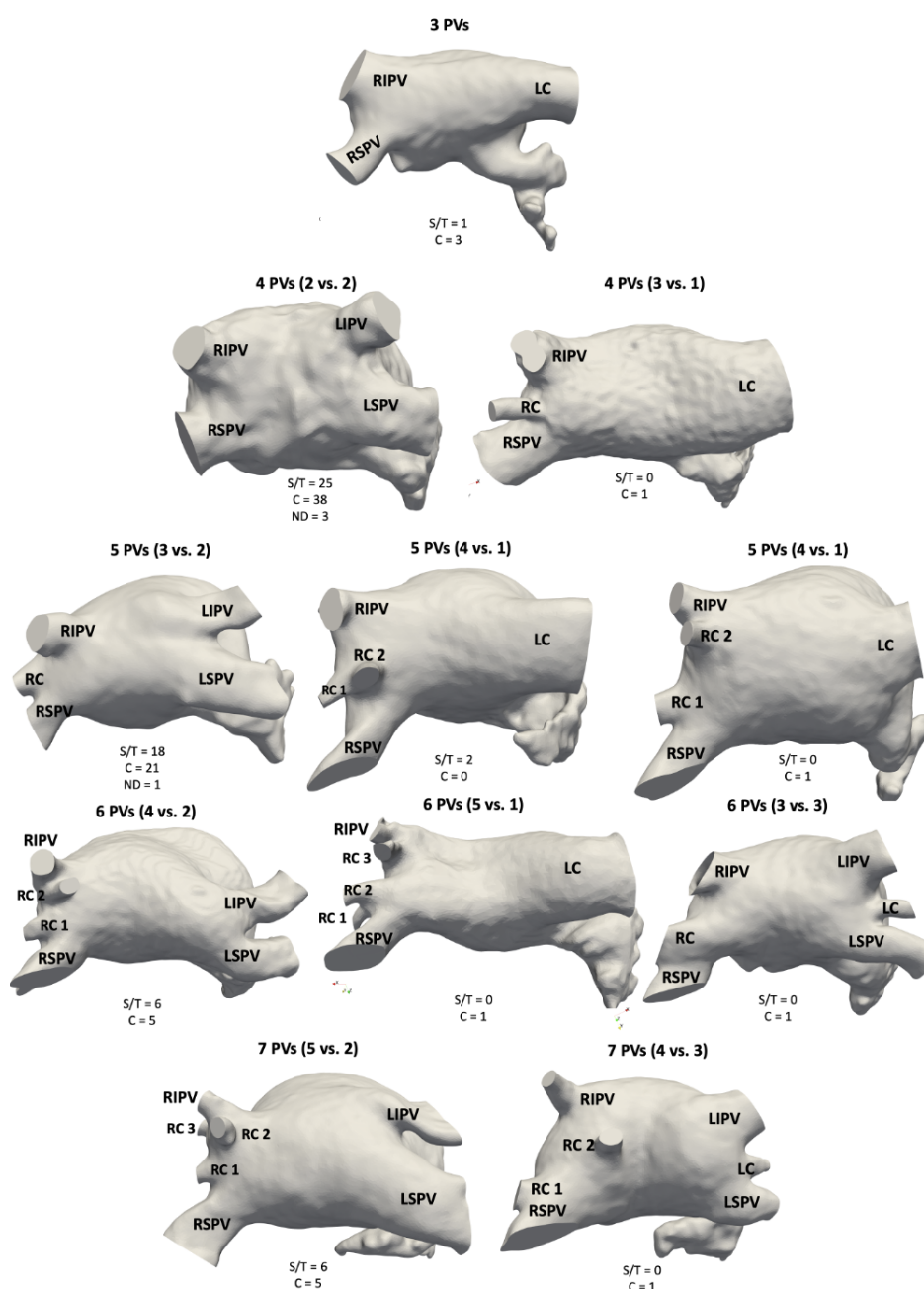


Figure 4.6: Different types of pulmonary vein (PV) topological configurations in the left atria (LA) found in the studied cohort. Between brackets the distribution of PV according to right vs. left side of the LA. RIPV/RSPV: right inferior/superior PV. LC/RC: left/right central pulmonary vein. LIPV/LSPV: left inferior/superior PV. RC1: right central PV that is closest to the RSPV; RC2: right central PV that is closest to the RIPV if there is no RC3; with an existing RC3, RC2 is in between RC1 and RC3; RC3: right central PV that is closest to the RIPV. T/S: thrombus or stroke group. C: control group.

Cases with 5 PVs also showed a higher inclination of the RIPV (ϕ angle in Scenario 5 of Figure 4.7). Furthermore, the presence of the additional RCPV shifted the RSPV towards a the right LA wall. Therefore, LA haemodynamics were mainly influenced by the α and ϕ angles (Scenarios 5 and 6 in Figure 4.7), as follows:

- With the RSPV being shifted to a more transverse position with respect to the main LA body, the flow crossed the LA, preventing the remaining right PV flows to collide with the left side flow (Scenario 5 in Figure 4.7).
- If the RCPV was located in a higher position than the RSPV, RCPV flow was the one colliding with the left PV flow, forcing RSPV flow to go under RCPV one (Scenario 6 in the figure).
- If the right PVs were very inclined (e.g., high ϕ angle), the collision point was shifted towards the right side; on the other hand if the α angle (angle between right PV) was also large, then the collision was clearly shifted to the left side; flow from the left PV could then reach the right LA wall (Scenario 7 in Figure 4.7).

Blood flow patterns observed in left atria with 6 and 7 PVs were qualitatively similar to the ones with 5 PV (Scenarios 5 and 6 in Figure 4.7).

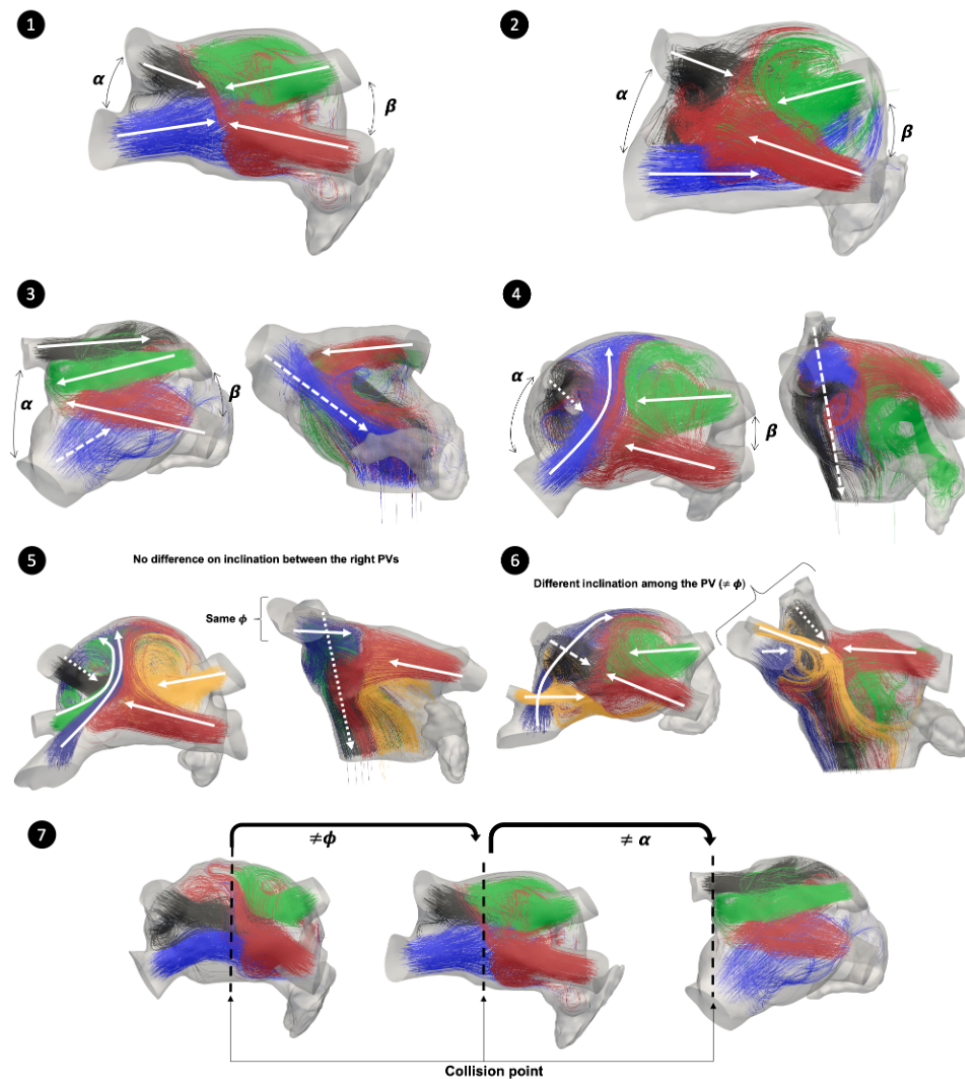


Figure 4.7: Different scenarios of pulmonary vein (PV) configurations and angles. Each colour represents flow coming from the same PV. Scenarios 1-4,7 (4 PV): green/red represents the left inferior/superior PV (LIPV/LSPV); black/blue represents the right inferior/superior PV (RIPV/RSPV). Scenario 5 (5 PV): orange/red represents LIPV/LSPV; black/blue/green represents right inferior/central/superior PV (RIPV/RSPV/RCPV). Scenario 6 (6 PV): green/red/black/blue/orange represents LIPV/LSPV/RIPV/RSPV/RCPV. The black dashed line depicts flow collision points. The solid white line is the direction of the flow coming from the PV, the white dashed line having a higher inclination (higher ϕ). The snapshots were taken at end diastole when the maximum velocity of the A wave is reached, just before mitral valve closing.

Table 4.4: Morphological, angular and haemodynamic features of the left atria (LA) and pulmonary veins that were significantly different (p-value < 0.05) between control (C) and thrombus/stroke groups (T/S). Feature values are presented as mean \pm SD or median (inter-quartile range). γ : angle between the LAA and the left superior PV main directions. LIPV: left inferior pulmonary vein. LAA: left atrial appendage. D1, D2: diameters of the ostium. In bold the parameter with most significance.

| Feature | Control | T/S group | p-value |
|---|-------------------------|-------------------------|-----------------|
| γ (degrees) | 7.25(4.33 – 10.76) | 11.48(5.38 – 16.65) | 0.00082 |
| Inclination of the LIPV (degrees): ϕ_3 | 12.54(9.49 – 16.53) | 14.74(11.68 – 17.71) | 0.022 |
| Mean inclination (degrees): $1/4(\phi_1 + \phi_2 + \phi_3 + \phi_4)$ | 7.48(7.02 – 8.96) | 8.67(7.62 – 9.80) | 0.0027 |
| Inclination of the left side (degrees): $1/2(\phi_3 + \phi_4)$ | 14.94(13.57 – 18.47) | 17.33(14.37 – 20.02) | 0.019 |
| Inclination of the right side (degrees): $1/2(\phi_1 + \phi_2)$ | 3.98(3.09 – 5.11) | 4.66(3.85 – 5.66) | 0.0089 |
| D1 (mm) | 27 \pm 5.88 | 29.63 \pm 5.81 | 0.01525 |
| D2 (mm) | 19.26(16.76 – 12.27) | 21.41(19.03 – 24.18) | 0.0078 |
| Tortuosity | 0.3871 \pm 0.0769 | 0.4217 \pm 0.0620 | 0.0065 |
| LA area (mm ²) | 23924 \pm 4709 | 21302 \pm 3674 | 0.00070 |
| LA volume (mL) | 172.27(146.1 – 223.86) | 153.02(119.91 – 188.97) | 0.0087 |
| Ostium perimeter (mm) | 74.32(64.5 – 80.47) | 81.57(71.24 – 91.94) | 0.0097 |
| Ostium area (mm ²) | 408.4(308 – 427) | 489.9(378 – 653) | 0.0096 |
| Ostium mean diameter (mm) | 23.342(20.384 – 25.368) | 25.26(22.12 – 28.79) | 0.0084 |
| Total number of particles | 130.0(83.0 – 184.2) | 211.5(158.5 – 257.8) | < 0.0001 |
| LAA/LA ratio (%) | 7.9(6.63 – 9.82) | 6.76(5.27 – 7.9) | 0.0014 |

Relevant left atrial and pulmonary vein morphological and haemodynamic characteristics in thrombus formation

We performed a statistical analysis to identify the set of extracted features (i.e., morphological, angular, haemodynamic) that were related to the presence of thrombus. Table 4.4 lists the features that were statistically different between thrombus and non-thrombus groups.

Most of the LA morphological features that appear in Table 4.4, such as the ostium characteristics, have already been reported in the literature (and in the analysis of the previous study in this chapter) as being associated to the risk of thrombus (i.e. larger ostia). Additionally, the LA volume and area, the LAA/LA ratio and the LAAO tortuosity were significant larger in thrombus cases (the latter was not in our previous study).

Angles characterising the LA topology were also significantly different between control and thrombus/stroke (T/S) cases, mainly the γ (i.e., angle between the main directions of the LAA and the LSPV) and ϕ angles from the left and right sides. In the studied cohort, T/S cases had larger γ angles than the control group, as illustrated in Figure 4.8. Moreover, the ϕ angles from the left and right

LA sides were also larger in thrombus cases, i.e. more inclined left and right PV.

Overall, the most significantly different parameter between controls and thrombus cases was the total number of particles found in the LAA after three cardiac cycles of the in-silico fluid simulations. The remaining in-silico haemodynamic indices were similar between the two studied groups.

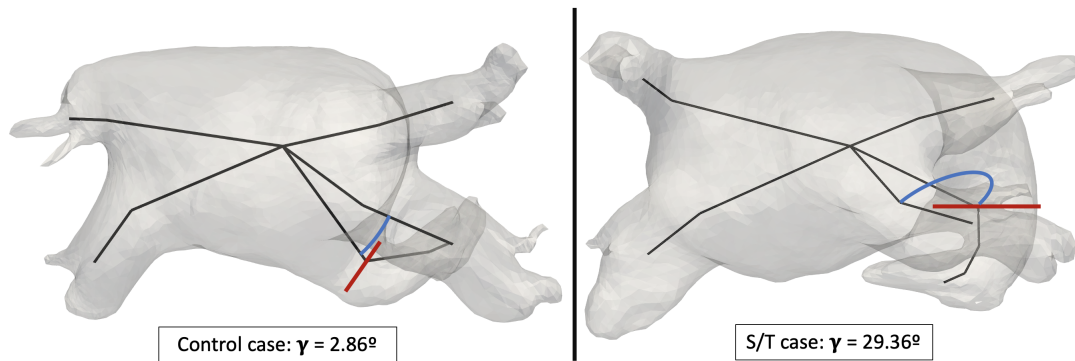


Figure 4.8: An example of the γ angle (blue line) between the left atrial appendage (LAA) ostium plane (red line) and the orientation of the left superior pulmonary vein (LSPV) for control (left) and thrombus/stroke (right) examples. Black lines represent the LA skeleton. The control case has a lower γ angle than the thrombus/stroke case, indicating a better alignment between the LSPV and LAA main axis.

Analysis with fluid-based particles

The number of particles was normalised to compare different cases, even if they had different LA volumes. First, the contribution from each PV side and individual PV to the particles staying in the LAA was estimated. The number of PV determined the origin of LAA particles. For instance, in LA geometries with 3 PV (i.e., only one PV in the left side) 76% of LAA particles came from the left side. Interestingly, the same situation occurs in cases with 7 PV where the left side only had two PV (bottom left in Figure 4.6, the left side representing 61% of LAA particles). The remaining LA cases (4-6 PV) had a more balanced distribution of the contribution of each PV side into LAA particles (56.92%, 55.94%, 52.43% from the left side, respectively). Analysing thrombus risk, we did not find any parameter related to the PV origin of LAA particles.

On the other hand, there was an association between the number of particles in the LAA and the alignment between the LAA and LSPV main directions, as quantified by the γ angle: lower values of γ , thus more aligned LAA and LSPV, were linked to having more particles entering the LAA. However, such observation was not valid for chicken-wing LA morphologies due to their extreme variations in

ostium positions, bending angles and tip directions (see Figure 4.9), which induce different LAA haemodynamics than in the rest geometries. Accordingly, a classification of the LA geometries was set to better explore LA haemodynamics, including the following groups: 1) alignment of the LAA and LSPV main directions (group A); 2) not-aligned LAA and LSPV main (group NA); 3) chicken-wing LAA geometries (CW group). Examples of LA geometries in each category are shown in Figure 4.9.

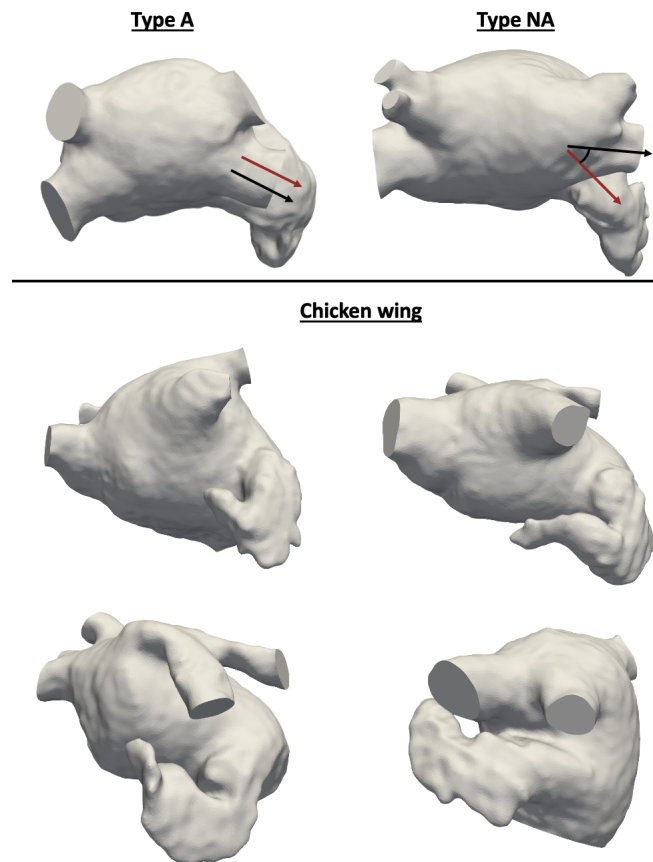


Figure 4.9: The three groups selected for the analysis of the fluid-particle results. A/NA (top row): left atrial appendage (LAA) and left superior pulmonary vein (LSPV) main directions are aligned or not, respectively. The black arrow indicates the direction of the left superior pulmonary vein (LSPV). The red arrow shows the main direction of the initial part of the left atrial appendage (LAA), i.e., the landing zone between the LAA ostium and neck. Chicken-wing LAA morphologies required an analysis independent of the LAA-LSPV alignment. Four different chicken-wing morphologies are shown (second and third row) to demonstrate their variability in localisation with respect to the left PVs, bending angles, and tip direction.

Table 4.5: Distribution of cases based on the number of pulmonary veins (PV) and alignment of left atrial appendage (LAA) and left superior PV (LSPV) main directions. Av. P.: Average of particles in the LAA at the end of the simulation, including control and thrombus cases. C: control group. T/S: thrombus or stroke. A/NA: LAA and LSPV main directions are aligned/not-aligned. CW: chicken-wing. % of T: % of thrombus cases in that group. The four cases in our database without follow-up were not included in this study.

| | A | | NA | | CW | | All groups | |
|-------------|----------|-----------|-----------|-----------|-----------|-----------|-------------------|-----------|
| | % of T | Av. Part. | % of T | Av. Part. | % of T | Av. Part. | % of T | Av. Part. |
| 3 PV | 100% | 353 | 0% | 113.33 | - | - | 25% | 173.25 |
| 4 PV | 46% | 230 | 35% | 122 | 23% | 147.5 | 37% | 170.66 |
| 5 PV | 57% | 215.05 | 45% | 253.62 | 33.33% | 129.07 | 47% | 194.19 |
| 6 PV | 60% | 215.6 | 40% | 176.2 | 33.33% | 192 | 46% | 195 |
| 7 PV | 0% | 204 | - | - | 33.33% | 132 | 25% | 150 |

Table 4.5 presents the distribution of the studied LA shapes based on the number of PV and the LAA-LSPV alignment-based categories, including the number of LAA particles at the end of the fluid simulations and the percentage of thrombus cases. Below there are some observations on LA haemodynamics when jointly analysing all these parameters.

3 PV

It was difficult to draw conclusions in this sub-set since it only contained 3 control cases and one with thrombus. The latter was the only one with the LAA and LSPV well aligned (small γ angle), also having more particles in the LAA at the end of fluid simulations than the healthy LA, as shown in Table 4.5. In addition, particles in the LA were predominantly coming from the left PV (around 80%) in these cases, with flow patterns being similar between controls and thrombus groups (see Table 4.6).

Table 4.6: Distribution of particles based on the PVs for 3 PVs. Each row represents the average percentage of particles originating from each pulmonary vein that end in the left atrial appendage (LAA) for control (C) and thrombus or stroke group (T/S). LCPV: left central pulmonary vein; RSPV: right superior pulmonary vein; RIPV: right inferior pulmonary vein; LS: pulmonary veins from the left side (i.e., LCPV); RS: pulmonary veins from the right side (i.e., RSPV and RIPV). The last row represents the average of particles found in the LAA for the C and T/S groups at the end of the simulation. There is only case in T/S group with 3PVs and is Type A, whereas all the control cases are Type NA. The major differences between the two groups are shown in bold.

| Pulmonary vein | T/S (Type A) | C (Type NA) |
|-------------------------|---------------------|--------------------|
| LCPV (%) | 83.29 | 73.96 |
| RSPV (%) | 15.58 | 18.31 |
| RIPV (%) | 1.13 | 7.72 |
| LS (%) | 83.29 | 73.96 |
| RS (%) | 16.71 | 26.04 |
| Particles (Total numb.) | 353 | 133.33 |

4 PV

In LA geometries with 4 PV, which was the most populated group, there was slightly more control than thrombus cases within the sub-group of high LAA-LSPV alignment (54% and 46%, respectively), as can be seen in Table 4.5. However, the percentage of thrombus cases in non-aligned LAA-LSPV was lower than for the aligned ones (35% vs 46%). The number of LAA particles in the aligned group was lower in controls than in thrombus cases (198.75 and 278.06, respectively). Similarly, the contribution of the left side flow into the LAA particles was different for these groups, being higher in controls than in thrombus cases (66.70% vs 55.91%, respectively), mainly led by the LSPV contribution (43.80% vs 36%, respectively) and to the detriment of the RSPV (Table 4.8). The same pattern was found in the non-aligned LA cases, i.e., having an increased contribution of the left side was associated to a lower risk of thrombosis (LSPV contribution of 58.12% and 48.26% in controls and thrombus, respectively), but this time, inferior PVs have a greater influence than the aligned cases (Table 4.9). The LA geometries with a chicken-wing morphology presented an opposite behaviour than the other LAA shapes, with control cases having the largest contribution from the right PV (thus, the RSPV) on LAA particles as is presented in Table 4.10. Moreover, controls had less particles in the LAA than thrombus cases (147.5 and 190, respectively). Overall, we could state that:

- Higher LAA-LSPV alignment is related to having more particles in the LAA but not so clearly to thrombogenic risk.
- Thrombus cases had more LAA particles within each sub-group (i.e., based on LAA-LSPV alignment, so in the aligned group, controls have less LAA particles than thrombus examples).
- Having more LAA particles is related to a lower participation of the left PV except for CW group.
- Thrombus cases are related to a higher participation of the right PV on LAA particles, in particular from the RSPV except for CW group.

Table 4.7: Distribution of particles based on the PVs for 4 PVs. Each row represents the average percentage of particles originating from each pulmonary vein that end in the left atrial appendage (LAA) for control (C) and thrombus or stroke group (T/S). LSPV: left superior pulmonary vein; LIPV: left inferior pulmonary vein; RSPV: right superior pulmonary vein; RIPV: right inferior pulmonary vein; LS: pulmonary veins from the left side (i.e., LSPV and LIPV); RS: pulmonary veins from the right side (i.e., RSPV and RIPV). The last row represents the average of particles found in the LAA for the C and T/S groups at the end of the simulation. The major differences between the two groups are shown in bold.

| Pulmonary vein | T/S | C |
|-------------------------|--------------|---------------|
| LSPV (%) | 31.51 | 35.68 |
| LIPV (%) | 21.5 | 24.27 |
| RSPV (%) | 28.45 | 24.67 |
| RIPV (%) | 18.71 | 16.40 |
| LS (%) | 53.01 | 59.95 |
| RS (%) | 47.15 | 41.07 |
| Particles (Total numb.) | 213.5 | 144.74 |

Table 4.8: Distribution of particles based on the PVs for the Type A shape with 4 PVs. Each row represents the average percentage of particles originating from each pulmonary vein that end in the left atrial appendage (LAA) for control (C), thrombus or stroke group (T/S) and the whole group (i.e., T/S + C). LSPV: left superior pulmonary vein; LIPV: left inferior pulmonary vein; RSPV: right superior pulmonary vein; RIPV: right inferior pulmonary vein. The last row represents the average of particles found in the LAA for the C and T/S groups at the end of the simulation. The major differences between the two groups are shown in bold.

| Pulmonary vein | Type A | Type A (T/S) | Type A (C) |
|-------------------------|---------------|---------------------|-------------------|
| LSPV (%) | 39.31 | 35.91 | 43.81 |
| LIPV (%) | 22.41 | 20.75 | 22.90 |
| RSPV (%) | 23.92 | 26.47 | 21.13 |
| RIPV (%) | 15.60 | 17.10 | 14.74 |
| Particles (Total numb.) | 230.16 | 278.06 | 198.75 |

Table 4.9: Distribution of particles based on the PVs for the Type NA shape with 4 PVs. Each row represents the average percentage of particles originating from each pulmonary vein that end in the left atrial appendage (LAA) for control (C), thrombus or stroke group (T/S) and the whole group (i.e., T/S + C). LSPV: left superior pulmonary vein; LIPV: left inferior pulmonary vein; RSPV: right superior pulmonary vein; RIPV: right inferior pulmonary vein. The last row represents the average of particles found in the LAA for the C and T/S groups at the end of the simulation. The major differences between the two groups are shown in bold.

| Pulmonary vein | Type NA | Type NA (T/S) | Type NA (C) |
|-------------------------|----------------|----------------------|--------------------|
| LSPV (%) | 29.85 | 25.77 | 31.56 |
| LIPV (%) | 22.23 | 17.35 | 26.11 |
| RSPV (%) | 29.88 | 34.51 | 26.45 |
| RIPV (%) | 17.95 | 22.11 | 15.86 |
| Particles (Total numb.) | 128.33 | 170.83 | 104.15 |

Table 4.10: Distribution of particles based on the PVs for the Type CW shape with 4 PVs. Each row represents the average percentage of particles originating from each pulmonary vein that end in the left atrial appendage (LAA) for control (C), thrombus or stroke group (T/S) and the whole group (i.e., T/S + C). LSPV: left superior pulmonary vein; LIPV: left inferior pulmonary vein; RSPV: right superior pulmonary vein; RIPV: right inferior pulmonary vein. The last row represents the average of particles found in the LAA for the C and T/S groups at the end of the simulation. The major differences between the two groups are shown in bold.

| Pulmonary vein | Type CW | Type CW (T/S) | Type CW (C) |
|-------------------------|----------------|----------------------|--------------------|
| LSPV (%) | 29.35 | 31.02 | 32.18 |
| LIPV (%) | 26.12 | 28.57 | 20.61 |
| RSPV (%) | 26.05 | 20.77 | 28.32 |
| RIPV (%) | 18.71 | 19.64 | 19.28 |
| Particles (Total numb.) | 147.5 | 190 | 117.65 |

5 PV

In LA geometries with 5 PV, thrombus cases had both aligned and non-aligned LAA-LSPV (see Table 4.5), even if, as for 4 PV cases, the percentage of thrombus in aligned cases was higher than in the non-aligned group (57% and 45%, respectively). A remarkable difference from the previous groups is that controls with 5 PV had a higher contribution of the right side in LAA particles than in thrombus (opposite behaviour with 4 PV, i.e., higher left side contribution in controls, see Table 4.11), could be due to the presence of the RCPV and shifting of the RSPV. Moreover, non-aligned LAA-LSPV cases has a higher average of LAA particles than the aligned LA geometries (253.62 vs 215.05, respectively), being the contrary trend than in previous categories, overall demonstrating important differences in LA haemodynamics between 4 and 5 PV configurations (see Table 4.5).

Complementary, chicken-wing LAA cases with 5 PV and thrombus history had more LAA particles than controls (193.5 vs 169.45, respectively). This time, the difference between control and thrombus group it is not explained by the difference in participation between the right and left side but by the difference in the participation pattern of the right side (Table 4.14). In the control group, RCPV contributes more than in the thrombus group (24.67% vs 7.46%, respectively) and to detriment of the RSPV (14.20% vs 27.71%, respectively). Moreover, as in A/NA groups, flow from the right PV is contributing more to LAA particles than the left one in controls (Tables 4.12 and 4.13). The reason is in A group is a higher weight of the RCPV flow in LAA particles of controls than in thrombus cases (21.13% and 12.87%, respectively), also compared to the RSPV flow percentage (21.13% on average and 12.71%, respectively). In NA group the the difference is found only in the RCPV (12.51% on average and 6.56 %, respectively).

Table 4.11: Distribution of particles based on the PVs for 5 PVs. Each row represents the average percentage of particles originating from that pulmonary vein that end in the left atrial appendage (LAA) for control (C) and thrombus or stroke group (T/S). LSPV: left superior pulmonary vein; LIPV: left inferior pulmonary vein; RSPV: right superior pulmonary vein; RIPV: right inferior pulmonary vein; RCPV: right central pulmonary vein; LS: pulmonary veins from the left side (i.e., LSPV and LIPV); RS: pulmonary veins from the right side (i.e., RSPV, RCPV and RIPV). The last row represents the average of particles found in the LAA for the C and T/S groups at the end of the simulation. The major differences between the two groups are shown in bold.

| Pulmonary vein | T/S | C |
|-------------------------|--------------|---------------|
| LSPV (%) | 33.40 | 30.48 |
| LIPV (%) | 27.82 | 21.60 |
| RSPV (%) | 15.99 | 17.49 |
| RCPV (%) | 10.57 | 18.82 |
| RIPV (%) | 13.05 | 13.52 |
| LS (%) | 61.24 | 52.08 |
| RS (%) | 39.61 | 49.82 |
| Particles (Total numb.) | 213.5 | 144.74 |

Table 4.12: Distribution of particles based on the PVs for the Type A shape with 5 PVs. Each row represents the average percentage of particles originating from each pulmonary vein that end in the left atrial appendage (LAA) for control (C), thrombus or stroke group (T/S) and the whole group (i.e., T/S + C). LSPV: left superior pulmonary vein; LIPV: left inferior pulmonary vein; RSPV: right superior pulmonary vein; RIPV: right inferior pulmonary vein; RCPV: right central pulmonary vein. The last row represents the average of particles found in the LAA for the C and T/S groups at the end of the simulation. The major differences between the two groups are shown in bold. *The result is taking into account outliers.

| Pulmonary vein | Type A | Type A (T/S) | Type A (C) |
|-------------------------|---------------|---------------------|-------------------|
| LSPV (%) | 33.87 | 33.17 | 31.2 |
| LIPV (%) | 23.64 | 27.58 | 22.90 |
| RSPV (%) | 15.83 | 12.71 | 21.13 |
| RCPV (%) | 14.94 | 12.87 | 21.13 |
| RIPV (%) | 14.41 | 17.10 | 15.01 |
| Particles (Total numb.) | 215.16 | 190.55 | 207.57* |

Table 4.13: Distribution of particles based on the PVs for the Type NA shape with 5 PVs. Each row represents the average percentage of particles originating from each pulmonary vein that end in the left atrial appendage (LAA) for control (C), thrombus or stroke group (T/S) and the whole group (i.e., T/S + C). LSPV: left superior pulmonary vein; LIPV: left inferior pulmonary vein; RSPV: right superior pulmonary vein; RIPV: right inferior pulmonary vein; RCPV: right central pulmonary vein. The last row represents the average of particles found in the LAA for the C and T/S groups at the end of the simulation. The major differences between the two groups are shown in bold.

| Pulmonary vein | Type NA | Type NA (T/S) | Type NA (C) |
|-------------------------|---------|---------------|---------------|
| LSPV (%) | 32.38 | 38.65 | 31.67 |
| LIPV (%) | 26.13 | 27.71 | 25.74 |
| RSPV (%) | 14.93 | 15.54 | 16.48 |
| RCPV (%) | 11.58 | 6.56 | 12.51 |
| RIPV (%) | 14.98 | 11.53 | 13.60 |
| Particles (Total numb.) | 253.63 | 210.5 | 175.75 |

Table 4.14: Distribution of particles based on the PVs for the Type CW shape with 5 PVs. Each row represents the average percentage of particles originating from each pulmonary vein that end in the left atrial appendage (LAA) for control (C), thrombus or stroke group (T/S) and the whole group (i.e., T/S + C). LSPV: left superior pulmonary vein; LIPV: left inferior pulmonary vein; RSPV: right superior pulmonary vein; RIPV: right inferior pulmonary vein; RCPV: right central pulmonary vein. The last row represents the average of particles found in the LAA for the C and T/S groups at the end of the simulation. The major differences between the two groups are shown in bold.

| Pulmonary vein | Type CW | Type CW (T/S) | Type CW (C) |
|-------------------------|---------|---------------|--------------|
| LSPV (%) | 23.23 | 27.28 | 31.2 |
| LIPV (%) | 22.58 | 28.89 | 28.9 |
| RSPV (%) | 17.14 | 27.71 | 14.20 |
| RCPV (%) | 17.06 | 7.46 | 24.67 |
| RIPV (%) | 11.25 | 10.02 | 14.18 |
| Particles (Total numb.) | 116.54 | 206.75 | 73.57 |

6 PV

Following the same trend as in other PV configurations, LA geometries with 6 PV had a higher percentage of thrombus cases in LAA-LSPV aligned subjects vs non-aligned ones (60% vs 40%, respectively). It is also confirmed that the right PV flow contributes more to LAA particles with higher LAA-LSPV misalignment (43.22% and 57.43% in aligned and non-aligned groups, respectively). Analysing the influence of each individual PV, in the aligned LAA-LSPV group, we could observe that the LIPV was the higher contributors of LAA particles in control group. On the other hand, in thrombus cases, LIPV contribution reduces and the RIPV increases (see Table 4.16). The chicken-wing group had the same trend as the aligned one (Table 4.18). As for the non-aligned group, the opposite behaviour was found, with the RIPV being the main player in controls, and LIPV in thrombus subjects (Table 4.17).

Table 4.15: Distribution of particles based on the PVs for 6 PVs. Each row represents the average percentage of particles originating from that pulmonary vein that end in the left atrial appendage (LAA) for control (C) and thrombus or stroke group (T/S). LSPV: left superior pulmonary vein; LIPV: left inferior pulmonary vein; RSPV: right superior pulmonary vein; RIPV: right inferior pulmonary vein; RSCPV: right superior central pulmonary vein; RICPV: right inferior central pulmonary vein; LS: pulmonary veins from the left side (i.e., LSPV and LIPV); RS: pulmonary veins from the right side (i.e., RSPV, RSCPV, RICPV and RIPV). The last row represents the average of particles found in the LAA for the C and T/S groups at the end of the simulation. The major differences between the two groups are shown in bold.

| Pulmonary vein | T/S | C |
|-------------------------|--------------|---------------|
| LSPV (%) | 27.76 | 29.58 |
| LIPV (%) | 26.17 | 25.15 |
| RSPV (%) | 9.74 | 10.72 |
| RIPV (%) | 11.71 | 13.99 |
| RSCPV (%) | 9.02 | 10.19 |
| RICPV (%) | 16.59 | 10.35 |
| LS (%) | 52.93 | 54.74 |
| RS (%) | 47.07 | 45.26 |
| Particles (Total numb.) | 213.5 | 144.74 |

Table 4.16: Distribution of particles based on the PVs for the Type A shape with 6 PVs. Each row represents the average percentage of particles originating from each pulmonary vein that end in the left atrial appendage (LAA) for control (C), thrombus or stroke group (T/S) and the whole group (i.e., T/S + C). LSPV: left superior pulmonary vein; LIPV: left inferior pulmonary vein; RSPV: right superior pulmonary vein; RIPV: right inferior pulmonary vein; RSCPV: right superior central pulmonary vein; RICPV: right inferior central pulmonary vein. The last row represents the average of particles found in the LAA for the C and T/S groups at the end of the simulation. The major differences between the two groups are shown in bold.

| Pulmonary vein | Type A | Type A (T/S) | Type A (C) |
|-------------------------|---------------|---------------------|-------------------|
| LSPV (%) | 28.63 | 27.96 | 29.65 |
| LIPV (%) | 29.12 | 23.41 | 37.68 |
| RSPV (%) | 10.20 | 10.12 | 10.31 |
| RIPV (%) | 12.94 | 15.57 | 9.01 |
| RSCPV (%) | 7.47 | 6.96 | 8.23 |
| RICPV (%) | 11.63 | 15.97 | 5.12 |
| Particles (Total numb.) | 215.6 | 260 | 149 |

Table 4.17: Distribution of particles based on the PVs for the Type NA shape with 6 PVs. Each row represents the average percentage of particles originating from each pulmonary vein that end in the left atrial appendage (LAA) for control (C), thrombus or stroke group (T/S) and the whole group (i.e., T/S + C). LSPV: left superior pulmonary vein; LIPV: left inferior pulmonary vein; RSPV: right superior pulmonary vein; RIPV: right inferior pulmonary vein; RSCPV: right superior central pulmonary vein; RICPV: right inferior central pulmonary vein. The last row represents the average of particles found in the LAA for the C and T/S groups at the end of the simulation. The major differences between the two groups are shown in bold.

| Pulmonary vein | Type NA | Type NA (T/S) | Type A (C) |
|-------------------------|----------------|----------------------|-------------------|
| LSPV (%) | 27.48 | 23.76 | 31.20 |
| LIPV (%) | 24.02 | 34.73 | 13.31 |
| RSPV (%) | 10 | 11.74 | 8.26 |
| RIPV (%) | 14.26 | 6.52 | 22 |
| RSCPV (%) | 13.09 | 14.10 | 12.08 |
| RICPV (%) | 11.13 | 9.13 | 13.14 |
| Particles (Total numb.) | 176.2 | 185 | 170.33 |

Table 4.18: Distribution of particles based on the PVs for the Type CW shape with 6 PVs. Each row represents the average percentage of particles originating from each pulmonary vein that end in the left atrial appendage (LAA) for control (C), thrombus or stroke group (T/S) and the whole group (i.e., T/S + C). LSPV: left superior pulmonary vein; LIPV: left inferior pulmonary vein; RSPV: right superior pulmonary vein; RIPV: right inferior pulmonary vein; RSCPV: right superior central pulmonary vein; RICPV: right inferior central pulmonary vein. The last row represents the average of particles found in the LAA for the C and T/S groups at the end of the simulation. The major differences between the two groups are shown in bold.

| Pulmonary vein | Type CW | Type CW (T/S) | Type CW (C) |
|-------------------------|----------------|----------------------|--------------------|
| LSPV (%) | 27.66 | 29.11 | 26.22 |
| LIPV (%) | 20.54 | 17.30 | 23.78 |
| RSPV (%) | 10.55 | 4.64 | 16.46 |
| RIPV (%) | 9.23 | 10.55 | 7.93 |
| RSCPV (%) | 7.71 | 6.96 | 8.23 |
| RICPV (%) | 24.29 | 33.33 | 15.24 |
| Particles (Total numb.) | 192 | 237 | 169.5 |

7 PV

The analysis of 7 PV cases was limited to four cases, including 3 CW LAA morphologies, thus few conclusions can be drawn. The non-CW case, which did not have thrombus, had a high LAA-LSPV alignment and a large left side contribution into LAA particles, following the trend described above. Finally, it was not possible to find consistent trends in the studied parameters for the CW cases.

Table 4.19: Distribution of particles based on the PVs for 7 PVs. Each row represents the average percentage of particles originating from that pulmonary vein that end in the left atrial appendage (LAA) for control (C) and thrombus or stroke group (T/S). LSPV: left superior pulmonary vein; LIPV: left inferior pulmonary vein; RSPV: right superior pulmonary vein; RIPV: right inferior pulmonary vein; RCPV: right central pulmonary vein; RSCPV: right superior central pulmonary vein; RICPV: right inferior central pulmonary vein; LS: pulmonary veins from the left side (i.e., LSPV and LIPV); RS: pulmonary veins from the right side (i.e., RSPV, RSCPV, RCPV, RICPV and RIPV). The last row represents the average of particles found in the LAA for the C and T/S groups at the end of the simulation. The major differences between the two groups are shown in bold. There is only case in T/S group with 7 PVs and is Type CW, whereas all the control cases are Type A or CW. No NA type in this group. The major differences between the two groups are shown in bold.

| Pulmonary vein | T/S - Type CW | C - CW and A |
|-------------------------|----------------------|---------------------|
| LSPV (%) | 25 | 44.03 |
| LIPV (%) | 32.58 | 18.91 |
| RSPV (%) | 16.7 | 11.10 |
| RCPV (%) | 9.09 | 7.92 |
| RIPV (%) | 4.55 | 11.82 |
| RSCPV (%) | 6.82 | 6.18 |
| RICPV (%) | 5.30 | 7.92 |
| LS (%) | 57.58 | 62.96 |
| RS (%) | 42.42 | 37.04 |
| Particles (Total numb.) | 132 | 156 |

4.4 Discussion

4.4.1 Joint analysis of left atrial morphological parameters and in-silico haemodynamic indices

In the first study presented in this chapter, we assessed the significance of parameters characterising the LAA morphology and haemodynamics to distinguish controls from TIA/CVA cases. Currently, there is not any robust approach in AF patients to predict the risk of events potentially leading to stroke such as TIA/CVA or thrombus formation. Despite being regularly used, it has been proven that scores such as the CHA₂DS₂-VASc are not fully reliable, with some patients having low score values still generating thrombus [81]; in fact, the CHA₂DS₂-VASc resulted to be not significant in our study. Characterising the LA/LAA morphology with qualitative, subjective, or too simple parameters is also insufficient to capture the high complexity and large variability of LAA shapes. The classical LAA morphology type classification (e.g., chicken wing, windsock, etc.) is not rigorous enough (i.e., high inter-observer variability), leading to confronted results [140, 130, 55] when related to the risk of thrombus formation. In the studied database, we did not find differences in the percentage of chicken-wing LAA morphologies in controls and TIA/CVA groups, disagreeing with Di Biase et al. [27] findings (e.g., less likelihood of an embolic event for chicken-wing LAA morphologies). Nevertheless, our models were extracted from angiography images that have a low resolution, and thus a precise assessment of the LAA shape was difficult. Additionally, none of the types of LAA shapes were significant. On the other hand, other volumetric and morphological parameters such as ostium measurements (i.e., diameters, radius, area, perimeter), the LAA area/volume, and the centreline length, were found to be good predictors of TIA/CVA events, in agreement with other studies [77, 75], suggesting a higher risk for larger LAA and ostium. But, as mentioned above, a lot of controversy exists with these parameters since contradictory results can be found in the literature [69] (i.e., smaller LAA and ostium having a higher risk of thrombus). The use of different criteria to identify the LAA ostium could explain these opposite conclusions.

The in silico haemodynamic indices resulting from our simulations showed trends in agreement with literature, i.e., TIA/CVA cases being associated with lower blood flow velocities, more complex patterns, larger residence times, and worse flow washout than controls. However, differences between controls and TIA/CVA cases were not statistically significant, having a large variability in each cohort (see standard deviations in Table 4.2). The use of generic boundary conditions in all simulated subjects, preventing more personalized outcomes that could have been obtained with patient-specific boundary conditions (e.g. mitral valve velocity profile from echocardiographic Doppler studies), could partially explain

these findings.

In our study, when only using clinical data and morphological parameters, the statistical studies produced regression models with limited accuracy, represented as high AIC metric values. Despite in-silico haemodynamic indices not being significantly different between controls and TIA/CVA cases, the joint analysis of morphological and haemodynamic indices achieved a better fitted predictive model than when analysed separately, with a substantial reduction of the AIC metric (from 85.96 with only morphological parameters to 14 when adding optimal haemodynamic indices). The model was obtained combining morphological features characterising ostium and LAA size (e.g., the maximum ostium diameter, LAA area, and centreline length) together with haemodynamic indices of the whole LAA, mainly representing blood flow velocity magnitude (e.g., TAWSS and Vel/LAAv values).

Some limitations of the performed study should be taken into consideration. First, the analysed cases were divided according to TIA/CVA history, which does not necessarily involve thrombus formation or degradation to stroke. In addition, we did not know if the TIA/CVA had its origin in the LAA. Moreover, the available imaging data were acquired with a 3DRA system, which has lower spatial resolution than CT scans, and prevented the building of in-silico simulations for all the available cases (i.e., image quality excessively dependent on factors such as contrast injection).

4.4.2 The role of the pulmonary veins on left atrial haemodynamics and thrombus formation

The second work presented in this chapter focused on studying the influence of PV configuration on LA haemodynamics, being the first time these factors were related to potential LAA flow stagnation and thus thrombus risk. In order to do so, we have created the largest database of patient-specific LA fluid simulations in the literature so far, with more than 130 simulated subjects. Until now, most of the studies had less than 10 processed real LA anatomies, with the exceptions of the preliminary results of our research, presented last year [92] on 52 cases, and the recent work published by Rigatelli et al., [115] with 60 individuals, comparing LA haemodynamics between AF and foramen ovale patients.

The large studied cohort allowed a detailed analysis of PV morphology and its variability depending on the number and distribution of pulmonary veins. Eleven different PV configurations were found, with cases having from 3 to 7 PV, the most common sub-group being the one with 4 PV, followed by 5 PV subjects (67 and 43 out of 131 cases, respectively). Most of the configurations found in our cohort coincide with those presented in the studies by Marom et al.[87] and Kato

et al.[68], except the F configuration reported by the latter (with a large deviation of the RSPV). On the other hand, two outlier LA geometries on our cohort, with 3 PV on the left side, with a total of 5 and 7 PV, respectively, were not described in previous research. Criteria used in our work to segment the PV in the CT images (e.g., PV ending cutting plane after the first outgoing branch could justify differences compared to the literature.

The number of PV did not directly correlated with thrombogenic risk since there were cases of thrombus in all sub-groups. However, a higher percentage of thrombus vs control cases were found in LA geometries with 5 and 6 PV. Beyond standard LA morphological parameters, to further investigate the PV configuration and its relation with LA haemodynamics and thrombus formation risk, we estimated several angles characterising the topological relationship between each PV and its LA environment. In addition, we derived indices from particle-based fluid analysis to estimate the weight of each PV in flow entering the LAA.

As in former investigations, we identified significant differences in controls vs thrombus cases in ostium characteristics. Furthermore, LA volume and surface were significantly smaller in thrombus examples than in controls, in disagreement with most of literature such as from Springer et al. [127]. A possible reason for this behaviour is that the processed database included CT scans acquired both at end-diastole and end-systole (68 and 63 scans, respectively), which could have a non-negligible impact on LA volumetric indices, thus making them untrustworthy.

On the other hand, the PV angular parameters and the total number of particles in the LAA were more reliable and significant parameters to differentiate controls from thrombus cases. Of special interest were the γ angle, defining the alignment between the LAA and LSPV main directions, and the inclination of the right PV.

Despite being the most significant descriptor, the total number of particles, a fluid-based parameter, none other in-silico haemodynamic indices (e.g., ostium velocities, ECAP, LAA washout) were helpful to discriminate controls vs thrombus cases. The most likely reason is the absence of patient-specific boundary conditions in the performed simulations, using the same generic velocity curve at the MV for all subjects (also, very close to LAA, thus leaving few degrees of freedom near where measurements are taking place). The total number of particles is not heavily affected by the generic BCs since it mainly depends on the velocity vector field, rather than its magnitude, with the LA geometry having the largest impact. On the other hand, the remaining in-silico haemodynamic indices are highly influenced by the velocity magnitude, which was not found significantly different between controls and thrombus cases in the studied cohort.

Although we did not find a direct relation between the number of PV and the probability to suffer a thrombotic event, PV configuration definitely had a strong impact on blood flow patterns, thus with a certain and complex link with thrombogenesis. For example, the angles (e.g., γ angle) and inclinations (e.g., ϕ

angles of the right side) of the PV fully determined the point of collision of the multiple PV flows in the LA, key to understand how blood patterns evolve and circulate through the LA main cavity and how they reach the LAA, as can be seen in Figure 4.6. Our experiments confirmed that the individual PV (and PV side) contributing the most to LAA flow fully depends on the number and configuration of PV. Yaghi et al. [141] already pointed the relation of LAA angles and blood stasis, but they did not include the PV in their studies.

The number and PV origin of particles in the LAA were studied in relation to PV sub-groups (i.e., from 3 PV to 7 PV) and the LAA-LSPV main direction alignment. The results showed that, independently on the number of PV, a higher LAA-LSPV alignment is associated to more LAA particles. Moreover, a higher misalignment of the LAA and LSPV makes the right PV contribute more to LAA haemodynamics; with aligned LAA and LSPV, the LSPV flow collides from the right PV one, bounces off, and goes straight into the LAA ostium.

Analysing all these factors independently, it was not possible to identify trends relating to thrombus formation. However, within each sub-group (e.g., aligned LAA-LSPV in 4 PV), the number of particles were related to the risk of thrombus, among other interesting relations. For instance, in LA geometries with 4 PV, a higher participation of the left side favours the washing of the LAA and, therefore, decreases the probability of thrombus formation. On the other hand, 5 PV LA cases had the contrary behaviour, with a higher right PV flow contribution into LAA particles in controls, as it also was the cases for chicken-wing LA morphologies. There were too few samples in 3, 6 and 7 PV groups to draw any relevant conclusions from their analysis.

The chicken-wing LAA morphologies were assessed independently of the LAA-LSPV alignment criteria since the variability in their LAA tip direction, bending angle and ostium position (i.e., anterior/posterior) was huge. In consequence, the number of particles in the LAA was heterogeneous in the CW cases. Less thrombus cases were found in the CW group, but no specific blood flow pattern could be derived to better understand thrombosis in these morphologies.

In summary, the three most relevant PV characteristics to understand LAA haemodynamics are the number of PV, their angular relations (especially in the right PV side) and the alignment between the LAA and LSPV main directions. The combination of these three factors creates a large spectrum of LA haemodynamics scenarios; arguably certain combinations will be more prone to favour thrombus formation, while others will be more protective.

The large number of possible complex PV configurations can explain the difficulties to find a simple PV topological descriptor linked to thrombogenesis, being then the total number of particles the best individual predictor of thrombus risk. It would be crucial in the future to develop a model combining the analysed factors for a better prediction, also including more advanced ones such as

indices quantifying the characteristics of blood flow collision points in the LA. Certainly, the availability of patient-specific BC would improve LA fluid simulations, and more in-silico haemodynamic indices could become significantly different between controls and thrombus cases. More advanced particle models such as discrete phase models with particles interacting with the LA wall and among themselves would improve the realism of the thrombus formation process, and obtain better in-silico haemodynamic indices.

4.5 Conclusions

Thrombus formation in the LAA, potentially leading to transient ischaemic attacks, cerebrovascular accidents, and stroke, results from the combination of multiple and complementary factors, including morphology and haemodynamics. However, their independent analysis does not offer the necessary holistic view to properly understand the underlying patho-physiological mechanisms and to estimate thrombogenic risk on an individual basis. In this chapter we have shown with two separate studies that the joint analysis of morphological parameters and in-silico haemodynamic indices provides a better stratification of patients with and without TIA/CVA history. In the first study, relevant factors including the maximum ostium diameter and centreline length, were found significant, whereas the LAA shape, centre of the debate in most of the literature, was not. None of the studied haemodynamic indices was individually significant, highlighting the need for patient-specific BC for more realistic and variable fluid simulations. However, when combined with morphological factors, prediction models were better. The second study of presented in this chapter confirmed these findings on the largest in-silico study of LA haemodynamics performed so far. The total number of particles in the LAA was found the best individual parameter to distinguish thrombus vs. non thrombus group. Furthermore, new morphological descriptors of the LA, based on the angles generated by the PVs, were computed, being good indicators of thrombus formation, specially if the LAA and the LSPV main directions were aligned and the right PV more inclined. However, better and more robust in-silico haemodynamic indices could be derived from fluid simulations if using more personalized boundary conditions, having a more complete analysis. In conclusion, the studies presented in this chapter demonstrate that the LAA morphology alone is not enough to stratify the risk of thrombus formation in AF patients (e.g., thrombus cases present for all LAA shapes). However, our findings suggest a protective role to chicken-wing morphologies, as previously reported in the literature. Unfortunately, understanding the reasons for it is complex due to the variability of CW LAA shapes, despite LAA orientation and PV configuration should certainly play a role.

Chapter 5

IN-SILICO HAEMODYNAMICS TO IDENTIFY THE LEFT ATRIAL APPENDAGE OCCLUSION SETTINGS INDUCING DEVICE-RELATED THROMBUS

5.1 Introduction

Left atrial appendage occlusion (LAAO) is progressively growing worldwide [13, 73]. In the early days, the complications were pericardial effusion or device embolisation. But with the passing of the years and the increasing experience of surgeons, device related thrombus (DRT) has remained possibly the last big challenge to overcome. Strategies have been developed to control and better manage DRT. Yet, these measures are corrective (i.e., increasing the intensity of anti-coagulation therapy) and are not exempt of risk, as they increase the risk of bleeding in patients, as well as the burden of care, since patient follow-up has to be more frequent. Moreover, DRT seems to be a multi-factorial process and cannot be prevented only with anti-thrombotic treatments. Several clinical variables (e.g., age, AF at time of implantation, congestive heart failure, CHA₂DS₂-VASc score) have been associated with a higher risk of DRT mainly due to their relation to hypercoagulability [125]. Aminian et al., [6] published that > 80% of DRTs with the Amulet device were located in the area below the pulmonary ridge (PR) (see Figure 5.1) although the results published are still controversial and have not been

proven [42].

As blood flow patterns are believed to be important in thrombogenesis, several computational fluid dynamics studies analysing blood flow patterns in the LA and LAA have been published but only a few studies, i.e., four, have considered LAAO implantation (see Table 2.4). Moreover, most of these have integrated very limited sets of patient-specific clinical data, without follow-up. One of the objectives was to identify patients who would need closer follow-ups after the intervention due to a higher risk of DRT through in-silico simulations.

The work presented in this Chapter is based on the hypothesis that flow recirculations plays an important role in DRT formation. As it has been discussed in the previous sections, acquiring reliable imaging data to characterise the complex 4D behaviour of blood flow patterns in the left atrium is a challenge. Thus, in-silico simulations appears as a particularly promising mean to study how the flow and PR might relate to DRT, with high spacial and temporal resolutions .

This chapter contains three different studies. The first one exploits a very well documented case-report and shows how the position of LAAO device deployment with respect to the pulmonary ridge (PR) favours flow eddies that would explain why most DRT are related to the PR. The second analysis shows that although the PR creates an area that favors flow re-circulation, the latter can also happen when the PR is covered. Then, the key factor for DRT development appears to be the velocity magnitude of those eddies. In this study, the importance of patient-specific boundary conditions (BC) to obtain reliable results for in silico explorations of DRT, is shown. The computational methodology was developed to build patients-specific models and achieve personalized in-silico indices from clinical data routinely available in patients treated with LAAO implantation. Data came from a retrospective, single-centre cohort of 6 patients (3 with DRT, and 3 without DRT, respectively) referred for LAAO implantation, post-implantation CT imaging of the whole atrium, and US of the MV.

The two studies mentioned so far, focused on possible effects of the position of the device on the occurrence of DRT. Nevertheless, the devices available in the market are diverse in terms of shape and design, and the impact of different LAAO designs on the haemodynamics within the LA remains poorly explored. Actually, there is strong clinical debate about whether one type of device is better than the others to avoid DRT. As it has been presented in Section 2.2.1 (Figure 2.5), LAAO devices can be divided into three groups: the ligation; the plug devices; the pacifier devices. On the one hand, the ligation method, is based on a completely external approach. On the other hand, the plug and the pacifier devices are implanted through endo-vascular delivery. To our knowledge, only one study in addition to the one presented in this chapter, has investigated the difference between pacifier (Amplatzer Amulet) and plug (Watchman FLX) devices, and the amount of clinical data was very reduced [25]. Some clinical studies have already

reported that plug devices lead to higher rates of DRT (Table 2.2) after LAAO, as their round design might make them prone to generate thrombus formation. More specifically, the small region between the device and the endothelial wall would favour local blood stagnation [126]. Accordingly, the third study presented in this chapter, introduces a modelling workflow that includes discrete phase modelling simulating platelets coupled to the fluid flow analyses, to analyse the risk of DRT in six patient-specific geometries with different LAAO. In particular, we studied the possible incidence of DRT depending on both the positioning (covering/uncovering the PR) and the type (Amplatzer Amulet and Watchman FLX) of device.

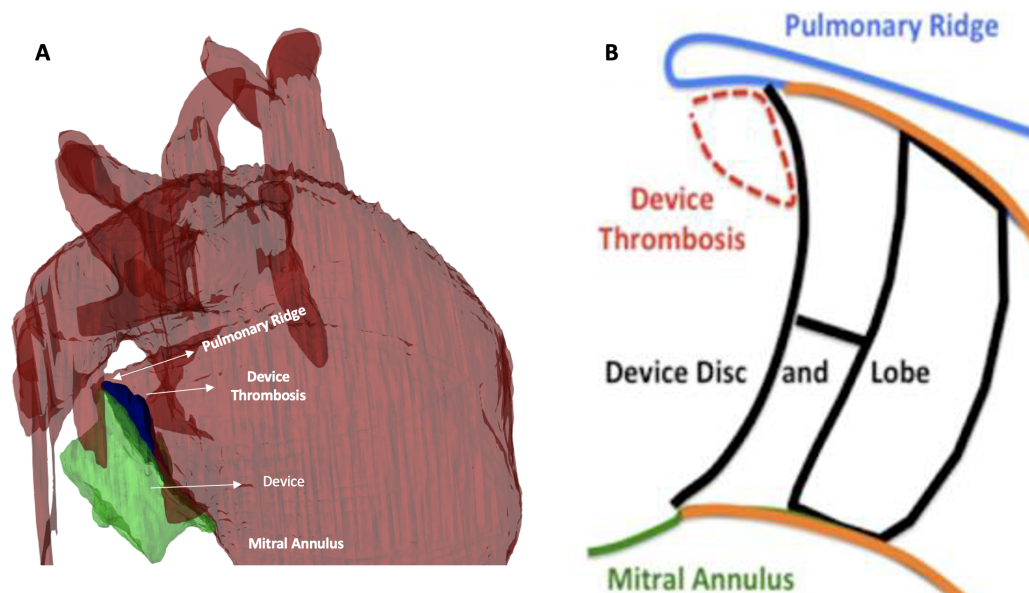


Figure 5.1: The image shows the most probable position of DRT formation, i.e., when the PR is uncovered. DRT is formed between the device's surface and the PR. A) DRT case presented in Section 5.2. B) Explanatory figure of device related thrombus in patients with uncovered PR. Image in B) is from Freixa et al. [42]

5.2 Methods

5.2.1 Databases

For the first study, i.e., the analysis of PR influence, a 78-year-old man with atrial fibrillation (CHA₂DS₂-VASc score of 3) and contraindication to oral anti-coagulation owing to intracranial haemorrhage, was selected as case study from

Hospital Clínic (Barcelona, Spain). The patient underwent successful LAAO with a 22-mm Amplatzer Amulet. He was discharged on 2.5 mg/12 h Apixaban without incidences. At three months, after ruling out DRT through trans-esophageal echocardiography (TEE), Apixaban was stopped and aspirin started. However, a subsequent imaging control with TEE at 6 months (3 months after changing from Apixaban to aspirin) detected the presence of DRT below the pulmonary ridge (Fig.5.1(A) and 5.2). Device thrombosis was successfully treated with 3 months of 2.5 mg/12 h Apixaban, and aspirin was restarted. Unfortunately, 3 months later, TEE revealed DRT recurrence at the same level. This time, Apixaban was maintained for 6 months. After this period, TEE showed no thrombus and aspirin treatment was restored. Six-month control TEE/angiographic computed tomography (angio-CT) showed a flat-tissue coverage of the “triangle-area” below the pulmonary-ridge with no clear image of thrombus (Fig.5.1(A) and 5.2). The present case of recurrent DRT was deemed to be optimal to evaluate whether haemodynamic factors might help to explain recurrent thrombus generation. The study protocol was approved by the Hospital Clínic ethics committee, and the patient gave its informed consent.

For the second study, six cases of patients treated with LAAO were modelled. For each case, CT images were acquired at least twice; first between months 1 and 3, then between months 3 and 6, after LAAO implantation. The six patients were implanted with the Amulet device and were selected from the overall LAAO database from Hospital de la Santa Creu i Sant Pau (Barcelona, Spain) based on the availability of complete CT imaging at follow-up including the whole atrium anatomy and an echocardiography study with mitral flow analysis at baseline. The indication for LAA closure was motivated by a history of major bleeding in 5 patients and high bleeding risk in the remaining one. The patients’ baseline characteristics are shown on Table 5.1 and Table 5.2 (DRT and control groups, respectively). Anti-thrombotic treatment post-LAAO was prescribed for a minimum of 3 months (Table 5.1 and Table 5.2). No cardio-embolic strokes occurred during a minimum clinical follow-up of 12 months. A prospective cardiac-gated computed tomography angiography was performed with a Phillips Brilliance iCT scanner (Philips Healthcare, The Netherlands). A biphasic contrast injection protocol was used: 40 cc of iodinated material (Iomeprol 350 mg/ mL, Bracco, Italy) were infused through an 18-gauge cubital catheter at a rate of 5 mL/s followed by a saline flush of 40 mL. The bolus-tracking method was used for the arterial phase images being the region of interest on the ascending aorta with a 100 HU threshold. A volumetric scan from heart to diaphragm (14 cm to 16 cm) was acquired. Cardiac phase reconstruction was performed at 30% to 40% of the interval between the QRS complex. Digital image post-processing and reconstruction were performed using the Phillips Brilliance Workstation to assess the LAAO device positioning and characterise the DRT (defined as a CT hypo-density on the device

left atrial extremity) as follow: a) unexplained by imaging artefacts, b) inconsistent with normal healing, c) visible in multiple CT planes, and d) in contact with the device. Patient data were anonymized prior to any computational processing. None of the patients showed leaks after assessing the CT, according to assessment guidelines provided by Linder et al., [80]. A 2D Doppler echocardiography was performed within 7 days from CT follow-up acquisition. Trans-mitral flow velocities as seen on the pulsed-wave Doppler echocardiography were recorded from the apical 4-chamber view with the Doppler samples placed between the tips of the mitral leaflets. Four out of the 6 patients were diagnosed with permanent AF and 2 with paroxysmal AF. One patient from the latter group was in sinus rhythm when the US images were acquired. Since these patients did not have A waves, the measurement of velocity curves corresponded to the mean of the measurements of their E waves over 3 or 5 beats. The study protocol was approved by the Hospital de la Santa Creu i Sant Pau ethics committee, and all patients gave their informed consent. In the third study, six patients were used from the database already described for the first study of Chapter 4 (Section 4.2.1).

Table 5.2: Characteristics of patients without device-related thrombus (control group). CHA₂DS₂-VASc score (congestive heart failure, hypertension, age 75, diabetes mellitus, prior stroke or transient ischemic attack or thromboembolism, vascular disease, age 65-74, sex); CT: computerized tomography; GI: gastrointestinal; HAS-BLED (hypertension, abnormal renal/liver function, stroke, bleeding history or predisposition, labile international normalized ratio, elderly, drugs/alcohol concomitantly); LAAO: left atrial appendage occlusion; LVEF: left ventricular ejection fraction; TIA: transient ischemic attack.

| | Patient 4 | Patient 5 | Patient 6 |
|--|------------------|------------------|----------------------|
| Age, years | 66 | 64 | 65 |
| Sex | Male | Male | Male |
| LVEF, % | 77% | 29% | 29% |
| Indication for LAAO | GI bleeding | GI bleeding | GI bleeding |
| Creatinine, mmol/L | 75 | 170 | 147 |
| AF | Permanent | Paroxysmal | Paroxysmal |
| Diabetes | No | Yes | No |
| Current smoker | No | Yes | No |
| Arterial Hypertension | Yes | Yes | Yes |
| History of stroke/TIA | No | No | No |
| CHA ₂ DS ₂ -VASc score | 3 | 4 | 4 |
| HAS-BLED score | 3 | 2 | 3 |
| Device size, mm | 28 | 28 | 22 |
| Time after LAAO, CT thrombus detection, in weeks | 25 | 5 | 38 |
| Therapy at time of thrombus detection | DAPT | Acenocumarol | Acetylsalicylic acid |

Table 5.1: Characteristics of patients with device-related thrombus. CHA₂DS₂-VASc score (congestive heart failure, hypertension, age 75, diabetes mellitus, prior stroke or transient ischemic attack or thromboembolism, vascular disease, age 65-74, sex); CT: computerized tomography; GI: gastrointestinal; HAS-BLED (hypertension, abnormal renal/liver function, stroke, bleeding history or predisposition, labile international normalized ratio, elderly, drugs/alcohol concomitantly); LAAO: left atrial appendage occlusion; LVEF: left ventricular ejection fraction; TIA: transient ischemic attack.

| | Patient 1 | Patient 2 | Patient 3 |
|--|-----------------------|------------------|--------------------|
| Age, years | 83 | 86 | 75 |
| Sex | Male | Male | Male |
| LVEF, % | 68% | 47% | 62% |
| Indication for LAAO | Intracranial bleeding | GI bleeding | High bleeding risk |
| Creatinine, mmol/L | 121 | 122 | 71 |
| AF | Permanent | Permanent | Permanent |
| Diabetes | No | No | No |
| Current smoker | No | No | No |
| Arterial Hypertension | Yes | Yes | No |
| History of stroke/TIA | Yes | No | No |
| CHA ₂ DS ₂ -VASc score | 6 | 4 | 3 |
| HAS-BLED score | 4 | 1 | 4 |
| Device size, mm | 31 | 28 | 22 |
| Time after LAAO, CT thrombus detection, in weeks | 12 | 22 | 15 |
| Therapy at time of thrombus detection | Clopidogrel | No treatment | No treatment |

5.2.2 The role of the pulmonary ridge on device-related thrombus

For the first study, the patient's anatomy was segmented from a CT images in ventricular diastole phase. Since there was no pre-procedural CT images available, and LAA could not be clearly observed in the post-procedural image, the shape of the LAA could not be segmented. As no leak was reported it was assumed that there were not peri-device leaks and only the LA and the device were segmented. The thrombus was segmented so that it was possible to simulate the scenario before the occurrence of the very same thrombus. In order to assess the influence of the PR on LA haemodynamics, two scenarios were generated: 1) actual device position, extracted from the patient-specific CT and 2) a device position that was considered optimal considering this experiment as it was covering completely the PR (see Figure 5.3).

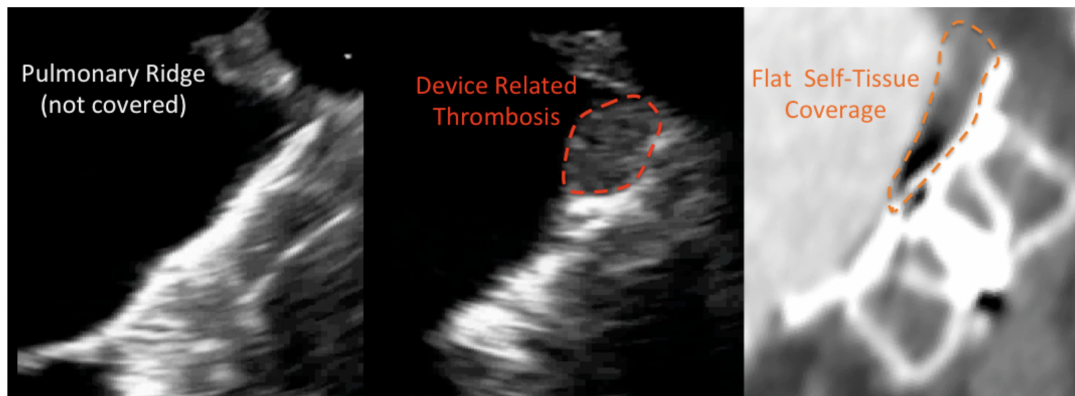


Figure 5.2: Generation and evolution of device related thrombosis. Device positioning showing the absence of pulmonary ridge coverage (left); recurrent device-related thrombus (DRT) location below the pulmonary ridge (center) and potential endothelization of the DRT area by angio-CT (right).

The volumetric mesh of the scenario 1 had 469,739 elements and the second 358,825 as the total LA volume was reduced due to the PR covering. The BC were the same for both scenarios. A velocity curve profile from the literature was applied through the pulmonary veins [40]. During ventricular systole, the MV was treated as a wall, whereas during ventricular diastole a pressure of 8 mmHg was defined at the MV. To approximate the wall's behaviour, a dynamic mesh (DM) diffusion strategy was applied. For the thrombus risk assessment, ECAP and streamlines were studied near the device's surface.

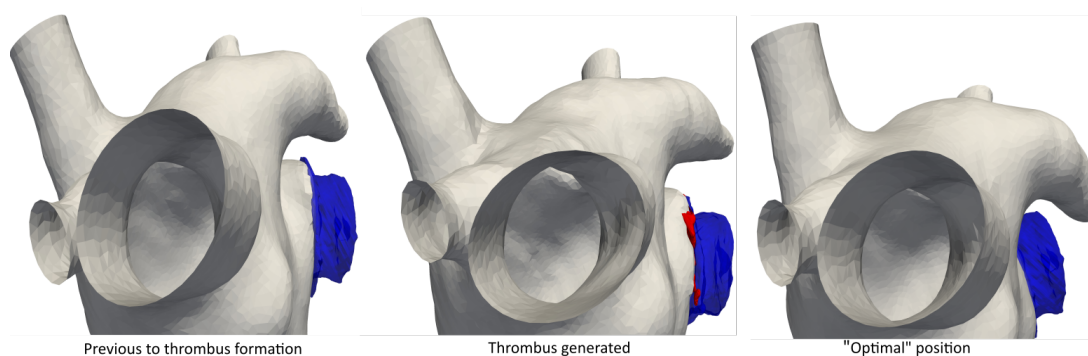


Figure 5.3: Different scenarios to study the influence of the PR. On the left, the 3D model segmented from the CT ignoring the thrombus. At the center, the same model but with the segmentation of the thrombus (red) formed at the device's surface. On the right, the 3D model of the optimal position simulated.

5.2.3 Prediction of device-related thrombus with fluid simulations

For the second study that involved six clinical cases, we developed a computational methodology to build patients-specific models and personalized in-silico indices from clinical data usually available for patients treated with LAAO implantation. Figure 5.5 shows the proposed methodological workflow. The personalized geometrical model of the whole left atrium was constructed for each patient from the CT images through semiautomatic segmentation by a collaborator not involved in the modelling process, in order to maintain the study blind to the modellers. The geometry and position of the LAAO device implanted were also extracted from the post-procedural CT scans. The thrombi were segmented so as to run simulations as if they hadn't appear yet. The segmented regions were then built on 3D mesh models for computational fluid dynamics simulations. The velocity curves at the mitral valve were obtained from the Doppler ultrasound imposing patient-specific boundary conditions in terms of outflow during the left atria flow simulations. All simulations used a generic pressure wave from a patient with AF at pulmonary vein level. The movement of the wall was a DM-diffusion approach. Post-processing and visualisation of simulation results were performed using ParaView 5.4.1.

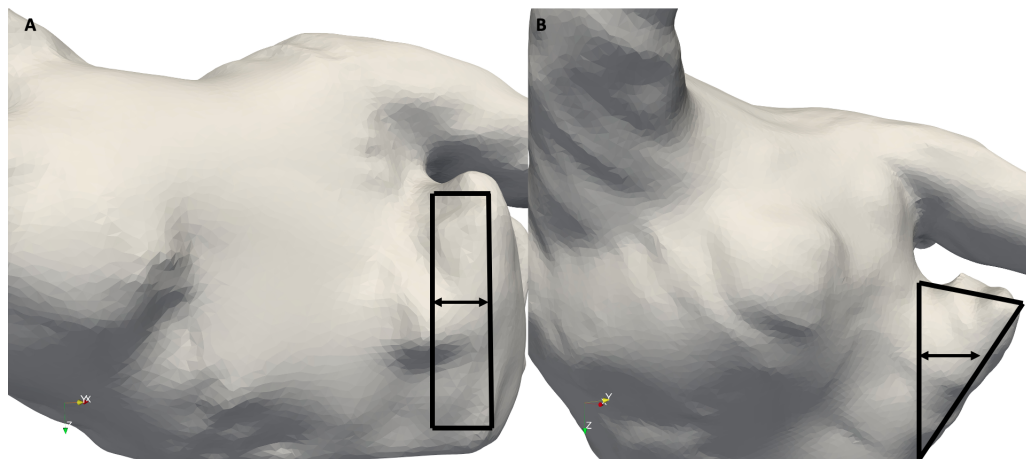


Figure 5.4: Two examples: patient 2 (A) and patient 6 (B): region (black rectangle and triangle, respectively) where velocities were estimated from flow simulation between the perpendicular line towards the pulmonary ridge and the device edge.

Patient-specific flow simulations allowed local analyses of the following in silico indices: a) the presence of swirling flows (e.g., eddies) or stagnating flow next to the device surface; b) the magnitude of the fluid velocity averaged over the whole cardiac cycle within the area outlined between the pulmonary ridge and

the device surface (see Figure 5.4); low velocity values (< 0.20 m/s) were defined as a strong indicator of thrombus formation [131]; and c) regions with complex flow patterns and low wall shear stress were characterised using the endothelial cell activation potential (ECAP) index ($ECAP > 0.5 \text{ Pa}^{-1}$)[26].

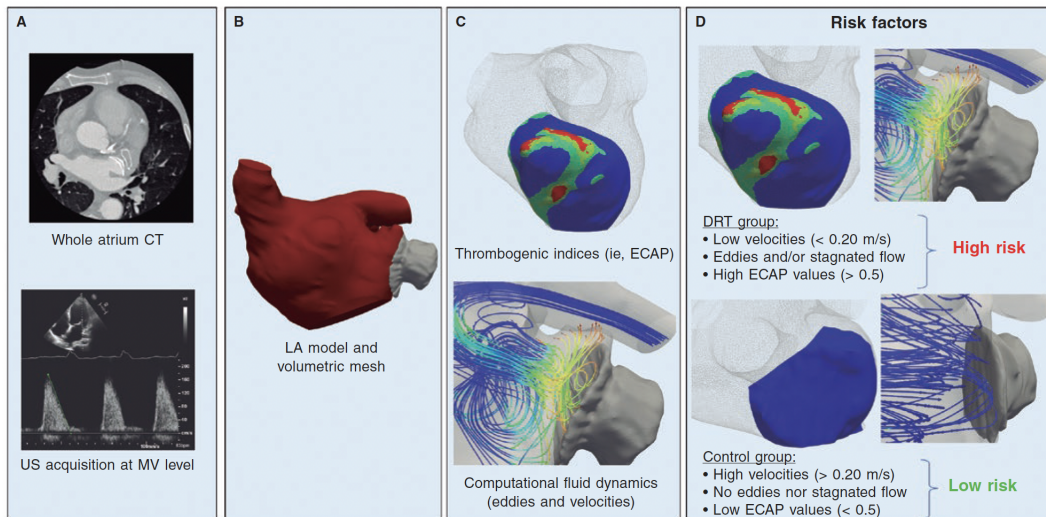


Figure 5.5: Scheme of the patient-specific computational workflow to predict the risk of device-related thrombus (DRT) formation after left atrial appendage occluder (LAAO) implantation. A: computerised tomography (CT) scan acquisition of whole left atrium (LA) and ultrasound (US) study with Doppler measurements at mitral valve (MV) level. B: 3D LA segmentation and model generation where finite volume analysis was performed. C: blood flow velocities and in silico indices like endothelial cell activation potential (ECAP) estimated from personalized computational fluid dynamics simulations. D: the risk factors predicting the presence of DRT were low velocities (< 0.20 m/s), and stagnated flow next to the device surface as well as high ECAP values ($> 0.5 \text{ Pa}^{-1}$, indicative of complex blood flow patterns and low wall shear stress).

5.2.4 Influence of left atrial appendage occluder positioning and design on device-related thrombus

Device creation and positioning

For the the third study that includes different LAAO designs, i.e., the Amplatzer Amulet and the Watchman FLX, the surface meshes of the deployed devices were built by using Meshmixer, out of the Computational Aided Design files, and introduced in the LA and LAA 3D models. Some simplifications had to be made to achieve high-quality meshes (e.g., removal of anchors in the Amulet device). During the virtual implantation, we considered rigid walls for the LA surface and a de-

formable device model (see Figure D.1 in Appendix). The latter assumption was based on the fact that the structure of the devices is highly deformable. This process is highly manual, once the device has been deformed inside the LA, device's mesh has to be corrected and improved to ensure a good aspect ratio whereas intersecting faces between the device and the LAA wall have to be avoided. For each LA geometry, two studied positions, covering and uncovering the PR, were previously defined and assessed before implanting the device, with the help of intervention cardiologists from the Hôpital de Haut-Lévêque (Bordeaux, France), Dr. Iriart and Dr. Cochet. According to their expert assessment, most of the device insertions were realistic, with some exceptions in Case 3 where the device needed to be too proximal, in order to cover the PR. In addition, in Case 6, the landing zone diameter happened to be too small to perform LAAO with the available sizes of the Watchman FLX device, so an unrealistic volumetric compression of the device was imposed, even when the smallest size was used (see Table D.2 in Appendix).

Similar landing regions of the Amulet and the Watchman FLX devices were achieved for each position, enabling proper assessment of the impact of the device design for each position. The small deviations that were present were caused by LAA morphology and where unrealistic deformations were needed, to deploy the devices at the required position. The largest deviation appeared in the uncovered PR position for Case 5, where the presence of a large lobe did not allow to deploy Watchman FLX at the same position as the Amulet device, so a more inner positioning had to be chosen for this occluder. The size of the implanted device in each case was assessed by using the VIDAA platform[1], based on morphological measurements such as the LAA ostium size and LAA depth. A total of 24 different configurations were successfully completed after placing the deployed devices at the corresponding positions in all studied geometries (see Figure 5.6). For the device sizes see Table D.1 in Appendix.

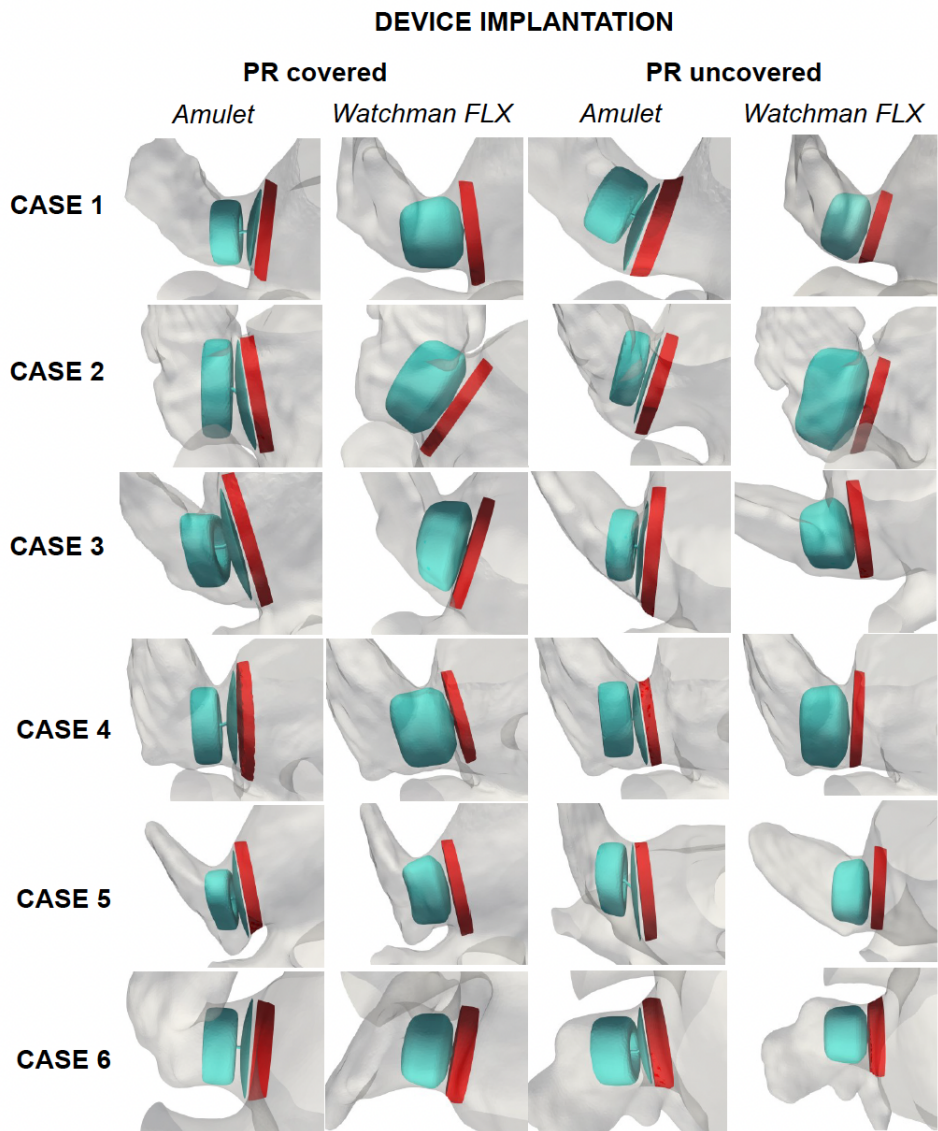


Figure 5.6: Resulting scenarios after device implantation (device painted in blue) and the corresponding regions where the average velocity profiles were computed (red).

Simulation setup

CFD simulations with a dynamic approach based on the spring-based model, and with MV annulus ring longitudinal movement, were carried out by using ANSYS Fluent solver. The BC consisted of a pressure inlet at the PV and a velocity outlet at the MV, same as defined in Chapter 4 for this same cohort. The average velocity magnitude near the device was computed throughout the last two heart beats (the first one was discarded as a warming-up beat), for each patient-specific geometry and all possible device configurations. The region of study consists of a cylindrical volume, the transverse plane of which was parallel to the sealing disc of the device. The cylindrical region of interest was 3 mm long and was 0.5-1 mm away from the sealing disc surface (see Figure 5.6, red areas). The diameter was set to be approximately the same as the largest dimension of the deployed device, subject to restrictions of the LA morphology. Other haemodynamic descriptors used were streamlines, ECAP, TAWSS, OSI, Lambda-2 and Q-criterion to visually identify regions with DRT risk and vortices in blood flow patterns. For this study, a Lambda-2 with negative value (-50) was used for vortex identification, as in other studies focused on the human heart [32]. The Q-criterion threshold to visualise vortices was set to 50.

Platelet adhesion model

In the computational fluid dynamics model, a discrete phase was added to the continuous phase (blood flow), to assess the platelet attachment to the LAA and better evaluate DRT risk. During simulations, particles were injected through the PV inlet and were then dragged by the flow, until they either attach to the LAA wall or escape through the MV. Particles were assumed to be clusters of platelets, thus the values of density ρ_p , viscosity μ_p , surface tension σ_p and platelet concentration in blood c_p were taken accordingly. Particle trajectories were computed individually by integrating the force balance of each particle within the continuous phase, as reflected by the following equation:

$$m_p \frac{d\mathbf{u}_p}{dt} = m_p \frac{\mathbf{u} - \mathbf{u}_p}{\tau_r} + \mathbf{F}, \quad (5.1)$$

where m_p is the particle mass, \mathbf{u} the fluid phase velocity, \mathbf{u}_p the particle velocity and ρ the fluid density. The term $m_p (\mathbf{u} - \mathbf{u}_p) / \tau_r$ corresponds to the drag force, where τ_r is the droplet relaxation time. \mathbf{F} corresponds to the forces that arise due to the pressure gradient in the fluid and the force required to accelerate the fluid surrounding the particles. In addition, an extra term, the Saffman lift force, was included in this variable, to represent the influence of shear rate on the particle attachment process[79].

Particles were injected through the PV surfaces during the first 10 time steps at the beginning of each beat. We assumed that, in the first injection, the number of injected particles, n_{part} , corresponded to a platelet concentration in blood of $c_p = 2 \cdot 10^8 \text{ mL}^{-1}$, which is within the normal range in physiological conditions¹. To feed the model, the following parameters were computed: the number of platelets per cluster, n_{ppc} ; the particle diameter, d_p ; and the total flow rate, Q . And for parameter calculations, the following values were assumed: number of time steps during the injection $n_{ts} = 10$, diameter of platelets $d_{plat} = 3 \mu\text{m}$, particle density $\rho_p = 1550 \text{ kg m}^{-3}$ and time steps for the injection $\Delta t = 0.01 \text{ s}$. As we fixed the concentration, all the parameters depended on the LA volume (V_{LA}). Therefore, the number of platelets per injection n_{plat} , was computed as: $n_{plat} = c_p \cdot V_{LA}$. In order to assess DRT, the number of particles attached to the LAA and their location were analysed at the end of the simulations. To do so, the LAA surface was separated from the rest of the LA and a wall-film condition was assumed. This condition implied that any particle that touched the LAA wall, independently of its velocity, stuck to this wall; they could eventually detach if the flow would drag them to the LAA boundary (see Figure D.2 in Appendix).

5.3 Results

5.3.1 The role of the pulmonary ridge on device-related thrombus

In this section, the results of the first study are presented. In the first scenario, i.e. original position of the device, results revealed a region of flow recirculation below the pulmonary ridge (where the thrombus was observed) with low velocities ($<0.1 \text{ m/s}$). ECAP maps also showed a high thrombogenic area at the same location. In the second scenario, when the pulmonary ridge was virtually covered by the disc of the device the re-circulations disappeared although velocities were still low. ECAP colour maps followed the same trend, and the highest areas were reached with the PR uncovered (Figure 5.7).

¹<https://bionumbers.hms.harvard.edu/search.aspx>

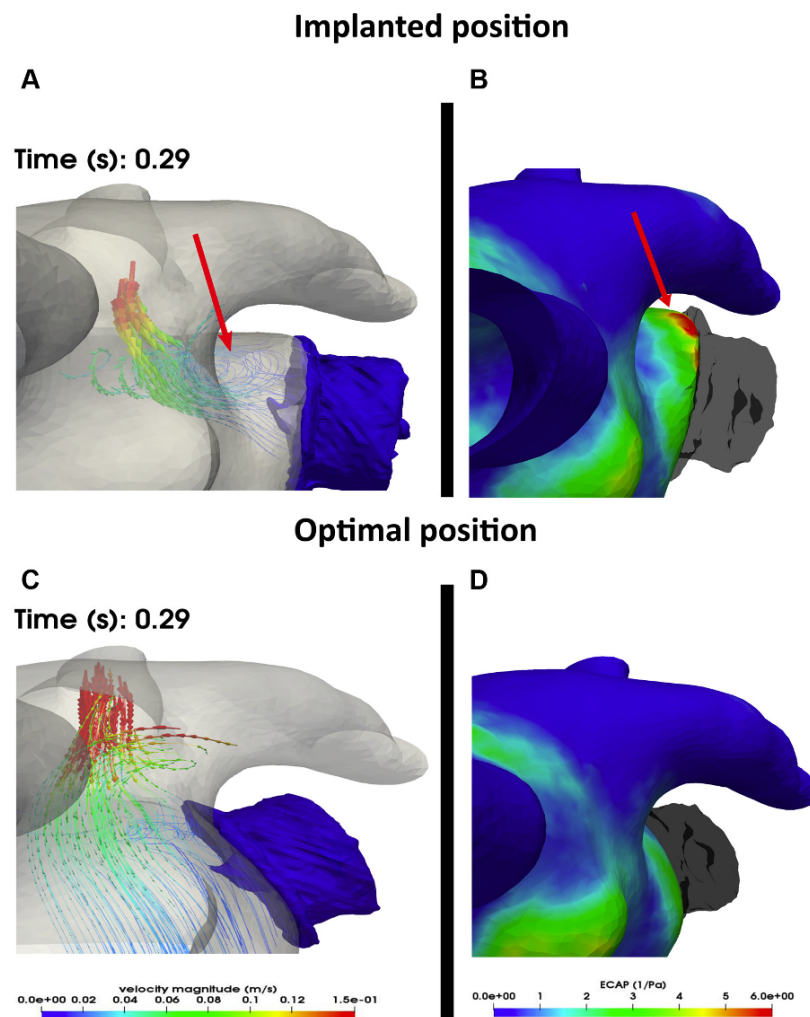


Figure 5.7: Flow-dynamics simulations. Computational fluid dynamic (CFD) simulations showing the presence of flow vortex with low velocities below the pulmonary ridge (arrow, A); High risk of thrombus generation according to Endothelial Cell Activation Potential (ECAP) values (arrow, B); When the pulmonary ridge is covered by the disc of the device, fluid recirculation does not occur, velocities are higher and ECAP values are lower, nearby the device (C, D).

5.3.2 Prediction of device-related thrombus with fluid simulations

Analysis of the simulated flows to predict the risk of DRT

Swirling flows or eddies (Figure 5.8, column 2, red markers) due to blood stagnation and re-circulation near the LAO device surface were found in all patients

except for patient 5. The areas with flow re-circulation in the simulations matched exactly the location where thrombi were found in the post-CT follow-ups (Figure 5.8, column 1) of patients with DRT. In addition, the magnitudes of blood velocities near the device surface, averaged over the whole beat, were different in the DRT group compared to the control cases: around 0.15 m/s for the DRT group, and > 0.20 m/s for the control cases. Table 5.3 shows the estimated average blood velocities at systole, diastole, and over the whole cardiac cycle. These velocities were generally higher during ventricular diastole. Remarkably, patient 5 who suffered severe mitral regurgitation had particularly high flow velocities (2-3 m/s during the E wave), according to simulations (0.87 m/s on average) in the LAAO region and Doppler data. On the contrary, patient 2 had the smallest average velocity value at 0.10 m/s.

Table 5.3: D: DRT group; C: control group; diast: diastole; ECAP: endothelial cell activation potential; max: maximum; syst: systole; vel: velocity (average \pm standard deviation); whole: whole cardiac cycle.* Velocity values averaged across the whole cardiac cycle < 0.20 m/s and ECAP values were > 0.5 since they are indicators of high risk of device-related thrombogenesis.

| | Vel-sys (m/s) | Vel-diast(m/s) | Vel-whole (m/s) | Max-ECAP (Pa ⁻¹) | Mean-ECAP (Pa ⁻¹) |
|------------|-----------------|-----------------|------------------|------------------------------|-------------------------------|
| Pat. 1 (D) | 0.07 \pm 0.02 | 0.27 \pm 0.08 | 0.16 \pm 0.11* | 1.23* | 0.23 \pm 0.14 |
| Pat. 2 (D) | 0.11 \pm 0.03 | 0.09 \pm 0.02 | 0.10 \pm 0.03* | 1.50* | 0.24 \pm 0.26 |
| Pat. 3 (D) | 0.10 \pm 0.03 | 0.19 \pm 0.07 | 0.14 \pm 0.07* | 0.61* | 0.25 \pm 0.11 |
| Pat. 4 (C) | 0.13 \pm 0.03 | 0.24 \pm 0.13 | 0.20 \pm 0.12 | 0.45 | 0.10 \pm 0.08 |
| Pat. 5 (C) | 0.28 \pm 0.10 | 1.6 \pm 0.77 | 0.87 \pm 0.83 | 0.07 | 0.01 \pm 0.01 |
| Pat. 6 (C) | 0.08 \pm 0.02 | 0.37 \pm 0.17 | 0.29 \pm 0.19 | 0.30 | 0.03 \pm 0.04 |

ECAP values $\pm 0.5 \text{ Pa}^{-1}$ were found near the device surface in all patients with DRT (see Table 5.3 for peak and average ECAP values). The peak ECAP values in patients 1 and 2 (Figure 5.8, column 3, red areas) allowed us to clearly locate the specific areas where simulations predicted the formation of DRT, which was later compared to the post-CT imaging analyses. For instance, the spatial location of the highest ECAP values in patient 2 (Figure 5.8, row 2) on the device upper region next to the pulmonary ridge matches the location of the thrombus in the follow-up images. However, the ECAP map of patient 1 suggested an inferior thrombogenic area whereas the real thrombus also formed on the device upper region. In patient 3, ECAP values were more homogeneously distributed over the entire device surface, yet the peak values were still found where the thrombus was formed (lower device region). Regarding the control group, ECAP results were very low except for those of patient 4. In any case, the threshold of 0.5 Pa^{-1} was not reached, and the follow-up confirmed that this patient did not develop DRT.

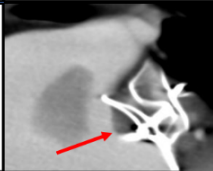
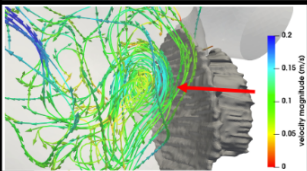
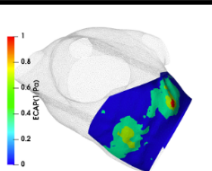

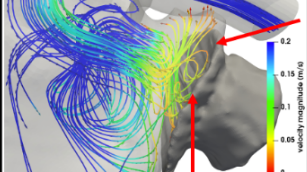
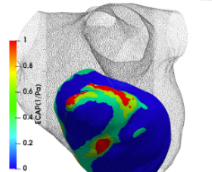
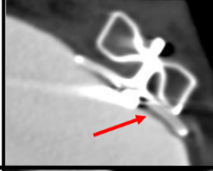
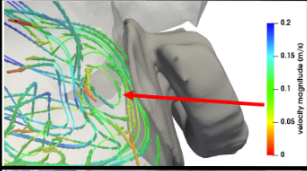
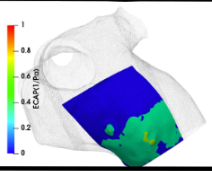
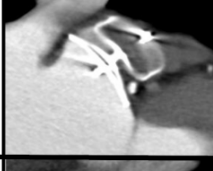
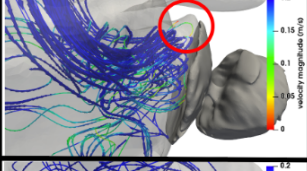
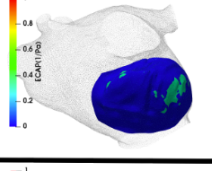
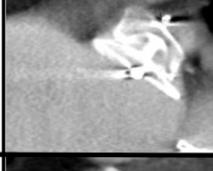

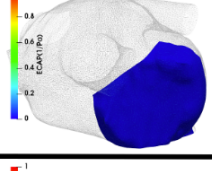
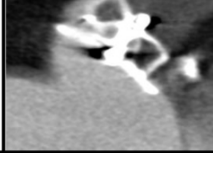
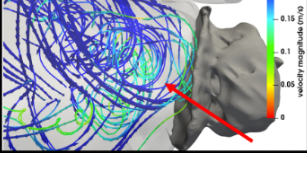
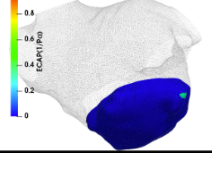
| | CT | Velocity streamlines | ECAP | Risk factors |
|-----------|---|---|--|--|
| Patient 1 |  |  |  | Velocities lower than 0.20 m/s Yes ECAP values higher than 0.5 Pa ⁻¹ Yes Eddies/stagnated flow Yes |
| Patient 2 |  |  |  | Velocities lower than 0.20 m/s Yes ECAP values higher than 0.5 Pa ⁻¹ Yes Eddies/stagnated flow Yes |
| Patient 3 |  |  |  | Velocities lower than 0.20 m/s Yes ECAP values higher than 0.5 Pa ⁻¹ Yes Eddies/stagnated flow Yes |
| Patient 4 |  |  |  | Velocities lower than 0.20 m/s No ECAP values higher than 0.5 Pa ⁻¹ No Eddies/stagnated flow Yes |
| Patient 5 |  |  |  | Velocities lower than 0.20 m/s No ECAP values higher than 0.5 Pa ⁻¹ No Eddies/stagnated flow No |
| Patient 6 |  |  |  | Velocities lower than 0.20 m/s No ECAP values higher than 0.5 Pa ⁻¹ No Eddies/stagnated flow Yes |

Figure 5.8: Results of the computational modelling analysis to predict device-related thrombogenesis (DRT). CT column: computerized tomography (CT) scan, red arrows indicate where the thrombus was found during the patient radiological exploration at follow-up. Column with velocity streamlines: simulated blood flow patterns coloured by velocity magnitude (blue, high values; red, low values), red arrows indicative of stagnated flow or recirculation. ECAP column: map of the endothelial cell activation potential (ECAP) in silico index near the device surface indicative of high and low DRT risk (red and blue, respectively). Column of risk factors: list of simulation-based risk factors for developing DRT.

5.3.3 Influence of left atrial appendage occluder positioning and design on device-related thrombus

Table 5.4 displays the mean velocities obtained from fluid simulations for all explored cases and LAAO configurations, part of the third study of this Chapter. In our study, mean velocities were below 0.20 m/s in almost all cases during systole, with the exception of Case 6 in the covered PR position with Amulet device. Low velocities during diastole were less common, due to the proximity of the LAA to the MV, which is open during this phase. Additionally, a higher incidence of low velocities in uncovered PR configurations was encountered, thus a higher risk of DRT. On the other hand, no significant differences between the two devices (i.e., Amulet and Watchman FLX) were encountered in this regard.

Figures D.5 D.6 in Appendix shows the streamlines for all the cases analysed (i.e., pulmonary ridge covered/uncovered and Amulet/Watchman FLX devices) during systole and diastole phase. As a general rule, flow re-circulation patterns with low velocities (i.e., conditions required for DRT) were more common at the edge of Watchman FLX at some point during the cardiac cycle, independently of the position of the occluder. However, this metric was too qualitative to claim that there was a clear pattern. Same conclusions were drawn from the analysis of vorticity indices. Conversely, vortices with low velocities were rarely detected in the covered PR configurations with the Amulet device. However, vortices were present in the uncovered PR position both for Amulet and Watchman FLX devices, being slightly more common in systole than in diastole (see Table D.3 and Figures D.7 and D.8 in Appendix). Overall, no relevant differences were appreciated between the ECAP maps of the covered and uncovered PR positions, fact that could reinforce the idea that patient-specific BC are key to obtain reliable ECAP results.

Table 5.4: Mean velocities during the second cardiac cycle in a region near the device, in systole (Sys) and diastole (Dias). In bold, values below 0.2 m/s. PR: pulmonary ridge.

| Average velocities near the device (m/s) | | | | | | | | | |
|--|-------------|-------------|-------------|-------------|--------------|-------------|-------------|-------------|--|
| | PR covered | | | | PR uncovered | | | | |
| | Amulet | | Watchman | | Amulet | | Watchman | | |
| | Sys | Dias | Sys | Dias | Sys | Dias | Sys | Dias | |
| Case 1 | 0.11 | 0.29 | 0.12 | 0.30 | 0.10 | 0.17 | 0.13 | 0.19 | |
| Case 2 | 0.16 | 0.28 | 0.18 | 0.29 | 0.11 | 0.18 | 0.07 | 0.17 | |
| Case 3 | 0.16 | 0.39 | 0.17 | 0.37 | 0.14 | 0.34 | 0.16 | 0.29 | |
| Case 4 | 0.19 | 0.36 | 0.18 | 0.36 | 0.11 | 0.22 | 0.11 | 0.25 | |
| Case 5 | 0.09 | 0.13 | 0.07 | 0.12 | 0.05 | 0.08 | 0.02 | 0.05 | |
| Case 6 | 0.22 | 0.29 | 0.18 | 0.25 | 0.09 | 0.16 | 0.13 | 0.15 | |

Figure 5.9 shows the platelet distribution at end diastole of the second cardiac cycle for the studied cases. It can be observed that platelets did not only stick to the wall in the PR region, but also attached to other uncovered regions of the LAA as the inferior part of the device. In all cases except Case 2 and 6, the LAA had a significant amount of platelets clustered in the PR configuration compared to the covered PR configuration (Figure 5.10). Overall, 75% of the analysed configurations has more platelets attached to the LAA (i.e., more risk of DRT) with an uncovered PR, as can be seen in Figure 5.10 a (yellow and purple bars higher than blue and red ones in all cases). Also, the Watchman FLX device appeared to have more platelets prone to get attached to the LAA than the Amulet one. This could be due to its rounded shape which creates more spaces between the wall and the device where flows can be retained. This would also explain the lower velocity results obtained with the Watchman FLX. It should also be noted that for both cases the pin is not simulated, part of which, according to the literature, is an area where the DRT can be found too. However, to determine the risk of DRT, not only the number of platelets has to be assessed, but also the blood velocity. For instance, Case 2, mentioned before, it is true that covered PR has more particles attached, but their velocity is also higher. On the contrary, the PR uncovered position has fewer particles attached but the blood velocity is close to 0 (Figure 5.10). Therefore, when it comes about assessing DRT risk, it seems logical that both variables have to be taken into account. In Case 5 no platelets were attached, the reason being the very inner position of the device forced by the patient's LAA anatomy. It was placed so deep, that the velocity in that area was 0 and no particle reached the area. In contrast, in Case 6, the PR and LAA were so well covered, that all the particles had high velocities towards the MV direction without being in contact with the region of interest. Therefore, few attached to the wall.

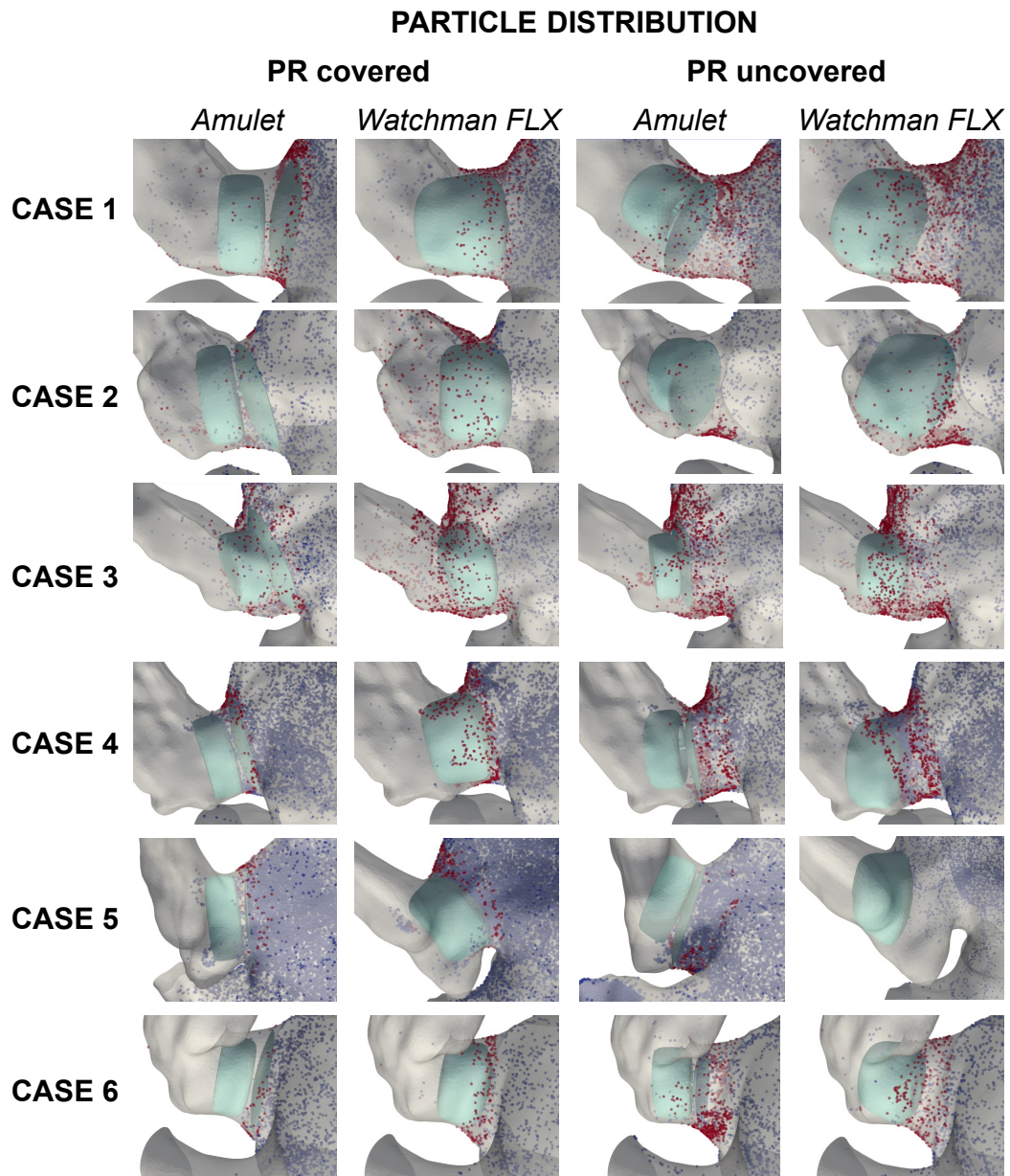


Figure 5.9: Particle distribution in the left atrial appendage in diastole for the two analysed devices (Amulet and Watchman FLX) in the covered and uncovered pulmonary ridge (PR) configurations. A higher density of attached particles (red) would be associated to a higher risk of device-related thrombus. Blue: free particles.

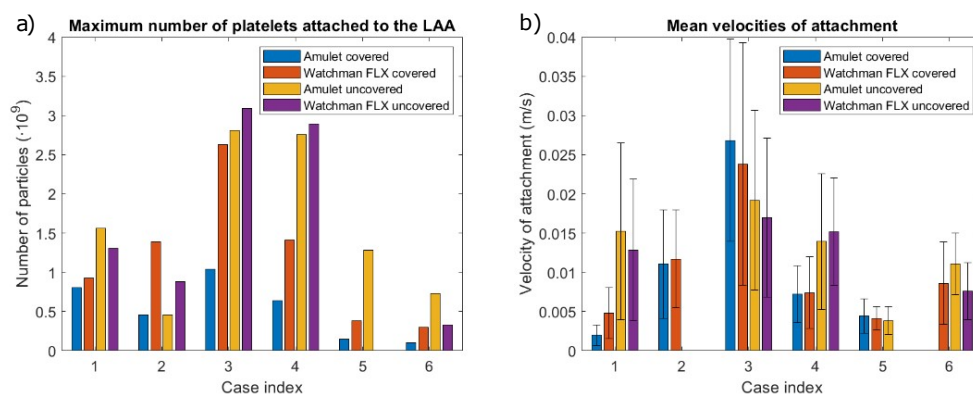


Figure 5.10: a) Maximum number of platelets attached to the left atrial appendage (LAA). b) Mean velocity of attachment for all the studied configurations (Cases 1-6): Amulet-uncovered pulmonary ridge (PR) (blue); Watchman FLX - uncovered PR (orange); Amulet - covered PR (yellow); and Watchman FLX - covered PR (purple).

5.4 Discussion

5.4.1 The role of the pulmonary ridge on device-related thrombus

Early diagnosis, and even prediction, of DRT is essential to reduce complications after LAAO implantation, like stroke or systemic embolism. It would also support individualized optimal antithrombotic therapies, for which there is still not consensus in the medical community. In the case report presented in the first study of this Chapter, a proof-of-concept exploration was carried out, to test the hypothesis that when the PR is uncover, a “triangle area” with unfavourable haemodynamic factors would be created, increasing the risk of DRT. When the PR was covered with an optimal position of the device, flow recirculation disappeared being the flow lines much straighter near the device, heading towards the MV. Still, low velocities were found in the neighbourhood of the optimally positioned device.

Arguably, the use of only one patient case is an obvious limitations, and further research with increased number of clinical cases was necessary to confirm the hypothesis. Moreover, the coverage or uncoverage of the PR does not explain all the cases of DRT. Some of the thrombi are found in the middle of inferior part of the device. Thus, testing more positions of the device was necessary [126]. Regarding the flow simulations, there were some limitations too. The US of the patient could not be acquired, and the velocities, that are a key component to predict thrombus formation, were not patient-specific, therefor. This last fact and the lack of individuals as a control group made also difficult to set an optimal

threshold of ECAP to differentiate the cases that are going to generate thrombus or not. For all these reasons, it was necessary to design another experiment to further investigate the effect of device positioning on DRT.

5.4.2 Prediction of device-related thrombus with fluid simulations

In the second study, the combination of several *in silico* indices successfully predicted the presence or lack of DRT in all simulated cases (3 controls and 3 patients with DRT diagnosed with follow-up CT imaging). The computational pipeline developed basically required the 3D reconstruction of the whole LA anatomy, obtained with regular cardiac CT imaging acquisition plus a standard US study, already routinely acquired for LAAO candidates, which allowed us to define patient-specific boundary conditions (such as the mitral flow velocity profile from Doppler data). Each patient-specific simulation lasted 48 hours on average. These requirements make the proposed tool particularly suitable for clinical use, as we estimate that an early evaluation of DRT risk is possible within 72 hours following device implantation (see Section 2.3 for workflow's details). The computational workflow and simulations might be further useful for virtual treatment prognosis and decision ahead of the intervention.

This is the first study to validate the ECAP index with a clear clinical endpoint and assess ECAP performance in patients treated with LAAO. The ECAP index could differentiate between DRT and non-DRT cases based on the characteristics of flow complexity. However, it could not robustly predict the exact location of thrombus formation in all cases as it wrongly suggested the formation of an inferior thrombus in patient 1, whereas a superior thrombus was identified clinically. Even though the cohort was small, thanks to their mechanistic nature, the results suggested that if thrombotic risk after LAAO needs to be studied, the ECAP index alone is not enough and needs to be combined with other variables.

The areas of flow re-circulation at low velocities could indicate potential regions with risk of thrombus formation, but its precise location depends on the patient's LA anatomy and the LAAO device final deployment. Our flow simulations revealed the device upper region with an uncovered pulmonary ridge (PR) as the preferred area for eddies as shown in Figure 5.8. This finding was consistent with the literature available on pulmonary ridge uncovering and a higher risk of DRT: 82% of DRT cases with uncovered left upper pulmonary venous ridge [6, 42, 93]. However, we showed that pulmonary ridge uncovering could increase the risk of DRT only if flow velocities are low and the whole pulmonary ridge area cannot be properly washed out. Therefore, covering the pulmonary ridge, which is not always possible due to anatomical constraints (e.g., proximity of a

circumflex to other structures) would only be critical if blood flow velocities are not high enough.

The velocity results obtained in our *in silico* analysis are consistent with ultrasound imaging studies that associate low blood velocities with thrombus formation since the former could favour the stagnation of flow and trigger the inflammatory process [93, 131]. Velocity results during systole were more similar among patients compared to results during diastole. The region where the velocity analysis was performed it was allocated near the device surface, very close to the MV. Therefore, in general, during ventricular systole when the valve is closed, blood velocities in that region tend to be low and differences are difficult to see. Once the MV is open the velocities increase. Also, the mean velocity of the entire cardiac cycle (Table 5.3, column 3) showed that patients who developed DRT had lower blood velocity values in all the beats compared to the control group. However, the process through which blood stasis triggers the inflammatory cascade is not fully understood. For instance, the spatial proximity of the left atrial appendage to the MV makes blood flow into the LAA be quite dependent on the dynamics of the MV as it occurred with patient 5. The unusual haemodynamic behaviour of this patient (e.g., very high blood velocities) was due to mitral regurgitation, an effect that was captured by the simulations thanks to the patient-specific US-based boundary conditions. Remarkably, these observations are consistent with studies that hypothesize a certain degree of protection against flow stagnation and thrombus formation in patients with mitral regurgitation due to a better blood washout of the LAA [67]. This also highlights the importance of having the patient's velocity profile: without the US it would not have been possible to replicate the haemodynamics produced by the regurgitation, thus proving that these patients have a better washout of the area making them DRT protectors, unlike patients suffering from mitral stenosis.

Yet this study also comes with limitations. The main limitation was that even though we had increased the number of patients, six is still a reduced number of patients to confirm the predictive value of our simulation-based factors. In addition, it is difficult to assess the possible impact on the interpretation of the results of: the different anticoagulant therapies used in the DRT group; the different timings of the follow-up CT imaging among the patients; the lack of a unified protocol for the follow-up explorations. Regarding the possible effect of combined drug therapies (i.e., anticoagulants, here), the use of computational biology models, e.g., agent-based model, or of particle simulations coupled to the flow simulations, could help to approximate different characteristics of the anticoagulant therapies. Actually, the reason why the current cohort gathered only six subjects is precisely the difficulty to achieve relatively unified protocols for both anticoagulant treatment and imaging follow-up. Nevertheless, our mechanistic and interpretable computational fluid dynamics-based descriptors for DRT

prediction should be viewed as novel potential biomarker candidates accessible through digital twin technologies.

Fortunately, CT imaging is increasingly becoming accepted as a key technology for LAAO planning and follow-up analysis [60], thus facilitating more extensive studies in the next future, through *in silico* modelling. More specifically, the requirement of having a whole LA CT image at follow-up for the computational model would not substantially change the clinical protocol in centers with access to this imaging technique. In the near future, the constant improvements in spatial and temporal resolution of echocardiographies would make it possible to build patient-specific models based on 3D reconstructions of the LA anatomy from these images. Hence, achieving a larger cohort of prospective cases is possible and shall allow more rigorous analyses and validations of the proposed *in silico* factors and thresholds (both in terms of blood velocities and ECAP), to predict the risk of DRT after LAAO implantation.

There is not a clear consensus on the optimal boundary conditions to model LA haemodynamics in a realistic way. On the one hand, we used a velocity profile as outlet in the mitral valve since such profile can be obtained from standard echocardiography images routinely acquired in LAAO candidates. On the other hand, a generic pressure waveform of a patient with AF from a former study was applied in the pulmonary veins as an inlet model while coping with the fact that patient-specific pressure measurements would require invasive catheterization, which is not usually performed in these patients. Similarly, in our study, the movement of the LA wall was not patient-specific. It was extrapolated from the passive movement of the mitral valve annular plane, imposed by the left ventricle, which was extracted from the medical literature available. Whereas our patient-specific component of the boundary conditions, *i.e.*, the US-derived blood velocities at the MV, uniquely allowed to simulate mitral regurgitation effects, a more realistic left atrial wall dynamics may be extracted from temporal imaging sequences. Simplifications are intrinsically associated with the concept of modelling, which was applied in the present study. Still, the integration of relevant patient-specific structural and functional information in our modelling and simulation workflow provided boundary conditions that were realistic enough to achieve accurate estimations of the risk of DRT after LAAO implantation.

5.4.3 Influence of left atrial appendage occluder positioning and design on device-related thrombus

In the third study a modelling pipeline has been developed to assess device performance after LAAO. Two types of device, *i.e.*, plug (Watchman FLX) and pacifier (Amulet) devices, have been tested in several positions within six LA/LAA mor-

phologies. Few similar studies were found in the literature, to compare different device designs and positioning. Such kind of study would be hugely helpful to determine the best option for each patient-specific LA geometry.

According to the results, the haemodynamic in-silico indices showed that uncovered PR device configurations generated higher DRT risk flow patterns, specially in ventricular diastole phase. The "triangle area" produced by this positioning favored blood stagnation since the flow from the systole phase gets trapped between the high-velocity jets going towards the open MV and the device acting as a wall. This is in agreement with the clinical studies published in the literature [42, 126]. During ventricular systole in almost all the studied scenarios and configurations the blood velocities reached were very low and did not allow to distinguish the covered and uncovered PR groups. However, in diastole, differences became clearer, and the DPM revealed that in most cases, more platelets tended to attach to the LAA when the devices were placed without covering the PR. Additionally, the DPM showed that the moment at which more particles attached was during the E-wave at early diastole. Also, when lower average flow velocities were predicted, such as in Case 6, platelet attachment was more distributed along the device but overall, less platelets attached. This implies that not only specific flow velocity and patterns conditions may cause clot formation, but device placement as well as morphological and patient-specific physiological features shall also intervene.

Regarding the respective performance of the Amulet and the Watchman FLX, the former showed better performance in our simulations, in general. Because of the disc, less swirls and vortices at low velocities were generated. The rounded shape at the edges of the lobe of the plug device produced little swirling at very low velocities, therefore decreasing the risk of DRT between the device and the LAA surface, according to the identified haemodynamic risk factors. Nevertheless, no significant differences have been found in terms of velocities between the two devices, but this could be an artefact of having averaged the results over a region. No significant differences were found in terms of ECAP index between the Amulet and the Watchman device, although color maps showed a tendency of the Watchman FLX to induce slightly higher values than the Amulet.

The present work presents some limitations and leaves room for future work. First of all, with respect to device implantation, some simulated cases may have deviated from reality (e.g. large volumetric deformation of the device in small LAA, forcing uncovered PR positioning when the LAA neck was particularly long), but they allowed to perform the sensitivity analysis in terms of positioning effect on the haemodynamic factors. Specialist clinicians also pointed out that considering a rigid LAA and the lack of adjustment of the latter to the device after deployment was a strong assumption. This caused the device to suffer from unrealistic deformations in order to fit in the desired position in the LAA. Mesh

refinement also lead to a simplification of the device geometries, so the absence of some elements compared to real-life designs, such as the catheter tip and the anchors in the Amulet device, should be taken into consideration. Moreover, the employed simulation scheme did not take into consideration the wall behaviour that could be relevant to better mimic the interaction between the device and the anatomy [142]

While the haemodynamic indices that we recomputed in the present study (e.g., DPM or ECAP) provide detailed and complementary information to assess the risk of DRT, further haemodynamic descriptors such as residence time[117] could help to assess quantitatively blood stagnation in the regions of interest. In this study, the boundary condition profiles were not patient-specific and limit, therefore, the accuracy of those haemodynamic indices in comparison with other studies presented in this Chapter.

Also, vortex criterion visualization should be considered cautiously as there is no consensus yet on the proper threshold to represent the vortex structures. Besides, for low-velocity vortex regions, the two studied criteria take a value close to 0, that is, less negative values in the case of λ_2 criterion, and some vortex regions might be missed.

To conclude, the discrete phase modelling also presents limitations. The wall-film condition of the LAA should be revised to make platelet attachment depend on the wall shear stress, rather than considering total attachment when a collision with the wall happens, as done by Hathcock et al.,[54]. This would avoid particle attachment at high velocities as it happened during the simulations of the present work. Particle detachment triggers could also be implemented to study not only how the particles get attached, but also how can they get loose when subject to high shear stresses.

5.5 Conclusions

Percutaneous left atrial appendage occlusion is becoming an effective alternative, to reduce the risk of ischemic stroke without the need for long-term oral anticoagulation in patients with non-valvular atrial fibrillation. Device-related thrombus (DRT) is a potential complication of LAAO, the incidence of which varies a lot depending on the studies, but usually ranges from 2% to 5% [6]. The difficulty to thoroughly understand and better control DRT might result from variations of device placement position, differences in patient medication, differences in devices designs, and from the impossibility to assess local flows re-circulations with current imaging techniques. In this chapter, we developed different simulation workflows to explore DRT through three different computational fluid dynamics studies. Recent data reported that DRT mostly occur below the pulmonary ridge

[6]. The potential presence of flow turbulence in this "triangle area" has been proposed as a DRT risk factor. The first work presented in this chapter supports this hypothesis, as the two flow simulations performed, pointed out pulmonary ridge coverage was a key factor to avoiding flow turbulence over the device. Accordingly, pulmonary ridge coverage should be pursued with LAAO device, to minimise flow recirculations at low velocities. However, further research with larger cohort was needed to confirm this hypothesis.

The second exploration presented in this chapter is a proof-of-concept study that presents a description of an in-silico modelling workflow capable to integrate patient-specific data and simulate hemodynamics within the LA, while predicting the risk of DRT after LAAO device implantation. The model was used to study 6 patients retrospectively: 3 patients with DRT and patients 3 without DRT. The simulations reproduced the flow dynamics inside the LA and showed that patients with DRT had low velocity blood flow re-circulation with complex patterns next to the device surface. The combination of several in-silico indices representing pro-thrombotic factors that cannot be measured in situ helped to identify key haemodynamic variations that distinguished patients with DRT from the control ones. Here we showed a first proof-of-concept study with in silico indices from personalized models capable of identifying potential complications of LAAO device implantation, to individualise follow-up therapies and minimize the rate of unfavourable clinical outcomes. Nevertheless, future studies should focus on validating the computational workflow developed against larger cohort explorations.

Finally, in the third study, a modelling pipeline using CFD and DPM has been developed to explore the differences between pacifier and plug LAAO devices in six patients implanted with several device positions. According to the resulting haemodynamic in-silico indices, uncovered PR device positioning generated more thrombogenic patterns, confirming the results obtained in the two previous works. The DPM analysis and simulated platelet attachment to the LA wall nicely supported the aforementioned outcome. Moreover, the Amplatzer Amulet device led to less virtual cases with low-velocity swirls and vortices than the Watchman FLX, thus being less prone to induce DRT after implantation, probably due to the presence of the disk in the device design. Future work will mainly focus on establishing a robust and rigorous validation framework for the fluid simulations, using advanced imaging such as 4D flow magnetic resonance imaging and blood speckle tracking as well as in-vitro set-ups like the one recently proposed by Dueñas-Pamplona et al. [30].

Chapter 6

GENERAL DISCUSSION AND CONCLUSIONS

In this dissertation we investigated the process of thrombus formation in the left atrium (LA), before and after left atrial appendage occlusion (LAAO), using computational fluid dynamics (CFD) simulations. Understanding why in patients with AF, certain LAA are subject to thrombus formation while others do not, could help to tailor improved personalized therapies, according to the risk of thrombus formation. Current thrombus risk stratifying indices (i.e., CHA₂DS₂-VASc score) still miss a part of the patient's risk as the exact process of thrombosis within the LAA is not fully understood. One of the possible treatments for the patients with a risk of blood clot formation in the LAA is LAAO, especially when oral anticoagulants (OAC) are contraindicated. In this minimally invasive intervention, the LAA is closed with a device implanted into the body through a catheter, from the femoral artery. Although the rate of success of this intervention is increasing over the years, thanks to the learning curve of the physicians, there are still a non-negligible number of patients who develop device-related thrombus (DRT). In any case, thrombus formation, either before intervention or because of the device (i.e., DRT), might lead to a stroke and must be avoided. It is known, that low velocity and stagnated flow play an important role on thrombus formation through the Virchow's triad [138, 131]. However, the resolution required to capture the local flow haemodynamics able to trigger this phenomena is not provided by the current imaging techniques. For this reason, in-silico simulations and patient-specific computational models of the heart are emerging as a valuable technology in clinics to back up clinical decisions and contribute to interventional planning, diagnosis, prognosis, and device optimization such as LAAO [19]. Several related studies have been published and use in-silico simulations, to try to predict which patients with AF will or will not develop thrombus. Nevertheless, the workflows used (i.e., boundary conditions, wall behaviour, haemodynamic indices analysed...) vary a

lot among studies, and the community has not reached any consensus about the procedure for best practice or clinical case explorations (Tables 2.3 and 2.4). Accordingly, this thesis aims to: 1) review the state-of-the-art and test the different methods used in the literature (Chapter 3); 2) understand better the role of flow haemodynamics in the LA and LAA for thrombus formation (Chapter 4); and 3) identify the left atrial appendage occlusion settings that would be more prone to induce device-related thrombus (Chapter 5).

Chapter 3 explored the different boundary condition setups and workflows found in the literature. For that purpose, two sensitivity analyses in two different datasets were carried out. The first dataset consists of six patients who underwent LAAO and had follow-up. The results showed that rigid wall assumption should be avoided whenever possible, since it can overestimate thrombus formation risk. Additionally, this assumption limits the number of configurations and data that can be used, as it can easily lead to simulations that cannot fulfil the mass conservation law. Simplified dynamic mesh (DM) approaches, as the ones presented in this manuscript, are diffusion- and spring-based methods that can be useful to capture local haemodynamics if the region of interest (the device surface in our studies) is sufficiently close to the region where the movement is imposed (the mitral valve in our studies). They induce higher fluid velocity values and lead to more realistic results, specially during the filling of the LA. Moreover, DM approaches allow to use velocity profiles during the ventricular systole phase, reducing the probabilities to have problems with continuity convergence in contrast to rigid wall simulations. Nevertheless, if the BC are not patient-specific there can be a mismatch between the movement created and the flow entering the LA, generating divergence. The problem of the mass mismatch can be completely avoided when the velocity profile is used at the MV. In such a case, the mass conservation law is always fulfilled because the income velocity to the LA it is not forced anymore and is regulated through the pressure at the PVs. The disadvantage of using pressure at the PVs is that systole velocity curve at the PVs, named S in the literature, is very difficult to replicate, and the velocities obtained are usually lower than the physiological ones. Hence, the movement applied has to simulate very well a very complex motion that produces enough negative pressure to make the flow entering the LA. However, with the rigid wall scheme this is directly impossible. DM approaches are particularly useful when the simulation of LAAO scenarios uses patient-specific data. In this scenario, the haemodynamics are well replicated nearby the device surface, which is crucial to obtain good results as shown in Chapter 5, where even the patient with mitral regurgitation was well replicated. Results showed how haemodynamic indices are affected when BC are not patient-specific, being not as accurate as when BC are patient-specific. DRT prediction can change completely depending on the velocity defined since most of those indices depend directly or indirectly on velocity. Yet a lot of caution it is

needed when the US measurements are acquired at the MV to gather personalized BC. If the transducer is placed in a deep LV position, the data gathered can largely overestimate the results. Also, the segmentation process can be a source of errors if the image is very noisy, higher velocities than the real ones could be predicted, even with patient-specific data.

Dynamic CT (dCT) could not be tested in the first sensitivity analysis, since this type of imaging technique was not available. In the second sensitivity analysis, dCT were available for the studied cohort. This second study aimed to verify: 1) Whether the assumption applied to the spring- and diffusion-based methods, only for the longitudinal movement, was a good approximation; 2) Whether when the dynamic mesh extracted from dCT imaging is applied, the velocity waveform in the pulmonary veins during ventricular systole could be replicated in contrast to the other two methods tested in the first sensitivity analysis, rigid walls and DM methods, which were not able to mimic it and; 3) The difference in results when using one method or the other. Results showed, that the movement was very different from the ones simulated so far. In the AF patient, although the movement did not follow any pattern, which was expected because of arrhythmia, the wall was far from being rigid, confirming that the rigid wall assumption might be too simplistic. In addition, the results showed how the longitudinal movement was not as long as the one imposed in the DM methods presented in this manuscript. From the dCT, the longitudinal movement generated was 3 mm. This value is far from the ones reported in the literature using US [133]. However, the movement in the MV ring is not homogeneous. Recent studies performed with higher resolution imaging reported that even among the different parts of the mitral annulus, the movement varies [35]. US imaging is highly dependent on the measurement position and on the user. Moreover the resolution is lower. Therefore, it is possible that the leaflets were included too in those measurements, explaining the discrepancy of the results.

Using the movement extracted from the dCT improved the generation of the S velocity curve (~ 0.1 m/s), although it was still below the normal values (~ 0.3 m/s). With the rigid wall scheme, this wave was not generated, and with the DM it was very small, far from the physiological values. Other studies that applied similar methods to extract the movement from the dCT and have reported results at the PVs, showed also difficulties to replicate the physiological behaviour of the pulmonary velocity S curve [50]. The Author of the present PhD thesis believes that one of the reasons could be the omission of the role of the rest of the circulatory system (i.e. resistances and compliance) in the simulation setup. This belief, which needs to be supported by further research, arose when the simulation setup tried to be replicated in a 3D printed flow loop using the MIT 3D printed model in collaboration with Ellen Roche Lab. In the 3D printed flow loop, the curves in the LA during the ventricular systole were generated, due to the different open-

close timing of system valves (simulating human heart valves), the compliance of the chambers and the resistance of the system, rather than a movement as we applied to the LA. In fact, the S curve at the PV was very difficult to replicate in the 3D printed flow-loop, as well. One option to overcome this problem could be the use of 0D Windkessel models as BC of the simulated system [139]. However, so far, the use of 0D models as BC for 3D models has not been very successful, because of the difficulty to find all the parameters needed to build the models, in the literature, and to subsequently tune these parameters for every patient.

On the clinical side, clinical cardiology has been looking for strategies to better stratify patients with AF who have thromboembolism risk, for years. Unfortunately, current risk stratification measures have not achieved sufficiently high prediction and the community continues to investigate new methods to detect patients with most risk to suffer from thrombosis-related cardiovascular events. One of the problems is that the process of thrombus formation in those patients is not fully understood. Like in every thrombogenesis, it is based on Virchow's triad, but there are unknown players. For example, blood stasis is a factor that is not included in CHA₂DS₂-VASc score. Better understanding the role of LA haemodynamics in the thrombus formation in AF patients was the objective sought in Chapter 4. As described throughout all this manuscript, several published studies have looked for new morphological parameters, to stratify better the patients, but few have explored the haemodynamics. In this chapter we have studied the impact of the orientation of the PVs on the LA haemodynamics and, as a consequence, on the LAA haemodynamics. PVs orientation determined the clashing point and the different directions of the jets. Those orientations, together with the ostium orientation determined not only the flow that goes inside the LAA but the washout too. The results also proved the complexity of the phenomena. The total number of particles which ended at the LAA after the simulation or the alignment of the LSPV with the LAA were factors able to distinguish between thrombus and control patient groups. However, it was not possible to establish a protocol to identify which specific LA are going to generate thrombi and anticipate, therefore, the event without running any simulation. Thus, further research needs to be done to understand better thrombus formation in the LAA.

Chapter 5 focused on LAAO simulations and how these can help to predict DRT. The results followed the trend of recent published clinical studies, indicating that leaving the PR uncovered could be a risk for device related thrombus. In one of our studies, thanks to a workflow using specific boundary conditions, we were able to predict correctly DRT formation in six patients who underwent LAAO and we showed that even if the PR is left uncovered, a key factor that can cause DRT is the blood velocity. PR creates a space for flow stagnation and re-circulation, and the low blood velocity would be the trigger of the coagulation cascade. This role of the velocity would explain why until now, there were documented case

in which the PR was left very uncovered and no thrombus formed. Or it would explain why even with the PR covered a thrombus can appear anyway. Examples of both scenarios have been presented in Chapter 5. Additionally, we showed how flow simulations could help companies with the optimisation of their devices as in-silico simulations are able to inform about local flow, especially near devices surface. Results showed how plug devices would favour flow retention and local re-circulations compared to pacifier devices. In the latter, the disc would adapt better to the LA anatomy and would produce straighter flow close the device's surface. To further explore such mechanisms, we used a first proof-of-concept workflow based on discrete phase modelling to simulate particles attachment. The results were in agreement with those found in the literature, which indicate that DRT levels are higher with the Watchman device (Table 2.2). Nevertheless, there were some limitations in our models that need to be considered. In this PhD thesis, hypercoagulability was assumed to be due to the clinical conditions of the patients. But since blood properties are key for thrombus formation, they should be studied carefully, either testing non-Newtonian models or incorporating different interactions among particles when discrete phase models are applied. The particles used in Chapter 4 were not based on discrete phase modelling, so they could not interact with the environment: they only followed the velocity vector field. The particles used in Chapter 5 interacted with the wall of the LAA but not with the device or among themselves. Therefore, the thrombus formation at the device surface (e.g. at device's pin where literature have been reporting as a spot of thrombus formation) could not be studied. In addition, the attachment was very simple, not depending on key factors such as the velocity. As a future work, these models could be greatly improved if particle attachment would depend on the dragging fluid velocity. Moreover, although this PhD thesis was focus on haemodynamics, if the LAAO deployment per-se is to be studied, structural simulations shall be added, to achieve a complete assessment of the thrombus formation and peri-device leaks [142].

As has been previously mentioned, there is a need in the LA fluid modelling field for generating ground truth data to benchmark the different approaches that have been published in the literature, including various numerical strategies, blood models (e.g., Newtonian vs. non-Newtonian flow, laminar vs. turbulent models, etc.) and solvers. Dueñas-Pamplona et al. [29] advanced in this direction developing an in-vitro phantom that could be the basis for detailed comparison studies, especially if more realistic LA geometries with moving walls could be incorporated. In this regard, vacuum-powered soft actuators, such as the ones developed by Gollob et al. [49], could be a good starting point, although dyssynchronised movements typical of AF patients can be very difficult to replicate. Moreover, properly setting up pressures in in-vitro studies is key for the correct functioning of the system since they are used to calibrate and to run all the flow loop. To

the best of our knowledge, none of the in-silico studies available in the literature have studied pressure patterns, despite their influence in heart functioning. The results of our sensitivity analysis demonstrated how different pressure patterns are depending on the used model configuration.

Thus, besides seeking new parameters related with thrombus formation, systematic verification and validation studies are needed to build the credibility of LAAO-based in-silico models required to integrate them as part of medical device certification procedures by the regulatory bodies such as the FDA (e.g., V&V20 and V&V40 guidelines [134]). However, as thrombus formation is an extremely complex problem, concrete relationships between the model inputs and outputs are needed for validation purposes, which is not straightforward. Moreover, the high complexity of the heart movement and its mechanical properties increase the difficulty to build in-vitro models to validate those simulations.

On the other hand, 4D flow MRI is a promising imaging modality that is already being used to study LA haemodynamics [85], and would certainly play a role in the near future for the validation of LA fluid models. If the resolution of 4D flow MRI is improved, the movement could directly be extracted from its anatomical segmentation without requiring additional imaging techniques. Advances in echocardiographic imaging could similarly allow in the future to extract a reliable 3D model along the cardiac cycle. With the current spatio-temporal resolution limitations of 4D flow MRI and echocardiography, the best imaging technique to capture LA wall motion, key for having the most realistic fluid simulations, remains dCT. Unfortunately, its high cost and the lack of differential diagnosis contribution with respect to other imaging techniques that are already integrated in the medical guidelines and hospital workflows, penalises this approach; it is then challenging to perform large simulation studies with available dCT data.

Actually, the limited number of processed cases in our first sensitivity analysis was due to the challenge in obtaining patient datasets including post-procedural CT scans, covering the whole LA. In most hospitals, LAAO patients are followed up with echocardiography or CT images, which only include part of the LA to minimise radiation. Additionally, in the analysed cases, there was a large variation in the CT and echocardiography acquisition times at follow-up for the different patients. Ideally, both imaging modalities should be acquired during the same day to better synchronise LA geometry (and deformation, if available) with echocardiographic measurements, if flow simulations are run afterwards. Furthermore, acquisition of mitral valve velocities is straightforward with echocardiography, thus being well suited for outlet boundary conditions. On the other hand, we could not reliably measure velocities in all pulmonary veins (issues with right and left superior PV) for the whole database, since the visual window was not good enough, hence limiting their use at the inlets.

Another bottleneck for in-silico simulations, especially for intervention plan-

ning and to be integrated in hospitals workflows, is the time invested on building and running the models. Although computers are becoming more and more powerful in terms of computational power, the models can still take hours and days to run, depending on their characteristics and complexity. Beyond solving the mathematical equations, the creation of the patient-specific geometrical domain is also cumbersome, including laborious and often manual tasks in the segmentation and 3D meshing steps. The post-processing and analysis of the simulation results can also take significant times. Ideally, the whole modelling pipeline needs to be carried out before the procedure takes place if the goal is to support clinical decisions related to the intervention. Although the timing for operating room scheduling in LAAO can vary a lot among hospitals, countries and health care systems, the time between the decision to intervene and the operation day is short (approximately one week, according to our experience). Thus, the coordination between the radiologists, the cardiologists, and the engineers, is crucial, often asking full dedication of engineers during those days, which can be implausible in certain periods.

Despite all these challenges in personalised in-silico modelling, we managed to generate some of the largest cohorts of patient-specific LA fluid simulations available in the literature, as it was presented in Chapter 4, including 30 and 131 simulated cases (with LA geometries extracted from 3DRA and CT images, respectively). Initially, the segmentation approach was semi-automatic, but with standardised criteria (e.g., segmentation up to first PV branching), which avoided excessive manual editions of the 3D mesh. Left atrial motion was incorporated with a dynamic mesh strategy with spring- and diffusion-based methods, in the same way for all cases. With this modelling pipeline, each case presented in this manuscript was performed in 48-72 hours.

During the last months, we have further optimised the modelling process by performing the LA segmentation with neural networks, reducing the time required per case to around 24 hours. Regarding computational time needed for simulation convergence, advanced parallelisation schemes with larger infrastructures (e.g., more nodes, etc.) could also accelerate the process, although communication overload should be considered. Numerical techniques alternative to traditional finite-element solvers, such as the Lattice Boltzmann methods ¹, or recent deep-learning-based schemes to create fast surrogates of fluid simulations [94] should also be studied and validated.

To conclude, although there are many challenges to overcome, computational fluid simulations have a lot of potential to have a substantial impact and support complex clinical decisions. In-silico simulations and other computational technologies (e.g., augmented/virtual reality, 2D/3D imaging viewers, etc.) can make

¹https://en.wikipedia.org/wiki/Lattice_Boltzmann_methods

a difference in both, the optimisation of existing devices and in the improvement of patient management. Specifically in LAAO, there is no current commercial tool giving functional information on blood flow velocity, which is key for thrombus formation. Also, pre-planning complex cardiology procedures such as LAAO with visual computing and 3D technologies can be beneficial to maximise interventional efficiency and minimise costs, estimated as procedural time and device expenditure. However, the clinical translation of advanced computational technologies is not straightforward, needing to fulfil the demanding requirements to be embedded in the existing workflows in hospitals. For instance, clinicians will not invest more than a few minutes on planning cases that can take 30 minutes for the intervention. Moreover, pre-planning should not add excessive complexity and cost to the overall clinical workflow, thus sufficient cost-effectiveness or patient safety impact must be proven to justify their routine use.

Appendix A

HEARTS IN THE ANIMAL KINGDOM

In 2018, Längin et al. [74] published an article in *Nature* in which they described the long-term survival of baboons that had received a heart transplant from genetically modified pigs. This was an important step forward on the way to being able to give humans porcine heart transplants. The reason is because pig hearts are very similar in size, anatomy and function to human hearts and they usually are the gold-standard in pre-clinical animal testing for all cardiovascular devices prior to use in humans to both test the safety and efficacy. But not in all mammals is like this although cardiac diseases affect most species in the animal kingdom, and AF it is not an exception. Understand how these diseases are develop in hearts that have different characteristics can be key to understand the disease's insights. In other species such as cats, AF rarely occurs due to the small size of their hearts. However, other cardiac diseases such as hypertrophic cardiomyopathy (HCM) is common in felines, with a prevalence of approximately 10–15% [104].

We studied the differences in the LA/LAA morphologies and blood flow patterns in the analysed cohorts with respect to thrombus formation and cardiac pathology. The obtained results showed significant differences between normal and pathological feline hearts, as well as in thrombus vs non-thrombus cases and asymptomatic vs symptomatic cases, while it was not possible to discern in congestive heart failure with thrombus and from non-thrombus cases. Additionally, in-silico fluid simulations demonstrated lower LAA blood flow velocities and higher thrombotic risk in the thrombus cases [104].

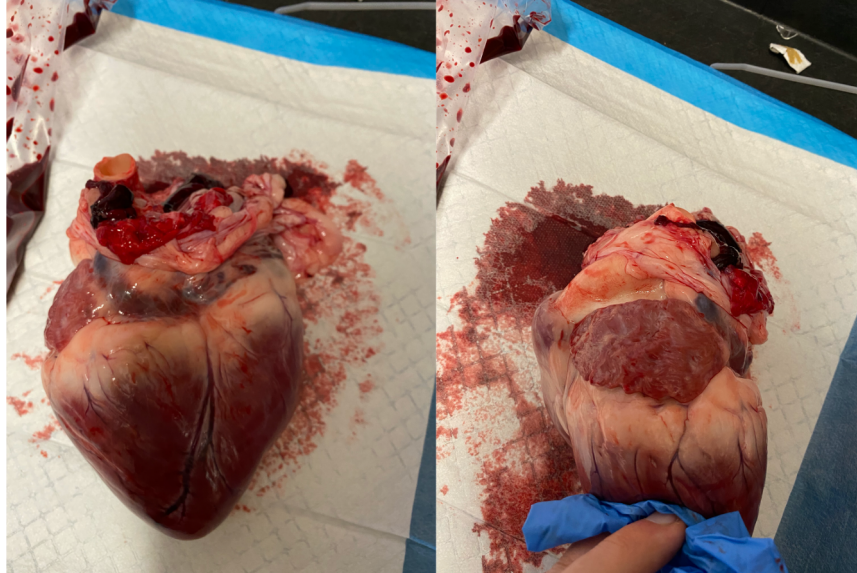


Figure A.1: Porcine heart extracted the 17th March 2022 by Manisha Singh and MIT team for device testing.

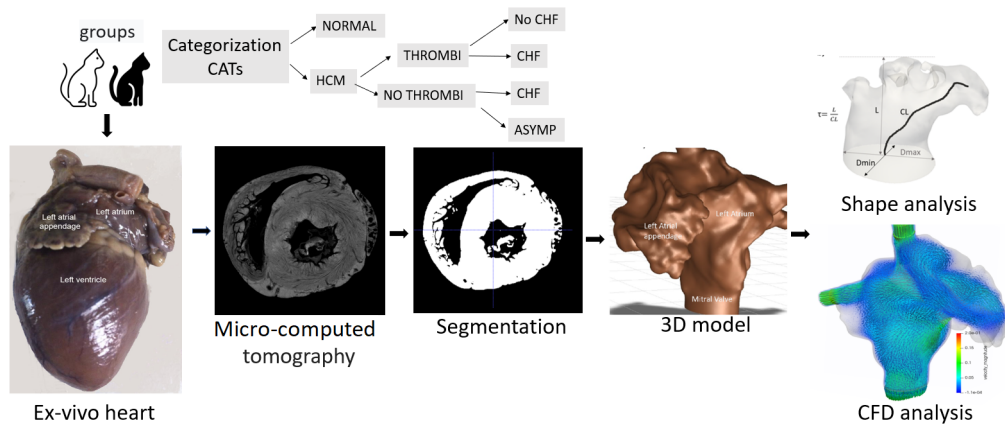


Figure A.2: Computational pipeline to derive morphological and haemodynamic descriptors of the feline hearts. Ex-vivo isolated feline hearts were evaluated with micro-computed tomography (micro-CT) images, from which the left atria were segmented prior to create 3D surface meshes. Then, shape and Computational Fluid Dynamics (CFD) analyses were performed to derive morphological and haemodynamic descriptors. HCM: hypertrophic cardiomyopathy; CHF: congestive heart failure; ASYMP: asymptomatic. From [104].

Appendix B

SENSITIVITY ANALYSES

B.1 In-silico thrombogenic indices from the first sensitivity analysis

In this Appendix all the time average wall shear stress (TAWSS), oscillatory shear index (OSI) and endothelial cell activation potential (ECAP) results obtained in the sensitivity analysis for all the scenarios tested are presented.

Scenario 4 had defined as boundary conditions (BC) a velocity curve at the pulmonary vein (PV) from the literature and a two stages at the mitral valve (MV): wall behaviour during ventricular systole and a constant pressure during the ventricular diastole. With this scenario only converge in 2 out of the 6 patients. For the walls, a dynamic mesh based on a diffusion method was applied. The divergence was caused by the mismatch in the continuity equation.

Scenario 1 diverged for one patient (case 5), which has a constant pressure (0 mmHg) at the pulmonary veins and velocity ultrasound curve at the MV, but the walls were considered rigid. The divergence was caused by the excess of fluid leaving the atrium through the PVs (non-physiological behaviour) during the ventricular systole trying to match the continuity equation.

The scenario that used velocities curves at the PVs showed an overestimation of the ECAP values due to the over-stagnation generated. This will always happen when non-patient specific BC are not being used and/or the movement cannot match the inlet profile defined or calculated through the PV.

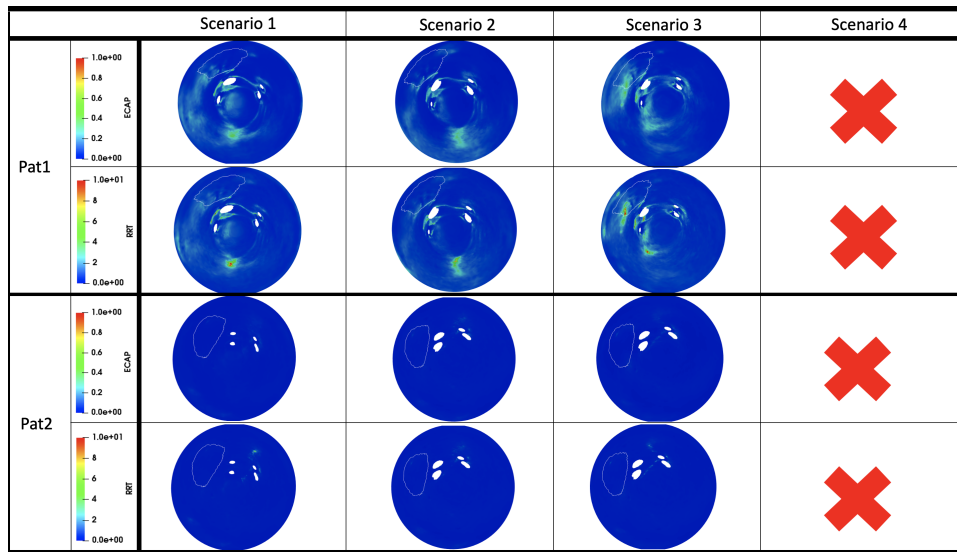


Figure B.1: ECAP: endothelial cell activation potential; RRT: relative residence time. ECAP and RRT results in patients 1 and 2 (controls cases) for all the scenarios. Red cross indicates divergence of the simulation. Higher values (red colour) indicate a higher risk of thrombosis. The white line in the 2D maps signals the position of the implanted device.

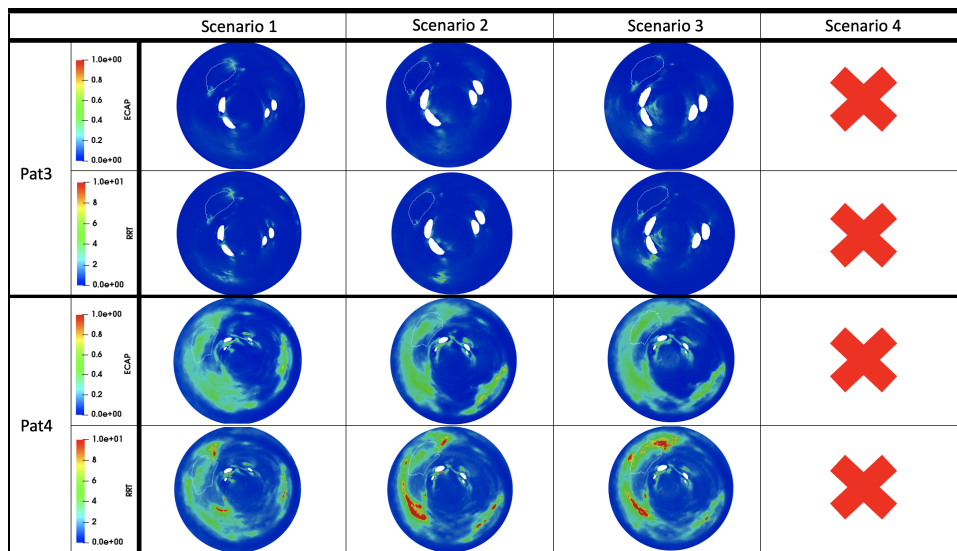


Figure B.2: ECAP: endothelial cell activation potential; RRT: relative residence time; DRT: device-related thrombus. ECAP and RRT results in patients 3 (controls case) and 4 (DRT case) for all the scenarios. Red cross indicates divergence of the simulation. Higher values (red colour) indicate a higher risk of thrombosis. The white line in the 2D maps signals the position of the implanted device.

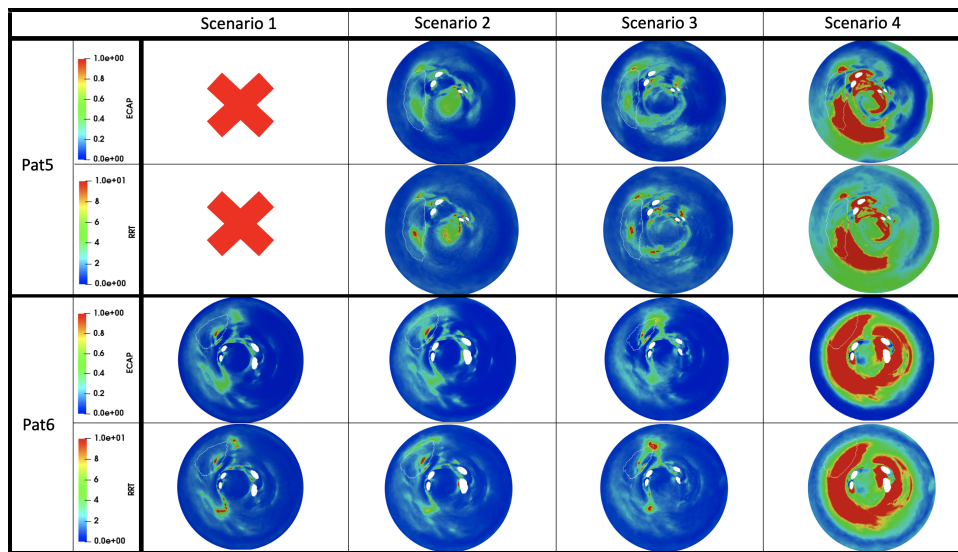


Figure B.3: ECAP: endothelial cell activation potential; RRT: relative residence time; DRT: device-related thrombus. ECAP and RRT results in patients 5 and 6 (DRT cases) for all the scenarios. Red cross indicates divergence of the simulation. Higher values (red colour) indicate a higher risk of thrombosis. The white line in the 2D maps signals the position of the implanted device.

B.2 Reynolds number in left atrial simulations

For the computation of the Reynolds numbers, the resulting best-case scenario from the first sensitivity analysis was used. That is Scenario 3. The BC for this scenario were composed by a pressure wave from AF patient in sinus rhythm at the PVs; a US velocity curve defined at the MV; and a diffusion based dynamic mesh for the movement of the walls. To compute the Reynolds number we measured the velocity in two points, one in the left superior pulmonary vein and the other one at the MV but a little above the place where we had defined the BC. The results obtained presented the flow obtained as laminar in both, PV and MV as Table B.1 shows.

Table B.1: Reynolds numbers obtained at the MV and PV using the average velocity. MV: mitral valve; PV: Pulmonary vein; Re: Reynolds number; vel: velocity.

| Case ID | Re MV | Re PV |
|-----------|---------|---------|
| Patient 1 | 2260.04 | 875.09 |
| Patient 2 | 1257.82 | 1129.74 |
| Patient 3 | 2139.8 | 1132.34 |
| Patient 4 | 1980.46 | 1132.34 |
| Patient 5 | 2120.12 | 1623.14 |
| Patient 6 | 1986.78 | 651.02 |

B.3 Second sensitivity analysis: Flow in the LAA

In Figure B.4, the velocities measured at the LAA ostium over time using the different scenarios are presented. As can be observed, the dynamic mesh extracted from the dCT is the scheme that reached higher velocities after the stabilisation of the first beat (i.e. second and third beat). But overall, scenarios with the velocity profile at the mitral valve reached higher velocities.

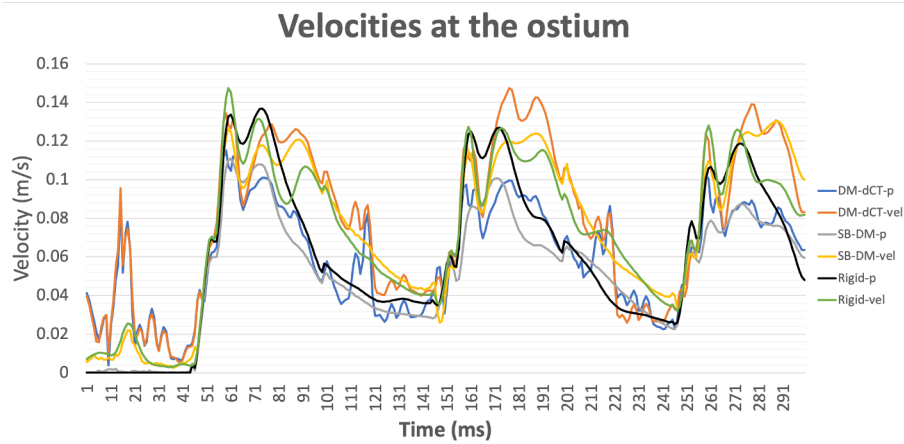


Figure B.4: Velocities at the ostium with the different scenarios. DM-dCT-p: dynamic CT movement with a pressure profile at the pulmonary veins; DM-dCT-vel: dynamic CT movement with a velocity profile at the pulmonary veins; SB-DM-p: dynamic mesh movement with a pressure profile at the pulmonary veins; SB-DM-vel: dynamic mesh movement with a velocity profile at the pulmonary veins; Rigid-p: rigid walls with a pressure profile at the pulmonary veins; Rigid-vel: rigid walls with a velocity profile at the pulmonary veins.

When the flow inside the LAA is assessed, dynamic mesh extracted from the dCT has better washing than the other schemes independently of the scenario

used. In the following images, complementary images of the beat from the one presented in the main text are attached (see Figure 3.11). More specifically, early systole, late systole and late diastole.

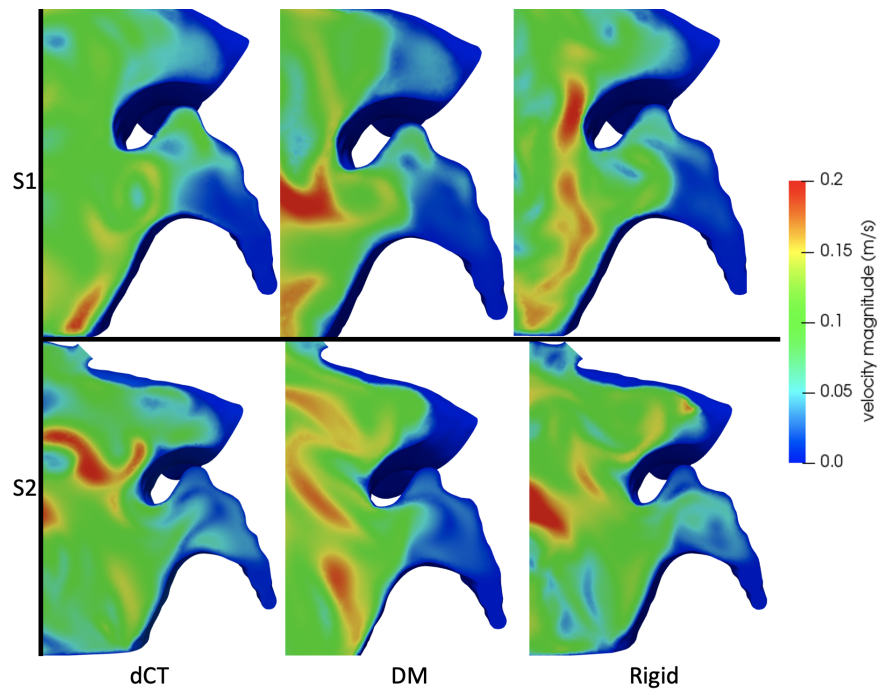


Figure B.5: Clip at the LAA for the different setups and movement schemes showing the velocities inside during early systole. First row, S1, velocities are defined as inlet at the PV and mixed BC is used at the MV. Second row, S2, pressure curve it is defined as the PV and a velocity curve is defined at the MV. Columns refer to the different movement schemes: first column: dCT; second column: DM; third column: Rigid.

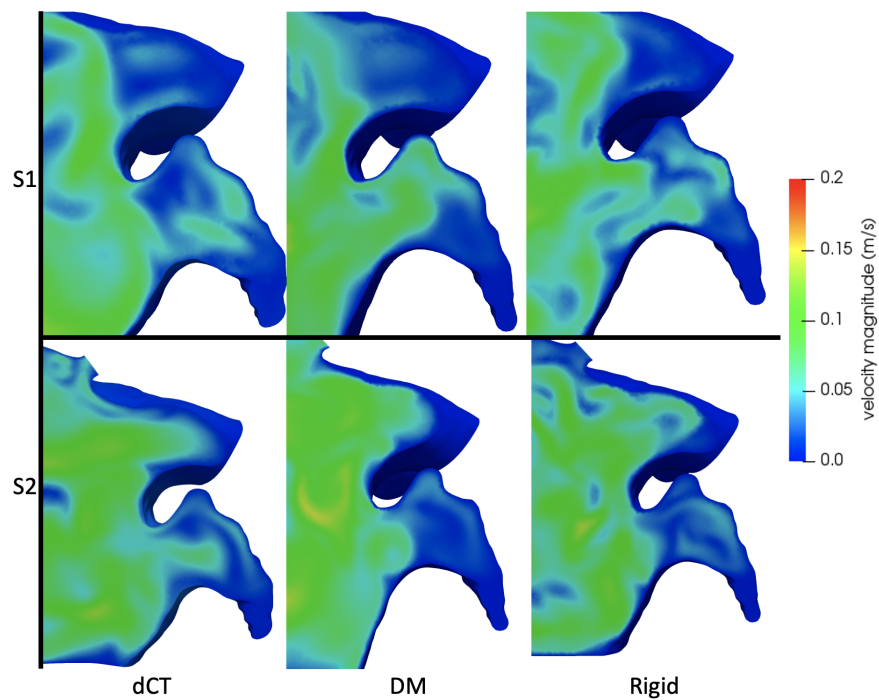


Figure B.6: Clip at the LAA for the different setups and movement schemes showing the velocities inside during late systole. First row, S1, velocities are defined as inlet at the PV and mixed BC is used at the MV. Second row, S2, pressure curve it is defined as the PV and a velocity curve is defined at the MV. Columns refer to the different movement schemes: first column: dCT; second column: DM; third column: Rigid.

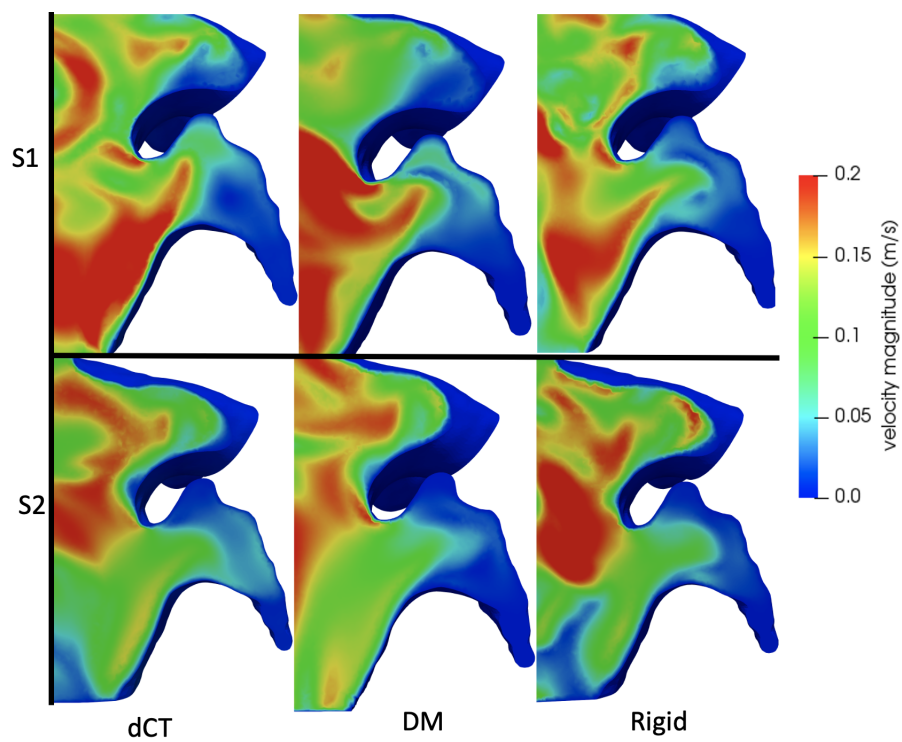


Figure B.7: Clip at the LAA for the different setups and movement schemes showing the velocities inside during late diastole. First row, S1, velocities are defined as inlet at the PV and mixed BC is used at the MV. Second row, S2, pressure curve it is defined as the PV and a velocity curve is defined at the MV. Columns refer to the different movement schemes: first column: dCT; second column: DM; third column: Rigid.

Appendix C

ANALYSIS WITH FLUID-BASED PARTICLES

In this Appendix the boxplots of the fluid-based particles for 5PVs are attached. On the left of Figure C.1, the boxplot of the results presented in Chapter 4, with all the cases included is presented. As can be observed there is one case within the control group that is over 700, far from the main distribution of the control group producing that the mean of the number of particles in the LAA is higher in the control group than the thrombus group. When this outlier is removed, the mean change (193.5 thrombus group vs. 169.5 control group). When all the outliers are removed, right side of the image, the differences between all the groups is higher but then you are at risk to commit the fallacy of incomplete evidence¹. For this reason, the results presented in the main text, are without removing any case, directly obtained from the simulations.

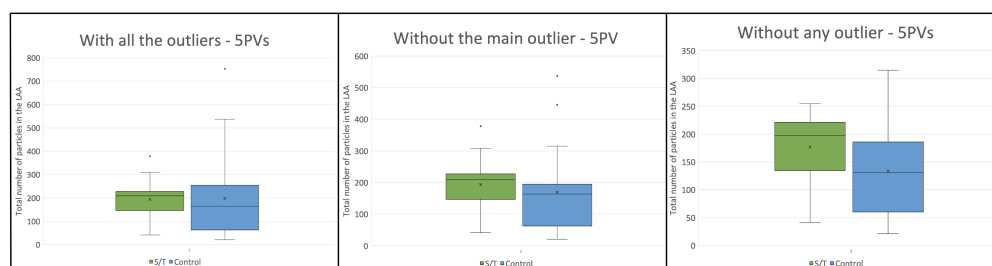


Figure C.1: On the left, the box plot for the 5PVs group. At the center, the boxplot with the main outlier (T/S group) removed from the cohort. On the right, the boxplot with all the outliers removed.

¹https://en.wikipedia.org/wiki/Cherry_picking

Appendix D

IN-SILICO HAEMODYNAMICS TO IDENTIFY THE LEFT ATRIAL APPENDAGE OCCLUSION SETTINGS INDUCED DEVICE-RELATED THROMBUS

D.1 Device positioning

The devices were designed internally from the scratch from Physense lab members. However these devices were not designed to be part of the simulation in the first place. Therefore, in order to make them as realistic as possible hooks were incorporated. Those hooks create a lot of problems due to the intersecting faces, specially when the volumetric fluid mesh is generated. For this reason the hooks were removed. In the Watchman FLX device, the part the metallic part was closed and covered in order to make the generation of the device's volume easier, and thus, the volumetric mesh. Once the devices were simplified, they were placed in the left atrial appendage (LAA). The final device sizes used for every position can be found in the table below (Table D.1).

Although the device selection presented above was done using VIDAA platform [1] in order to choose the device which suited the best, and the results validated by the physicians, there were parts that stand out from the LAA. This also happens in the reality. In fact, it's good for the device to have some compression, therefore, the hooks can attach well to the wall, and the risk of embolisation is

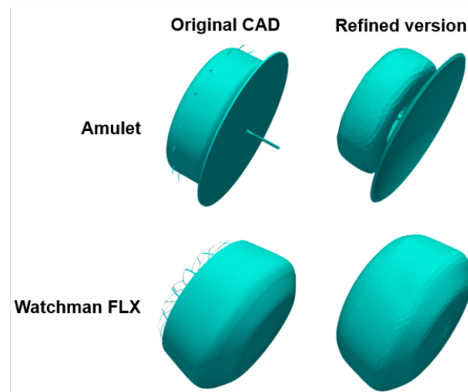


Figure D.1: Original CAD designs and refined versions of the Amulet and Watchman FLX devices.

Table D.1: Resulting Amulet(A)and WatchmanFLX (W) device sizes necessary for a good sealing of the left atrial appendage (LAA) for each configuration.

| Device sizes | | | | |
|---------------------|-------------------|----------|---------------------|----------|
| | PR covered | | PR uncovered | |
| | A | W | A | W |
| Case 1 | 22 | 24 | 20 | 20 |
| Case 2 | 22 | 24 | 20 | 24 |
| Case 3 | 25 | 25 | 20 | 24 |
| Case 4 | 31 | 31 | 25 | 27 |
| Case 5 | 22 | 24 | 20 | 20 |
| Case 6 | 16 | 20 | 16 | 20 |

very low. The compression results are presented in the table below. Some of the compression reached very high values, specially Watchman ones. One of the reasons it is due that the compression is computed taking into account all the closed volume. As we have been mentioned above, for the Watchman, we closed the part of the hooks to simplify the model and be able to generate the volumetric meshes. Nevertheless, it is clear that this action affects on the compression results. Thus, they need to be read carefully. However, the compression was not used for any analysis performed nor had an impact to the computational fluid simulations presented in Chapter 5.

Table D.2: Device volumetric compression (%) comparing the original device volume and the volume after deployment of the Amulet(A) and WatchmanFLX (W) devices.

| Device volumetric compression (%) | | | | |
|--|------------|------|--------------|------|
| | PR covered | | PR uncovered | |
| | A | W | A | W |
| Case 1 | 32.2 | 42.8 | 37.0 | 30.3 |
| Case 2 | 16.2 | 32.2 | 9.9 | 28.2 |
| Case 3 | 42.6 | 45.7 | 24.7 | 44.6 |
| Case 4 | 38.4 | 42.3 | 21.9 | 36.0 |
| Case 5 | 23.7 | 44.8 | 36.8 | 39.7 |
| Case 6 | 41.6 | 67.1 | 42.1 | 64.1 |

D.2 Discrete phase modelling

In Figure D.2 the area delimited to the particles to be attached can be observed in red. Therefore, all the particles that touched the wall, independently on the velocity they attached to the wall. The device's surface was not selected, therefore the particles only could attach to the LA's wall and other regions that the literature reported as possible places of DRT generation (e.g. pin of the devices, [6]) could not been studied. However, the main objective of the work presented in Chapter 5 it was to study the influence of the pulmonary ridge (PR) depending on the device used. The PR risk factor depends more on the flow rather than the device-related thrombus generated at the pin's devices [93].

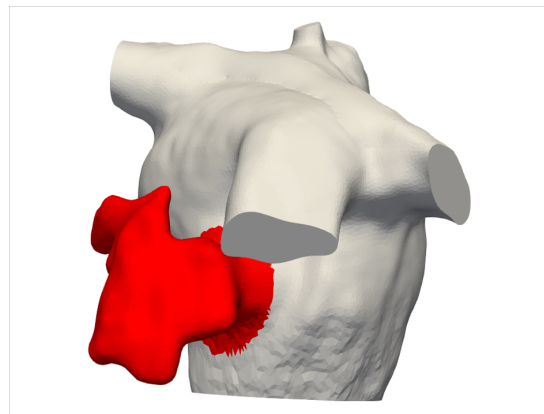


Figure D.2: Example of LAA separation for the definition of wall-film conditions. The geometry corresponds of Case6 of the cohort.

In Figure D.3 the results of the number of attached particles over time using the discrete phase method are presented. Every patient has four scenarios tested as has been explained in Chapter 5: 1) PR covered with the Amulet device; 2) PR covered with the Watchman device; 3) PR uncovered with the Amulet device; and 4) PR uncovered with Watchman device. Results showed a higher number of platelets attached in the PR uncovered scenarios, whereas between devices, depended on the case. Similar results were found when the velocity near the device surface was assessed. Slightly and non significant differences were found in terms of velocity between WatchmanFLX and Amulet, but higher velocities were measured in cases where the PR was covered.

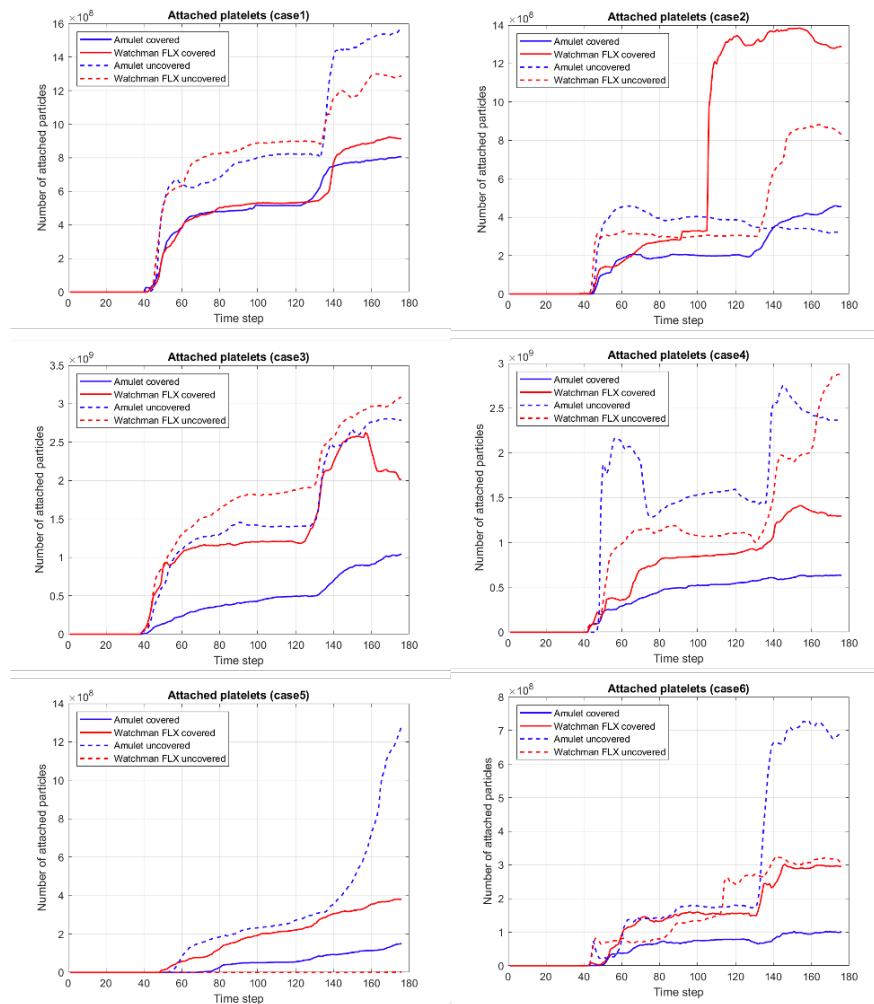


Figure D.3: Number of attached particles in the LAA as a function of time. The profiles are shown for Amulet (blue) and WatchmanFLX (red) in covered PR (solid) and uncovered PR (dashed) positions.

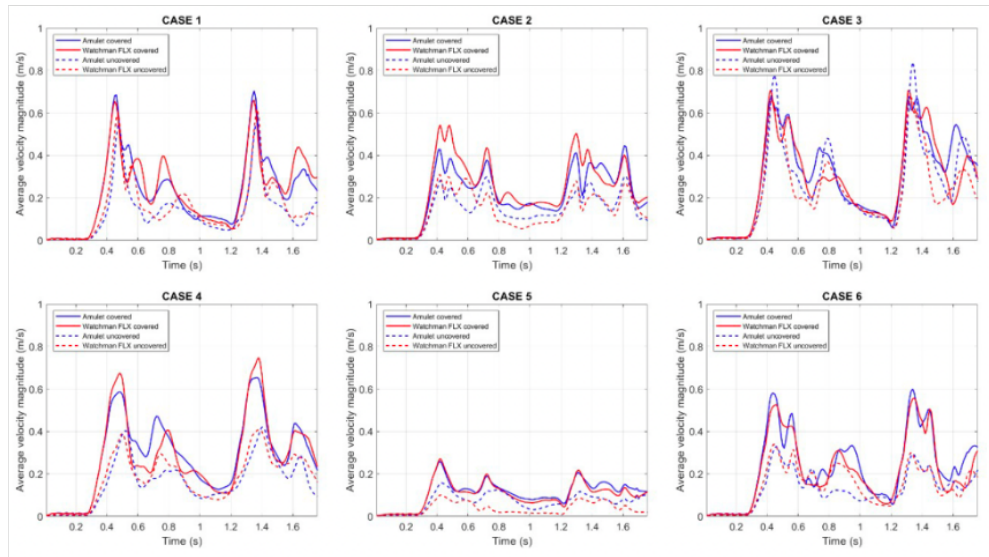


Figure D.4: Average velocity profiles in a region near the device throughout two cardiac cycles. The profiles are shown for Amulet (blue) and WatchmanFLX (red) in covered PR (solid) and uncovered PR (dashed) positions.

D.3 Analysis of the blood flow re-circulations

In the following images the results obtained with streamlines, λ_2 and Q-criterion are presented. For each geometry and position, we attempted to detect the time step where more re-circulation patterns and low velocities were detected during the second heart beat. The streamlines and the velocity field near the device are shown for each case and at the time step where the most complex patterns appeared in each geometry and position are shown in Figure D.5 at systole and in Figure D.6 at diastole.

In Table D.3 a summary of the observations from streamline visualisation is shown for both systole and diastole of the second simulated heart beat. As a general rule, flow re-circulation patterns at low velocities are commonly detected at the edge of WatchmanFLX at some point during the cardiac cycle, independently of the position of the occluder. Besides, similar patterns appear in both systole and diastole, that is, whether flow re-circulations and stagnation are detected in both parts of the cardiac cycle or they are not. Notice the remarkable difference between the Amulet device in the covered PR position and the WatchmanFLX device in the uncovered position. While in the first case few simulations predict the presence of swirls and blood stagnation, in the latter case they are detected in all the studied geometries and parts of the cardiac cycle.

Table D.3: Detection of flow re-circulations and stagnation near the device using streamline visualisation and mid-end systole (Sys.) and end diastole (Dias.).

| Presence of flow re-circulation and stagnation | | | | | | | | | |
|---|------------|------|----------|------|--------------|------|----------|------|--|
| | PR covered | | | | PR uncovered | | | | |
| | Amulet | | Watchman | | Amulet | | Watchman | | |
| | Sys | Dias | Sys | Dias | Sys | Dias | Sys | Dias | |
| Case 1 | NO | NO | YES | YES | YES | YES | YES | YES | |
| Case 2 | NO | NO | YES | YES | YES | YES | YES | YES | |
| Case 3 | NO | NO | NO | NO | YES | NO | YES | YES | |
| Case 4 | YES | NO | YES | YES | YES | YES | YES | YES | |
| Case 5 | NO | YES | YES | YES | YES | YES | YES | YES | |
| Case 6 | YES | NO | YES | YES | NO | NO | YES | YES | |

D.4 Vorticity analysis

In Figures D.7 and D.8 the results of the λ_2 criterion analysis are shown for all the simulated scenarios at mid-end systole and mid-end diastole, respectively. All cases are shown at the same time step where velocity re-circulations were found and shown in the previous section. The chosen value were the following $\lambda_2 = 50$ for mid-end systole and $\lambda_2 = 200$ at end diastole. According to the results, for the most part, in covered PR Amulet configurations vorticity at low velocities was not detected during end diastole and was less common during mid-end systole than in other configurations. The opposite happened with the Watchman-FLX device, where relevant low-velocity vortex regions were commonly detected at the edge of the device both in systole and diastole (see Case 1, 2, 4, 5 and 6). Vortices were also present in the uncovered PR position both for Amulet and Watchman-FLX device. Notice also that vorticities at low velocities were slightly more common at mid-end systole than at end diastole.

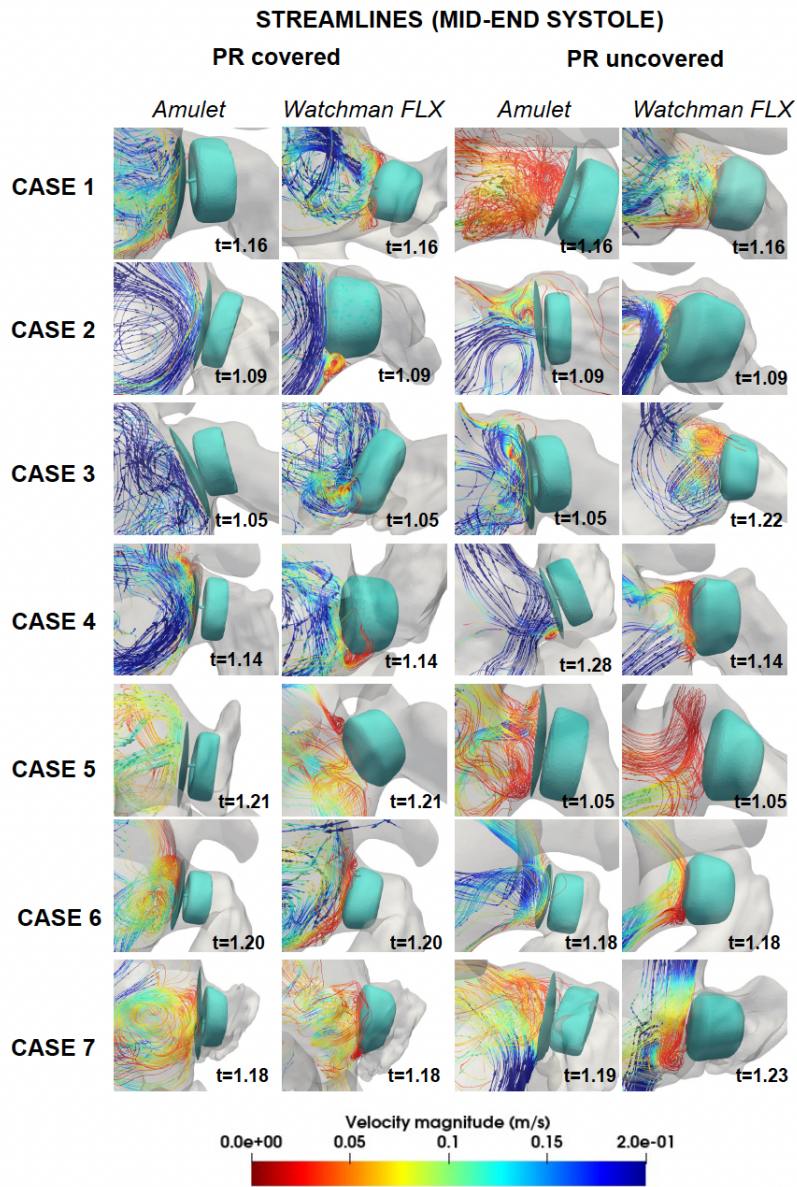


Figure D.5: Flow velocity field visualization with streamlines of all the tested configurations at mid-end systole. Time is expressed in seconds.

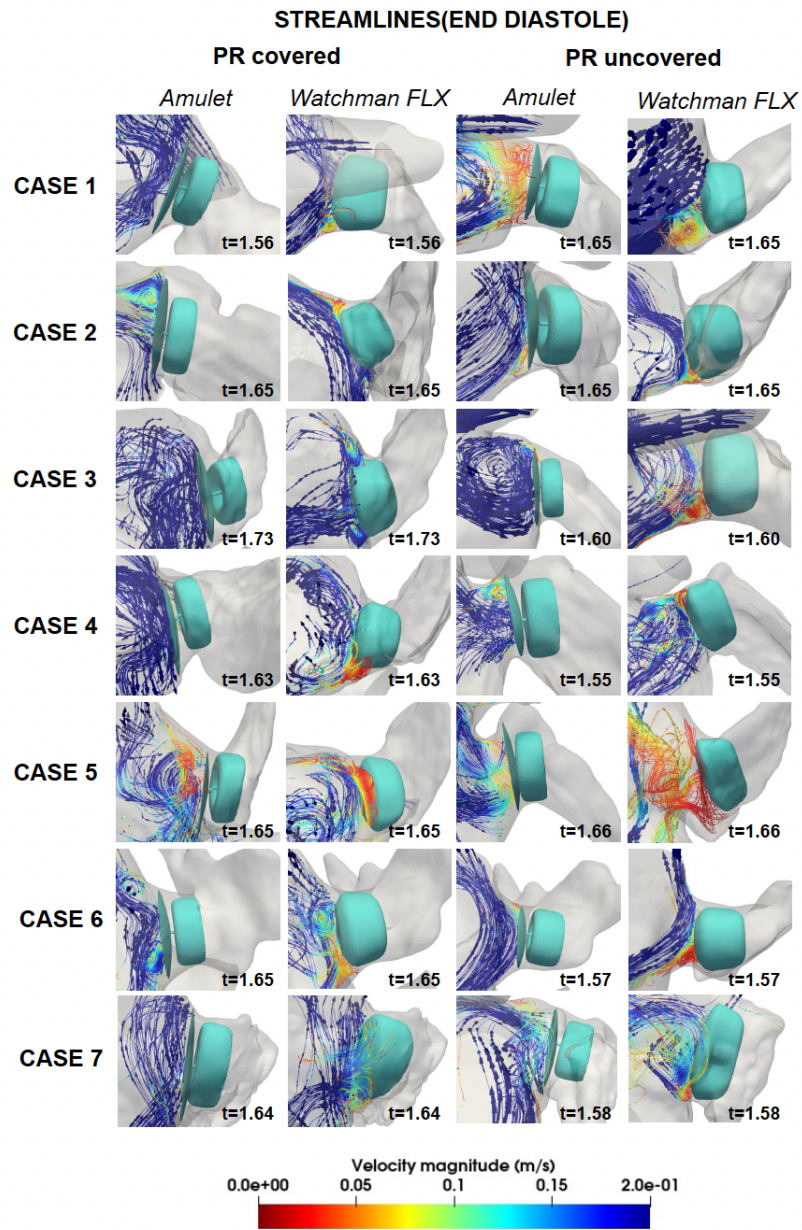


Figure D.6: Flow velocity field visualization with streamlines of all the tested configurations at end diastole. Time is expressed in seconds.

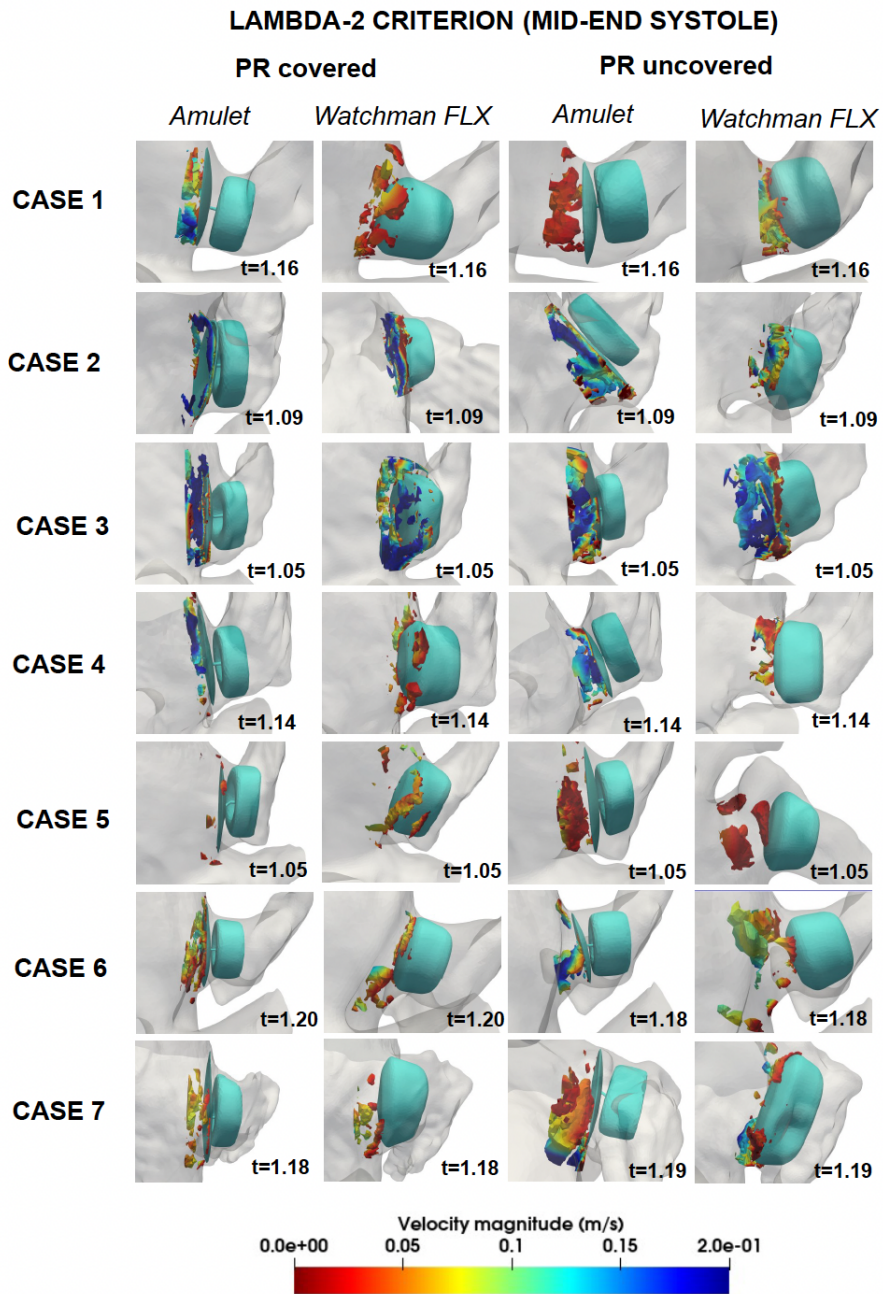


Figure D.7: Visualization of the isovolumes defined by $\lambda_2 = 50$ for the different LAO configurations at mid-end systole. Time is expressed in seconds.

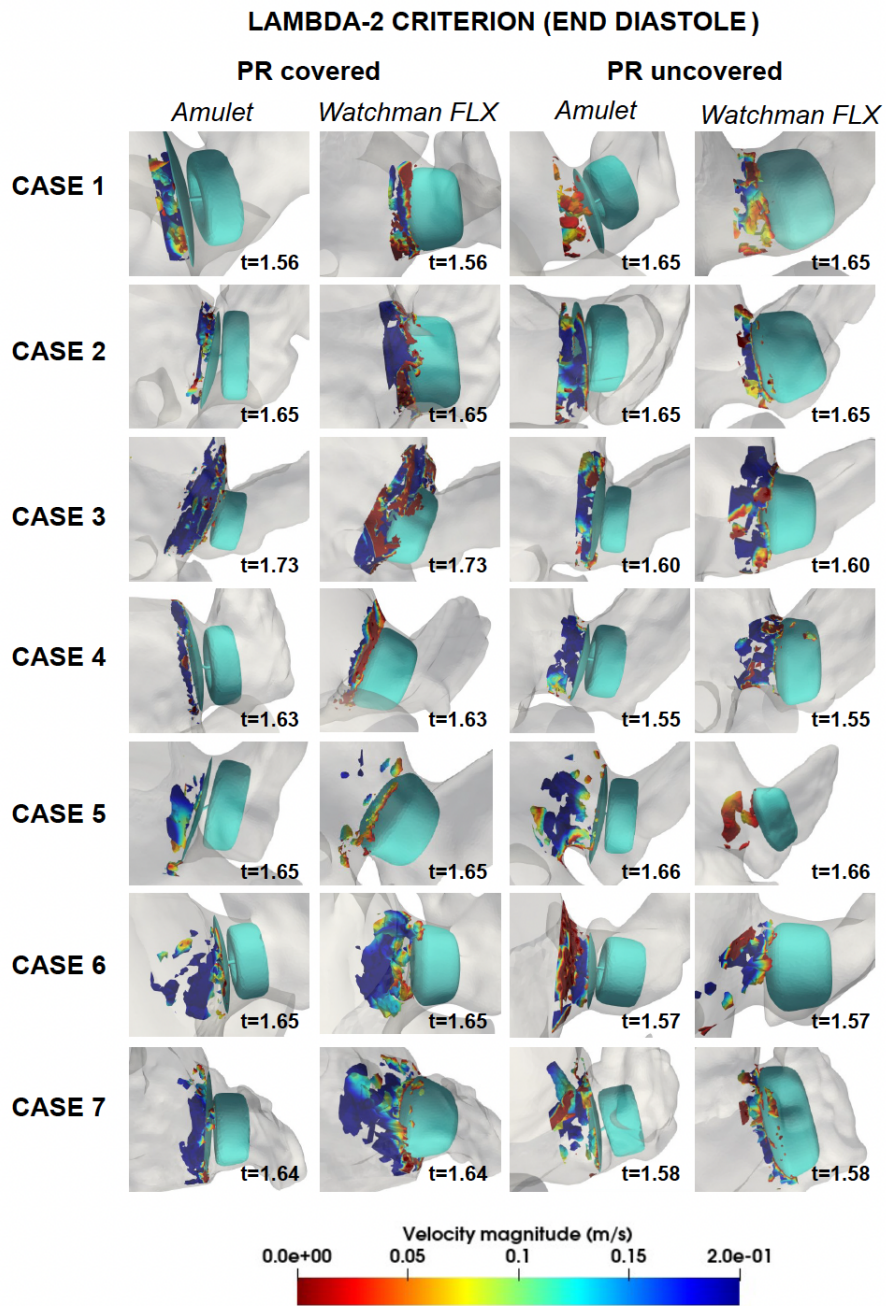


Figure D.8: Visualization of the isovolumes defined by $\lambda_2 = 200$ for the different LAAO configurations at end diastole. Time is expressed in seconds.

Bibliography

- [1] A. M. Aguado, A. L. Olivares, C. Yagüe, E. Silva, M. Nuñez-García, Á. Fernandez-Quilez, J. Mill, I. Genua, D. Arzamendi, T. De Potter, X. Freixa, and O. Camara. In silico Optimization of Left Atrial Appendage Occluder Implantation Using Interactive and Modeling Tools. *Frontiers in Physiology*, 10:1–26, 2019.
- [2] H. Akaike. A new look at the statistical model identification. *IEEE Transactions on Automatic Control*, 19(6):716–723, 1974.
- [3] N. M. Al-Saady, O. A. Obel, and A. J. Camm. Left atrial appendage: structure, function, and role in thromboembolism. *Heart*, 82(5):547 LP – 554, nov 1999.
- [4] M. Alkhouli, C. Du, A. Killu, T. Simard, P. A. Noseworthy, P. A. Friedman, J. P. Curtis, J. V. Freeman, and D. R. Holmes. Clinical Impact of Residual Leaks Following Left Atrial Appendage Occlusion: Insights From the NCDR LAAO Registry. *JACC: Clinical Electrophysiology*, 8(6):766–778, 2022.
- [5] D. Altinkaynak and A. Koktener. Evaluation of pulmonary venous variations in a large cohort. *Wiener klinische Wochenschrift*, 131(19):475–484, 2019.
- [6] A. Aminian, B. Schmidt, P. Mazzone, S. Berti, S. Fischer, M. Montorfano, S. C. C. Lam, J. Lund, F. M. Asch, R. Gage, I. Cruz-Gonzalez, H. Omran, G. Tarantini, and J. E. Nielsen-Kudsk. Incidence, Characterization, and Clinical Impact of Device-Related Thrombus Following Left Atrial Appendage Occlusion in the Prospective Global AMPLATZER Amulet Observational Study. *JACC: Cardiovascular Interventions*, 12(11):1003–1014, 2019.
- [7] N. Ammash, E. A. Konik, R. D. McBane, D. Chen, J. I. Tange, D. E. Grill, R. M. Herges, T. G. McLeod, P. A. Friedman, and W. E. Wysokinski. Left

Atrial Blood Stasis and Von Willebrand Factorx2013;ADAMTS13 Homeostasis in Atrial Fibrillation. *Arteriosclerosis, Thrombosis, and Vascular Biology*, 31(11):2760–2766, 2011.

- [8] L. Asmarats, C.-G. Ignacio, N.-F. Luis, A. Dabit, P. Vicente, N. Fabian, L. Azeem, M. Diego, G.-F. Rocío, R.-G. Tania, A. Victor, A. Marta, G. R. A., M. Antonio, B. Mathieu, and R.-C. Josep. Recurrence of Device-Related Thrombus After Percutaneous Left Atrial Appendage Closure. *Circulation*, 140(17):1441–1443, oct 2019.
- [9] W. Bai, Z. Chen, H. Tang, H. Wang, W. Cheng, and L. Rao. Assessment of the left atrial appendage structure and morphology: comparison of real-time three-dimensional transesophageal echocardiography and computed tomography. *The International Journal of Cardiovascular Imaging*, 33(5):623–633, 2017.
- [10] K. Bedeir, S. Warriner, E. Kofsky, C. Gullett, and B. Ramlawi. Left Atrial Appendage Epicardial Clip (AtriClip): Essentials and Post-Procedure Management. *Journal of atrial fibrillation*, 11(6):2087, apr 2019.
- [11] R. Beigel, N. C. Wunderlich, S. Y. Ho, R. Arsanjani, and R. J. Siegel. The left atrial appendage: anatomy, function, and noninvasive evaluation. *JACC. Cardiovascular imaging*, 7(12):1251–1265, dec 2014.
- [12] D. S. Beutler, R. D. Gerkin, A. I. Loli, D. S. Beutler, R. D. Gerkin, and A. I. Loli. The Morphology of Left Atrial Appendage Lobes: A Novel Characteristic Naming Scheme Derived through Three-Dimensional Cardiac Computed Tomography. *World Journal of Cardiovascular Surgery*, 04(03):17–24, mar 2014.
- [13] L. V. Boersma, H. Ince, S. Kische, E. Pokushalov, T. Schmitz, B. Schmidt, T. Gori, F. Meincke, A. V. Protopopov, T. Betts, D. Foley, H. Sievert, P. Mazzone, T. De Potter, E. Vireca, K. Stein, and M. W. Bergmann. Efficacy and safety of left atrial appendage closure with WATCHMAN in patients with or without contraindication to oral anticoagulation: 1-Year follow-up outcome data of the EWOLUTION trial. *Heart rhythm*, 14(9):1302–1308, sep 2017.
- [14] L. V. Boersma, H. Ince, S. Kische, E. Pokushalov, T. Schmitz, B. Schmidt, T. Gori, F. Meincke, A. V. Protopopov, T. Betts, P. Mazzone, D. Foley, M. Grygier, H. Sievert, T. De Potter, E. Vireca, K. Stein, and M. W. Bergmann. Evaluating Real-World Clinical Outcomes in Atrial Fibrillation Patients Receiving the WATCHMAN Left Atrial Appendage Closure

Technology: Final 2-Year Outcome Data of the EWOLUTION Trial Focusing on History of Stroke and Hemorrhage. *Circulation: Arrhythmia and Electrophysiology*, 12(4):1–13, 2019.

- [15] A. Bône, M. Louis, B. Martin, and S. Durrleman. Deformetrica 4: an open-source software for statistical shape analysis. In *International Workshop on Shape in Medical Imaging*, pages 3–13. Springer, 2018.
- [16] G. M. Bosi, A. Cook, R. Rai, L. J. Menezes, S. Schievano, R. Torii, and G. Burriesci. Computational Fluid Dynamic Analysis of the Left Atrial Appendage to Predict Thrombosis Risk. *Frontiers in Cardiovascular Medicine*, 5, apr 2018.
- [17] A. C. Boyd, T. McKay, S. Nasibi, D. A. B. Richards, and L. Thomas. Left ventricular mass predicts left atrial appendage thrombus in persistent atrial fibrillation. *European Heart Journal - Cardiovascular Imaging*, 14(3):269–275, mar 2013.
- [18] S. J. Connolly, M. D. Ezekowitz, S. Yusuf, J. Eikelboom, J. Oldgren, A. Parekh, J. Pogue, P. A. Reilly, E. Themeles, J. Varrone, S. Wang, M. Alings, D. Xavier, J. Zhu, R. Diaz, B. S. Lewis, H. Darius, H.-C. Diener, C. D. Joyner, and L. Wallentin. Dabigatran versus Warfarin in Patients with Atrial Fibrillation. *New England Journal of Medicine*, 361(12):1139–1151, sep 2009.
- [19] J. Corral-Acero, F. Margara, M. Marciniak, C. Rodero, F. Loncaric, Y. Feng, A. Gilbert, J. F. Fernandes, H. A. Bukhari, A. Wajdan, M. V. Martinez, M. S. Santos, M. Shamohammdi, H. Luo, P. Westphal, P. Leeson, P. DiAchille, V. Gurev, M. Mayr, L. Geris, P. Pathmanathan, T. Morrison, R. Cornelussen, F. Prinzen, T. Delhaas, A. Doltra, M. Sitges, E. J. Vigmond, E. Zacur, V. Grau, B. Rodriguez, E. W. Remme, S. Niederer, P. Mortier, K. McLeod, M. Potse, E. Pueyo, A. Bueno-Orovio, and P. Lamata. The ‘Digital Twin’ to enable the vision of precision cardiology. *European Heart Journal*, mar 2020.
- [20] M. Corti, A. Zingaro, L. Dede’, and A. M. Quarteroni. Impact of atrial fibrillation on left atrium haemodynamics: A computational fluid dynamics study, 2022.
- [21] A. Cresti and O. Camara. Left Atrial Thrombus—Are All Atria and Appendages Equal? *Interventional Cardiology Clinics*, 11(2):121–134, 2022.

- [22] A. Cresti, M. A. García-Fernández, H. Sievert, P. Mazzone, P. Baratta, M. Solari, A. Geyer, F. De Sensi, and U. Limbruno. Prevalence of extra-appendage thrombosis in non-valvular atrial fibrillation and atrial flutter in patients undergoing cardioversion: a large transoesophageal echo study. *EuroIntervention : journal of EuroPCR in collaboration with the Working Group on Interventional Cardiology of the European Society of Cardiology*, 15(3):e225–e230, jun 2019.
- [23] P. Cronin, A. M. Kelly, B. Desjardins, S. Patel, B. H. Gross, E. A. Kazerouni, F. Morady, H. Oral, and R. C. Carlos. Normative Analysis of Pulmonary Vein Drainage Patterns on Multidetector CT With Measurements of Pulmonary Vein Ostial Diameter and Distance to First Bifurcation. *Academic Radiology*, 14(2):178–188, 2007.
- [24] S. K. Dahl, E. Thomassen, L. R. Hellevik, and B. Skallerud. Impact of Pulmonary Venous Locations on the Intra-Atrial Flow and the Mitral Valve Plane Velocity Profile. *Cardiovascular Engineering and Technology*, 3(3):269–281, sep 2012.
- [25] N. D’Alessandro, A. Masci, A. Andalo, L. Dede, C. Tomasi, A. Quarteroni, and C. Corsi. Simulation of the Hemodynamic Effects of the Left Atrial Appendage Occlusion in Atrial Fibrillation: Preliminary Results. In *Computing in Cardiology*, volume 2020-September. IEEE Computer Society, 2020.
- [26] P. Di Achille, G. Tellides, C. A. Figueroa, and J. D. Humphrey. A haemodynamic predictor of intraluminal thrombus formation in abdominal aortic aneurysms. *Proceedings of the Royal Society A: Mathematical, Physical and Engineering Sciences*, 470(2172):20140163–20140163, 2014.
- [27] L. Di Biase, P. Santangeli, M. Anselmino, P. Mohanty, I. Salvetti, S. Gili, R. Horton, J. E. Sanchez, R. Bai, S. Mohanty, A. Pump, M. Cereceda Brantes, G. J. Gallinghouse, J. D. Burkhardt, F. Cesarani, M. Scaglione, A. Natale, and F. Gaita. Does the left atrial appendage morphology correlate with the risk of stroke in patients with atrial fibrillation? Results from a multicenter study. *Journal of the American College of Cardiology*, 60(6):531–538, aug 2012.
- [28] D. Dillon-Murphy, D. Marlevi, B. Ruijsink, A. Qureshi, H. Chubb, E. Kerfoot, M. O’Neill, D. Nordsletten, O. Aslanidi, and A. De Vecchi. Modeling left atrial flow, energy, blood heating distribution in response to catheter ablation therapy. *Frontiers in Physiology*, 9:1757, dec 2018.

- [29] J. Dueñas-Pamplona, J. G. García, F. Castro, J. Muñoz-Paniagua, J. Goicolea, and J. Sierra-Pallares. Morphing the left atrium geometry: A deeper insight into blood stasis within the left atrial appendage. *Applied Mathematical Modelling*, 108:27–45, 2022.
- [30] J. Dueñas-Pamplona, J. Sierra-Pallares, J. García, F. Castro, and J. Muñoz-Paniagua. Boundary-Condition Analysis of an Idealized Left Atrium Model. *Annals of Biomedical Engineering*, 49(6):1507–1520, 2021.
- [31] S. R. Dukkupati, S. Kar, D. R. Holmes, S. K. Doshi, V. Swarup, D. N. Gibson, B. Maini, N. T. Gordon, M. L. Main, and V. Y. Reddy. Device-Related Thrombus After Left Atrial Appendage Closure. *Circulation*, 138(9):874–885, aug 2018.
- [32] M. S. El Baz, B. P. Lelieveldt, J. J. Westenberg, and R. J. Van Der Geest. Automatic extraction of the 3D left ventricular diastolic transmitral vortex ring from 3D whole-heart Phase Contrast MRI using Laplace-Beltrami signatures. In *Lecture Notes in Computer Science (including subseries Lecture Notes in Artificial Intelligence and Lecture Notes in Bioinformatics)*, volume 8330 LNCS, 2014.
- [33] K. Emilsson and B. Wandt. The relation between ejection fraction and mitral annulus motion before and after direct-current electrical cardioversion. *Clinical Physiology*, 20(3):218–224, 2000.
- [34] B. M. Fadel, P. Pibarot, B. E. Kazzi, M. Al-Admawi, D. Galzerano, M. Alhumaid, B. Alamro, H. Mahjoub, N. Echahidi, and D. Mohty. Spectral Doppler Interrogation of the Pulmonary Veins for the Diagnosis of Cardiac Disorders: A Comprehensive Review. *Journal of the American Society of Echocardiography*, 34(3):223–236, mar 2021.
- [35] F. F. Faletra, L. A. Leo, V. L. Paiocchi, A. Caretta, G. M. Viani, S. A. Schlossbauer, S. Demertzis, and S. Y. Ho. Anatomy of mitral annulus insights from non-invasive imaging techniques. *European heart journal. Cardiovascular Imaging*, 20(8):843–857, aug 2019.
- [36] R. Fang, Y. Li, Y. Zhang, Q. Chen, Q. Liu, and Z. Li. Impact of left atrial appendage location on risk of thrombus formation in patients with atrial fibrillation. *Biomechanics and Modeling in Mechanobiology*, 2021.
- [37] B. M. Fanni, K. Capellini, M. Di Leonardo, A. Clemente, E. Cerone, S. Berti, and S. Celi. Correlation between laa morphological features and computational fluid dynamics analysis for non-valvular atrial fibrillation patients. *Applied Sciences*, 10(4), 2020.

- [38] L. Fauchier, A. Cinaud, F. Brigadeau, A. Lepillier, B. Pierre, S. Abbey, M. Fatemi, F. Franceschi, P. Guedeney, P. Jacon, O. Paziand, S. Venier, J. C. Deharo, D. Gras, D. Klug, J. Mansourati, G. Montalescot, O. Piot, and P. Defaye. Device-Related Thrombosis After Percutaneous Left Atrial Appendage Occlusion for Atrial Fibrillation. *Journal of the American College of Cardiology*, 71(14):1528 LP – 1536, apr 2018.
- [39] L. Feng, H. Gao, B. Griffith, S. Niederer, and X. Luo. Analysis of a coupled fluid-structure interaction model of the left atrium and mitral valve. *International journal for numerical methods in biomedical engineering*, 35(11):e3254, nov 2019.
- [40] G. C. Fernandez-Perez, R. Duarte, M. Corral de la Calle, J. Calatayud, and J. Sanchez Gonzalez. Analysis of left ventricular diastolic function using magnetic resonance imaging. *Radiologia*, 54(4):295–305, 2012.
- [41] A. Ferrer, R. Sebastián, D. Sánchez-Quintana, J. F. Rodríguez, E. J. Godoy, L. Martínez, and J. Saiz. Detailed Anatomical and Electrophysiological Models of Human Atria and Torso for the Simulation of Atrial Activation. *PLOS ONE*, 10(11):e0141573, nov 2015.
- [42] X. Freixa, P. Cepas-Guillen, E. Flores-Umanzor, A. Regueiro, L. Sanchís, A. Fernandez-Valledor, S. Brugaletta, M. J. Carretero, B. Vidal, M. Masotti, V. Martin-Yuste, M. Roqué, M. Sitges, and M. Sabaté. Pulmonary ridge coverage and device-related thrombosis after left atrial appendage occlusion. *EuroIntervention*, 16(15):e1288–e1294, feb 2021.
- [43] A. Fyrenius, L. Wigström, T. Ebbers, M. Karlsson, J. Engvall, and A. F. Bolger. Three dimensional flow in the human left atrium. *Heart*, 86(4):448 LP – 455, oct 2001.
- [44] M. A. García-Fernández, E. G. Torrecilla, D. S. Román, J. Azevedo, H. Bueno, M. Moreno, and J. L. Delcán. Left atrial appendage doppler flow patterns: Implications on thrombus formation. *American Heart Journal*, 124(4):955–961, 1992.
- [45] G. García-Isla, A. L. Olivares, E. Silva, M. Nuñez-Garcia, C. Butakoff, D. Sanchez-Quintana, H. G. Morales, X. Freixa, J. Noailly, T. De Potter, and O. Camara. Sensitivity analysis of geometrical parameters to study haemodynamics and thrombus formation in the left atrial appendage. *International Journal for Numerical Methods in Biomedical Engineering*, 34(8):1–14, 2018.

- [46] M. García-Villalba, L. Rossini, A. Gonzalo, D. Vigneault, P. Martínez-Legazpi, E. Durán, O. Flores, J. Bermejo, E. McVeigh, A. M. Kahn, and J. C. Del Álamo. Demonstration of patient-specific simulations to assess left atrial appendage thrombogenesis risk. *Frontiers in physiology*, 12:596596–596596, 02 2021.
- [47] B. J. Gersh, J. E. Freedman, and C. B. Granger. Antiplatelet and Anticoagulant Therapy for Stroke Prevention in Patients With Non-Valvular Atrial Fibrillation: Evidence Based Strategies and New Developments. *Revista Española de Cardiología (English Edition)*, 64(4):260–268, 2011.
- [48] M. Glikson, R. Wolff, G. Hindricks, J. Mandrola, A. J. Camm, G. Y. H. Lip, L. Fauchier, T. R. Betts, T. Lewalter, J. Saw, A. Tzikas, L. Sternik, F. Nietlispach, S. Berti, H. Sievert, S. Bertog, and B. Meier. EHRA/EAPCI expert consensus statement on catheter-based left atrial appendage occlusion - an update. *Europace : European pacing, arrhythmias, and cardiac electrophysiology : journal of the working groups on cardiac pacing, arrhythmias, and cardiac cellular electrophysiology of the European Society of Cardiology*, 22(2):184, feb 2020.
- [49] S. D. Gollob, C. Park, B. H. B. Koo, and E. T. Roche. A Modular Geometrical Framework for Modelling the Force-Contraction Profile of Vacuum-Powered Soft Actuators. *Frontiers in Robotics and AI*, 8, 2021.
- [50] A. Gonzalo, M. García-Villalba, L. Rossini, E. Durán, D. Vigneault, P. Martínez-Legazpi, O. Flores, J. Bermejo, E. McVeigh, A. M. Kahn, and J. C. del Alamo. Non-Newtonian blood rheology impacts left atrial stasis in patient-specific simulations. *International Journal for Numerical Methods in Biomedical Engineering*, 38(6):e3597, jun 2022.
- [51] C. B. Granger, J. H. Alexander, J. J. V. McMurray, R. D. Lopes, E. M. Hylek, M. Hanna, H. R. Al-Khalidi, J. Ansell, D. Atar, A. Avezum, M. C. Bahit, R. Diaz, J. D. Easton, J. A. Ezekowitz, G. Flaker, D. Garcia, M. Gerardes, B. J. Gersh, S. Golitsyn, S. Goto, A. G. Hermosillo, S. H. Hohnloser, J. Horowitz, P. Mohan, P. Jansky, B. S. Lewis, J. L. Lopez-Sendon, P. Pais, A. Parkhomenko, F. W. A. Verheugt, J. Zhu, and L. Wallentin. Apixaban versus Warfarin in Patients with Atrial Fibrillation. *New England Journal of Medicine*, 365(11):981–992, aug 2011.
- [52] R. Granger. *Fluid Mechanics*. Dover Publications, 1995.
- [53] J. Harrison, M. Lorenzi, B. Legghe, X. Iriart, H. Cochet, and M. Sermesant. Phase-Independent Latent Representation for Cardiac Shape Analysis BT -

Medical Image Computing and Computer Assisted Intervention – MICCAI 2021. pages 537–546, Cham, 2021. Springer International Publishing.

- [54] J. J. Hathcock. Flow Effects on Coagulation and Thrombosis. *Arteriosclerosis, Thrombosis, and Vascular Biology*, 26(8):1729–1737, aug 2006.
- [55] J. He, Z. Fu, L. Yang, W. Liu, Y. Tian, Q. Liu, Z. Jiang, L. Tian, J. Huang, S. Tian, and Y. Zhao. The predictive value of a concise classification of left atrial appendage morphology to thrombosis in non-valvular atrial fibrillation patients. *Clinical Cardiology*, 43(7):789–795, jul 2020.
- [56] H. A. Himburg, D. M. Grzybowski, A. L. Hazel, J. A. LaMack, X.-M. Li, and M. H. Friedman. Spatial comparison between wall shear stress measures and porcine arterial endothelial permeability. *American Journal of Physiology-Heart and Circulatory Physiology*, 286(5):H1916–H1922, 2004.
- [57] A. M. Holbrook, J. A. Pereira, R. Labiris, H. McDonald, J. D. Douketis, M. Crowther, and P. S. Wells. Systematic Overview of Warfarin and Its Drug and Food Interactions. *Archives of Internal Medicine*, 165(10):1095–1106, may 2005.
- [58] D. R. Holmes, S. Kar, M. J. Price, B. Whisenant, H. Sievert, S. K. Doshi, K. Huber, and V. Y. Reddy. Prospective Randomized Evaluation of the Watchman Left Atrial Appendage Closure Device in Patients With Atrial Fibrillation Versus Long-Term Warfarin Therapy: The PREVAIL Trial. *Journal of the American College of Cardiology*, 64(1):1–12, 2014.
- [59] D. R. Holmes and R. S. Schwartz. Left Atrial Appendage Occlusion Eliminates the Need for Warfarin. *Circulation*, 120(19):1919–1926, nov 2009.
- [60] M. Jaguszewski, C. Manes, G. Puipe, S. Salzberg, M. Müller, V. Falk, T. Lüscher, A. Luft, H. Alkadhi, and U. Landmesser. Cardiac CT and echocardiographic evaluation of peri-device flow after percutaneous left atrial appendage closure using the AMPLATZER cardiac plug device. *Catheterization and Cardiovascular Interventions*, 85(2):306–312, feb 2015.
- [61] J. Jalife and K. Kaur. Atrial remodeling, fibrosis, and atrial fibrillation. *Trends in cardiovascular medicine*, 25(6):475–484, aug 2015.
- [62] W. K. Jeong, J.-H. Choi, J. P. Son, S. Lee, M. J. Lee, Y. H. Choe, and O. Y. Bang. Volume and morphology of left atrial appendage as determinants of

stroke subtype in patients with atrial fibrillation. *Heart rhythm*, 13(4):820–827, apr 2016.

- [63] D. Jia, B. Jeon, H. B. Park, H. J. Chang, and L. T. Zhang. Image-Based Flow Simulations of Pre- and Post-left Atrial Appendage Closure in the Left Atrium. *Cardiovascular Engineering and Technology*, 10(2):225–241, jun 2019.
- [64] W. D. Johnson, A. K. Ganjoo, C. D. Stone, R. C. Srivivas, and M. Howard. The left atrial appendage: our most lethal human attachment! Surgical implications. *European Journal of Cardio-Thoracic Surgery*, 17(6):718–722, jun 2000.
- [65] A. Kandathil and M. R. Chamrathy. Pulmonary vascular anatomy & anatomical variants. *Cardiovascular diagnosis and therapy*, 8 3:201–207, 2018.
- [66] A. Kanmanthareddy, Y. M. Reddy, A. Vallakati, M. B. Earnest, J. Nath, R. Ferrell, B. Dawn, and D. Lakkireddy. Embryology and Anatomy of the Left Atrial Appendage: Why Does Thrombus Form? *Interventional cardiology clinics*, 3(2):191–202, apr 2014.
- [67] G. T. Karatasakis. Influence of Mitral Regurgitation on Left Atrial Thrombus and Spontaneous Contrast With Rheumatic Valve Disease. *The American journal of cardiology*, 76(4):279–281, 1995.
- [68] R. Kato, L. Lickfett, G. Meininger, T. Dickfeld, R. Wu, G. Juang, P. Angkeow, J. LaCorte, D. Bluemke, R. Berger, H. R. Halperin, and H. Calkins. Pulmonary Vein Anatomy in Patients Undergoing Catheter Ablation of Atrial Fibrillation. *Circulation*, 107(15):2004–2010, apr 2003.
- [69] I. M. Khurram, J. Dewire, M. Mager, F. Maqbool, S. L. Zimmerman, V. Zipunnikov, R. Beinart, J. E. Marine, D. D. Spragg, R. D. Berger, H. Ashikaga, S. Nazarian, and H. Calkins. Relationship between left atrial appendage morphology and stroke in patients with atrial fibrillation. *Heart rhythm*, 10(12):1843–1849, dec 2013.
- [70] R. Koizumi, K. Funamoto, T. Hayase, Y. Kanke, M. Shibata, Y. Shiraishi, and T. Yambe. Numerical analysis of hemodynamic changes in the left atrium due to atrial fibrillation. *Journal of Biomechanics*, 48(3):472–478, feb 2015.
- [71] M. Korhonen, A. Muuronen, O. Arponen, P. Mustonen, M. Hedman, P. Jäkälä, R. Vanninen, and M. Taina. Left atrial appendage morphology in

patients with suspected cardiogenic stroke without known atrial fibrillation. *PLoS ONE*, 10(3):1–12, 2015.

- [72] D. Lakkireddy, M. R. Afzal, R. J. Lee, H. Nagaraj, D. Tschopp, B. Gidney, C. Ellis, E. Altman, B. Lee, S. Kar, N. Bhadwar, M. Sanchez, V. Gadiyaram, R. Evonich, A. Rasekh, J. Cheng, F. Cuoco, S. Chandhok, S. Gunda, M. Reddy, D. Atkins, S. Bommana, P. Cuculich, D. Gibson, J. Nath, R. Ferrell, E. Matthew, and D. Wilber. Short and long-term outcomes of percutaneous left atrial appendage suture ligation: Results from a US multicenter evaluation. *Heart rhythm*, 13(5):1030–1036, may 2016.
- [73] U. Landmesser, B. Schmidt, J. E. Nielsen-Kudsk, S. C. C. Lam, J.-W. Park, G. Tarantini, I. Cruz-Gonzalez, V. Geist, P. Della Bella, A. Colombo, T. Zeus, H. Omran, C. Piorkowski, J. Lund, C. Tondo, and D. Hildick-Smith. Left atrial appendage occlusion with the AMPLATZER Amulet device: periprocedural and early clinical/echocardiographic data from a global prospective observational study. *EuroIntervention : journal of EuroPCR in collaboration with the Working Group on Interventional Cardiology of the European Society of Cardiology*, 13(7):867–876, sep 2017.
- [74] M. Längin, T. Mayr, B. Reichart, S. Michel, S. Buchholz, S. Guethoff, A. Dashkevich, A. Baehr, S. Egerer, A. Bauer, M. Mihalj, A. Panelli, L. Issl, J. Ying, A. K. Fresch, I. Buttgereit, M. Mokolke, J. Radan, F. Werner, I. Lutzmann, S. Steen, T. Sjöberg, A. Paskevicius, L. Qiuming, R. Sfriso, R. Rieben, M. Dahlhoff, B. Kessler, E. Kemter, M. Kurome, V. Zakhartchenko, K. Klett, R. Hinkel, C. Kupatt, A. Falkenau, S. Reu, R. Ellgass, R. Herzog, U. Binder, G. Wich, A. Skerra, D. Ayares, A. Kind, U. Schönmann, F.-J. Kaup, C. Hagl, E. Wolf, N. Klymiuk, P. Brenner, and J.-M. Abicht. Consistent success in life-supporting porcine cardiac xenotransplantation. *Nature*, 564(7736):430–433, 2018.
- [75] J. M. Lee, J.-B. Kim, J.-S. Uhm, H.-N. Pak, M.-H. Lee, and B. Joung. Additional value of left atrial appendage geometry and hemodynamics when considering anticoagulation strategy in patients with atrial fibrillation with low CHA(2)DS(2)-VASc scores. *Heart rhythm*, 14(9):1297–1301, sep 2017.
- [76] J. M. Lee, J. Seo, J.-S. Uhm, Y. J. Kim, H.-J. Lee, J.-Y. Kim, J.-H. Sung, H.-N. Pak, M.-H. Lee, and B. Joung. Why Is Left Atrial Appendage Morphology Related to Strokes? An Analysis of the Flow Velocity and Orifice Size of the Left Atrial Appendage. *Journal of cardiovascular electrophysiology*, 26(9):922–927, sep 2015.

- [77] J. M. Lee, J. Shim, J.-S. Uhm, Y. J. Kim, H.-J. Lee, H.-N. Pak, M.-H. Lee, and B. Joung. Impact of Increased Orifice Size and Decreased Flow Velocity of Left Atrial Appendage on Stroke in Nonvalvular Atrial Fibrillation. *The American Journal of Cardiology*, 113(6):963–969, 2014.
- [78] M. Lempereur, A. Aminian, X. Freixa, S. Gafoor, J. Kefer, A. Tzikas, V. Legrand, and J. Saw. Device-associated thrombus formation after left atrial appendage occlusion: A systematic review of events reported with the Watchman, the Amplatzer Cardiac Plug and the Amulet. *Catheterization and cardiovascular interventions : official journal of the Society for Cardiac Angiography Interventions*, 90(5):E111–E121, nov 2017.
- [79] A. Li and G. Ahmadi. Dispersion and Deposition of Spherical Particles from Point Sources in a Turbulent Channel Flow. *Aerosol Science and Technology*, 16(4):209–226, jan 1992.
- [80] S. Lindner, M. Behnes, A. Wenke, B. Sartorius, U. Ansari, M. Akin, K. Mashayekhi, N. Vogler, H. Haubenreisser, S. O. Schoenberg, M. Borggreffe, and I. Akin. Assessment of peri-device leaks after interventional left atrial appendage closure using standardized imaging by cardiac computed tomography angiography. *The international journal of cardiovascular imaging*, 35(4):725–731, apr 2019.
- [81] G. Y. H. Lip, R. Nieuwlaat, R. Pisters, D. A. Lane, and H. J. G. M. Crijns. Refining clinical risk stratification for predicting stroke and thromboembolism in atrial fibrillation using a novel risk factor-based approach: the euro heart survey on atrial fibrillation. *Chest*, 137(2):263–272, feb 2010.
- [82] J. R. López-Mínguez, J. Eldoayen-Gragera, R. González-Fernández, C. Fernández-Vegas, M. E. Fuentes-Cañamero, V. Millán-Nuñez, J. M. Nogales-Asensio, A. Martínez-Naharro, S. Sánchez-Giralt, M. Doblado-Calatrava, and A. Merchán-Herrera. Immediate and One-year Results in 35 Consecutive Patients After Closure of Left Atrial Appendage With the Amplatzer Cardiac Plug. *Revista Española de Cardiología (English Edition)*, 66(2):90–97, 2013.
- [83] I. Mahé, L. Drouet, O. Chassany, E. Mazoyer, G. Simoneau, A. L. Knellwolf, C. Caulin, and J. F. Bergmann. D-dimer: a characteristic of the coagulation state of each patient with chronic atrial fibrillation. *Thrombosis research*, 107(1-2):1–6, jul 2002.
- [84] F. Marin, V. Roldan, V. Climent, A. Garcia, P. Marco, and G. Y. Lip. Is Thrombogenesis in Atrial Fibrillation Related to Matrix Metalloproteinase-1 and Its Inhibitor, TIMP-1? *Stroke*, 34(5):1181–1186, may 2003.

- [85] M. Markl, D. C. Lee, M. L. Carr, C. Foucar, J. Ng, S. Schnell, J. C. Carr, and J. J. Goldberger. Assessment of left atrial and left atrial appendage flow and stasis in atrial fibrillation. *Journal of Cardiovascular Magnetic Resonance*, 17(1):M3, 2015.
- [86] M. Markl, D. C. Lee, N. Furiasse, M. Carr, C. Foucar, J. Ng, J. Carr, and J. J. Goldberger. Left Atrial and Left Atrial Appendage 4D Blood Flow Dynamics in Atrial Fibrillation. *Circulation: Cardiovascular Imaging*, 9(9):e004984, sep 2016.
- [87] E. M. Marom, J. E. Herndon, Y. H. Kim, and H. P. McAdams. Variations in Pulmonary Venous Drainage to the Left Atrium: Implications for Radiofrequency Ablation. *Radiology*, 230(3):824–829, 2004.
- [88] A. Masci, M. Alessandrini, D. Forti, F. Menghini, L. Dedé, C. Tomasi, A. Quarteroni, and C. Corsi. A Proof of concept for computational fluid dynamic analysis of the left atrium in atrial fibrillation on a patient-specific basis. *Journal of Biomechanical Engineering*, 142(1), jan 2020.
- [89] A. Masci, L. Barone, L. Dedè, M. Fedele, C. Tomasi, A. Quarteroni, and C. Corsi. The impact of left atrium appendage morphology on stroke risk assessment in atrial fibrillation: A computational fluid dynamics study. *Frontiers in Physiology*, 9(January):1–11, 2019.
- [90] A. Michalska, I. Gorczyca, M. Chrapek, A. Kaplon-Cieslicka, B. Uzieblo-Zyczkowska, K. Starzyk, O. Jelonek, M. Budnik, M. Gawalko, P. Krzesinski, A. Jurek, P. Scislo, J. Kochanowski, M. Kiliszek, G. Gielerak, K. J. Filipiak, G. Opolski, and B. Wozakowska-Kaplon. Does the CHA2DS2-VASc scale sufficiently predict the risk of left atrial appendage thrombus in patients with diagnosed atrial fibrillation treated with non-vitamin K oral anticoagulants? *Medicine*, 99(25), 2020.
- [91] J. Mill, V. Agudelo, A. L. Olivares, M. I. Pons, E. Silva, M. Nuñez-Garcia, X. Morales, D. Arzamendi, X. Freixa, J. Noailly, and O. Camara. Sensitivity Analysis of In Silico Fluid Simulations to Predict Thrombus Formation after Left Atrial Appendage Occlusion. *Mathematics*, 9(18), 2021.
- [92] J. Mill, J. Harrison, B. Legghe, A. L. Olivares, X. Morales, J. Noailly, X. Iriart, H. Cochet, M. Sermesant, and O. Camara. In-Silico Analysis of the Influence of Pulmonary Vein Configuration on Left Atrial Haemodynamics and Thrombus Formation in a Large Cohort. *Lecture Notes in Computer Science (including subseries Lecture Notes in Artificial Intelligence and Lecture Notes in Bioinformatics)*, 12738 LNCS:605–616, jun 2021.

- [93] J. Mill, A. L. Olivares, D. Arzamendi, V. Agudelo, A. Regueiro, O. Camara, and X. Freixa. Impact of flow-dynamics on device related thrombosis after left atrial appendage occlusion. *Canadian Journal of Cardiology*, apr 2020.
- [94] X. Morales Ferez, J. Mill, K. A. Juhl, C. Acebes, X. Iriart, B. Legghe, H. Cochet, O. De Backer, R. R. Paulsen, and O. Camara. Deep Learning Framework for Real-Time Estimation of in-silico Thrombotic Risk Indices in the Left Atrial Appendage. *Frontiers in Physiology*, 12, 2021.
- [95] D. P. Morin, M. L. Bernard, C. Madias, P. A. Rogers, S. Thihalolipavan, and N. A. M. r. Estes. The State of the Art: Atrial Fibrillation Epidemiology, Prevention, and Treatment. *Mayo Clinic proceedings*, 91(12):1778–1810, dec 2016.
- [96] A. Mügge, H. Kühn, P. Nikutta, J. Grote, J. A. Lopez, and W. G. Daniel. Assessment of left atrial appendage function by biplane transesophageal echocardiography in patients with nonrheumatic atrial fibrillation: identification of a subgroup of patients at increased embolic risk. *Journal of the American College of Cardiology*, 23(3):599–607, mar 1994.
- [97] T. V. N. The Dilemma of Peri-Device Leaks After Left Atrial Appendage Closure. *JACC: Clinical Electrophysiology*, 7(12):1585–1587, dec 2021.
- [98] H. Naci, M. Salcher-Konrad, A. Mcguire, F. Berger, T. Kuehne, L. Goubergrits, V. Muthurangu, B. Wilson, and M. Kelm. Impact of predictive medicine on therapeutic decision making: a randomized controlled trial in congenital heart disease. *npj Digital Medicine*, 2(1):17, 2019.
- [99] H. Nakagami, K. Yamamoto, U. Ikeda, T. Mitsuhashi, T. Goto, and K. Shimada. Mitral regurgitation reduces the risk of stroke in patients with non-rheumatic atrial fibrillation. *American heart journal*, 136(3):528–532, sep 1998.
- [100] N. Naksuk, D. Padmanabhan, V. Yogeswaran, and S. J. Asirvatham. Left Atrial Appendage: Embryology, Anatomy, Physiology, Arrhythmia and Therapeutic Intervention. *JACC: Clinical Electrophysiology*, 2(4):403–412, 2016.
- [101] R. Nieuwlaat, A. Capucci, A. J. Camm, S. B. Olsson, D. Andresen, D. W. Davies, S. Cobbe, G. Breithardt, J.-Y. Le Heuzey, M. H. Prins, S. Lévy, and H. J. G. M. Crijns. Atrial fibrillation management: a prospective survey in ESC Member Countries: The Euro Heart Survey on Atrial Fibrillation. *European Heart Journal*, 26(22):2422–2434, nov 2005.

- [102] G. Nucifora, F. F. Faletra, F. Regoli, E. Pasotti, G. Pedrazzini, T. Moccetti, and A. Auricchio. Evaluation of the left atrial appendage with real-time 3-dimensional transesophageal echocardiography: implications for catheter-based left atrial appendage closure. *Circulation. Cardiovascular imaging*, 4(5):514–523, sep 2011.
- [103] M. Nunez-Garcia, G. Bernardino, F. Alarcon, G. Caixal, L. Mont, O. Camara, and C. Butakoff. Fast Quasi-Conformal Regional Flattening of the Left Atrium. *IEEE Transactions on Visualization and Computer Graphics*, 26(8):2591–2602, aug 2020.
- [104] A. L. Olivares, M. I. Pons, J. Mill, J. N. Matos, P. Garcia-Canadilla, I. Cerrada, A. Guy, J. C. Hutchinson, I. C. Simcock, O. J. Arthurs, A. C. Cook, V. L. Fuentes, and O. Camara. Shape Analysis and Computational Fluid Simulations to Assess Feline Left Atrial Function and Thrombogenesis BT - Functional Imaging and Modeling of the Heart. pages 619–628, Cham, 2021. Springer International Publishing.
- [105] T. Otani, A. Al-Issa, A. Pourmorteza, E. R. McVeigh, S. Wada, and H. Ashikaga. A Computational Framework for Personalized Blood Flow Analysis in the Human Left Atrium. *Annals of Biomedical Engineering*, 44(11):3284–3294, 2016.
- [106] M. R. Patel, K. W. Mahaffey, J. Garg, G. Pan, D. E. Singer, W. Hacke, G. Breithardt, J. L. Halperin, G. J. Hankey, J. P. Piccini, R. C. Becker, C. C. Nessel, J. F. Paolini, S. D. Berkowitz, K. A. A. Fox, and R. M. Califf. Rivaroxaban versus Warfarin in Nonvalvular Atrial Fibrillation. *New England Journal of Medicine*, 365(10):883–891, aug 2011.
- [107] J. Pillarisetti, Y. M. Reddy, S. Gunda, V. Swarup, R. Lee, A. Rasekh, R. Horton, A. Massumi, J. Cheng, K. Bartus, N. Badhwar, F. Han, D. Atkins, S. Bommana, M. Earnest, J. Nath, R. Ferrell, S. Bormann, B. Dawn, L. Di Biase, M. Mansour, A. Natale, and D. Lakkireddy. Endocardial (Watchman) vs epicardial (Lariat) left atrial appendage exclusion devices: Understanding the differences in the location and type of leaks and their clinical implications. *Heart rhythm*, 12(7):1501–1507, jul 2015.
- [108] M. I. Pons, J. Mill, A. Fernandez-Quilez, A. L. Olivares, E. Silva, T. de Potter, and O. Camara. Joint Analysis of Morphological Parameters and In Silico Haemodynamics of the Left Atrial Appendage for Thrombogenic Risk Assessment. *Journal of Interventional Cardiology*, 2022:9125224, 2022.

- [109] D. V. Porres, Ó. P. Morenza, E. Pallisa, A. Roque, J. Andreu, and M. Martínez. Learning from the Pulmonary Veins. *RadioGraphics*, 33(4):999–1022, jun 2013.
- [110] A. Qureshi, O. Darwish, D. Dillon-Murphy, H. Chubb, S. Williams, D. Nechipurenko, F. Ataulakhanov, D. Nordsletten, O. Aslanidi, and A. De Vecchi. Modelling Left Atrial Flow and Blood Coagulation for Risk of Thrombus Formation in Atrial Fibrillation. In *Computing in Cardiology*, volume 2020-September. IEEE Computer Society, 2020.
- [111] F. Rahman, G. F. Kwan, and E. J. Benjamin. Global epidemiology of atrial fibrillation. *Nature reviews. Cardiology*, 11(11):639–654, nov 2014.
- [112] V. Y. Reddy, S. K. Doshi, S. Kar, D. N. Gibson, M. J. Price, K. Huber, R. P. Horton, M. Buchbinder, P. Neuzil, N. T. Gordon, and D. R. Holmes. 5-Year Outcomes After Left Atrial Appendage Closure: From the PREVAIL and PROTECT AF Trials. *Journal of the American College of Cardiology*, 70(24):2964–2975, 2017.
- [113] V. Y. Reddy, D. Holmes, S. K. Doshi, P. Neuzil, and S. Kar. Safety of percutaneous left atrial appendage closure: results from the Watchman Left Atrial Appendage System for Embolic Protection in Patients with AF (PROTECT AF) clinical trial and the Continued Access Registry. *Circulation*, 123(4):417–424, feb 2011.
- [114] V. Y. Reddy, S. Möbius-Winkler, M. A. Miller, P. Neuzil, G. Schuler, J. Wiebe, P. Sick, and H. Sievert. Left atrial appendage closure with the Watchman device in patients with a contraindication for oral anticoagulation: the ASAP study (ASA Plavix Feasibility Study With Watchman Left Atrial Appendage Closure Technology). *Journal of the American College of Cardiology*, 61(25):2551–2556, jun 2013.
- [115] G. Rigatelli, M. Zuin, and L. Roncon. Increased Blood Residence Time as Markers of High-Risk Patent Foramen Ovale. *Translational stroke research*, jun 2022.
- [116] V. Roldán, F. Marín, P. Marco, J. G. Martínez, R. Calatayud, and F. Sogorb. Hypofibrinolysis in atrial fibrillation. *American heart journal*, 136(6):956–960, dec 1998.
- [117] L. Rossini, P. Martinez-Legazpi, V. Vu, L. Fernández-Friera, C. Pérez Del Villar, S. Rodríguez-López, Y. Benito, M.-G. Borja, D. Pastor-Escuredo, R. Yotti, M. J. Ledesma-Carbayo, A. M. Kahn, B. Ibáñez, F. Fernández-Avilés, K. May-Newman, J. Bermejo, and J. C. Del Álamo. A clinical

method for mapping and quantifying blood stasis in the left ventricle. *Journal of biomechanics*, 49(11):2152–2161, jul 2016.

- [118] D. N. Salem, P. D. Stein, A. Al-Ahmad, H. I. Bussey, D. Horstkotte, N. Miller, and S. G. Pauker. Antithrombotic therapy in valvular heart disease—native and prosthetic: the Seventh ACCP Conference on Antithrombotic and Thrombolytic Therapy. *Chest*, 126(3 Suppl):457S–482S, sep 2004.
- [119] S. Sanatkhani, S. Nedios, P. G. Menon, A. Bollmann, G. Hindricks, and S. G. Shroff. Subject-Specific Calculation of Left Atrial Appendage Blood-Borne Particle Residence Time Distribution in Atrial Fibrillation. *Frontiers in Physiology*, 12:633135, 2021.
- [120] J. M. Sanchez, A. Lee, K. Bartus, and R. J. Lee. Percutaneous epicardial approach for LAA ligation. *Journal of interventional cardiac electrophysiology : an international journal of arrhythmias and pacing*, oct 2020.
- [121] D. Sánchez-Quintana, J. R. López-Mínguez, Y. Macías, J. A. Cabrera, and F. Saremi. Left atrial anatomy relevant to catheter ablation. *Cardiology Research and Practice*, 2014, 2014.
- [122] A. J. Sanfilippo, V. M. Abascal, M. Sheehan, L. B. Oertel, P. Harrigan, R. A. Hughes, and A. E. Weyman. Atrial enlargement as a consequence of atrial fibrillation. A prospective echocardiographic study. *Circulation*, 82(3):792–797, sep 1990.
- [123] A. Santiago, J. Aguado-Sierra, M. Zavala-Aké, R. Doste-Beltran, S. Gómez, R. Arís, J. C. Cajas, E. Casoni, and M. Vázquez. Fully coupled fluid-electro-mechanical model of the human heart for supercomputers. *International Journal for Numerical Methods in Biomedical Engineering*, 34(12):1–30, 2018.
- [124] J. Saw, A. Tzikas, S. Shakir, S. Gafoor, H. Omran, J. E. Nielsen-Kudsk, J. Kefer, A. Aminian, S. Berti, G. Santoro, F. Nietlispach, A. Moschovitis, I. Cruz-Gonzalez, F. Stammen, T. Tichelbäcker, X. Freixa, R. Ibrahim, W. Schillinger, B. Meier, H. Sievert, and S. Gloekler. Incidence and Clinical Impact of Device-Associated Thrombus and Peri-Device Leak Following Left Atrial Appendage Closure With the Amplatzer Cardiac Plug. *JACC. Cardiovascular interventions*, 10(4):391–399, feb 2017.
- [125] A. Sedaghat, J.-W. Schrickel, R. Andrié, R. Schueler, G. Nickenig, and C. Hammerstingl. Thrombus Formation After Left Atrial Appendage Oc-

clusion With the Amplatzer Amulet Device. *JACC: Clinical Electrophysiology*, 3(1):71–75, 2017.

- [126] A. Sedaghat, V. Vij, B. Al-Kassou, S. Gloekler, R. Galea, M. Fürholz, B. Meier, M. Valgimigli, G. O’Hara, D. Arzamendi, V. Agudelo, L. Asmarats, X. Freixa, E. Flores-Umanzor, O. De Backer, L. Søndergaard, L. Nombela-Franco, A. McInerney, K. Korsholm, J. E. Nielsen-Kudsk, S. Afzal, T. Zeus, F. Operhalski, B. Schmidt, G. Montalescot, P. Guedeney, X. Iriart, N. Miton, J. Saw, T. Gilhofer, L. Fauchier, E. Veliqi, F. Meincke, N. Petri, P. Nordbeck, S. Rycerz, D. Ognerubov, E. Merkulov, I. Cruz-González, R. Gonzalez-Ferreiro, D. L. Bhatt, A. Laricchia, A. Mangieri, H. Omran, J. W. Schrickel, J. Rodes-Cabau, and G. Nickenig. Device-Related Thrombus After Left Atrial Appendage Closure: Data on Thrombus Characteristics, Treatment Strategies, and Clinical Outcomes From the EUROOC-DRT-Registry. *Circulation. Cardiovascular interventions*, 14(5):e010195, may 2021.
- [127] A. Springer, R. Schleberger, F. Oyen, B. A. Hoffmann, S. Willems, C. Meyer, F. Langer, R. B. Schnabel, P. Kirchhof, R. Schneppenheim, and M. D. Lemoine. Genetic and Clinical Predictors of Left Atrial Thrombus: A Single Center Case-Control Study. *Clinical and applied thrombosis/hemostasis : official journal of the International Academy of Clinical and Applied Thrombosis/Hemostasis*, 27:10760296211021171, 2021.
- [128] K. Suwa, T. Saitoh, Y. Takehara, M. Sano, M. Nobuhara, M. Saotome, T. Urushida, H. Katoh, H. Satoh, M. Sugiyama, T. Wakayama, M. Alley, H. Sakahara, and H. Hayashi. Characteristics of Intra-Left Atrial Flow Dynamics and Factors Affecting Formation of the Vortex Flow. *Circulation Journal*, advpub, 2014.
- [129] F. F. Syed, A. Noheria, C. V. DeSimone, and S. J. Asirvatham. Left Atrial Appendage Ligation And Exclusion Technology In The Incubator. *Journal of atrial fibrillation*, 8(2):1160, 2015.
- [130] M. Taina, P. Sipola, A. Muuronen, M. Hedman, P. Mustonen, A.-M. Kantanen, P. Jäkälä, and R. Vanninen. Determinants of Left Atrial Appendage Volume in Stroke Patients without Chronic Atrial Fibrillation. *PLOS ONE*, 9(3):e90903, mar 2014.
- [131] H. Tamura, T. Watanabe, O. Hirono, S. Nishiyama, S. Sasaki, T. Shishido, T. Miyashita, T. Miyamoto, J. Nitobe, T. Kayama, and I. Kubota. Low Wall Velocity of Left Atrial Appendage Measured by Trans-Thoracic

Echocardiography Predicts Thrombus Formation Caused by Atrial Appendage Dysfunction. *Journal of the American Society of Echocardiography*, 23(5):545–552.e1, 2010.

- [132] J. P. Veinot, P. J. Harrity, F. Gentile, B. K. Khandheria, K. R. Bailey, J. T. Eickholt, J. B. Seward, A. J. Tajik, and W. D. Edwards. Anatomy of the normal left atrial appendage: a quantitative study of age-related changes in 500 autopsy hearts: implications for echocardiographic examination. *Circulation*, 96(9):3112–3115, nov 1997.
- [133] F. Veronesi, C. Corsi, L. Sugeng, E. G. Caiani, L. Weinert, V. Mor-Avi, S. Cerutti, C. Lamberti, and R. M. Lang. Quantification of Mitral Apparatus Dynamics in Functional and Ischemic Mitral Regurgitation Using Real-time 3-Dimensional Echocardiography. *Journal of the American Society of Echocardiography*, 21(4):347–354, 2008.
- [134] M. Viceconti, F. Pappalardo, B. Rodriguez, M. Horner, J. Bischoff, and F. Musuamba Tshinanu. In silico trials: Verification, validation and uncertainty quantification of predictive models used in the regulatory evaluation of biomedical products. *Methods*, 185:120–127, jan 2021.
- [135] D. D. Wang, Z. Qian, M. Vukicevic, S. Engelhardt, A. Kheradvar, C. Zhang, S. H. Little, J. Verjans, D. Comaniciu, W. W. O’Neill, and M. A. Vannan. 3D Printing, Computational Modeling, and Artificial Intelligence for Structural Heart Disease. *JACC. Cardiovascular imaging*, 14(1):41–60, jan 2021.
- [136] Y. Wang, Y. Qiao, Y. Mao, C. Jiang, J. Fan, and K. Luo. Numerical prediction of thrombosis risk in left atrium under atrial fibrillation. *Mathematical Biosciences and Engineering*, 17(3):2348–2360, feb 2020.
- [137] Y. A. N. Wang, L. Di Biase, R. P. Horton, T. Nguyen, P. Morhanty, and A. Natale. Left Atrial Appendage Studied by Computed Tomography to Help Planning for Appendage Closure Device Placement. *Journal of Cardiovascular Electrophysiology*, 21(9):973–982, 2010.
- [138] T. Watson, E. Shantsila, and G. Y. H. Lip. Mechanisms of thrombogenesis in atrial fibrillation: Virchow’s triad revisited. *The Lancet*, 373(9658):155–166, jan 2009.
- [139] N. Westerhof, N. Stergiopoulos, M. I. M. Noble, and B. E. Westerhof. *Snapshots of hemodynamics: an aid for clinical research and graduate education*, volume 7. Springer, 2010.

- [140] L. Wu, E. Liang, S. Fan, L. Zheng, Z. Du, S. Liu, F. Hu, X. Fan, G. Chen, L. Ding, and Y. Yao. Relation of Left Atrial Appendage Morphology Determined by Computed Tomography to Prior Stroke or to Increased Risk of Stroke in Patients With Atrial Fibrillation. *American Journal of Cardiology*, 123(8):1283–1286, apr 2019.
- [141] S. Yaghi, A. D. Chang, R. Akiki, S. Collins, T. Novack, M. Hemendinger, A. Schomer, B. M. Grory, S. Cutting, T. Burton, C. Song, A. Poppas, R. McTaggart, M. Jayaraman, A. Merkler, H. Kamel, M. S. V. Elkind, K. Furie, and M. K. Atalay. The left atrial appendage morphology is associated with embolic stroke subtypes using a simple classification system: A proof of concept study. *Journal of cardiovascular computed tomography*, 14(1):27–33, 2020.
- [142] A. Zaccaria, F. Danielli, E. Gasparotti, B. M. Fanni, S. Celi, G. Pennati, and L. Petrini. Left atrial appendage occlusion device: Development and validation of a finite element model. *Medical Engineering Physics*, 82:104–118, 2020.
- [143] L. T. Zhang and M. Gay. Characterizing left atrial appendage functions in sinus rhythm and atrial fibrillation using computational models. *Journal of Biomechanics*, 41(11):2515–2523, aug 2008.

Publications

Journal papers

1. Aguado AM, Olivares AL, Yagüe C, ..., **Mill J**, et al (2019) In silico optimization of left atrial appendage occluder implantation using interactive and modeling tools. *Front Physiol* 10:1–26.
<https://doi.org/10.3389/fphys.2019.00237>
2. **Mill J**, Olivares AL, Arzamendi D, et al (2020) Impact of flow-dynamics on device related thrombosis after left atrial appendage occlusion. *Can J Cardiol*. <https://doi.org/10.1016/j.cjca.2019.12.036>
3. **Mill J**, Agudelo V, Li CH, et al (2021) Patient-specific flow simulation analysis to predict device-related thrombosis in left atrial appendage occluders. *REC Interv Cardiol* 3:278–285.
<https://doi.org/10.24875/RECICE.M21000224>
4. **Mill J**, Agudelo V, Olivares AL, et al (2021) Sensitivity analysis of in silico fluid simulations to predict thrombus formation after left atrial appendage occlusion. *Mathematics* 9:. <https://doi.org/10.3390/math9182304>
5. Morales Ferez X, **Mill J**, Juhl KA, et al (2021) Deep Learning Framework for Real-Time Estimation of in-silico Thrombotic Risk Indices in the Left Atrial Appendage. *Front Physiol* 12:.
<https://doi.org/10.3389/fphys.2021.694945>
6. Pons MI, **Mill J**, Fernandez-Quilez A, et al (2022) Joint Analysis of Morphological Parameters and In Silico Haemodynamics of the Left Atrial Appendage for Thrombogenic Risk Assessment. *J Interv Cardiol* 2022:9125224.
<https://doi.org/10.1155/2022/9125224>
7. Olivares AL, Pons MI, **Mill J**, et al (2021) Shape Analysis and Computational Fluid Simulations to Assess Feline Left Atrial Function and Thrombogenesis BT - *Functional Imaging and Modeling of the Heart*. In: Ennis

DB, Perotti LE, Wang VY (eds). Springer International Publishing, Cham, pp 619–628

8. **Mill J**, Montoliu H, Moustafa AH, et al (2022) Domain expert evaluation of advanced visual computing solutions for the planning of left atrial appendage occluder interventions. medRxiv 2022.04.11.22273553. <https://doi.org/10.1101/2022.04.11.22273553> (submitted, International Journal of Bioprinting)
9. **Mill J***, Harrison J*, Legghe B, Olivares AL, Morales X, Noailly J, Iriart X, Cochet H, Sermesant M, Camara O. In-silico analysis of the influence of pulmonary vein configuration and ostium orientation on left atrial haemodynamics and thrombus formation in a large cohort (In preparation). * shared first authorship.

Peer-reviewed conference papers

1. **Mill J**, Olivares AL, Silva E, et al (2019) Joint Analysis of Personalized In-Silico Haemodynamics and Shape Descriptors of the Left Atrial Appendage BT - Statistical Atlases and Computational Models of the Heart. Atrial Segmentation and LV Quantification Challenges. In: Pop M, Sermesant M, Zhao J, et al (eds). Springer International Publishing, Cham, pp 58–66
2. Genua I, Olivares AL, Silva E, ..., **Mill J**, et al (2019) Centreline-Based Shape Descriptors of the Left Atrial Appendage in Relation with Thrombus Formation BT - Statistical Atlases and Computational Models of the Heart. Atrial Segmentation and LV Quantification Challenges. In: Pop M, Sermesant M, Zhao J, et al (eds). Springer International Publishing, Cham, pp 200–208
3. Morales X, **Mill J**, Juhl KA, et al (2019). Deep learning surrogate of computational fluid dynamics for thrombus formation risk in the left atrial appendage. In International Workshop on Statistical Atlases and Computational Models of the Heart (pp. 157-166). Springer, Cham.
4. **Mill J**, Olivares AL, Noailly J, et al (2019) Optimal Boundary Conditions in Fluid Simulations for Predicting Occluder-Related Thrombus Formation in the Left Atria. In: 6th International Conference on Computational and Mathematical Biomedical Engineering – CMBE2019. Sendai, Japan, pp 256–259.

5. Medina E, Aguado AM, **Mill J**, et al (2020) VRIDAA: Virtual Reality Platform for Training and Planning Implantations of Occluder Devices in Left Atrial Appendages. *Eurographics Work Vis Comput Biol Med*. <https://doi.org/10.2312/vcbm.20201168>
6. Morales X, **Mill J**, Delso G, et al (2021) 4D Flow Magnetic Resonance Imaging for Left Atrial Haemodynamic Characterization and Model Calibration BT - Statistical Atlases and Computational Models of the Heart. MMs and EMIDEC Challenges. In: Puyol Anton E, Pop M, Sermesant M, et al (eds). Springer International Publishing, Cham, pp 156–165
7. Morales X, **Mill J**, Simeon G, et al (2021) Geometric Deep Learning for the Assessment of Thrombosis Risk in the Left Atrial Appendage BT - Functional Imaging and Modeling of the Heart. In: Ennis DB, Perotti LE, Wang VY (eds). Springer International Publishing, Cham, pp 639–649
8. **Mill J**, Harrison J, Legge B, et al (2021) In-Silico Analysis of the Influence of Pulmonary Vein Configuration on Left Atrial Haemodynamics and Thrombus Formation in a Large Cohort. In: Ennis DB, Perotti LE, Wang VY (eds) *Functional Imaging and Modeling of the Heart*. Springer International Publishing, Cham, pp 605–616
9. Planas E, **Mill J**, Olivares AL, et al (2022) In-silico Analysis of Device-Related Thrombosis for Different Left Atrial Appendage Occluder Settings BT - Statistical Atlases and Computational Models of the Heart. Multi-Disease, Multi-View, and Multi-Center Right Ventricular Segmentation in Cardiac MR. In: Puyol Antón E, Pop M, Martín-Isla C, et al (eds). Springer International Publishing, Cham, pp 160–168
10. Albors C*, **Mill J***, et al (2022) Sensitivity Analysis of modelling wall configurations to analyze the mechanisms of thrombus formation (submitted, STACOM 2022). *first authorship shared.
11. Morales X, Albors C, **Mill J***, Camara O (2022) Optimization of left atrial appendage occlusion device placement through physics-informed neural networks (submitted, STACOM 2022).
12. Saiz M, **Mill J**, Harrison J et al (2022) Unsupervised machine learning exploration of morphological and haemodynamic indices to predict thrombus formation in the left atrial appendage (submitted, STACOM 2022).

